Advances in using three-dimensional mantle convection models to address global geochemical cycles

James Panton

School of Earth and Environmental Sciences
Cardiff University

Submitted in partial fulfilment of the requirements for the degree of

Doctor of Philosophy

October 2020

ABSTRACT

Mantle convection models are now well established as a tool for addressing geochemical problems. This thesis focusses on understanding the processes which affect long-standing observations relating to the U-Th-Pb, K-Ar and He isotope systems.

Pb isotope ratios display a linear trend in ^{207}Pb/^{204}Pb vs ^{206}Pb/^{204}Pb space, the gradient of which corresponds to the pseudo-isochron age. Scatter in the data also encodes information about differentiation which has not previously been considered. The problem is addressed by including processes which have not been incorporated into geodynamic models before, allowing for the timing and magnitude of different fractionation processes to be investigated. A combination of preferential removal of Pb from the mantle after 3.0 Ga and recycling of U from the continental reservoir after 2.4 Ga achieves a higher degree of scatter than previous modelling methods whilst maintaining a pseudo-isochron age similar to mantle derived rocks.

Noble gases constrain mantle degassing from the ^{40}Ar/^{36}Ar composition of the atmosphere and the degassing rate of primordial ^{3}He. The noble gas composition of oceanic basalts provides additional constraints on mantle convection models. The degassing efficiency of the mantle, dynamic effects, and the initial distribution of trace elements in the mantle are all considered for the effect they have on the noble gas composition of mantle derived rocks and the atmosphere. Recycling of noble gases (incomplete degassing) and high degrees of processing are shown to be important for the development of MORB-like helium ratios. In the standard model setup the present day flux of ^{3}He is higher than what is predicted for Earth but can be reduced through increased processing, increased degassing efficiency or increased segregation of basalt to the lower mantle. It is shown that an Earth-like atmospheric ^{40}Ar/^{36}Ar can be achieved through a combination of mantle and continental crust degassing, provided the system is sufficiently enriched in ^{36}Ar. A model initialised with a heterogeneous distribution of trace elements can produce the range of helium ratios observed in Ocean Island Basalts.

The Pb pseudo-isochron age and associated scatter are not directly correlated to the density of basalt in the lower mantle, but to consequences of increased basalt density. Re-melting times generally get longer for excess lower mantle basalt densities greater than 4% (relative to harzburgite) and for longer re-melting times the Pb pseudo-isochron age increases. The degree of scatter correlates to the fraction of recycled basaltic material which constitutes the melt, which in turn has a non-linear dependency on the lower mantle density of basalt.

DECLARATION

This work has not been submitted in substance for any other degree or award at this or any other university or place of learning, nor is being submitted concurrently in candidature for any degree or other award.

STATEMENT 1

This thesis is being submitted in partial fulfilment of the requirements for the degree of PhD.

STATEMENT 2

This thesis is the result of my own independent work/investigation, except where otherwise stated, and the thesis has not been edited by a third party beyond what is permitted by Cardiff University's Policy on the Use of Third Party Editors by Research Degree Students. Other sources are acknowledged by explicit references. The views expressed are my own.

STATEMENT 3

I hereby give consent for my thesis, if accepted, to be available online in the University's Open Access repository and for inter-library loan, and for the title and summary to be made available to outside organisations.

Signed ______________________________ (candidate) Date ______________

ACKNOWLEDGEMENTS

The completion of this PhD thesis has been a long, and sometimes trying, process. However, any ill sentiment that I may have had towards 'it' along the way is dwarfed by the overwhelming sense of fulfilment and achievement that I feel and the myriad of enriching experiences I have had. As all doctoral students know, behind the name on the front of the thesis are a wealth of others who have shared their knowledge, experience, time and friendship to shape what is in the following pages.

Officially Huw Davies has been my supervisor for the past 4 years, but in reality he has been much more than this. Huw's relentless enthusiasm for science, gentle encouragement and whole-hearted openness has been instrumental in me completing this work. Our on-topic discussions are always thought provoking and our off-topic discussions always enlightening.

I owe a great deal of thanks to Matthew Price for familiarising me with TERRA and many of the other tools which I have used over the years, correcting dodgy code, and taking time to discuss my work even when he was no longer working at the university.

I also thank the many people with whom I have had constructive discussions, especially Morten Andersen, Tim Elliott, and Don Porcelli. Our extended sessions with Huw and Matthew are always as stimulating as they are enjoyable.

My PhD has been funded by partially by the consortia, 'Mantle volatiles: processes, reservoirs and fluxes' (grant number NE/M000397/1 and NE/M000427/1), part of the wider Deep Volatiles Programme, and also by the School of Earth and Environmental Sciences, Cardiff University. I have also received funds from the Deep Volatiles Programme. Thank you to all those involved in securing this funding and ensuring the success of the project, which it was a pleasure to be a part of.

I extend my thanks to the teams who run and support Supercomputing Wales, ARCCA, and the UK's national supercomputing facility, ARCHER. The simulations that I have conducted would not have been possible without access to such systems and their continued maintenance and support has ensured a largely problem-free experience.

Support throughout my PhD journey has not been limited work-related discussion. The students who started at the same time as me and those who were already well into their studies really made Cardiff feel like my new home. Heated T-Ball tournaments, rambling lunch chats and F@5 made even the dreariest of weeks enjoyable. General chit-chat and tea/coffee breaks have been an essential part of daily life in the department. Particular thanks goes to the Tea Club (Bob, Joanna, Kate, Liam and Matt), the Brodies Bunch (Aidan, Harry, Liam, Max, Will), the Bute Park Bobble (hosted by Duncan) and to my office companions, Evie and Lei, with honourable mentions for Chantelle, Chris, G^2, Dr JA, James W, Jamie G, Jamie P, Jian, Manny, Matt H, Nairn, Niall, Nick, and Sarah. Thank you all.

Away from the department, I'm lucky to have a great network of family and friends to keep me motivated and my life full. A special thanks to my friends Granger and Ant, for always injecting a healthy dose of adventure, boardgames and sneaking into whatever we find ourselves doing and of course thank you to my family for feigning interest in my work and for all the things they do for me, big and small.

Finally I want to thank Lucy, who has accompanied me through the toughest year of my studies. Thank you for picking me up when morale ran low, for celebrating with me when riding a high, for encouraging me and motivating me to do my best and to be the best person I can be. Thank you for all you do.

For Nana, Grandad, and Gung Gung.

TABLE OF CONTENTS

CHAPTER 1

INTRODUCTION

Geoscientists think of the solid Earth as a dynamic system, ever changing through creative and destructive processes. The expressions of some of these processes have long been known about, even if the underlying cause has not been well understood. For example earthquakes and volcanic eruptions are sudden, often catastrophic, events that have perpetually affected human civilisations. Other dynamic processes required us to look more closely in order to be revealed, for example the erosion of solid rock and deposition of sediment. It was the slow nature of these processes that kept them hidden from human observation for so long, but also what led people to question how old Earth really is. Modern geoscience now allows us to investigate processes not only at the surface, but also deep within Earth's interior, and the interconnectivity of the two. This introductory chapter intends to give a short background on Earth's history and structure, followed by an overview of the current understanding of mantle dynamics from geophysical observation and geochemical inference.

1.1 Formation

1.1.1 Accretion

Following the formation of the sun from a swirling disk of inter-stellar gases and dust, smaller accumulations of material began to form from what remained. The accumulations combined and grew, developing a stronger gravitational field and attracting more material to become planetesimals. These bodies coalesced with one another to form increasingly large objects, one of which would become the proto-Earth. Collisions were violent and the melting that they induced allowed for geochemical fractionation to occur, ultimately leading to the segregation of Earth's metallic core from its silicate mantle (de Vries et al. 2016). Being relatively dense the metallic core 'sank' to the centre of the newly formed planet with the less dense silicates 'floating' on top of it. As well as steady accretion, enormously energetic giant impacts are thought to have contributed to the formation of Earth. One such collision, between the proto-Earth and a Mars-sized planetesimal, is hypothesised to have ejected the material which now makes up the moon (Hartmann and Davis 1975).

1.1.2 Composition

The bulk composition of Earth cannot be measured directly, so we rely on inference from geochemical data in order to determine a best fit. Having a good model for Earth's bulk composition, or more precisely the bulk silicate Earth (BSE) composition, is clearly important when we are modelling mantle chemistry. It is assumed that Earth, the planets, the sun and the many meteorites which populate our solar system all accreted from the solar nebula. Based on this assumption, by comparing the composition of primordial (used in this sense to mean relatively unchanged since accretion) terrestrial material to that of meteorites, we can begin to estimate what sort of material Earth is made from. One method of the determining the BSE composition is by analysing the composition of basalts and peridotites and their relationship through melting (Ringwood 1962). This 'pyrolite' model for the BSE composition has striking similarities to the composition of CI carbonaceous chondrites.

In another class of models, Earth's BSE composition is compared to that of CI chondrites. These CI chondritic models have been popular due to the similarities in the major-element composition of CI chondrites and Earth (Taylor 1964). Ratios of some refractory lithophile elements (RLEs), such as the rare earth elements, U and Th are similar for many different types of carbonaceous chondrites (McDonough and Sun 1995). It is therefore reasonable to assume that the BSE shares similar ratios of these elements. BSE is estimated from the intersection of the chondritic ratio and trends measured in upper mantle material such as primordial komatiites, mantle xenoliths and massif peridotites (Fig. 1.1).

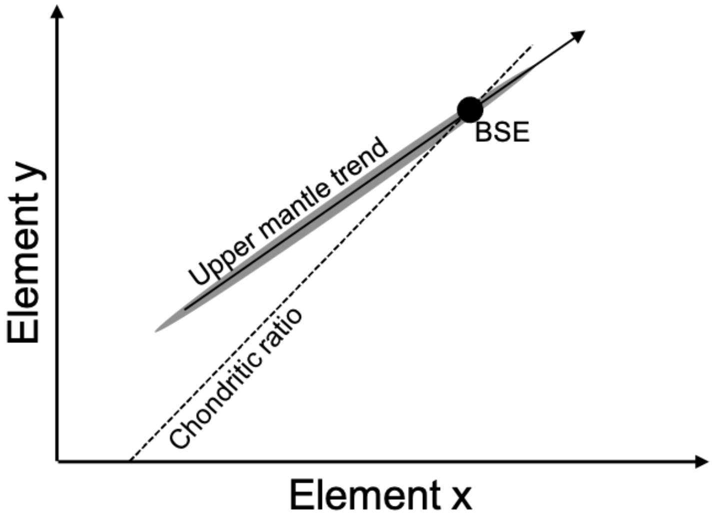

Fig. 1.1 Schematic diagram of how BSE is estimated from the chondritic ratio of RLEs and the trend in measurements taken from upper mantle samples.

However, accretion solely of CI chondrites fails to predict Earth's upper mantle Si, Mg, and volatile trace element compositions which are depleted relative to CI chondrites (Gast 1960). Early differentiation may account for the depletion of volatiles trace-elements, concentrating them in the lower mantle where they are not sampled by shallow volcanism (Gast et al. 1964). For many this is unsatisfactory as geophysical evidence points towards considerable communication of material between the upper and lower mantle (French and Romanowicz 2015). Heterogenous accretion has been offered up as a solution to Earth's unique composition (Wänke 1981; Allègre et al. 2001). This is characterised by accreting material gradually becoming more oxidising and having a variable composition with time. Core formation plays a key role here in extracting volatile elements from the newly forming mantle. It has also been suggested that depletion in Si relative to CI chondrites may be partially accommodated by Si entering the core during its formation (O'Neill 1991). The extent to which this may happen is uncertain, though it is unlikely the core can accommodate all of the mantle's Si depletion (McDonough and Sun 1995).

A limitation of both pyrolite and CI chondrite models for predicting BSE is that they are biased towards predicting the composition of the upper mantle. If the mantle is well mixed, with no chemical difference between the upper and lower mantle then this limitation does not matter. However, if the lower mantle is compositionally distinct and perhaps a 'hidden reservoir'

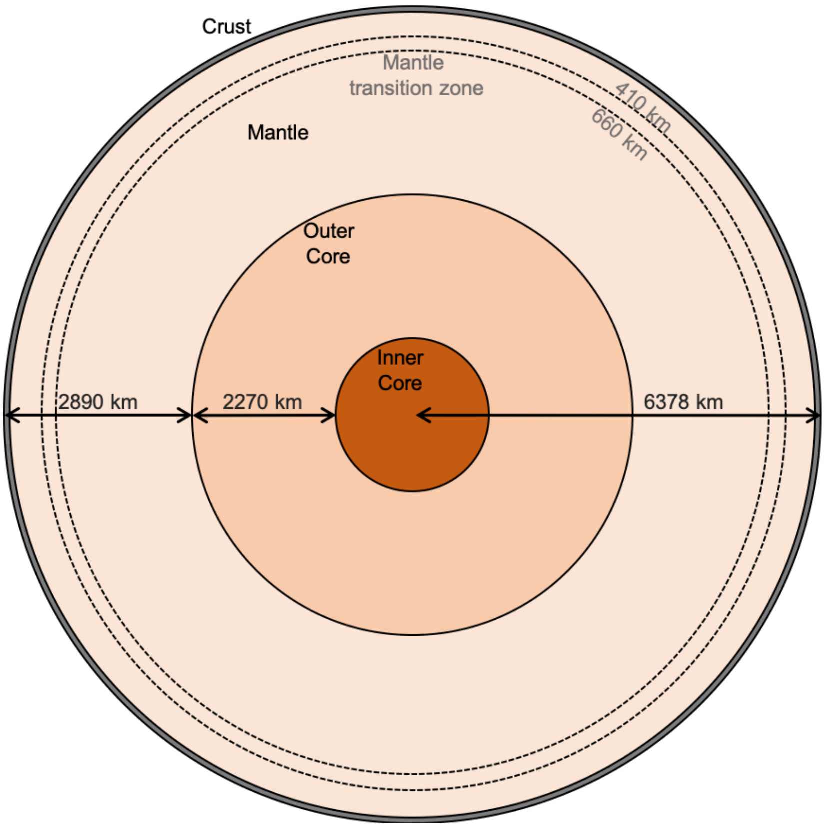

Fig. 1.2 Earth's interior structure, not to scale. Dashed grey lines indicate the 410 km and 660 km seismic discontinuities.

of certain elements, then this is a problem. Lyubetskaya and Korenaga (2007) began to address this problem by considering the effect that scatter in geochemical data from the upper mantle affects estimates of BSE and more recently Korenaga (2009) presented a method by which to estimate BSE if a hidden geochemical reservoir exists within the mantle.

1.2 Earth's structure

Earth scientists have discerned that Earth can be broken down in to 3 basic layers; the crust, the mantle and the core. This section will give a brief overview of each, particularly the mantle as this is the region of focus of this body of work.

1.2.1 The crust

The crust is the skin of the Earth (Fig.1.2), and comes in two distinct flavours. Continental crust covers around 35% of Earth's surface and on average is 35-40 km thick, though may reach 70 km thick beneath mountain ranges. It is low in density (~2.8 g cm^{-3}) and long-lived, with some samples displaying isotopic ages of up to 4 Gyr. The precise history of continental crust extraction from the mantle is still an open discussion. Arguments range from rapid early formation, to slow continuous formation, to episodic formation (Fig.1.3). When continental crust is created by the melting of mantle material it become enriched in incompatible elements. Depending on the element, the continental crust may contain up to 20-70% of the Earth's entire budget, despite constituting just 1% of the total volume (Rudnick and Gao 2013). The second type of crust is oceanic crust. This covers the remaining 65% of Earth's surface and is significantly thinner than continental crust, generally around 7 km. Compared to continental crust, oceanic crust is short lived, with the oldest currently on Earth having formed 300 Myr ago. Oceanic crust is in a constant and cycle of creation and destruction, forming along Earth's network of mid-ocean ridges, and being recycled into the mantle at subduction zones. This constant cycling is extremely important in geodynamics and geochemistry, as it gives a line of communication between the inaccessible mantle and the surface.

1.2.2 The mantle

The mantle is by far Earth's largest layer, accounting for 84% of the total volume. It sits between the base of the crust and the top of the core, with a thickness of 2890 km. Due to its great thickness, the average density of the mantle increases with depth from 3.3 g cm^{-3} near the base of the crust to 5.7 g cm^{-3} at the core-mantle boundary (CMB) (Dziewonski and Anderson 1981). Although the mantle is not directly observable, its structure and composition is indirectly inferred numerous Earth science disciplines. The uppermost portion of the mantle which lies directly beneath the crust is cool and stiff, giving it the term lithospheric mantle. This is underlain by the remaining portion of the upper mantle, which extends to depths of 670 km and finally the lower mantle. Seismology has revealed global scale structures such as seismic discontinuities at depths of 410 and 660

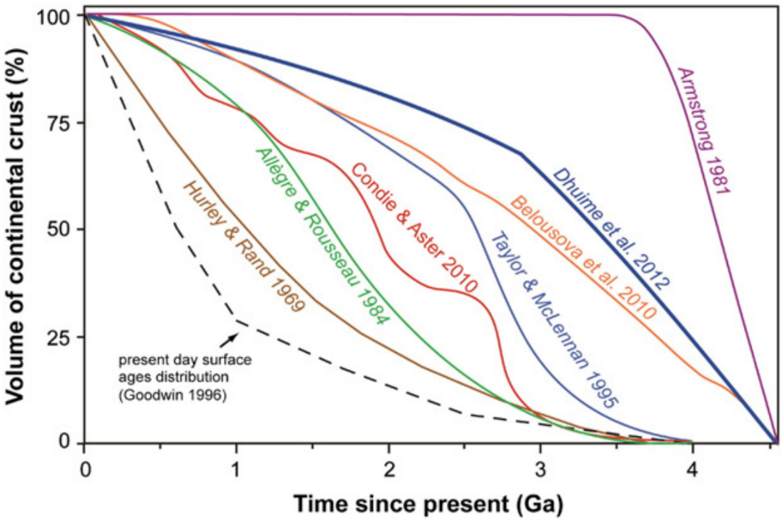

Fig. 1.3 A summary of various crustal growth models with a comparison to age distribution of continental crust observed today. Reproduced from Hawkesworth et al. (2013).

km. Mineral physics experiments have shown these seismic anomalies to be caused by mineral phase changes at these depths (Ringwood 1968), thus giving the mantle transition zone its name (Fig.1.2). As the resolution of seismic data at depth has improved, seismology has been able to confirm hypothesised mantle structures, such as hot mantle plumes rooted deep in mantle that rise up beneath hot-spot volcanos (French and Romanowicz 2015). We have also been able to image subducted oceanic crust penetrating the mantle transition zone, confirming communication of material between the upper and lower mantle. The mantle studies community is currently puzzling over deep mantle structures. The largest of these are the large low-shear-velocity provinces (LLSVPs) of which there are two, one under continental Africa and the other beneath the Pacific Ocean (Cottaar and Lekić 2016). There is debate whether LLSVPs are purely thermal, chemical, or thermo-chemical structures and what their origins are. Also currently subject to much scrutiny are the ultra low-velocity zones (ULVZs) which are found just above the CMB (Yu and Garnero 2018).

On the timescales that humans are used to the mantle can more or less be considered a solid, with low flow rates of just a few cm yr^{-1}, however on timescales of hundred of millions to billions of years the mantle behaves more like a fluid. The crystals that make up mantle rocks deform under various creep mechanisms which over geologic time equates to viscous flow of the mantle. Apart from the thin lithospheric portion, the upper mantle is characterised by relatively low viscosities (10^{21} Pa s), compared to the lower mantle, which has viscosities up to a few orders of magnitude higher. Strain rates in the mantle are extremely low, generally of the order $10^{-14} - 10^{-16}$ s^{-1}, despite the huge stresses that mantle material experience. There are two major sources of thermal energy that drive mantle convection. One is conductive heat transfer across the CMB from the hot core to cooler mantle, and the second is internal heating from the decay of radioactive isotopes. The principal extant radioactive nuclides are ^{40}K, ^{232}Th, ^{235}U, and ^{238}U. Each of these are extremely long lived, with ^{235}U having the shortest half life at 7.04×10^8 years, and ^{232}Th having the longest half life at 1.40×10^{10} years. Due to the nature of radioactive decay, thermal input by this mechanism would have been twice what it is today around 3 Byr ago. The implication of this is that the mantle is likely to have convected more vigorously in the past. The Rayleigh number associated with mantle convection is generally to be of the order 10^9, indicating strong, turbulent convection.

1.2.3 The core

Earth's core lies at the centre of the planet and is separated in to the liquid outer core and solid inner core (Fig. 1.2. Both layers are metallic with the inner core being mostly iron (12.8 g cm^{-3}) and the outer core being largely composed of a nickle-iron alloy (9.9 g cm^{-3}). The core is therefore the densest region of Earth's interior. Conductive heat transfer across the CMB causes the core to cool down and so over time the inner core has been growing as more of the outer core solidifies. Convection within the outer core is thought to be the source of Earth's magnetic field (Malkus 1968), shielding the surface of the planet from harmful solar winds which may otherwise strip the atmosphere of crucial ozone. The magnetic field has also proved useful to Earth scientists, as magnetisation of rocks records the last time they were exposed to temperatures above a certain threshold (the Curie point). The recording of magnetic reversal in oceanic crust ultimately became evidence for theory of plate tectonics, back when it was a contentious subject.

1.3 Chemistry and geodynamics

Numerical geodynamic models are becoming increasingly powerful tools in narrowing down answers to long standing questions. However numerical models by themselves are of little use, they require input from multiple fields of mantle studies. Seismology and geodesy provides knowledge on the depth and density of the mantle and together with mineral physics and geochemistry gives information on viscosity and phase transformations that are crucial if we want to model an Earth-like mantle. By measuring the composition of mantle derived rocks, geochemistry gives strong constraints on melting and the composition of the mantle. Geochemistry does not only provide information on what comes out of the mantle, but also on what is input to the mantle at subduction zones. It is the link between between geochemistry and geodynamics that this thesis is primarily concerned with. In this section I will give a brief outline chemical geodynamics in order to frame this body of work.

1.3.1 Chemical geodynamics

In its most simple form, Earth can be broken down in to six distinct geochemical reservoirs. The core at the centre, the mantle, oceanic crust continental crust, the oceans, and the atmosphere. Despite their distinctions, these reservoirs are linked together through various magmatic, tectonic and chemical processes. The mantle is arguably the centre of all these reservoirs as the largest and most interconnected. The pulling apart of plates at mid-ocean ridges accommodates the creation of new oceanic crust composed of mid-ocean ridge basalt (MORB), which are enriched in incompatible elements due to partial melting of the upper mantle, fluids and gasses associated with the production of MORBs are added to the atmosphere and oceans. Hydrothermal circulation in the warm crust and sediments surrounding mid-ocean ridges exchanges material between the crust and ocean and also causes alteration of the upper portions of oceanic crust. New oceanic crust is also created in the form of ocean-island basalts (OIBs), which are the surface expression thermal upwellings. Sediments that are created from the erosion of continental crust are ultimately deposited in the oceans. At subduction zones ocean crust is recycled into the mantle, along with a portion of the sediments that have accumulated on its surface. Partial melting of this subducted material and the overlying mantle wedge gives rise to volcanic arcs, running parallel to subduction zones on the continental side. It is here that new continental crust is generated, although this is more mafic in composition than the relatively felsic material that makes up the majority Earth's continents.

The chemical inputs to the mantle play an important role in determining the chemistry of volcanic rocks that are sampled at the surface. With knowledge of what goes in and comes out of the mantle, geochemists have inferred how recycled material becomes distributed throughout the volume until it is ultimately re-sampled. Isotopic analysis of MORBs and OIBs reveals that while they are both generated from the partial melting of mantle material, their trace element compositions are distinctly different. The trace element composition of MORBs is globally uniform, indicating that they are all derived from a single, approximately chemically homogeneous reservoir. OIBs share a very similar major element composition with MORBs, both being basaltic in composition, however the trace element composition of OIBs is highly variable, with different ocean islands having unique compositions, which in themselves may have high degrees of variability (Sun and McDonough 1989). The wide compositional spectrum that OIBs cover ranges from high enrichment similar to continental crust, to highly depleted even more so than MORBs, and everything in between. These compositional differences between MORBs and OIBs have led to conceptual models of the structure of Earth's mantle. Classically this has been interpreted as meaning enriched OIB requires a separate, un-depleted reservoir to MORB. In the past this has been accounted for by a layered mantle model. This separates the mantle into an upper and lower region with the lower mantle having a largely un-depleted, primordial composition and the upper mantle being the depleted complimentary reservoir to the continental and oceanic crust (Fig. 1.4). In this model there is little communication between the two reservoirs with only small amount of lower mantle material being entrained into plumes that rise off of the thermo-chemical boundary between the upper and lower mantle. Variable amounts of entrainment of lower mantle material mixed with upper mantle material could explain much of the compositional variability between oceanic basalts, in particular those compositions that lie on a binary mixing line between depleted MORB source and bulk silicate Earth (BSE) compositions. This model has fallen out of favour since seismic tomography has imaged mantle plumes rooted near the CMB that rise into

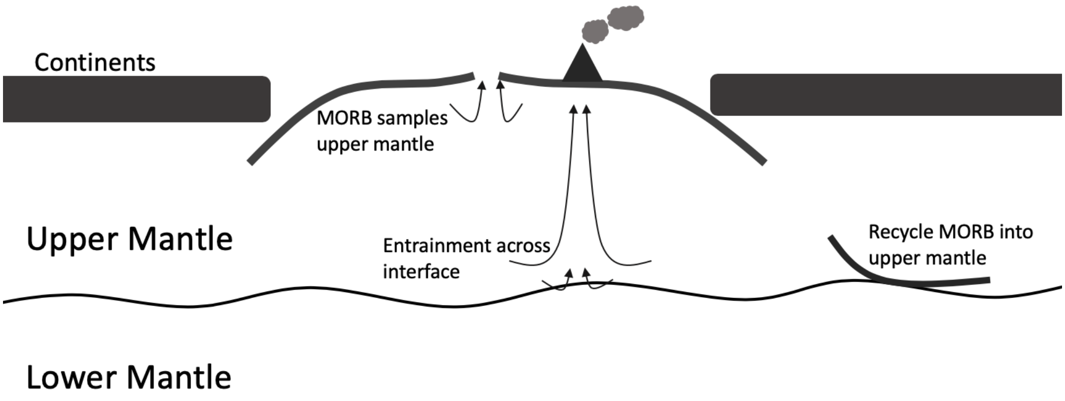

Fig. 1.4 Schematic of layered mantle model. Plumes that feed OIBs rise of the thermal boundary layer separating the upper and lower mantle, entraining small amount of primordial material.

the upper mantle (French and Romanowicz 2015), and subducted oceanic crust penetrating the mantle transition zone (Grand et al. 1997). Additionally, numerical geodynamic modelling finds that layered mantle convection is highly unlikely given the predicted conditions in Earth's mantle (Van Keken and Ballentine 1998; Ferrachat and Ricard 2001).

Other models to explain the heterogeneous compositions oceanic basalts include the 'plum pudding' model, in which blobs of relatively enriched material exist throughout the lower mantle (Morris and Hart 1983). The blobs may be sampled by plumes and various degrees of melting, plus addition of some recycled oceanic lithosphere accounts for the range of observed compositions. It is now well accepted that the composition of OIBs representsthe mixing of various end member compositions. Originally these compositions were defined as depleted MORB mantle (DMM), high μ (high $^{238}U/^{204}Pb$ HIMU), and enriched mantle types 1 and 2 (EM1, EM2) (Zindler and Hart 1986). DMM is generally associated with the upper mantle compositions, HIMU is thought to represent recycled oceanic crust, and enriched mantle compositions may be caused by recycling of continental material or metasomatic processes. These four end member compositions form the vertices of a tetrahedron in $^{87}Sr/^{86}Sr$-$^{143}Nd/^{144}Nd$-$^{206}Pb/^{204}Pb$ space (Hart et al. 1992), within which most measured mantle arrays plot. A fifth composition, focal zone (FOZO), has also been identified, plotting within the bounds of the tetrahedron. FOZO is so called as most mantle arrays converge back to this point, implying that this could be the common mantle source (Stracke et al. 2005). Analysis of multiple isotope systems can help geochemists to conceive a given sample's history and with the use of geodynamic models it may be possible to determine the validity of certain hypotheses or even come up with new ones.

Essentially what chemical geodynamics boils down to is understanding the sources and distribution of chemical heterogeneity in Earth's mantle. A major source of heterogeneity into the mantle is via subduction of enriched material, which may be chemically enriched oceanic crust or continentally derived sediments. The composition of material that enters the mantle is well known from geochemical measurements of seafloor sediments and oceanic basalts close to subduction zones. The composition of arc lavas must also be considered to understand how subducting material is heterogeneously stripped of trace elements (Pearce and Peate 1995). Once recycled material has entered the mantle, it may still be observed seismically, but this only gives us a snapshot of subducted material in time. Another potential source of heterogeneity in the mantle is from material that has managed to evade being processed by melting and so carries a primordial geochemical signature. Evidence for the existence of such material includes high helium ratios (^{3}He/^{4}He) in OIBs (Jackson et al. 2017), a constraint that will be investigated in this thesis. It is commonly thought that if material with a primordial composition exists, it would likely be intrinsically dense in a layer near the base of the mantle (Labrosse et al. 2007; Lee et al. 2010). The seismically observed LLSVPs and ULVZs are potentially primordial structures that are the source of ancient isotopic signatures, however their true origins are poorly understood. Geochemical and geophysical observations alone can only tell us so much about the dynamics of Earth's mantle. The oceanic basalt record only stretches back as far as around 200 Myr (Müller et al. 2008), and seismic observations give us just a snapshot of the mantle as it is at present day. Numerical geodynamic models are a powerful tool which can be used to test parameter spaces and hypotheses and attempt to understand observations that have been made.

Integrating geochemistry into numerical geodynamic models is not a new idea, with one of the earliest examples being Christensen and Hofmann (1994). This paper is still regularly cited today, a testament to how influential it has been. Before this, geochemical problems would often be interrogated using box models. Sophisticated statistical box models (eg. Rudge et al. (2005)) allow for rigorous investigation of parameters due to their comparative low running costs compared to numerical models. Where numerical geodynamic models excel is in investigating mantle structures, dynamical feedbacks, and the effects of earth-like geometries on mantle processing. Early examples were conducted in 2D cartesian box geometries (Christensen and Hofmann 1994; Ferrachat and Ricard 2001). The use of 2D cylindrical domains (eg. Xie and Tackley (2004a)) greatly improved the resemblance of an Earth-like mantle in numerical models, however their nature meant that either mantle volume may be preserved or the ratio of the surface to the CMB, but not both. More advanced models have used 2D spherical annulus domain which removes this problem (Hernlund and Tackley 2008; Nakagawa and Spiegelman 2017), however these fail to capture the intricacies of mantle convection in 3D spherical geometry. Consider a pile of intrinsically dense, slow moving material at the CMB. In 2D geometry the only way for higher velocity material to move past the dense pile is to go over the top, whereas in 3D geometry there is also the possibility for material to flow around the sides of the piles. The computational expense of carrying out whole-Earth scale calculations in three dimensions is not trivial, so it is not surprising that few studies have been carried out integrating geochemistry with numerical geodynamic models (Price et al. 2019).

1.4 Thesis outline

In writing this thesis I hope to improve on current methods for combined geodynamic and geochemical modelling. Doing so will unlock greater understanding of the processes which govern mantle composition. In the following chapters I will specifically be addressing the U-Th-Pb system, and the noble gases He and Ar. Detailed explanations of these isotope systems can be found in the relevant chapters, but I will provide a brief explanation here in order to contextualise the thesis.

The U-Th-Pb systems is of particular interest because of the linear trend of Pb isotopes ratios measured in MORBs and OIBs. The regression through the data in ^{207}Pb/^{204}Pb-^{206}Pb/^{204}Pb space (the Pb pseudo-isochron) corresponds to an age, however the meaning of the age is poorly understood. Additionally there is scatter in the measured Pb ratios which may be another important constraint on Pb evolution in the mantle. Simple numerical mantle convection models which include only fractionation due to melting are unable to explain the relatively low pseudo-isochron age obtained from measurements of Pb isotope ratios in mantle derived rocks. Both deep and shallow processes may play a role in producing the Pb distribution that is observed. Sequestration of enriched, recycled oceanic crustal material in the deep mantle has been identified as a mechanism for producing highly radiogenic Pb ratios (Christensen and Hofmann 1994; Brandenburg and Van Keken 2007). Near the surface, recycling of continental U and preferential removal of Pb from the convecting mantle have also been identified as processes which may be key in producing the measured mantle Pb distribution and associated Pb pseudo-isochron age (Xie and Tackley 2004b; Brandenburg et al. 2008). It is well accepted that oceanic crustal material can be transported all the way to the CMB upon subduction, therefore these shallow geochemical processes have implications for the composition of the whole mantle. In this thesis U recycling and Pb removal will be modelled as separate processes, allowing for their effects to be examined individually. The methods used allow for preliminary estimates of mantle U and Pb fluxes to be estimated using mantle convection models for the first time. I will also investigate the effect that long-term sequestration of recycled oceanic crustal material in the lower mantle has on the Pb pseudo-isochron and the associated scatter. Investigating these shallow and deep processes allow two of the long-standing Pb paradoxes (eg. Kramers and Tolstikhin (1997)) to be addressed. The first of these paradoxes is that measured Pb ratios from the upper crust and mantle almost exclusively plot to the right of the 4.55 Ga geochron, with no significant complementary reservoir which plots to the left of the geochron being detected (Sinha and Tilton 1973). The second paradox is that the measured upper mantle Th/U is lower than what is implied by Pb isotopes (Galer and O'Nions 1985). Simultaneously considering both of these paradoxes will help in better understanding Earth's U-Th-Pb system.

The inert nature of noble gases makes them ideal to track in numerical mantle convection models. They also impose strong constraints on mantle degassing and the composition of mantle derived melts. The present day degassing rate of primordial ^{3}He provides a limit on how much undegassed material is currently being processed while the atmospheric ratio of radiogenic ^{40}Ar to primordial ^{36}Ar gives information on the total amount of degassing over Earth's history (Allégre et al. 1996). Noble gas ratios measured in mantle derived rocks can be used to help us understand melting history and mixing associated with the source. The ratio ^{3}He/^{4}He is particularly distinct in MORBs and OIBs, with MORBs being characterised by an almost uniform $^{3}He/^{4}He$ (Farley and Neroda 1998) and OIBs recording a much wider range (Kurz et al. 1982; Stuart et al. 2003). The differences between MORB and OIB compositions may be implicit of a heterogeneous mantle, composed of a mixture of enriched, depleted and primordial material. Through our knowledge of the noble gas composition of the mantle questions arise, for example is the lower mantle a reservoir of high ^{40}Ar (Allégre et al. 1996) and does the He composition of OIBs indicate sampling of a primordial reservoir (Anderson 1998b). Developing numerical models which can better simulate Earth's noble gas cycles may help pave the way in providing answers to some of these questions.

Work in this thesis focusses on understanding how the degassing efficiency and the resampling rate of melts affects global cycle of noble gases. Degassing throughout Earth's history is poorly constrained but is important for the evolution of the atmospheric and mantle noble gas compositions. Resampling rates are controlled by retention of recycled oceanic crust in the lower mantle affecting how often material may be fractionated and degassed. I investigate various degrees of degassing efficiency and lower mantle basalt density to assess their effect on the noble gas composition of the mantle, melts and the atmosphere. I also explore the effect that early mantle scale differentiation could have on the present day noble gas composition of melts.

CHAPTER 2

MODELLING METHODS

2.1 Introduction

The aim of this chapter is to give the reader an introduction to the mantle convection code, TERRA which has been used through this body of work. In here I will give a brief overview of convection in Earth's mantle. I will then give a quick overview of the history of TERRA followed by the governing equations for the model. I will then detail how particles are use in TERRA and explain the melting process, which is critical to this body of work.

2.2 Mantle convection

It has long been known that Earth's interior is not static, but is in motion. Direct evidence for this comes from earthquakes, which can be a devastating manifestation of the unsettled mantle. Advances in seismic tomography have even allowed us to image the velocity structure of the inside of our planet. Seismically fast regions beneath collisional plate boundaries are interpreted as dense subducted oceanic crust (Grand et al. 1997), and columnar seismically slow regions interpreted as relatively warm and low density mantle upwellings in the form of plumes (Rhodes and Davies 2001; French and Romanowicz 2015). Mantle flow is driven by heating, both from the cooling of Earth's core and from internal heating due to the decay of radioactive nuclides. This heating provides the energy required to induce movement within and on the boundaries of the crystals that constitute mantle material. Example types of such movement include dislocation creep, dislocation slide, and diffusion creep (Gordon 1965; Weertman 1978; Cordier 2002). These be-have as plastic deformation mechanisms, so the mantle can be approximated as a viscous fluid, allowing for it to be modelled numerically.

2.3 TERRA

2.3.1 A brief history

Numerical mantle modelling was pioneered by Mckenzie et al. (1974) and opened the door to the rapid development of a new field. From simple iso-viscous box shaped models more complex ones were born that better resemble the conditions of Earth's mantle. TERRA, a 3D finite element code, was initially developed by Baumgardner (1983). Over the years there have been some major improvements to the original code that have evolved it to its current capable state.

- Parallelisation of the code by Bunge and Baumgardner (1995) removed the limitations of running the code on a single processor, allowing for faster calculation at higher resolutions. In turn this has allowed for increasingly more Earth-like parameters to be investigated.

- Variable viscosity, dependent on temperature and pressure, was introduced by Yang (1997).

- The incorporation of plate motion history models as a surface boundary condition by Bunge et al. (1998) evolved TERRA from a mantle convection code. It allows for the reproduction of Earth's tectonic features such as mid-ocean ridges and subduction zones.

- The introduction of tracer particles to the code by Stegman et al. (2002) has allowed users to address geochemical questions using the geodynamic code.

- A method for mesh refinement at the upper and lower boundaries was added by **Davies2008a** and TERRA was also benchmarked for accuracy in an associated paper (Davies et al. 2013).

- Most recently melting was added to the models by van Heck et al. (2016) which has allowed even more complex geochemical questions to be addressed. This is key to this body of work.

All of these developments have made TERRA into a robust, capable code that has found uses in addressing many of the questions that the geodynamic community poses. In this thesis I will now be using it to address questions from the geochemical community.

2.3.2 Governing equations for numerical modelling

As mentioned in 2.2, the mantle is modelled as a viscous fluid, but with high viscosities on the order of $\approx 10^{18} - 10^{22}$ Pa s. Such viscosities allow for certain assumptions to be made. The Prandtl Number (ratio of viscous to inertial forces, Pr) is extremely large due to the high viscosity and may be assumed to be infinite so inertial terms may be set to zero. Coriolis forces may also be ignored due to high Ekman numbers (ratio of viscous to Coriolis forces) of the order $\approx 10^9$. Finally the centripetal force, which is smaller than the Coriolis force may also be disregarded. The mantle convection equations are a modification of the Navier-Stokes equations for viscous fluid flow (e.g. **Baumgardner1985**; Baumgardner (1983)). For compressible cases the equations for conservation of mass momentum and energy are,

$$\frac{\partial \rho}{\partial t} + \nabla \cdot (\rho \mathbf{u}) = 0 \tag{2.1}$$

$$0 = -\nabla P + \rho \mathbf{g} + \nabla \cdot \tau \tag{2.2}$$

$$\frac{\partial T}{\partial t} = -\nabla \cdot (T\mathbf{u}) - (\gamma - 1) T \nabla \cdot \mathbf{u} + \frac{[\tau : \nabla \mathbf{u} + \nabla \cdot (k \nabla T) + \rho H]}{\rho C_v}. \tag{2.3}$$

Given the assumption of a Newtonian fluid, the constitutive law is

$$\tau = \eta \left\{ \nabla \boldsymbol{u} + (\nabla \boldsymbol{u})^T - \frac{2}{3} \mathbb{I} (\nabla \cdot \boldsymbol{u}) \right\}. \tag{2.4}$$

An appropriate equation of state is given by

$$P = P(\rho, T). \tag{2.5}$$

Variables and parameters in the above are density ρ, time t, the fluid velocity $\mathbf{u}$, pressure P, acceleration due to gravity $\mathbf{g}$, deviatoric stress field τ, temperature T, Grüneisen parameter γ, specific heat at constant volume C_v, thermal conductivity k, radiogenic heat production H, and dynamic viscosity η.

The anelastic approximation may be applied to filter seismic waves as they act on extremely short timescales compared to that of mantle convection (Jarvis and Mckenzie 1980). The time dependency of Eq. 2.1 is set to zero, giving

$$\nabla \cdot (\rho \boldsymbol{u}) = 0 \tag{2.6}$$

The equations can be further simplified by applying the Boussinesq approximation, under which density variations are neglected unless coupled with **g**. If we assume incompressibility of the mantle (Mckenzie et al. 1974), that is that the density does not change with changes in pressure and temperature, then the divergence of velocity is to zero,

$$\nabla \cdot \boldsymbol{u} = 0. \tag{2.7}$$

Under this formaulation changes in density arise principally from thermal effects (Spiegel and Veronis 1960),

$$\Delta\rho = \alpha\rho\left(T_{\text{av}} - T\right) \tag{2.8}$$

where α is the coefficient of thermal expansion and T_{av} is reference temperature for a radial layer. Given these approximations the equations for conservation of mass, momentum and energy can be simplified to

$$\nabla \cdot \boldsymbol{u} = 0 \tag{2.9}$$

$$\nabla \cdot \left(\eta \left\{\nabla \boldsymbol{u} + (\nabla \boldsymbol{u})^T\right\}\right) - \nabla P + \alpha\rho\left(T_{\text{av}} - T\right) g = 0 \tag{2.10}$$

$$\frac{\partial T}{\partial t} + u \cdot \nabla T - \kappa \nabla^2 T - \frac{H}{C_v} = 0. \tag{2.11}$$

Additionally conservation of bulk composition C is ensured with the equation

$$\frac{\partial C}{\partial t} = -\nabla \cdot (Cu). \tag{2.12}$$

The Rayleigh number is a dimensionless number that describes the vigour of convection in a system. In this work models are heated internally as well as basally. For such cases the Rayleigh number is given by

$$Ra_H = \frac{\rho^2 g\alpha H h^5}{k\kappa\eta} \tag{2.13}$$

where h is the distance between the top and bottom radial shells (representing the surface and the CMB) and κ is thermal diffusivity.

The use of the above equations requires boundary conditions for both the CMB and the surface. The CMB is the interface between the base of the mantle and the liquid outer core, for this I prescribe a free slip boundary condition as it is assumed there will be no shear stresses caused by the low viscosity outer core. This sets the tangential stress at the boundary to zero (Eq. 2.14) and makes the boundary impermeable, that is that the normal component of velocity at the boundary is zero (Eq. 2.15).

$$\sigma \cdot \mathbf{n} \cdot \mathbf{t} = 0, \tag{2.14}$$

$$\mathbf{u} \cdot \mathbf{n} = 0 \tag{2.15}$$

In the above σ is the stress tensor, $\mathbf{n}$ and $\mathbf{t}$ are the normal and tangential vectors. The temperature at the CMB is fixed across the whole layer, generally 3000 K for incompressible models.

As the thickness of the continental crust is much less than that of the mantle, it can be assumed that the continental crust is included as part of the top most radial layer of the mantle. For this boundary I generally also prescribe the free slip boundary condition and assign a lower temperature of 300 K. An alternative to free slip is using reconstructions of plate motion to impose velocities ($\mathbf{u}_P$) at the surface.

$$\mathbf{u} = \mathbf{u}_P. \tag{2.16}$$

This forcing of plates generates features that are associated with plate tectonics such as hot linear zones at ridges and cool linear downwellings at subduction zones and deep rooted mantle plumes. While these features make for a more Earth-like regime, they are imperfect as forcing the plates from above imparts a shearing at the top of mantle which does not exist in reality. However, models which can self consistently generate a plate tectonic-like regime cannot reproduce the geographic positions of our past or

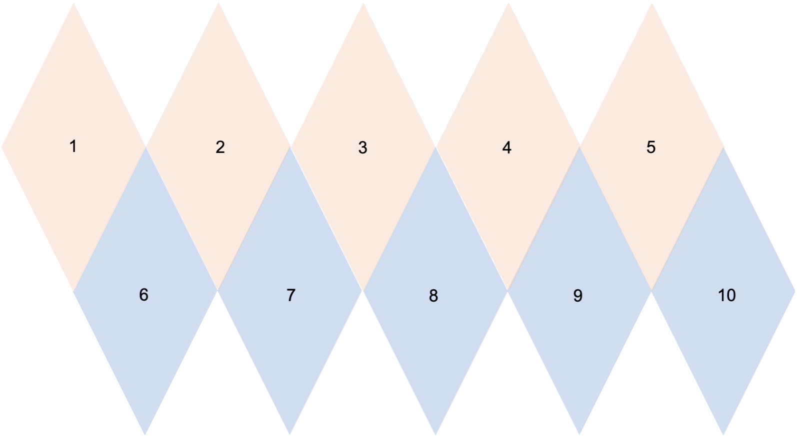

Fig. 2.1 Numbered icosahedral diamonds that are the basis of the TERRA grid. Red diamonds have a vertex located at the north pole and blue diamonds have a vertex located at the south pole.

present continental and oceanic crust (Crameri and Tackley 2015). Examples of plates motion history models include Merdith et al. (2017) with plate motion histories between 1000 Myr and 520 Myr, and Young et al. (2018) with plate motion histories betwen 410 Myr and 0Myr.

2.3.3 The TERRA grid

The basis of the TERRA grid is a regular icosahedron composed of 10 diamonds (Fig. 2.1) each of which is formed of 2 equilateral triangles. Each diamond has one vertex that located at either the north or south pole. The icosahedron is projected onto a sphere to give an approximation of Earth's shape (Fig. 2.2a). The first refinement of the grid to provide greater lateral resolution is achieved by joining the midpoints of each triangle along great circles, forming four smaller triangles (Fig. 2.2b). This refinement creates a mesh that has about four times as many triangles and nodes (vertices) as the original, with each triangle being of approximately similar proportions. Repetition of this process allows for increasingly fine resolution to be achieved whilst maintaining an almost perfectly uniform grid spacing (Fig. 2.2c, 2.2d). In each case all of the nodes are surrounded by 6 triangles except for the 12 vertices of the original icosahedron which are surrounded by 5. The number of edges that each original triangle edge is split into is referred to as mt. For example, Fig. 2.2b, 2.2c, 2.2d have $mt = 2, 4, 8$ respectively.

To extend into three dimensional space, the spherical mesh is repeated at different radii between the surface and CMB. The 3D finite element cells

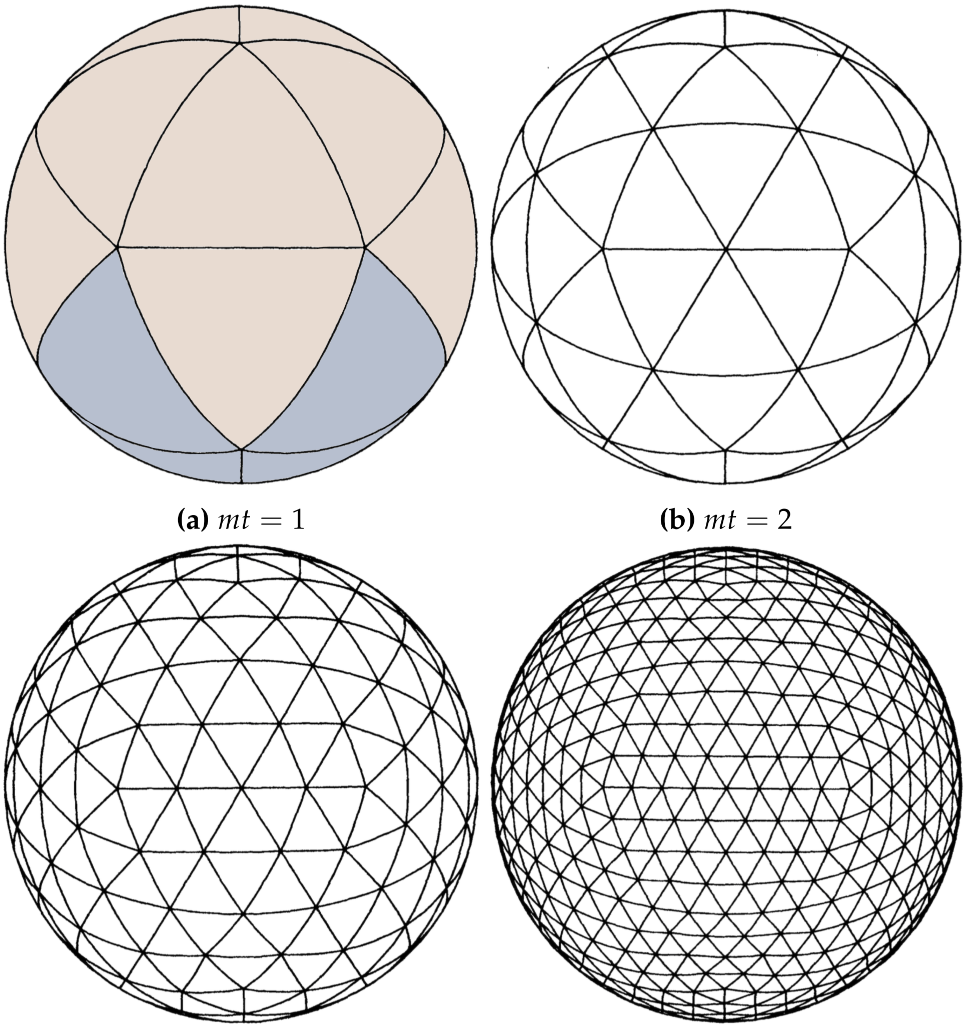

(a) $mt = 1$ **(b)** $mt = 2$

(c) $mt = 4$ **(d)** $mt = 8$

Fig. 2.2 (a) The original icosahedron projected onto a sphere, colours reflect the diamonds in Fig. 2.1. (b-d) Recursive refinement of the TERRA grid.

are therefore triangular prisms in between the radial shells and the number radial layers (nr) is equal to the number of radial shells minus one.

For the best numerical stability, it is important to choose nr that gives the finite element cells an aspect ratio close to 1 (Yang 1997). In order to achieve this and to have a ratio of CMB to surface radii the same as Earth's (0.546), $nr = mt/2$ is the optimum configuration. Table 2.1 details the average radial and lateral resolutions that are achieved for various mt. With both nr and mt known it is possible to calculate the total number of nodes

$$n_{nodes} = (nr + 1)(10mt^2 + 2) \tag{2.17}$$

Table 2.1 Number of global nodes, and resolution for different mt.

mt	**nodes**	**Average Spacing (km)**		
		CMB	**Surface**	**Radial**
16	23,058	261.9	479.4	361.2
32	174,114	131.0	239.8	180.6
64	1,351,746	65.6	119.9	90.3
128	10,649,730	32.7	59.9	45.2
256	84,541,698	16.4	30.0	22.6
512	673,710,594	8.2	15.0	11.3

and the total number of finite element grid cells

$$n_{cells} = 20nr \times mt^2. \tag{2.18}$$

As mt increases, the computational requirements also increase. The number of processes required for a given calculation is given by

$$n_{proc} = \left(\frac{mt}{nt}\right)^2 \frac{10}{nd} \tag{2.19}$$

where nt is the number of grid interval along the edge of a local subdomain and nd is the number of diamonds that are mapped to a local process (either 5 or 10).

2.4 Particles

2.4.1 Particle information

Tracer particles are used in the model to carry information on bulk chemistry and trace elements. The particles are advected through the model using a second-order Runge-Kutta method which produces negligible error in particle location, even after running for 20 mantle overturn times (Stegman et al. 2002). A schematic showing particles in a cell can be seen in Figure 2.3. Information for each particle is stored in a line of an array. The basic information held in the array is three values to indicate the particle's position in the model and a value for the mass that the particle represents. The mass that a particle represents is assigned when the particles are initialised and is equal to the volume of the cell multiplied by the density and divided by the number of particles in that cell. The mass of a particle then does not change unless a particle is split or merged (further explanation of this process can be found in 2.4.2). There is then also space assigned to hold information on:

- Bulk composition: This takes a value between 0 and 1 with zero being fully depleted in basalt (harzburgitic) and 1 being completely enriched in basalt.
- Temperature: Interpolated to the particle from the grid.
- Melt age: The time that the particle last underwent a melt event or received melt.
- Melt zone counter: Counts the number of time a particle has been in a melting zone.
- Melt fraction: Saves the degree of melting experienced during the last melt event.
- Radiogenic heating: The amount of thermal energy produced by radioactive decay on the particle during a given time step.

Each particle also stores the abundance of certain isotopes of interest. Four radioactive isotopes are tracked in this body of work, ^{40}K, ^{232}Th, ^{235}U, and ^{238}U. The stable isotopes at the end of their decay chains, ^{40}Ar, ^{208}Pb, ^{207}Pb, and ^{206}Pb respectively, are also tracked. Radioactive parent isotopes decay following the decay equation, from which the new abundance of daughter isotopes can also be calculated.

$$P_{\mathrm{n}} = P_0 e^{-\Delta t \lambda_P} \tag{2.20a}$$

$$D_{\mathrm{n}} = D_0 + ((P_0 - P_{\mathrm{n}}) R_{\mathrm{P:D}}) \tag{2.20b}$$

In the above, P_{n} and D_{n} are the new abundances of parent and daughter isotopes, P_0 and D_0 are the old abundances of the parent and daughter isotopes, Δt is the time step, λ_P is the decay constant, and $R_{\mathrm{P:D}}$ is the ratio of parent to daughter isotopes (Table 2.2). There is little use in tracking any other isotopes in the decay chains as their half lives are short compared to the half lives of the original isotopes. The decay chains of ^{232}Th, ^{235}U, and ^{238}U include a number of alpha decays, producing ^{4}He which is also tracked. Information on radioactive particles can be found in Table 2.2. I also track

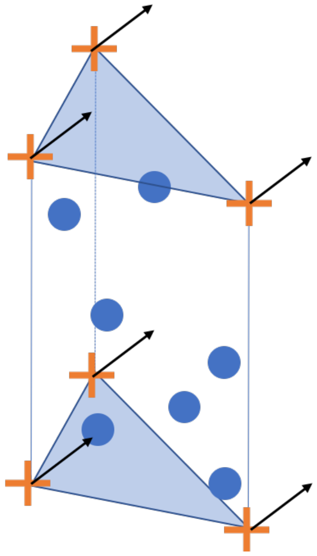

Fig. 2.3 Schematic of a finite element cell. Nodes are represented by orange crosses, and particles by blue circles. Arrows show the velocity field which is calculated on the grid.

Table 2.2 Information about radioactive isotopes

	$t_{1/2}$ (Gyr)	Decay energy (MeV)	Daughter	P:D	^{4}He/decay
^{40}K	1.25	1.34	^{40}Ar	0.1048	-
^{232}Th	14.1	42.66	^{208}Pb	1	6
^{235}U	0.704	46.40	^{207}Pb	1	7
^{238}U	4.47	51.70	^{206}Pb	1	8

^{3}He, ^{36}Ar, and ^{204}Pb, all of which are primordial stable isotopes, i.e. they have present since Earth's accretion.

Particles may be passive or active. Passive particles are simply advected through the model and do not affect the flow. If particles are active then attributes that they carry may affect the flow. An example of this is bulk composition affecting local density.

The radioactive isotopes that are tracked are also the principal producers of radiogenic heat in Earth's mantle. Tracking these radioactive isotopes gives the additional advantage of being able to heat the mantle heterogeneously, depending on the amount of radioactive decay occurring in a cell for any given time step. The energy imparted per decay of each isotope is listed in Table 2.2. With such a heating regime the heating rate of the mantle decreases over time with decreasing abundances of radioactive isotopes.

2.4.2 Splitting and merging

If particles were left unchecked advecting through the model there is a possibility some cells would end up with no particles while other would end up with many. To prevent this from happening, there is an upper and lower limit set on how many particles may exist in a cell at any one time. If the lower limit, generally set to 3, is exceeded then all particles in that cell will split to double the number of particles in the cell. Each new particle inherits half the mass of the original particles. Trace element isotopes are also shared evenly between the two particles. Attributes such as the bulk composition, melt age and melt zone counter are copied from the old particle to the new one. The new particle is positioned in the same cell as the old one but mirrored about the z axis.

If the upper limit of particles is exceeded then merging of particles must occur. Particles are selected to be merged based on their positions in the cell. When particles merge, attributes such as their mass and trace element abundances are summed, while the location and bulk composition are taken as an average of the two particles, weighted by their masses. The attributes of melt age and melt zone counter are copied at random from one of the particles.

2.4.3 Melting

The self-consistent melting process in TERRA is described in van Heck et al. (2016). As it is critical to this body of work I will reiterate it in detail here. The melting process is implemented to ensure conservation of energy, mass, bulk composition, and abundance of trace elements. A simple linear solidus (Fig. 2.4), dependent on depth z, and composition C, is defined by

$$T_{\text{solidus,dry}}(z, C) = T_{\text{meltsurf}} + zT_{\text{meltslope}} + (1 - C)T_{\text{meltcomp}} \tag{2.21}$$

where $T_{meltsurf}$ = 1200 K, $T_{meltslope}$ = 2.5 K km^{-1}, and $T_{meltcomp}$ = 500 K. Each time step, every particle in the melting zone (set to be the top 135 km unless otherwise stated) is checked to see if it is above the solidus. For particles that are above the solidus, melting will occur. In order to conserve energy the bulk composition of the particle must be changed rather than the temperature. The composition of a particle following a melting event will be the composition of the solidus for the particle's temperature. The new composition (C_n) of a

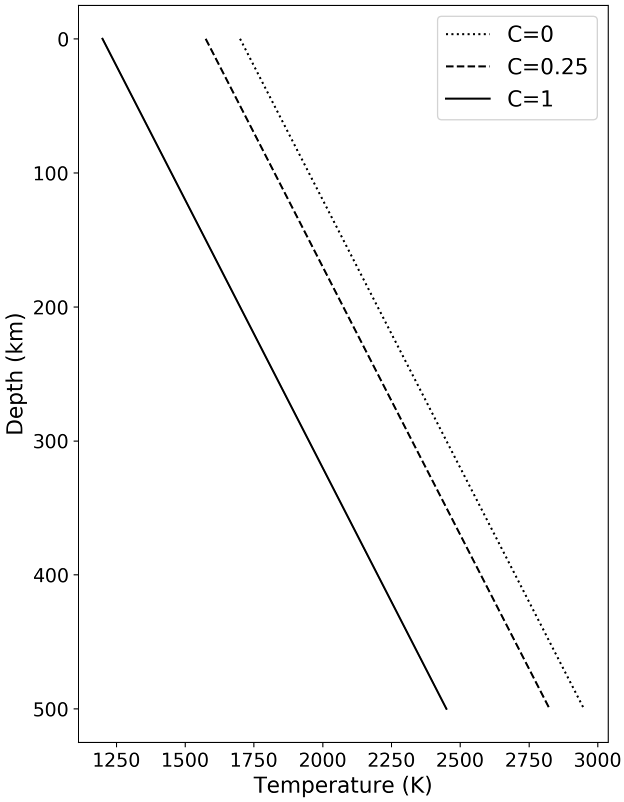

Fig. 2.4 Depth and compositional dependent melt curve. The solidi has a slop of 2.5 K km^{-1} and a difference of 500 K between $C = 0$ and $C = 1$ compositions.

melting particle is therefore

$$C_n = C(T) \tag{2.22}$$

under the assumption that the particle is in thermal equilibrium with the new solidus (T). Note that for a melting particle the compositional value will alway decrease, i.e. the particle becomes more depleted in basaltic component. This depletion may occur up to $C = 0$, at which point the particle is so refactory in composition that it can no longer melt. While the current melting process does conserve energy, it neglects the effects of latent heat and thermal advection due to melt movement. These processes would only have a small effect on the thermal evolution of calculations so it is reasonable to discount them.

The degree of melting F is given by

$$F = C_0 - C_n \tag{2.23}$$

with C_0 being the original bulk composition. The amount of melt that a melting particle produces is calculated by multiplying the mass of the particle by the degree of melting. The C that is lost from the particle forms a 'melt package' with composition of basalt ($C = 1$) which moves chemistry away from the melting particle(s) in cells vertically above (Fig. 2.5b). This differs from the melting implementation in other models by moving chemical information, rather than the melting particles, to the surface (eg. Christensen and Hofmann (1994) and Brandenburg et al. (2008)). Melt is instantaneously migrated to the surface, a good approximation considering that the average time step is around 150 kyrs for models run at $mt = 256$, or around 500 kyrs for models runs at $mt = 128$. The melt is added to particles that are not yet completely enriched ($C \neq 1$). If all particles in the surface cell are completely enriched in basaltic component, then the cell below is searched for particles to accept the melt until all the melt has been accommodated (Fig. 2.5c). The total amount of melt that needs to be accommodated is dictated by the melt volume. The melting and receiving particles do not change mass during the melting process, only chemical information is exchanged and the melting age of the particles changed to the current time. This reflects the subsidence of the melt column as basaltic material is emplaced at the surface.

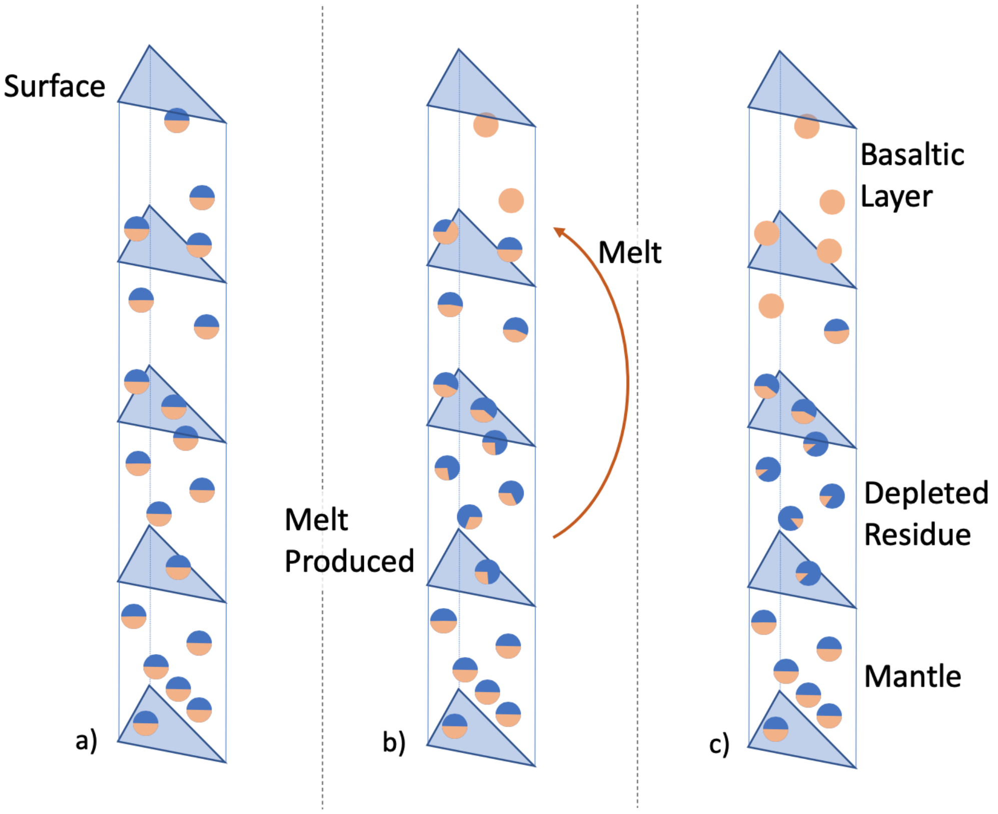

Fig. 2.5 Schematic of the melting process in TERRA. Four radial finite element cells are shows with the top most cell being at the surface. Circles represent particles with red indicating basaltic component and blue indicating harzburgitic (depleted) component. Only a few particles are drawn per cell for simplicity. (a) Shows the particles before melting occurs, in this instance all the particles have $\approx C = 0.5$. In (b) a melting has taken place and basaltic material has been moved from the melting particles to those in the surface layer. This leaves the melting cells depleted in basaltic component and the surface layer enriched. In (c) further melting has taken place. The surface layer is now completely enriched in basalt and the layer beneath is being filled with basalt. There is a clear basalt layer, which is also enriched in incompatible trace elements, underlain by a depleted layer harzburgitic layer.

Trace elements are also removed from the melting particle in the melt package according to

$$A_m = \frac{FA_0}{F + (D_i(1 - F))} \tag{2.24}$$

where A_m is the number of atoms of an isotope to be removed from the melting particle, F is the degree of melting (Eq. 2.23), A_0 is the initial number of atoms of the isotope on the particle, and D_i is the partition coefficient for isotope. The melting process therefore fractionates isotopes that have different partition coefficients.

2.5 Conclusion and Solution Scheme

The reader should now have a good idea of the how a mantle simulation runs in TERRA, from the governing equations (2.3.2) to the melting processing (2.4.3). In subsequent chapters there will be information on more detailed methods. Below is an outline of the order in which the equations are solved in a time step.

- Particles advected using interpolation of velocity field to particle
- Conduct melting on particles that are above the solidus and move isotopes accordingly.
- The pressure field is calculated from the pressure and temperature fields.
- The equations for the conservation of mass and momentum (Eqs. 2.9,2.10) are solved simultaneously for velocity **u** and pressure P.
- The equation for conservation of energy (Eq. 2.11) is solved for rate of change of temperature T.
- Advance time step.

CHAPTER 3

INFLUENCES ON THE LEAD COMPOSITION OF MANTLE-DERIVED ROCKS

Abstract

Lead isotopes display broad correlations that correspond to an isochron ′age′ (τ_{Pb}). For mid-ocean ridge basalts (MORBS), the best fit line in $^{207}Pb/^{204}Pb$ v $^{206}Pb/^{204}Pb$ space corresponds to τ_{Pb} just under 2 Gyr, but the exact meaning of this ′age′ is debated. We attempt to decipher this information by tracking Pb, U and Th isotopes in 3D spherical mantle convection models with self-consistent melting. In addition to reconciling τ_{Pb}, we also consider the observed scatter of Pb ratios and the mantle Pb paradoxes. The effect of using exaggerated partition coefficients to model multiple geochemical processes, as has been used in previous studies, is compared against new methods for modelling the recycling U from the continents to the mantle and sequestering Pb to the continental reservoir. Our method allows for the magnitude and timing of different fractionation effects to be considered individually. All the models utilising exaggerated Pb partition coefficients, no matter when they are applied, do not fit the observed scatter. Models which both recycle U from the continent to the mantle after the great oxygenation event (2.4 Ga), and remove Pb from melts into the continent after the onset of plate tectonics (3.0 Ga), are found to generate scatter that better resembles that seen in MORBs and also maintain a low τ_{Pb} near to 1.9 Gyr. In the best case for the parameters that have been investigated this corresponds to 1.1×10^{14} mol of ^{235}U and 4.6×10^{15} mol of ^{238}U recycled from the continents into the mantle from 2.4 Ga and Pb removal rates of $\sim 2.5 \times 10^{5}$ mol ^{204}Pb yr^{-1} since

3.0 Ga. Our results suggest that the recycling of U steadily increased as the atmosphere and ocean became more oxidised.

Declarations

The work on this chapter is in preparation as a paper under the title, Investigating influences on the Pb pseudo-isochron using 3D mantle convection models, Panton, J., Davies, J. H., Andersen, M., Elliott, T., Porcelli, D., Price, M. G.

Author contributions and declarations: James Panton is the main author of this work and undertook the numerical modelling, data processing, and analysis. Huw Davies, Morten Andersen, Tim Elliott, and Don Porcelli all assisted with supervision of the manuscript, providing feedback and constructive comments. Matthew Price contributed code that made this work possible.

3.1 Introduction

Measurements of isotope ratios provide geochemists with a window into the deep Earth. They record processes that act upon rocks and the time scales that these processes act over. Information is stored in the form of chemical heterogeneity. One way that chemical heterogeneity is generated is thorough melting, the majority of which takes place beneath mid-ocean ridges. Eruption of melt here generates mid-ocean ridge basalts (MORBs), which constitute the mafic oceanic crust. The upper mantle is left depleted in incompatible elements as this is thought to be the source region for ridge volcanism (Hofmann 1997). Although heterogeneity exists within MORBs, they are thought of as being relatively chemically homogenous when compared to ocean island basalts (OIBs) (Sun and McDonough 1989). OIBs can show both enrichment and depletion in their trace elements composition compared to MORB compositions. For a time it was widely accepted that in order to accommodate these two different compositions there must be two separate source reservoirs. The solution was a layered mantle separated into upper and lower parts (Turcotte et al. 2001; Albarede 1998). In this model ridge volcanism is fed by the well mixed, depleted upper mantle, hence the similarities in MORB composition across the globe. The lower mantle is thought of as being volatile rich, less depleted and less well mixed than the upper mantle. Mantle plumes which form on the boundary between the two layers are the source of intra-plate volcanism that produces OIBs. The plumes may entrain some lower mantle material, explaining the enriched compositions of OIBs. The upper and lower mantle convect separately in this model, so there is little mixing between the two reservoirs over time. The layered mantle model has largely fallen out of favour now, due to evidence for whole mantle convection from seismic tomography. Seismically fast regions, interpreted as old, cold subducted slabs, have been imaged penetrating the mantle transition zone and descending into the lower mantle (Grand et al. 1997). Mass balance dictates that material must also be exchanged from the lower mantle to the upper mantle. Seismic tomography also images columnar slow regions, reaching across upper and lower mantle, interpreted as mantle plumes (Rhodes and Davies 2001; French and Romanowicz 2015). Both plumes and subducted slabs crossing the mantle transition zone demonstrate some level of communication between the upper and lower mantle, indicating that the layered mantle hypothesis is not applicable to Earth. Indeed, numerical geodynamic models with Earth-like parameters fail to produce layered mantle convection (Van Keken and Ballentine 1998). The revelation that subducted lithosphere could penetrate into the lower mantle brings along an explanation for the high degree of heterogeneity observed in OIBs as recycled material can introduce heterogeneity into the deep mantle which in turn can be resampled by plumes.

It is generally accepted now that OIBs represent a mixture of different mantle compositions. The most well accepted classification was originally laid out by Zindler and Hart (1986) and defines end member mantle compositions by their geochemical compositions. HIMU is characterised by high μ ($\mu \equiv {}^{238}\text{U}/{}^{204}\text{Pb}$) and so has the most radiogenic Pb ratios. DMM (depleted MORB mantle) is formed from the extraction of oceanic crust and features very low Sr and Pb ratios. Also defined are EM1 and EM2 (enriched mantle types 1 and 2). Different sources of recycled material contribute different isotopic signatures, allowing geochemists to interpret where the observed heterogeneity originates from in some cases. For example, highly radiogenic Pb isotope ratios (${}^{206}\text{Pb}/{}^{204}\text{Pb} > 20.5$), associated with the HIMU end member composition, are thought to indicate input from recycled oceanic crust (White 1985).

Geochemists measure isotope ratios in a variety of different isotope systems but Pb isotope ratios, and the U-Th-Pb system in general, have historically been of particular interest (Gast et al. 1964; Tatsumoto 1966). The isotopes ^{238}U, ^{235}U, and ^{232}Th decay into different isotopes of lead - ^{206}Pb, ^{207}Pb, and ^{208}Pb respectively, at different rates. The relative ingrowth rates of each radiogenic Pb isotope differ due to the different half lives and concentrations of each parent isotope. Of these three radioactive isotopes, ^{235}U has the shortest half life at 7.04×10^8 yr , followed by ^{235}U at 4.468×10^9 yr, and ^{232}Th at 1.405×10^{10} yr. Additionally there is a stable, non-radiogenic isotope - ^{204}Pb. ${}^{208}\text{Pb}/{}^{204}\text{Pb}$ and ${}^{206}\text{Pb}/{}^{204}\text{Pb}$ are also useful as they contain information on the time integrated ${}^{232}\text{Th}/{}^{238}\text{U}$ (κ), recording important events in Earth's history such as planetary differentiation and the rise of atmospheric oxygen (Elliott et al. 1999). Variations in Pb isotope ratios, as measured in MORBs and OIBs, are driven by variations in U/Pb causing Pb isotope ratios to evolve along different paths. The U/Pb of the source material of OIBs is likely to be affected by more than one process. Subduction of continentally derived uranium (Michard and Albarede 1985; Elliott et al. 1999) and preferential removal of Pb from the subducted slab (Peucker-Ehrenbrink et al. 1994; Kelley et al. 2005; Chauvel et al. 1992; Miller et al. 1994) have been identified as processes that generate material which will contribute a strong radiogenic Pb signature. Melting at mid-ocean ridges could also play a role in separating U from Pb but the effect, if any, would be small due to both U and Pb being highly incompatible (Hofmann 1997). The ratios ^{206}Pb/^{204}Pb and ^{207}Pb/^{204}Pb contain information on the time integrated U/Pb while ^{208}Pb/^{204}Pb informs us on the time-integrated κ.

3.2 Constraints From Pb Isotopes

3.2.1 The Pb pseudo-isochron

Lead ratios measured in MORBs and OIBs show a linear trend in both ^{207}Pb/^{204}Pb - ^{206}Pb/^{204}Pb and ^{208}Pb/^{204}Pb - ^{206}Pb/^{204}Pb space (Fig. 3.1). This characteristic has been noted since the earliest days of measurements of Pb isotopes (Tatsumoto 1966; Gast et al. 1964). A regression line fitted to ^{207}Pb/^{204}Pb vs ^{206}Pb/^{204}Pb can be thought of a pseudo-isochron; 'pseudo' as rather than dating a single melt event this represents the sum of multiple melting events. The exact meaning of this age is unclear, but it may be thought of as the bulk melting age (Rudge 2006).

Rocks evolve different lead isotope ratios due to fractionation of U and Th from Pb. The pseudo-isochron age (τ_{Pb}) may be determined from the regression line drawn through points in ^{207}Pb/^{204}Pb - ^{206}Pb/^{204}Pb space. The equation

$$\frac{\delta^{207}Pb/^{204}Pb}{\delta^{206}Pb/^{204}Pb} = \frac{(e^{\lambda_{235}t} - 1)}{137.88(e^{\lambda_{238}t} - 1)} \tag{3.1}$$

(derived in B) is solved numerically for t, where the left hand side is the gradient of the regression line through the lead isotope ratios, and λ_{235} & λ_{238} are the decay constants for ^{235}U and ^{238}U respectively.

For a global set of MORB Pb ratios, the age given by the pseudo-isochron τ_{Pb} is 1.9 Ga (Fig. 3.1a). Despite OIBs having a different source region to MORBs, ^{207}Pb/^{204}Pb vs ^{206}Pb/^{204}Pb plots on a similar array and has a remarkably similar τ_{Pb} of 1.8 Ga (Fig. 3.1a). What distinguishes MORB from OIB in ^{207}Pb/^{204}Pb vs ^{206}Pb/^{204}Pb space is that the OIB signature is generally more radiogenic. When the MORB ^{207}Pb/^{204}Pb vs ^{206}Pb/^{204}Pb array is split into measurements taken along different ridges, it becomes apparent that

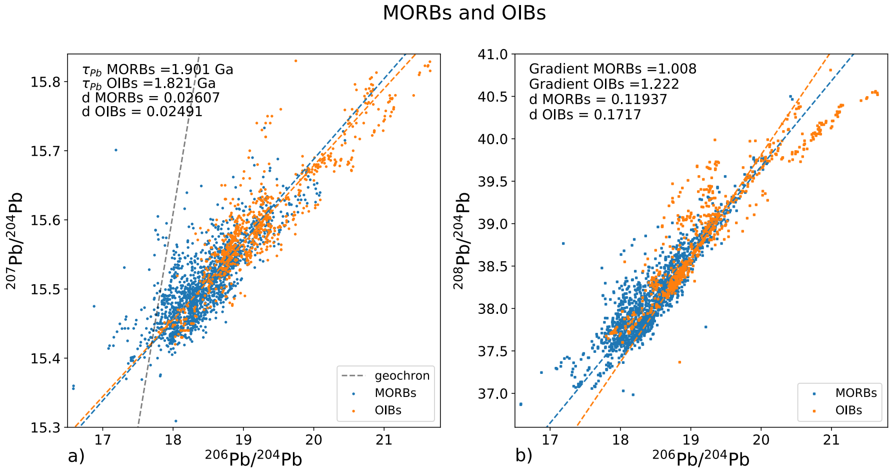

Fig. 3.1 a) ^{207}Pb/^{204}Pb vs ^{206}Pb/^{204}Pb for MORBs and OIBs. MORBs and OIBs have similar pseudo-isochron ages however OIBs are generally more radiogenic. Coloured dashed lines indicate the regression line through the data, the gradient of the regression line is used to calculate τ_{Pb}. Grey dashed line is the 4.55 Ga geochron on which the bulk Earth lead isotope ratio should fall. The 'd' value is the average orthogonal distance from each data point to the regression line, which gives a measure of scatter. b) ^{208}Pb/^{204}Pb vs ^{206}Pb/^{204}Pb for MORBs and OIBs. Data obtained from PetDB (Lehnert et al., 2000, www.earthchem.org/petdb) on 18th February, 2020, using search criteria, 'Spreading Ridges & Ocean Islands', 'igneous:volcanic:mafic:basalt'.

individual ocean ridges have distinct Pb isotope compositions (Fig. 3.2). This evidences mantle heterogeneity at the ocean basin scale.

3.2.2 The Pb paradoxes

Assuming that Earth is chondritic, the sum of its reservoirs, namely the crust and mantle, should plot on the 4.55 Byr geochron. However, when Pb is measured it is found that most samples plot to the right of the geochron (Fig. 3.1)a). The question as to why MORBs are more radiogenic than the geochron when they are the depleted complement to continental crust was first raised by Allégre (1969). In fact almost all terrestrial Pb measurements of mantle and continentally derived rocks plot to the right of the geochron. The apparent lack of a complementary reservoir has been termed the first Pb paradox (Sinha and Tilton 1973; Allégre 1982). A second Pb paradox also exists in that the Th/U of the upper mantle, which is measured at ≈ 2.6-2.7, is significantly lower what is inferred from time-integrated ^{206}Pb/^{204}Pb and

^{206}Pb/^{204}Pb ratios, which is ≈ 3.8 (Galer and O'Nions 1985; Allégre et al. 1986a; Elliott et al. 1999).

Various solutions to the Pb paradoxes have been proposed, some of which involve sequestering Pb from the convecting mantle. If this happens early on or continuously over geological time then it can account for the high Pb ratios observed in mantle rocks. The core has been suggested as a reservoir in which to sequester Pb, with Pb entering either rapidly during segregation or continuously over time via sulphide melts (Kramers and Tolstikhin 1997; Hart and Gaetani 2006; Maltese and Mezger 2020). It has also been suggested that Pb is removed from the convecting mantle by being stripped from subducting oceanic lithosphere and stored in the lower continental crust or mantle wedge (Kramers and Tolstikhin 1997; Kellogg et al. 2007). Alternatively, enrichment of the mantle in high μ material or continentally derived U^{6+} is also a suggested mechanism which would account for the radiogenic Pb ratios observed in mantle-derived rocks (Elliott et al. 1999; Castillo 2016; Wipperfurth et al. 2018). There is motivation for this being a time dependent process that would not have initiated until after the great oxygenation event (GOE), around 2.4 Ga (Holland 1985). Higher levels of atmospheric oxygen allowed continental U to oxidise from U^{4+} to U^{6+}. In this state U becomes fluid mobile so can make its way into oceanic crust by hydrothermal addition and subsequently be subducted and incorporated into the mantle (Michard and Albarede 1985; Elliott et al. 1999).

3.2.3 Scatter of Pb ratios

Further to τ_{Pb} and the Pb paradoxes, an additional constraint that is often overlooked is the scatter observed in Pb isotopic data. In Fig. 3.1, the scatter in the data is quantified by the 'd' value, which is the average orthogonal distance of each point away from the linear regression line, and the standard deviations along each axis. A value is given for both MORBs and OIBs. This scatter is a complex sum of the differentiation/enrichment events, time, and mixing that the sampled material has undergone (Oversby and Gast 1970; Allégre et al. 1980).

There is also a possibility that some of the measured scatter is due to analytical error. Of course care is taken to reduce this, but there may be different errors associated with different analytical techniques, or even by the same technique but at different laboratories. Pb isotope data is plotted

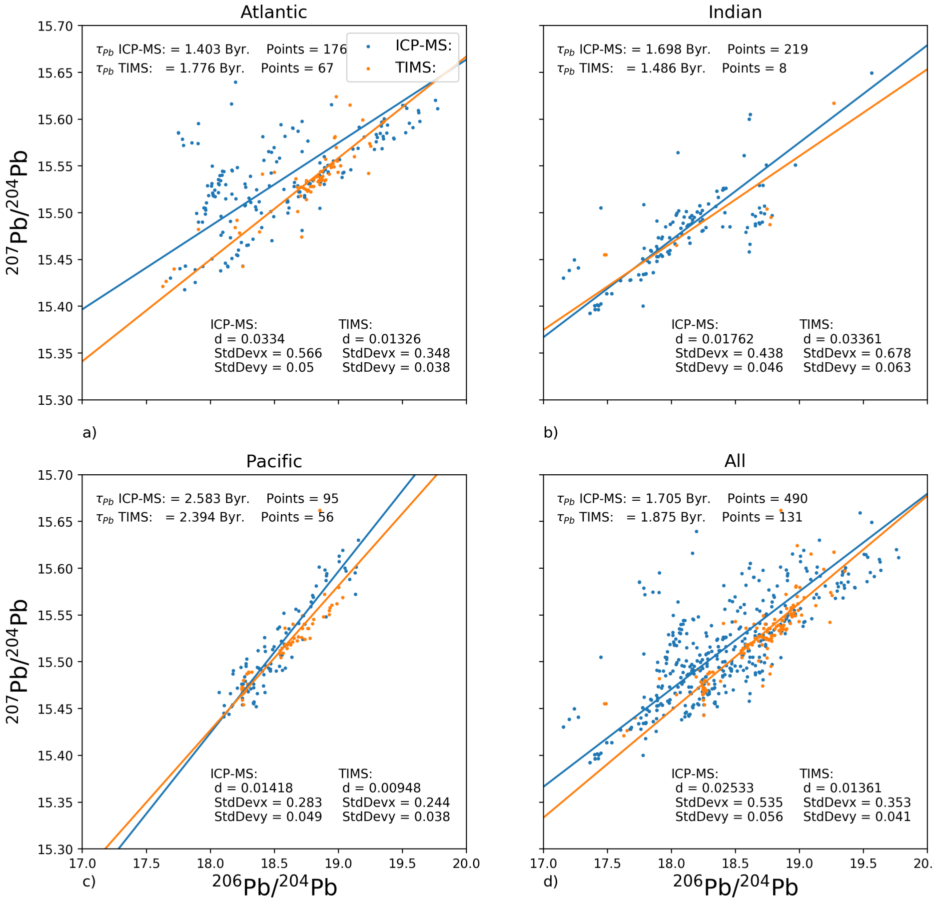

Fig. 3.2 Pb isotope composition of basalts sampled at different spreading ridges. Data obtained from PetDB (Lehnert et al. (2000), www.earthchem.org/petdb) on 18th February, 2020, using search criteria, 'Spreading Ridges, 'igneous:volcanic:mafic:basalt'. Data has been subsequently been filtered by the analytical method used, TIMS or ICP-MS. Measurements where the analytical method is recorded simply as 'MS' are omitted.

for different ocean basins in figure 3.2 for both Thermal Ionisation Mass Spectrometry (TIMS) and Inductively Coupled Plasma Mass Spectrometry (ICP-MS). Pb ratios measured by TIMS in samples from both the Atlantic and Pacific oceans have less scatter than those taken by ICP-MS. For samples from the Indian ocean, the opposite is true, however in this case there are only 8 data points for TIMS measurements. When data from all of the ocean basins are considered, measurements by TIMS have lower scatter than those measured by ICP-MS as measured by 'd' and the standard deviation. This could be interpreted as meaning that analytical method does affect the scatter and therefore a significant element of the measured scatter may be attributed to the analysis. It is also quite possible the measurements are all associated with a similar error and that the measured scatter is real. Comparisons of TIMS versus ICP-MS methods on the same zircon samples has shown the distribution of ages obtained from the U-Pb measurements is the same regardless of technique (Scott and Gauthier 1996). Comparisons have also been conducted between ICP-MS measurements taken at different laboratories on the same reference standards, finding excellent agreement between measurements of Pb ratios (Weis et al. 2006). Reported errors are small, commonly of the order 1×10^{-3}. These studies instil confidence that the scatter observed in Pb isotope ratios measured in MORBs and OIBs is indeed real and therefore worth considering as a constraint on combined geodynamic and geochemical models.

3.3 Modelling

Modelling of mantle circulation and melting processes is well established, both from box modelling and more complex numerical modelling. By integrating processes that fractionate trace elements, such models can be used to reconcile τ_{Pb}, the Pb paradoxes, and the scatter observed in Pb ratios of oceanic basalts. Early statistical box models of the Pb isotope composition of mantle derived rock yielded τ_{Pb} too high, on the order of 3.0 Ga (Allégre et al. 1980). More sophisticated box modelling by Rudge et al. (2005) and Rudge (2006) relate τ_{Pb} to the melting history of Earth's mantle. Given frequent enough remelting, an Earth-like τ_{Pb} of 2.0 Gyr can be achieved, but this does not consider the role of the continental crust as a reservoir for U, Th and Pb and can not offer a resolution to the Pb paradoxes or fit the observed scatter.

Christensen and Hofmann (1994) were the first to employ a numerical convection model to investigate the Pb composition of the mantle. They focussed on understanding whether subduction of dense basalt could cause thermo-chemical piles to form at the core-mantle boundary (CMB) which could isolate U-rich material for a long enough time to develop a strongly radiogenic Pb signature and a low τ_{Pb}. Deep-rooted mantle plumes could then sample this material (Hofmann and White 1982), explaining the strong radiogenic Pb signature of some oceanic islands. A setup that uses an excess density of basalt in the lower mantle of 3% results in 1/6 of the subducted material segregating into a layer at the CMB. When an assumption that the mantle is well mixed and chemically homogeneous at 3.6 Ga is used, $\tau_{\mathrm{Pb}} \approx 2.1$ Ga at present day. It is noted that these model were conducted at Rayleigh number much lower than what is expected for Earth's mantle and the sampling method for calculating τ_{Pb} may not be representative of the way oceanic basalt sample the mantle. This model falls short at reconciling the Pb paradoxes as they do not consider other geochemical reservoirs such as the continental crust. The initial concentration of trace elements in the mantle was therefore chosen so that they would evolve to match present day oceanic basalts. Brandenburg and Van Keken (2007) revisited segregation to the base of the mantle as a means for developing radiogenic Pb. Their simulations were run at more Earth-like Rayleigh numbers but to get the same amount of segregation as Christensen and Hofmann (1994), they required that basalt has very high excess density compared to ambient mantle.

Xie and Tackley (2004b) also approach the Pb problem numerically but in 2D cylindrical geometry, rather than the 2D Cartesian grid used in Christensen and Hofmann (1994). They also consider processes other than melting that might affect the Pb composition of the mantle. In their favoured model, material with high U/Pb (HIMU) is not created before 2.5 Ga due to the atmosphere being too reducing before this time (Holland 1985; Andersen et al. 2015). This is modelled by setting $D_{\mathrm{U}} = D_{\mathrm{Th}} = D_{\mathrm{Pb}}$ until 2.5 Ga, after which $D_{\mathrm{Pb}} > D_{\mathrm{U}} = D_{\mathrm{Th}}$. With this setup they achieve $\tau_{\mathrm{Pb}} = 1.75$Ga. As fractionation of U and Pb is prevented before 2.5 Ga the same τ_{Pb} would be achieved when initiating the calculation anywhere between 4.55 Ga and 2.5 Ga. This removed the need for the assumption that the mantle is well mixed until 3.6 Ga, as required by Christensen and Hofmann (1994).

Another process which perturbs the U/Pb ratio is the preferential stripping of Pb from subducted slabs at shallow depths relative to U (Chauvel et al. 1992; Miller et al. 1994; Kelley et al. 2005). Stripped Pb is incorporated into arc lavas, or sequestered to the mantle lower continental crust or lithospheric mantle wedge (Kramers and Tolstikhin 1997; Kellogg et al. 2007), removing it from the convecting mantle. Lead removal from the subducting slab plays an important role developing MORBs with radiogenic signatures (Hofmann 1988). We note that the method of using an elevated D_{Pb} (Xie and Tackley 2004b) causes relatively more U to move with the melt compared to Pb during a melting event. This also means that more Pb remains in the residue, which does not fit with the process of Pb removal. Another shortcoming of this model, similar to Christensen and Hofmann (1994), is that the initial Pb composition is based on present day isotopic ratio of oceanic basalts, so the Pb paradoxes are not considered. Additionally, although an Earth-like τ_{Pb} can be produced using this model, an accompanying Earth-like scatter cannot (Fig. 3.3).

More recent box modelling by Kellogg et al. (2007) considered the role of the continental crust as a geochemical reservoir. By removing Pb from subducted oceanic crust the first Pb paradox could be satisfied as well as Earth-like τ_{Pb}. A caveat of this model is that there is not considered to be any communication between the upper and lower mantle, so the latter remains primitive and is not considered. Additionally the scatter produced by the model cannot match that of Earth's. The full range of observed values for $^{206}\mathrm{Pb}/^{204}\mathrm{Pb}$, $^{207}\mathrm{Pb}/^{204}\mathrm{Pb}$, and $^{208}\mathrm{Pb}/^{204}\mathrm{Pb}$ was reproduced in numerical models by Brandenburg et al. (2008). In order to achieve this, increased fractionation between U and Pb was required at 2.25 Ga, similar to Xie and Tackley (2004b) & Kellogg et al. (2007). This was achieved by changing the relative extraction rates between U and Pb after 2.25 Ga. Although the authors did consider the slope of the pseudo-isochrons, these were not quantified.

More frequent remelting has been shown to reduce the Pb age as it erases old heterogeneity that has developed a radiogenic signature (Xie and Tackley 2004b; Rudge 2006). In Earth's past, high temperatures from formation and rapid decay of radioactive isotopes would have meant an extremely hot, low viscosity mantle that was subject to much more rapid overturns than seen today. To account for this variation, (Davies 2002) used a scaling law to convert Earth time to model time based on the decline of heat generation and plate velocities over time. This has also been applied to 3D models, such

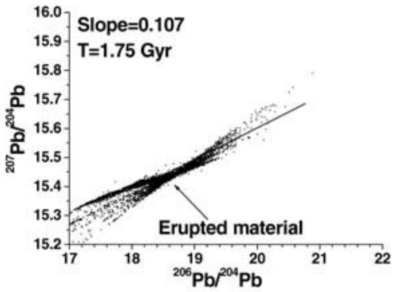

Fig. 3.3 From Xie and Tackley (2004b), scatter of ^{207}Pb/^{204}Pb vs ^{206}Pb/^{204}Pb for case with reference parameters but with no fractionation between U and Pb prior to 2.5 Ga.

as the ones we use here, and leaves <3% of the mantle remains unprocessed by the present day (Huang and Davies 2007).

In this chapter we present some cases that use similar partition coefficient setups to Xie and Tackley (2004b) to test the reproducibility of their results in 3D geometry. Subsequently we present cases where a continental reservoir that sits external to the mantle is employed to better model some of the processes that act upon U and Pb. Trace elements may be removed from the continental reservoir into the mantle and vice versa. Using the continental reservoir rather than the elevated partition coefficients parameterisation allows the separation of the processes of continental U addition and preferential Pb removal from subducted oceanic crust, even having them begin at different times as well as affording control over the amount of U that is added into the mantle. We will consider ^{206}Pb/^{204}Pb, ^{207}Pb/^{204}Pb, and ^{208}Pb/^{204}Pb, looking at both the pseudo-isochron and scatter of the Pb ratios of melts. We will also consider implications for the first and second Pb paradoxes.

3.4 Methods

3.4.1 Dynamic model

We run mantle convection models using the 3D geodynamic code TERRA, the mechanics of which are described in 2.3. Model parameters are listed in Table 3.1. We implement a simple two-layer viscosity profile with a ×30 viscosity jump at 660 km (Van Keken and Ballentine 1998). This gives the models a mobile surface to mimic the mobility of plate tectonics. The model

Table 3.1 Model parameters. Note that thermal diffusivity (κ) is derived from the relationship $\kappa = k/(\rho C_p)$ and the upper mantle viscosity is equal to the reference viscosity.

Parameter	**Symbol**	**Value**
Surface temperature	T_s	300 K
CMB temperature	T_{CMB}	3000 K
Internal heating rate	H	5×10^{-12} W kg^{-1}
Reference viscosity	η	3×10^{22} Pa s
Density	ρ_0	4500 kg m^{-3}
Thermal conductivity	k	4 W m^{-1} K^{-1}
Thermal expansivity	α	2.5×10^{-5} K^{-1}
Specific heat capacity	C_p	1100 J kg^{-1} K^{-1}

is internally heated homogeneously at a constant rate (Table 3.1) and by the isothermal CMB, with the exception of case HEAT. All simulations start with the same initial temperature field. This is generated by running a random temperature field forward in time for 5 Gyr. The heating rate during this 5 Gyr 'spin up' period is carefully chosen so that models run for 3.6 Gyr will have a present day surface heat flow that is similar to Earth's. In every case except 4.5GYR we run forward from 3.6 Ga to present day, as in previous studies (van Heck et al. 2016; Brandenburg et al. 2008; Brandenburg and Van Keken 2007; Xie and Tackley 2004b; Christensen and Hofmann 1994), to avoid modelling during early Earth time. Early Earth conditions are uncertain but it is likely that the mantle would have had a significantly lower viscosity due extremely high temperatures.

In our models, the composition and depth of particles affects the local density, with completely basaltic material (C=1) being 4% denser than harzburgitic material (C=0) in the upper mantle and 3% denser in the lower mantle (Ono et al. 2001). The 'basalt barrier' in the mantle transition zone causes the transition to dense, lower-mantle mineral phases to be delayed in subducted oceanic crust from 660 km to 750 km (Irifune and Ringwood 1993). We model this by making basalt 5% more buoyant in the transition zone compared to ambient mantle compositions (Davies 2008). The olivine system phase transitions are included in the model, parameters for which can be found in Table 3.2.

Table 3.2 Olivine phase change parameters

Depth (km)	$\Delta\rho$ kg m^{-3}	Clapeyron slope MPa K^{-1}
410	230	1.5
660	380	-1.0

Table 3.3 Parameters for calculating isotope initial values

Parameter	Value	Reference
^{235}U conc BSE	20.0e-9 g_U g^{-1}	
^{238}U/^{235}U	137.88	Tatsumoto et al. (1973)
^{238}U/^{204}Pb	8.0	White (1993)
Th/U	3.8	Galer and O'Nions (1985)
^{206}Pb/^{204}Pb$_{CD}$	9.3066	Tatsumoto et al. (1973)
^{206}Pb/^{204}Pb$_{CD}$	10.293	Tatsumoto et al. (1973)
^{208}Pb/^{204}Pb$_{CD}$	29.475	Tatsumoto et al. (1973)

3.4.2 Initialising Chemistry

Unless otherwise stated, the models are initialised from 3.6 Ga. This value is chosen as it follows the method of Christensen and Hofmann (1994) and implies that any fractionation that had taken place before 3.6 Ga had been mixed into the mantle and homogenised. At the start of the calculation, trace elements are shared out in equal ratios across all particles. Trace element concentrations are calculated, then converted to abundances using the mass of the particle. Parameters used to calculate initial concentrations can be found in Table 3.3 and initial concentrations can be found in Table 3.4. The value for ^{238}U is calculated from an estimate of its current concentration in bulk silicate Earth (BSE). From this, the concentration of ^{235}U and ^{232}Th are estimated from their respective present day molar and mass ratios to ^{238}U. ^{204}Pb is stable and so its present day abundance, calculated by its molar ratio to ^{238}U, is equal to its starting abundance. Initial values for radiogenic lead isotopes ^{206}Pb, ^{207}Pb, and ^{208}Pb are estimated from their abundances at the formation of Earth plus ingrowth from decay of their parent isotopes via the equation:

$$^{20x}\mathrm{Pb_s} = {}^{204}\mathrm{Pb} \times {}^{20x/204}\mathrm{Pb_{CD}} + P_D \tag{3.2}$$

^{20x}Pb$_s$ is the abundance of a radiogenic lead isotope at the start of the calculation (T_s = 3.6 Ga), $^{20x/204}$Pb$_{CD}$ is its ratio to ^{204}Pb at the formation of Earth (T_0 = 4.56 Ga) as measured from Canyon Diablo iron meteorites (Tatsumoto et al. 1973), and P_D difference in abundance of the parent isotope between T_0

Table 3.4 Isotope information

Isotope	Initial values	Decay Constant (s^{-1})
^{235}U	2.11×10^{-11} mol g^{-1}	9.85×10^{-10}
^{238}U	1.47×10^{-10} mol g^{-1}	1.55×10^{-10}
^{232}Th	3.91×10^{-10} mol g^{-1}	4.95×10^{-11}
^{204}Pb	1.05×10^{-11} mol g^{-1}	-
$^{206}Pb/^{204}Pb$	11.52	-
$^{207}Pb/^{204}Pb$	13.52	-
$^{208}Pb/^{204}Pb$	31.33	-

and T_s. These abundances are calculated from the decay equation:

$$P_T = P_{pd} e^{\Delta t \lambda} \tag{3.3}$$

where P_T is the parental abundance at time T, P_{pd} is the present day parental abundance, Δt is the difference in time between T and present day, and λ is the decay constant for the parent isotope.

We implement a continental reservoir which sits external to the mantle. This is used to store trace elements that make up the continental crust, similar to Brandenburg et al. (2008). For models which include recycling of continental uranium, 1/3 of the global budget of U, Th, Pb (see inital values in Table 3.4) is taken from the mantle and stored in the continental reservoir at the start of the calculation. This assumes that U, Th, and Pb are equally incompatible during continent extraction.

3.4.3 Geochemical Processes

Using Terra and the numerical modelling methods described in 2, we will investigate a wide parameter space including degree of fractionation, fractionation between the mantle and the continental reservoir, timing of fractionation, and processing rate of the mantle. Variations in Pb isotope ratios develop due to elemental fractionation which perturbs parent/daughter isotope ratio. In previous studies, the effects of many geochemical processes were approximated into a single model process. Christensen and Hofmann (1994) used an elevated D_{Pb} to account for the effects of both addition of continental U into the mantle (Michard and Albarede 1985; Elliott et al. 1999) and preferential removal of Pb from subducted slabs (Kelley et al. 2005) as well as melting fractionation. Brandenburg and Van Keken (2007) use the same method and values whilst Xie and Tackley (2004b) use the same method with smaller partition coefficient for Pb isotopes. In this chapter we will present some cases that use elevated partition coefficients similar to Xie and Tackley (2004b) and evaluate the effect this has on Pb isotope ratios.

For some cases, uranium isotopes are recycled from the continental reservoir into the mantle. When model has evolved to a time at which recycling of U is permitted, a set fraction of those isotopes in the continental reservoir (50% in the case of U) is set aside to be recycled into the mantle. When decay is taken into account, the amount of U recycled from the continental reservoir into the mantle is $\sim 1.7 \times 10^{14}$ mol of ^{235}U and 6.9×10^{15} mol of ^{238}U. The amount of U to be recycled for the current time step (R_U) is evenly distributed across all the particles in the surface layer according to

$$R_U =^X U_{cont} \frac{\delta t}{(t_E - t)} \tag{3.4}$$

where δt is the time step, t_E is the time that the chemical model was initialised at (3.6 Ga for the standard case) and $^X U_{cont}$ is the amount of isotope ^{X}U available to be eroded from the continent at time t. This process begins either at 2.4 Ga to coincide with the GOE (Andersen et al. 2015) or at 0.6 Ga to coincide with full oceanic oxidation (Lyons et al. 2014). In modelling the preferential removal of Pb from subducted slabs we assume that all melt will become oceanic crust and eventually be subducted. A set fraction (25%) of all isotopes of Pb are taken from any melt produced and added to the continental reservoir. This removes the Pb from the convecting mantle, akin to Pb from the slab being taken to the surface through arc volcanism (Kelley et al. 2005). Pb removal to the continent commences at 3.0 Ga, an estimate of the onset of plate tectonics (Tang et al. 2016; Laurent et al. 2014; Shirey and Richardson 2011). These methods allows for the separation of melting fractionation from uranium addition and lead removal.

As well as better separating different processes that act to alter U/Pb, our method removes the requirement for exaggerated D_{Pb} compared to D_U. This is advantageous as it makes the melting process more representative of Earth's. We prevent the depleted residue layer from forming very low U/Pb, which is what happens when other non magmatic processes are combined into an exaggerated D_{Pb}.

3.4.4 Parameter space

Parameters for cases presented in this chapter are summarised in the Table 3.5. The first case, MELT, examines the effect of just a small difference between D_{Pb} and D_{U} & D_{Th}, as if only melt fractionation occurred. We set $D_{\mathrm{Pb}} = 0.01$, taken from the cpx/melt partition coefficient for Pb in Hauri et al. (1994). Case Hi-DPb uses an artificially high D_{Pb}, similar to Xie and Tackley (2004b), in order to draw some level of comparison between previous studies and evaluate the effect of 2D vs 3D simulations. This is followed by cases XIE007 and XIE010 which use the method of Xie and Tackley (2004b) in which D_{Pb} is increased at 2.4 Ga, modelling the mobilisation of continental U after the GOE. XIE007, as in a preferred case of Xie and Tackley (2004b), does not have any fractionation between Pb and its parent isotopes before the GOE, whilst XIE010 includes melt fractionation during this time. For all subsequent cases D_{Pb} is fixed at 0.01 for the whole calculation. We vary the processes that are being modelled and the time at which we begin U erosion from the continent in cases CONTU, UPb2.4, and UPb0.6 (see Table 3.5). Case CONTU investigates recycling of continental uranium from 2.4 Ga, UPb2.4 additionally includes Pb removal from 3.0 Ga, and UPb0.6 includes Pb removal from 3.0 Ga as well as U recycling from 0.6 Ga.

In the past processing rates may have been much higher than they are presently due to increased radioactive heat production and lower mantle viscosities. We test the effect of increased processing in two ways. Firstly by heating via decay of radioactive isotopes stored on particles similar to Van Keken et al. (2001) and Xie and Tackley (2004b). This makes for a time and space varying heat regime as heat producing elements will be concentrated by fractionation mechanisms such as melting. SCALE uses a scaling law to extend the length of time that the simulation is run in order to achieve an arguably more reasonable amount of processing. Following the method of Huang and Davies (2007) a scaling factor of 13.7 is used. As many more melting events will occur over the course of the calculation, the amount of Pb that is removed from the melt to the continental reservoir reduced by a factor of 1/13.7 in order to prevent the mantle from becoming too depleted in Pb.

Table 3.5 Parameter settings for cases. Note that $D_U = D_{Th} = 0.007$ for all cases. Dashes indicate that a particular process is absent in this model and times indicate the time a parameter or process begins.

Case	D_{Pb}	Recycle U	Pb removal	Heating	Scaling
(A) MELT	0.01	-	-	Constant	-
(B) Hi-DPb	0.025	-	-	Constant	-
(C) XIE007	0.007, 0.025 @2.4 Ga	-	-	Constant	-
(D) XIE010	0.01, 0.025 @2.4 Ga	-	-	Constant	-
(E) CONTU	0.01	2.4 Ga	-	Constant	-
(F) UPb2.4	0.01	2.4 Ga	3.0 Ga	Constant	-
(G) UPb0.6	0.01	0.6 Ga	3.0 Ga	Constant	-
(H) 4.5GYR	0.01	2.4 Ga	3.0 Ga	Constant	-
(I) HEAT	0.01	2.4 Ga	3.0 Ga	Radiogenic	-
(J) SCALE	0.01	2.4 Ga	3.0 Ga	Constant	13.7×

3.5 Dynamic Results

3.5.1 Temperature evolution

Figure 3.4 shows the final temperature and bulk composition structure for Hi-DPb. The dynamics for all the unscaled cases with a constant heating rate are similar to this, with numerical error accounting for any differences. Although the dynamics of HEAT and SCALE will be different to that of unscaled cases with constant heating, some features are generally similar across these cases. For example, large, stable plumes (like in Fig. 3.4a) develop in the mantle in all cases, a behaviour which is known to occur in models with a free slip surface (Davies 2005). Return flow from the surface is dominated by cold, linear downwellings which are generally more mobile than the plumes (see supplementary Video1 in Appendix C) although the increased early heating rate in HEAT sees the plume mobility increase. Fig. 3.5a shows the volume averaged temperature decreases from 2010 K to around 1550 K over the course of the calculation for unscaled, constantly heated cases. This leaves the present day mantle cooling rate at $60\,\mathrm{K\,Gyr^{-1}}$, slightly lower than current estimates of Earth's current mantle cooling rate of $73\,\mathrm{K\,Gyr^{-1}}$ (Labrosse and Jaupart 2007). Surface heat flow (Fig. 3.5b) decreases from 54 TW to 39 TW over the same period. This is in line with current best estimates of Earth's surface heat flux, which is around 39 TW, excluding energy lost from radioactive decay in the continents(Davies and Davies 2010). It should be noted that while the surface heat flux of the model is a

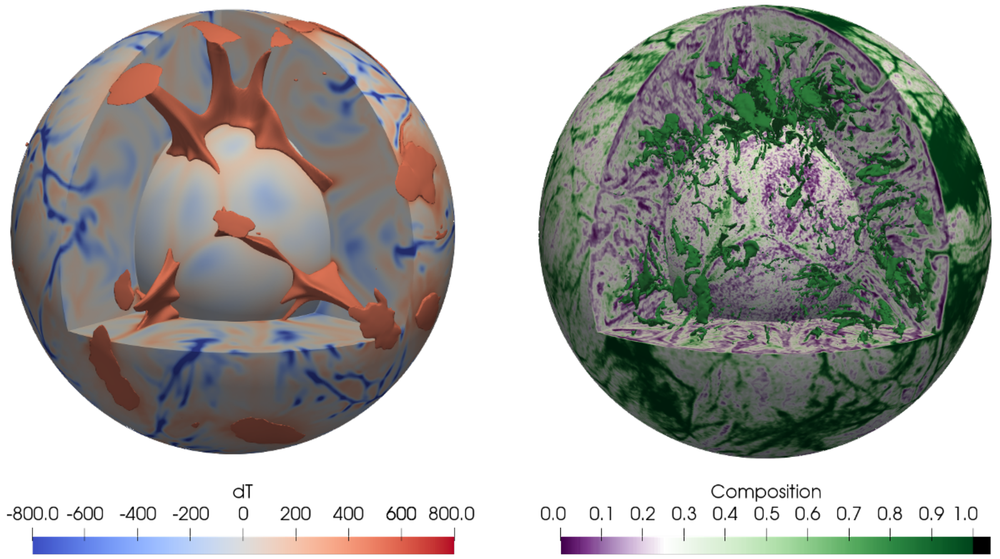

Fig. 3.4 Volume slices taken after the final time step of MELT. (a) Coloured by temperature anomaly with iso-surface for dT $\geq$ +500 K. View is clipped at 25 km depth as surface is fixed at 300 K. (b) Same volume slice coloured by bulk composition C. The colour scale is centred on ambient mantle composition of $C = 0.25$. The purple colour indicate harzburgitic material while green colours show basaltic material. Surfaces are drawn around regions with $C \geq 0.9$

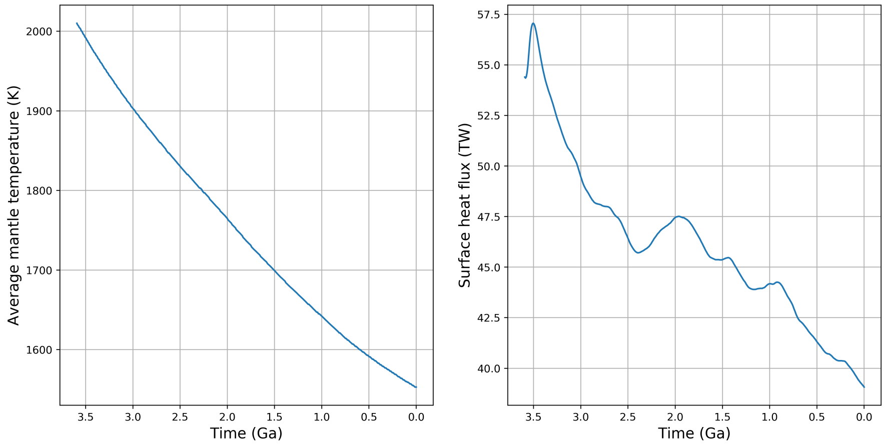

Fig. 3.5 (a) Volume averaged temperature of the mantle for unscaled cases with constant internal heating rate, over time. (b) Surface heat flux over time.

good match with Earth's, the mean surface velocity is considerably lower at 0.73 cm yr^{-1} compared to $\approx$ 5.00 cm yr^{-1}. This is due to the model being a mantle convection model which lacks the dynamics of plate tectonics.

3.5.2 Bulk composition

Fig. 3.4b shows a snapshot of the bulk composition of the mantle after the final time step of the calculation. The melting process, as described in section 2, generates a basaltic 'oceanic crust' at the surface, on top of a depleted layer. The basaltic material forms at the heads of plumes, where the majority of melting takes place (Fig. 3.4a). Material at the surface is pushed laterally as the upwellings encounter the surface. As surface material is cooled it becomes dense and begins to sink into the mantle at sinuous regions of downwelling, akin to subduction zones on Earth. The delayed phase transition in basaltic material from 660 km to 720 km creates somewhat of a barrier to subducted material, preventing a fraction of it from reaching the lower mantle. As a result the transition zone is slightly enriched in basaltic material compared to the ambient mantle. The amount of mantle that has been processed (% of particles that have melted) increases steadily for the first 1.7 Gyr of calculation (Fig. 3.6). Remelting of particles and lower melting rates cause a slower increase in % processed later on in the calculation. At present day 67% of particles have undergone at least one melt event for unscaled cases with constant internal heating rates.

Video 1 in Appendix C shows large volumes of basaltic material being subducted for the first 1 Gyr of the calculation. The high proportion of basalt reaching the base of the mantle allows small piles to form here. The piles are short lived, quickly being heated up sufficiently to become positively buoyant and rise into the lower mantle. As the calculation progresses the mantle cools and less basalt is produced, leaving just small accumulations of basaltic material at the base of plumes. The mantle mixes the enriched basaltic, depleted, and unmelted components efficiently, stretching out heterogeneity into thin strands aligned with the direction of flow. Strong mixing coupled with decreasing melting rates leads to a decrease in the wavelength of basaltic accumulations at the surface and within the mantle over time.

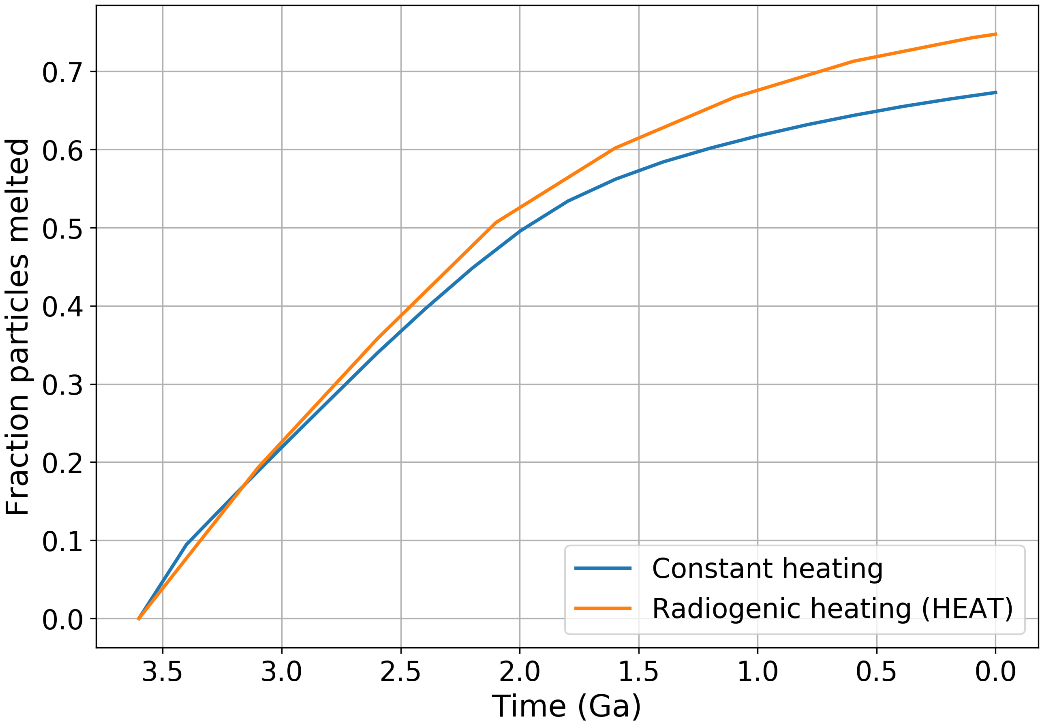

Fig. 3.6 Fraction of particles that have melted over time. Blue line is taken from case MELT but is applicable to all cases with a constant, homogeneous heating rate. Orange line represents rate for case HEAT.

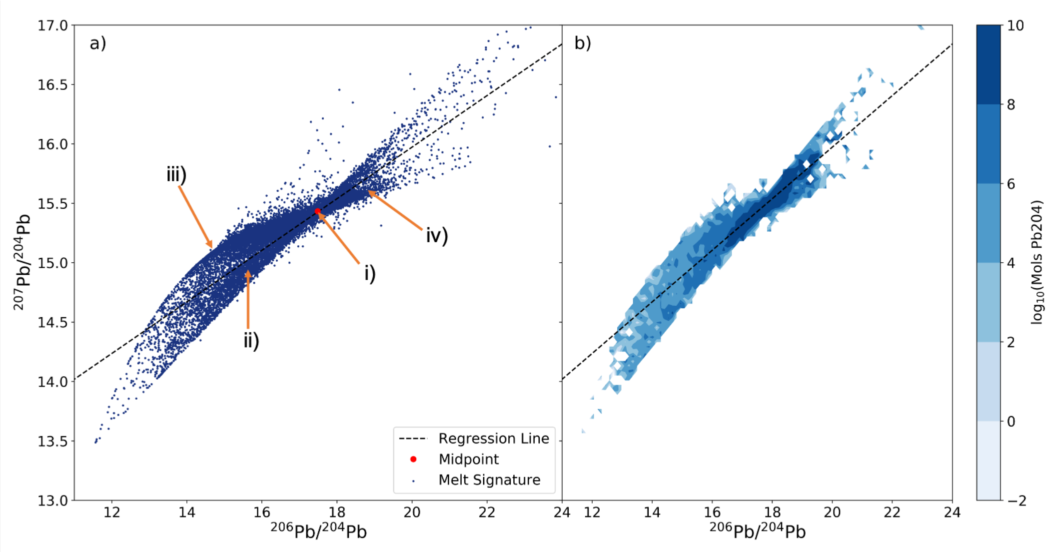

Fig. 3.7 (a) Scatter of lead isotope ratios of melt packages from the final time step of case Hi-DPb. Regression line calculated using the orthogonal distance method. Mid point of the data is taken as the median value in ^{207}Pb/^{204}Pb and ^{206}Pb/^{204}Pb. (b) Data from a) contoured by ^{204}Pb abundance within each cell of a 100×100 grid.

3.6 Understanding Pb ratio outputs

Fig. 3.7a shows sample output data in ^{207}Pb/^{204}Pb-^{206}Pb/^{204}Pb space. Each point is generated from the ratio of lead isotopes carried in a single 'melt package' - the information being transferred from a melting particle to a particle vertically above at the surface. The four labelled areas of the plot represent melt compositions with distinct melting histories. It is immediately clear that a high density of melt packages exists at or close to a single, central point, labelled 'i'. This point more or less coincides with the bulk silicate Earth (BSE) lead isotope ratio for the present day as given by our input parameters. The melt recorded here is either from particles that have melted for the first time or particles that are remelting having recently melted and not had enough time to accumulate a significantly different Pb composition.

Melt packages that have less radiogenic lead isotope ratios than the BSE value, labelled 'ii', are re-melts of residue. These have had much of their uranium stripped by melting and so their lead isotope ratios evolve more slowly. The well defined straight line represents the re-melting of residue that first melted at the beginning of the calculation.

A subset of the re-melts of residue form a well defined arc, labelled 'iii'. The most radiogenic end coincides with the present day BSE value and the less radiogenic end lies on the initial lead isotope ratio. This arc traces the evolution of the BSE lead isotope ratio. Points that lie on it underwent extremely high degrees of melting when they melted for the first time. This removed almost all of their U, so with no more radiogenic ingrowth their lead isotope ratio is frozen in place.

Melt packages which have more radiogenic lead isotope ratios than present day BSE, labelled 'iv', are interpreted to be remelts of melts. These are particles which had melt added to them, so they have relatively more uranium than lead and so a high μ. Excess radiogenic ingrowth of lead causes the lead isotope ratios of these particles to grow faster than the BSE, pushing them to high ratios.

Comparing the isotope ratios of melts in Figure 3.7a to the MORB data in Figure 3.1a, there is a much greater range of isotope ratios in the model. What is not immediately clear though is how dense the points are and how much lead is represented by them. Fig. 3.7b is the same data but contoured by abundance of ^{204}Pb. Points around the BSE value carry significantly more lead than those further away with more extreme lead isotope ratios. This is significant because the regression is weighted by ^{204}Pb abundance. In this chapter model Pb isotope ratios will be presented as contour plots coloured by ^{204}Pb abundance.

3.7 Fractionation via differences in partition coefficients

Here we will present results for models where the only fractionation is via partition coefficients, similar to the modelling in Christensen and Hofmann (1994), Xie and Tackley (2004b), and Brandenburg and Van Keken (2007). There will then be a discussion on the results and we will use what has been learned to feed into the class of models that include a continental reservoir.

3.7.1 Results

Overall features: In each of the cases MELT, Hi-DPb, XIE007, and XIE010 the mantle has only short wavelength Pb ratio anomalies which are randomly

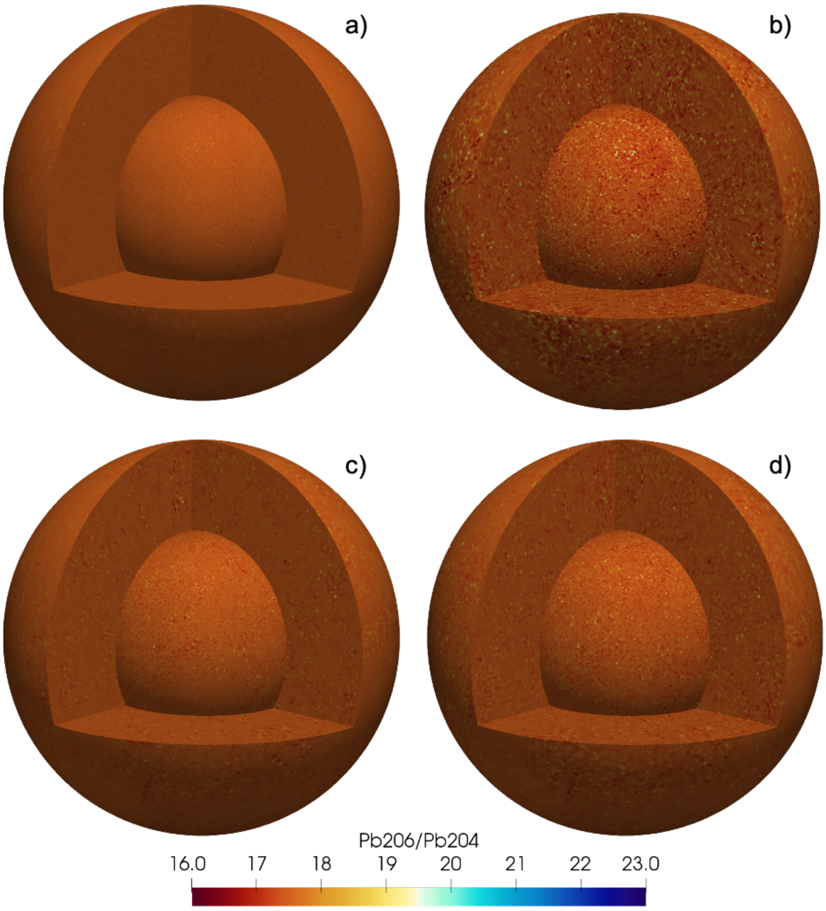

Fig. 3.8 Snapshots of the mantle at the end of the calculation for cases MELT, Hi-DPb, XIE007, XIE010 coloured according to the values of ^{206}Pb/^{204}Pb

.

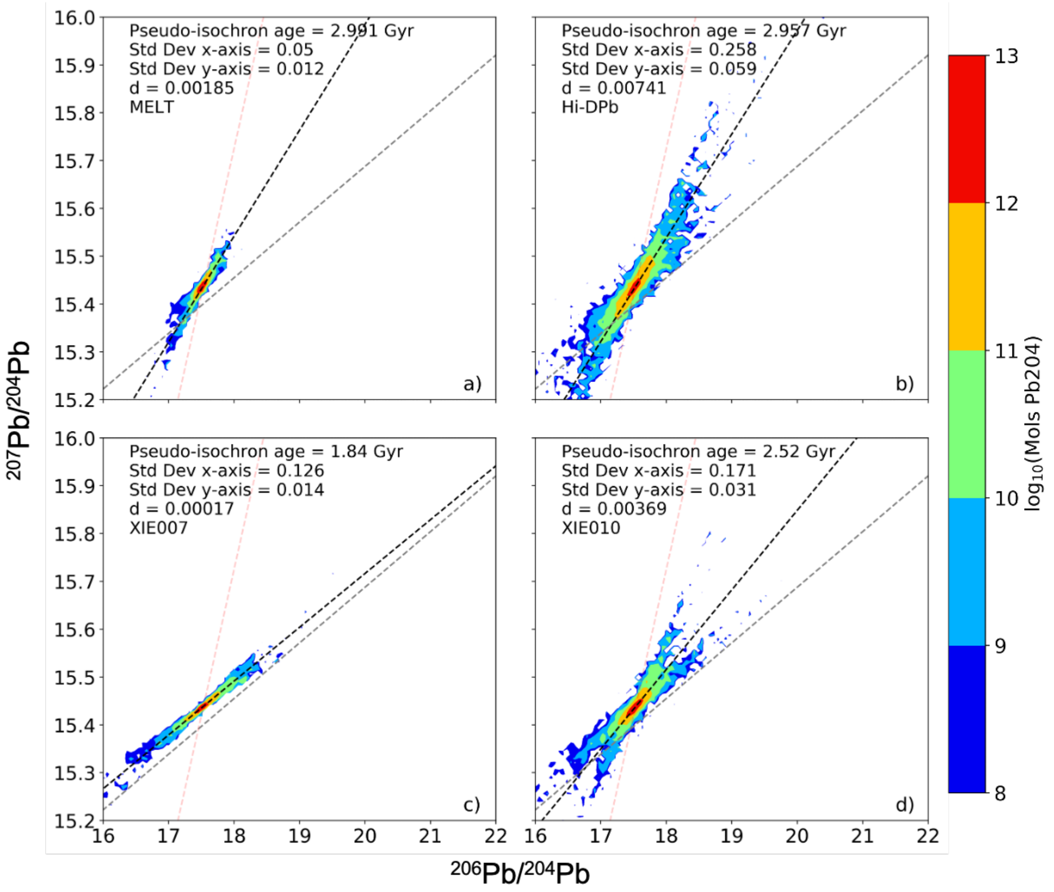

Fig. 3.9 ^{207}Pb/^{204}Pb vs ^{206}Pb/^{204}Pb for cases MELT, Hi-DPb, XIE007, XIE010. The graph area is divided into a 100×100 grid and each cell coloured by ^{204}Pb abundance. Dark dashed line is the pseudo-isochron for each case and light dashed line is pseudo-isochron for MORB data as in Fig. 3.1a. The red dashed line is the 4.55 Gyr geochron for the initial isotopes used in these calculations. The 'd' value is the average orthogonal distance of each melt package from the pseudo-isochron. The d-values are weighted by ^{204}Pb abundance.

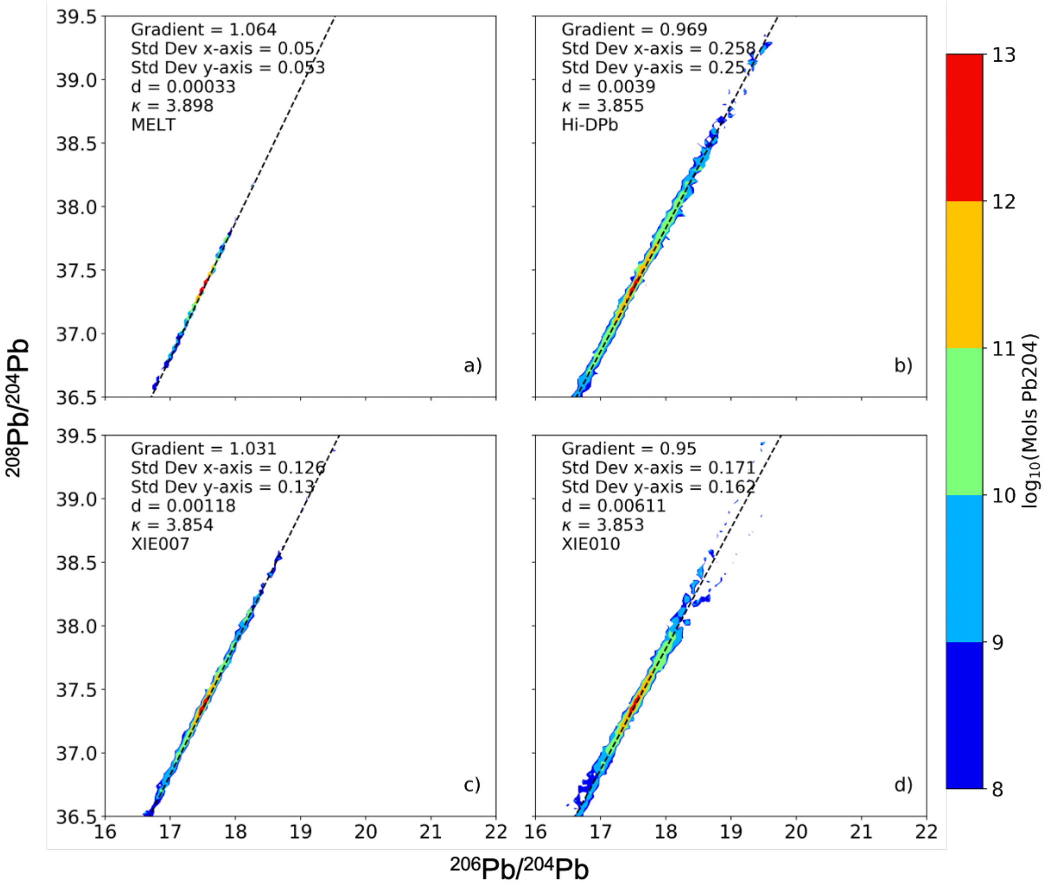

Fig. 3.10 ^{208}Pb/^{204}Pb vs ^{206}Pb/^{204}Pb for cases MELT, Hi-DPb, XIE007, XIE010. Axes are divided into a 100 by 100 grid and contoured by ^{204}Pb absolute abundance. Gradient is the gradient of the regression line through the data. The value κ is the ^{232}Th/^{238}U of all the melt produced at the final time step.

distributed (Fig. 3.8a-d). These anomalies vary in magnitude depending on the degree of fractionation between U and Pb permitted in each case. The similar values of κ (≈ 3.9) for each case is because U and Th are not fractionated in these cases. In ^{207}Pb/^{204}Pb vs ^{206}Pb/^{204}Pb space there is central point of highest Pb density that plots at ^{206}Pb/^{204}Pb = 17.5 and ^{207}Pb/^{204}Pb = 15.43 in each of these four cases (Fig. 3.9a-d). This point falls on the 4.55 Gyr geochron and approximately equal proportions of melt compositions plot to the left and right of the geochron. The gradient in ^{208}Pb/^{204}Pb vs ^{206}Pb/^{204}Pb space (Fig. 3.10) is ≈ 1.0 for each case and scatter measured by the 'd' value is very low.

The radial average of both μ, ^{206}Pb/^{204}Pb, and ^{204}Pb is constant throughout almost all of the mantle for each of these cases (Fig. 3.11). The Pb ratio of melt is plotted against ^{204}Pb as a proxy for the total amount of Pb on the particle in Fig. 3.12a and shows that most of the melt plots well within the measured range of ^{206}Pb/^{204}Pb $\approx$ 17 - 22.

MELT: When only melt fractionation is considered $\tau_{\mathrm{Pb}} = 2.99$ Gyr, considerably higher than anything measured in MORBs or OIBs. The melts produced at 3.6 Gyr all have a very similar Pb composition (Fig. 3.9,3.10a), leading to very low standard deviations in all Pb ratios. Due to the small difference between D_{Pb} and D_U, the degree of fractionation is low and so little scatter develops.

Hi-DPb: Increasing D_{Pb} by 2.5× results in a much greater scatter to develop in the Pb isotope ratios measured at 3.6 Gyr. The standard deviations in ^{206}Pb/^{204}Pb, ^{207}Pb/^{204}Pb, and ^{208}Pb/^{204}Pb have increased by 5.2×, 4.9×, and 4.7× respectively and the scatter as measured by 'd' has increased by 4.0× and 11.8× (Figs 3.9,3.10b), though are still much lower than what is measured in oceanic basalts. τ_{Pb} remains fairly unchanged at 2.96 Gyr, indicating the importance of considering other processes.

XIE007: Fractionation of Pb from U and Th was prevented until 2.4 Ga. As would be expected, the standard deviations of all Pb ratios are much lower than in Hi-DPb. Most strikingly the scatter away from the regression is significantly decreased with most of the melt plots on just a very narrow line (Figs. 3.9,3.10c). This shows up strongly in the 'd' values, which are an order of magnitude smaller than those of mantle-derived rocks. τ_{Pb} is significantly reduced to 1.84 Gyr, similar to that of MORBs and OIBs. There is a lack of highly radiogenic Pb signatures.

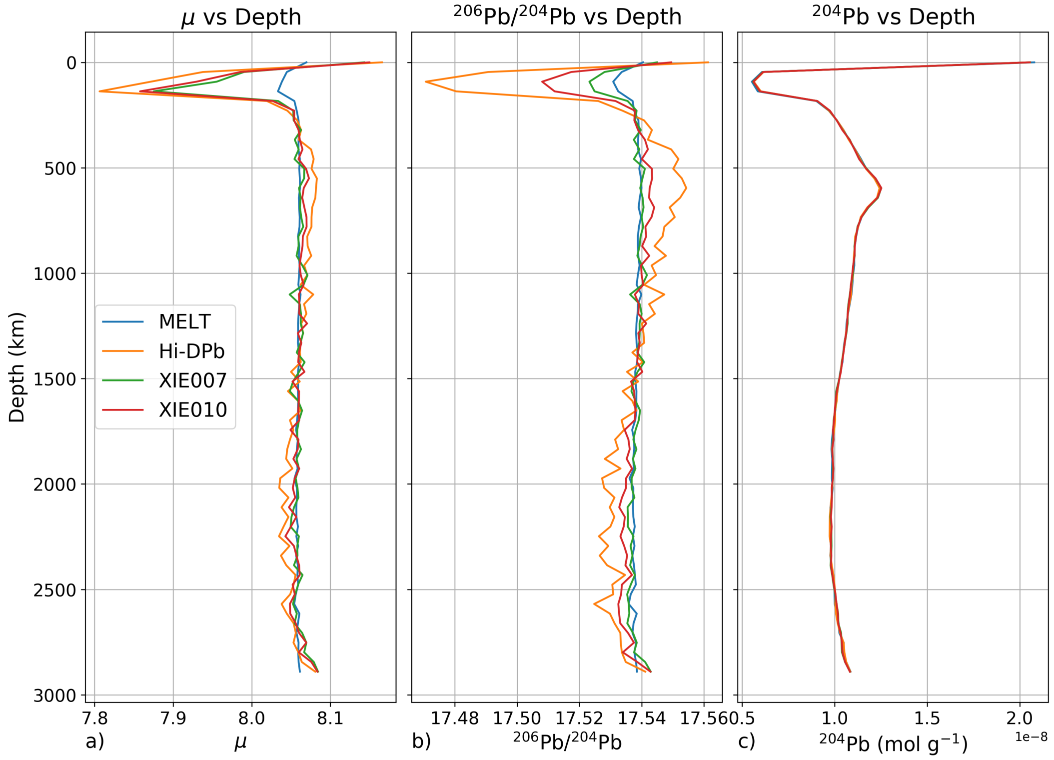

Fig. 3.11 Layer averaged depth plots for cases MELT, Hi-DPb, XIE007, XIE010 (a) μ, (b) ^{206}Pb/^{204}Pb, (c) ^{204}Pb abundance.

XIE010: Allowing for fractionation to occur before 2.4 Ga increases the scatter as measured by the standard deviation and ’d’. The overall shape of the scatter is similar to Hi-DPb (Fig. 3.9d), with melt dispersing in a ’V’ shape away from the most common Pb composition, along the regression line towards more and less radiogenic values. The early fractionation has a strong effect on τ_{Pb}, causing it to increase to 2.52 Ga.

3.7.2 Discussion

Quantitative modelling by Allégre et al. (1980) found it difficult to achieve τ_{Pb} lower than 2.5 Gyr with simple steady state models, indicating more complex processes are at work. Similarly, in Davies (2002), the model predicts the average age of mantle heterogeneity to be higher than the observed pseudo-isochrons. Our case MELT uses $D_{\mathrm{Pb}} = 0.010$ to consider only melting fractionation. The result of this is a high τ_{Pb} of 2.99 Gyr, and melt with a very narrow range of Pb isotope compositions (Figs. 3.9,3.10a).

Both Xie and Tackley (2004b) and Christensen and Hofmann (1994) present a ’standard’ case in which artificially high D_{Pb} is used to account

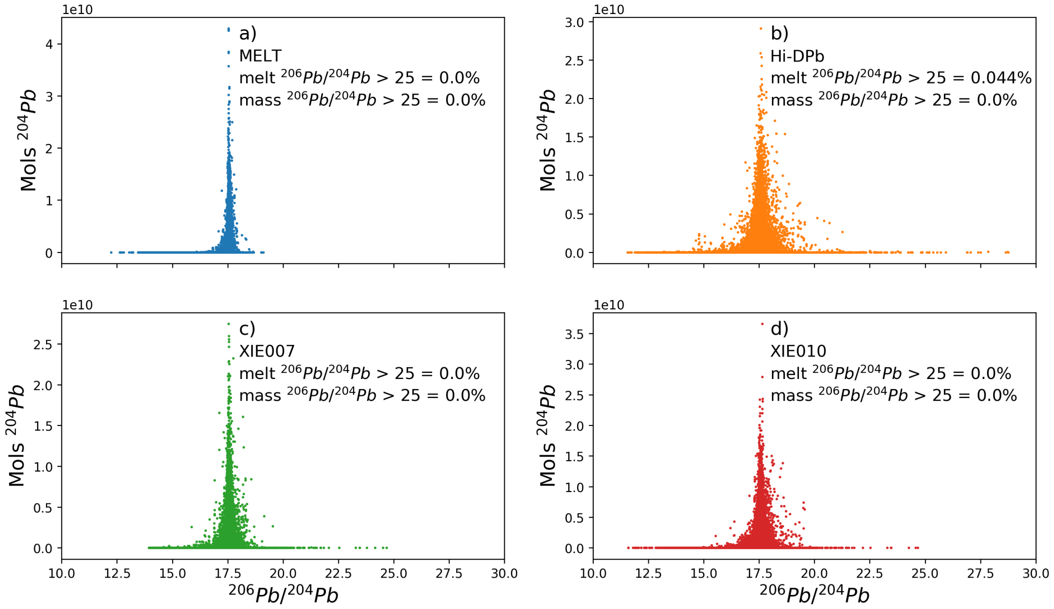

Fig. 3.12 For cases MELT, Hi-DPb, XIE007, XIE010 ^{206}Pb/^{204}Pb vs concentration ^{204}Pb for melt produced at present day. Labelled % of melting particles that have $^{206}\text{Pb}/^{204}\text{Pb} > 25$, and the % Pb mass that this represents of all the melt.

for non-melting processes that fractionate Pb from U and Th. They used $D_{\text{Pb}} = 0.15$ and $D_{\text{Pb}} = 0.025$ respectively. These values were chosen to reproduce the highly radiogenic signature of OIBs by increasing the μ of oceanic crust at the surface. Case Hi-DPb also uses $D_{\text{Pb}} = 0.025$, effectively beginning strong differentiation of Pb from U and Th at 3.6 Ga. τ_{Pb} is only weakly affected by this increase in partitioning, dropping from 2.98 Gyr to 2.93 Gyr when compared against MELT. This does not mean that the magnitude of the difference between D_{Pb} and $D_{\text{U,Th}}$ does not affect τ_{Pb}. For example if $D_{\text{Pb}} = D_{\text{U,Th}}$ then no fractionation would take place and no τ_{Pb} could be measured. Increasing fractionation does however have a strong effect on the scatter observed in the melt (Figs 3.9,3.10b). Both higher and lower Pb ratios are recorded in Hi-DPb compared to MELT and the average orthogonal distance away from the regression line is five time greater. A higher D_{Pb} increases the U/Pb of the melt enriched basaltic crust and decreases the U/Pb of the depleted residue. In turn, larger/smaller anomalies develop over the same amount of time (Fig. 3.8), hence the increased scatter.

Case XIE007, similar to cases run in Xie and Tackley (2004b), effectively assumes that U, Pb and Th are well mixed and uniform at 2.4 Ga. Between Hi-DPb and XIE007 τ_{Pb} is reduced from 2.96 Gyr to 1.84 Gyr, so it is clear

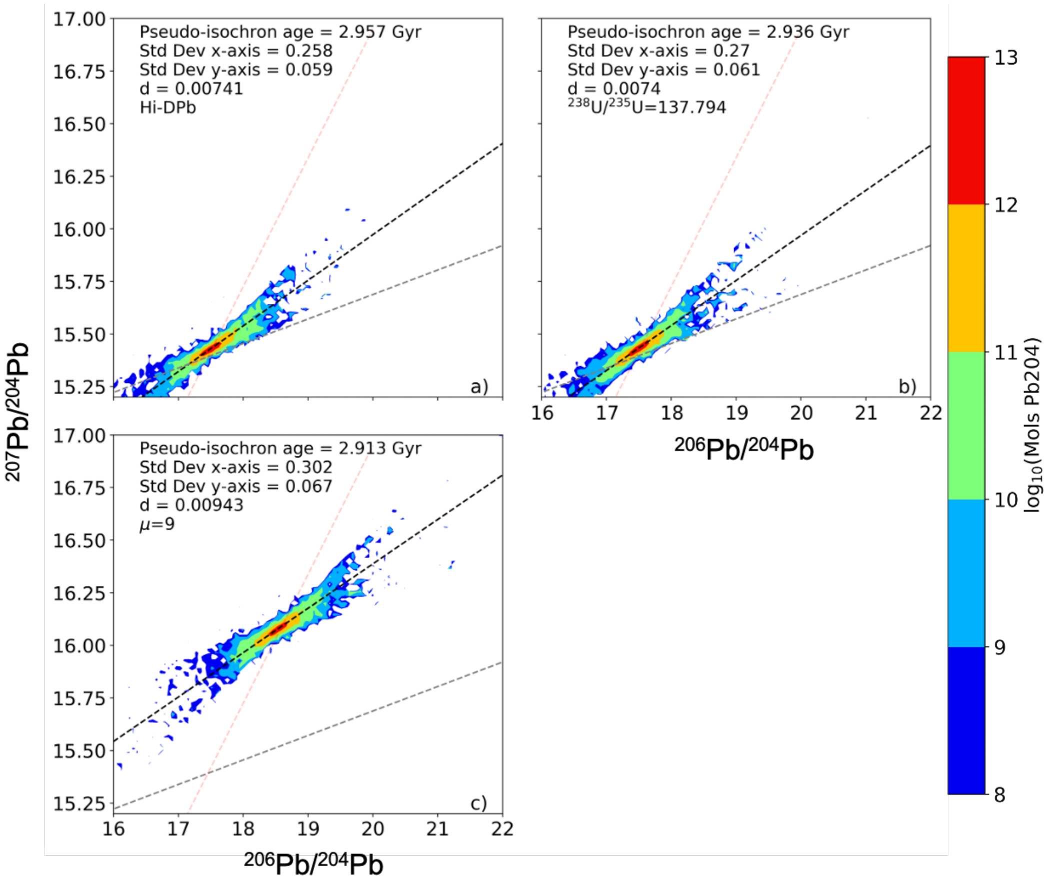

Fig. 3.13 Case Hi-Pb is replotted in (a). Plotted in (b) are the results for a model run with the same parameters except ^{238}U/^{235}U 137.794. Plotted in (c) are the results for a model run with the same parameters as (a) but with ^{238}U/^{204}Pb=9.0

that ancient heterogeneity has a strong influence on τ_{Pb}. The narrow range of isotope ratios produced and the low 'd' values in both $^{207}Pb/^{204}Pb$ vs $^{206}Pb/^{204}Pb$ and $^{208}Pb/^{204}Pb$ vs $^{206}Pb/^{204}Pb$ space is not a good match with the observations. The 2.4 Byr from when fractionation begins to present day must not be long enough to accumulate a significant Pb isotope anomalies from the degree of fractionation that occurs. A greater degree of scatter is achieved in XIE010 by allowing material to fractionate from 3.6 Ga. This earlier fractionation can accumulate greater Pb anomalies before being re-sampled, but also increases τ_{Pb} to 2.59 Gyr.

In each of the cases MELT, Hi-DPb, XIE007, and XIE010 there is a lack of strongly radiogenic Pb compositions, with the majority of melts having Pb compositions similar to BSE (Fig. 3.9a-d). Un-radiogenic compositions in our models could be due to how the initial concentrations of U, Th and Pb were chosen. Initial U concentrations are calculated from well accepted Canyon Diablo Pb ratios Patterson (1956) and Tatsumoto et al. (1973), $^{238}U/^{235}U$ of the BSE, and the concentration of U in the BSE (20.00e-9 g/g). We used the generally well accepted value of $^{238}U/^{235}U = 137.88$ (Tatsumoto et al. 1973). One re-evaluation of this ratio suggests a value of 137.794 (Goldmann et al. 2015), whilst other studies put it slightly higher at 137.818 (Livermore et al. 2018; Hiess et al. 2012). Taking the smaller of these values and using it in our calculations has no significant effect on Pb composition of melts when re-run for case Hi-DPb (Fig. 3.13b). τ_{Pb} is only only sightly reduced compared to Hi-DPb and there is negligible effect on the scatter. Some error also lies in the concentration of ^{204}Pb, which is calculated using μ. We have used the widely accepted bulk earth μ value of 8.0, which is usually given with an uncertainty of $\pm$ 2 (White 1993). Using a larger μ would lead to more radiogenic values. In Fig. 3.13c the Pb composition of melts is shown for a case with the same partition coefficient setup as Hi-DPb but where μ was set to 9.0 when calculating the ^{204}Pb of the system. All of the data is shifted to more radiogenic values along the 4.55 Gyr geochron, taking model results further from the oceanic basalt values. These tests also discount the revised primordial Pb composition of the solar system (Blichert-Toft et al. 2010) from having a significant effect on our results.

Another explanation for the lack of radiogenic material produced in these models could that combining the effects of many geochemical processes into just an elevated partition coefficient neglects some of the realities of isotope evolution on Earth. For example it leaves melt residue strongly enriched in Pb, leading to highly un-radiogenic compositions developing (Fig. 3.9). This method also neglects the continental crust as a geochemical reservoir. Similarly, the low κ that is measured in oceanic basalts, around 2.6-2.7 (Elliott et al. 1999), can not be reproduced by any of these cases. As the composition throughout the mantle is extremely homogeneous for these cases (Fig. 3.8a-d) this implies we are missing a reservoir that can store high κ material, allowing the mantle to become a reservoir with overall low κ.

3.8 Fractionation with a continental reservoir

The cases presented above have some common issues when comparing them against oceanic basalt data:

- Lack of scatter in Pb ratio plots
- Equal amounts of melt with Pb compositions to the left and right of the 4.55 Gyr geochron
- κ of the melt $\approx$ the same as BSE

More radiogenic Pb ratios require either more radiogenic Pb ingrowth or removal of ^{204}Pb from the mantle. To model either of these processes we need a reservoir to act as the continental crust. In this section models are initialised with a continental reservoir at the start of the calculation, similar to the end member crustal generation style of Armstrong (1968). As described in 3.4.2, 1/3 of the total U, Th, Pb, and K are initialised in the continental reservoir. The treatment of U and Pb is varied between different cases, the parameters for which are outlined in Table 3.5. In this section we will present the results for these cases. In the discussion further cases will be investigated to help us to understand the sensitivity towards different processes.

3.8.1 Results

A common feature of the results for each case shown in figure 3.15 is that almost all of the melt plots off of the 4.55 Gyr geochron to more radiogenic values. Most of the material therefore plots to the right of the geochron, with just a small fraction plotting to the left.

CONTU: Recycling continental U generates large scale heterogeneity in Pb isotope ratios throughout the mantle (Fig. 3.14a). These are almost

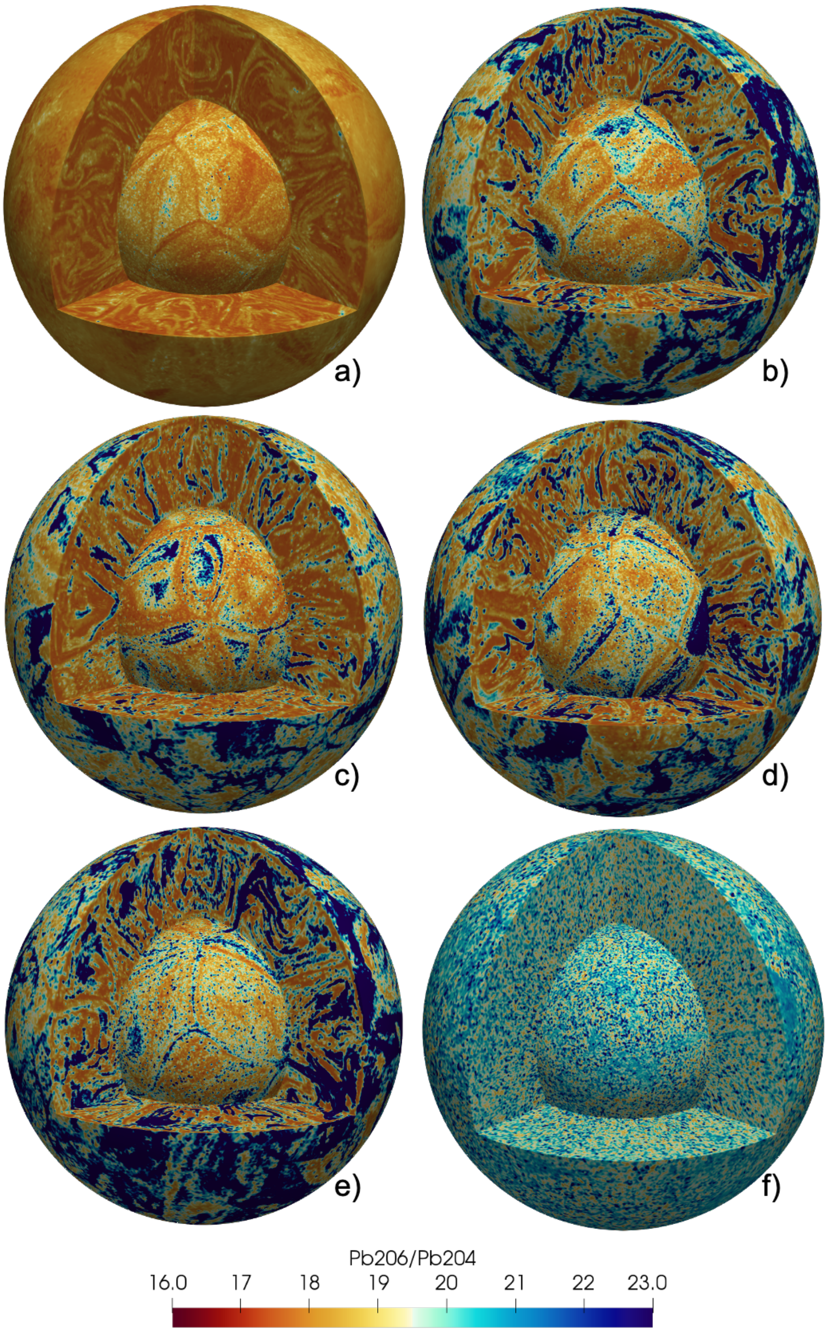

Fig. 3.14 Snapshots of the mantle at the end of the calculation for cases (a) CONTU, (b) UPb2.4, (c) UPb0.6, (d) 4.5GYR, (e) HEAT, (f) SCALE, coloured by ^{206}Pb/^{204}Pb.

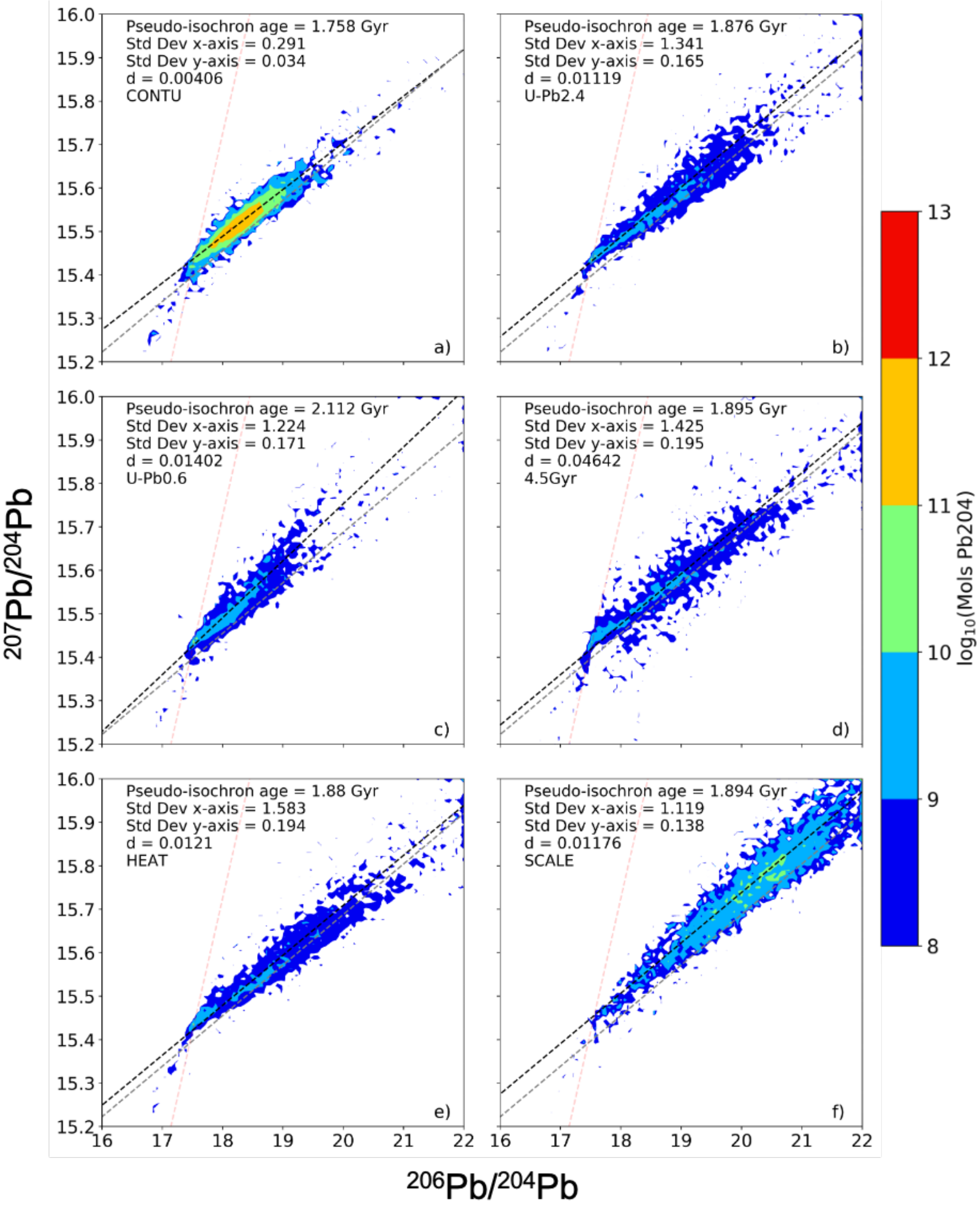

Fig. 3.15 ^{207}Pb/^{204}Pb vs ^{206}Pb/^{204}Pb for cases (s) CONTU, (b) UPb2.4, (c) UPb0.6, (d) 4.5GYR, (e) HEAT, and (f) SCALE. The graph area is divided into a 100×100 grid and each cell coloured by ^{204}Pb abundance. Dark dashed line is the pseudo-isochron for each case and light dashed line is pseudo-isochron for MORB data as in Fig. 3.1a. The red dashed line is the 4.55 Gyr geochron for the initial isotopes used in these calculations. The 'd' value is the average orthogonal distance of each melt package from the pseudo-isochron. The d-values are weighted by ^{204}Pb abundance.

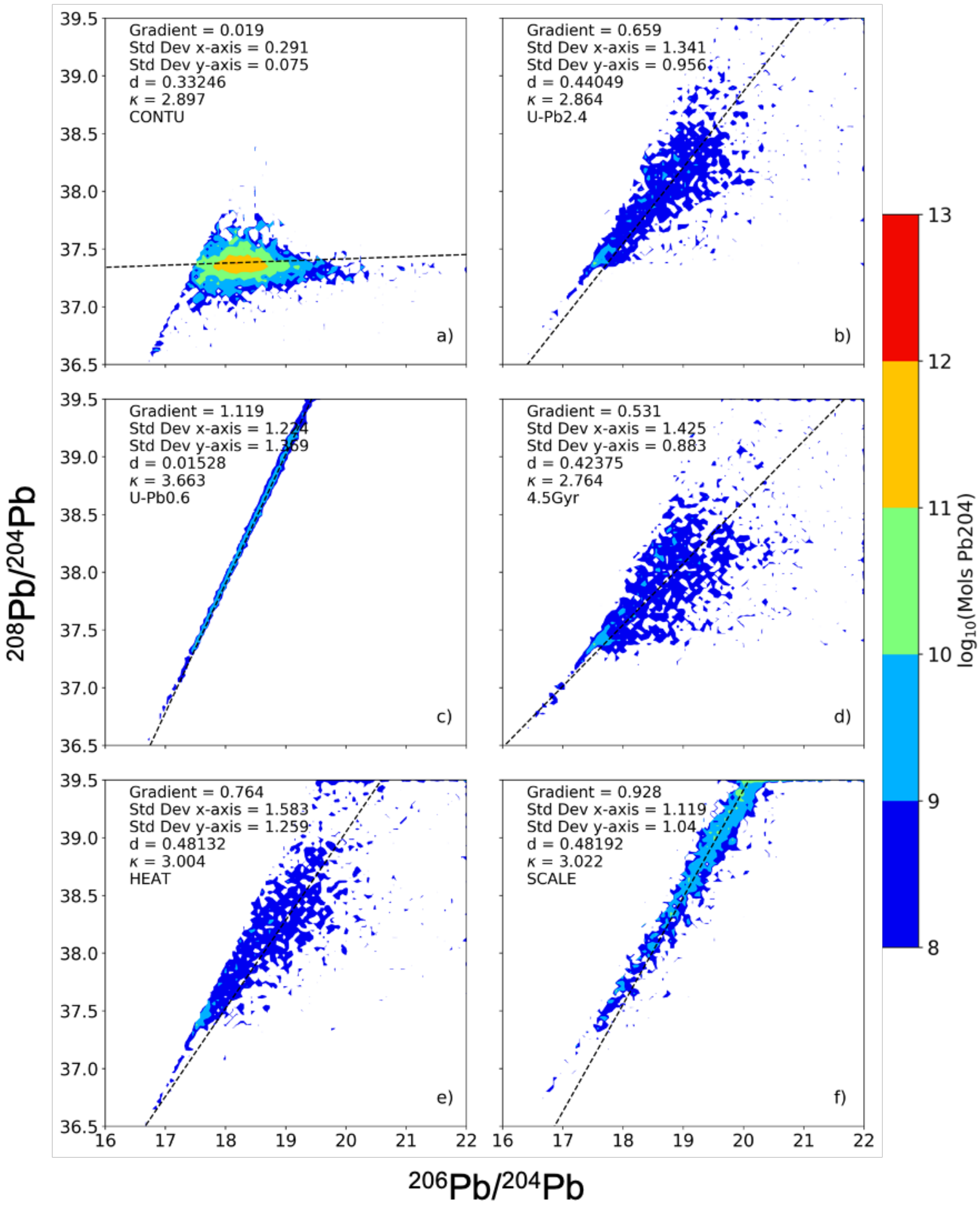

Fig. 3.16 ^{208}Pb/^{204}Pb vs ^{206}Pb/^{204}Pb for cases CONTU, UPb2.4, UPb0.6, 4.5GYR, HEAT, and SCALE. Axes are divided into a 100 by 100 grid and contoured by ^{204}Pb absolute abundance. Gradient is the gradient of the regression line through the data. The value κ is the ^{232}Th/^{238}U of all the melt produced at the final time step.

exclusively composed of material with a more radiogenic Pb signature. The radiogenic signatures are found particularly in basaltic material. Material with the highest μ is located at the surface (Fig. 3.17a), underlain by low μ and with a slight uranium enrichment relative to ^{204}Pb in the transition zone. The shape of the scatter in Fig. 3.15a differs from cases where fractionation only occurs due to differences in partition coefficients. There are no 'V' shapes at the extremities of the data (as seen in Figs. 3.9b,d) and there is no pronounced pinch near the BSE composition. The most common Pb composition is shifted to more radiogenic values and there is a much wider range of Pb ratios recorded. τ_{Pb} is significantly reduced from case MELT to 1.76 Gyr. A stark difference compared to MORB and OIB Pb distributions is seen in ^{208}Pb/^{204}Pb vs ^{206}Pb/^{204}Pb (Fig. 3.16a) which is not comparable to observations. κ is significantly reduced compared to the previous cases, to values just slightly above that of the depleted MORB mantle.

UPb2.4: In this case, 25% of Pb in melt produced after 3.0 Ga is removed and stored in the continental reservoir to account for Pb removal from subducted oceanic crust. This process leaves less Pb in the mantle and so Pb concentrations in the melt are reduced (Figs. 3.15,3.16b). There is a greater range of Pb compositions compared to CONTU (Figs. 3.15,3.16b) and the melts tend not to cluster so much around a narrow range of values. More highly radiogenic compositions are recorded whilst there is little change in the amount of un-radiogenic compositions. There is a clear linear trend to the data and the spread away from the pseudo-isochron increases with increasing Pb isotope ratios (Fig. 3.15b). τ_{Pb} = 1.98 Gyr, a slight increase on CONTU but similar to the global MORB value. The Pb compositions in Fig. 3.16b display a high degree of scatter with a large 'd' value that exceeds that of oceanic basalts. The gradient in ^{208}Pb/^{204}Pb vs ^{206}Pb/^{204}Pb is considerably lower than what is observed. There is strong enrichment of U at the surface and in the transition zone relative to ^{204}Pb (Fig. 3.17a) whilst the melting layer, just below the surface, is more depleted. Like CONTU, κ is just slightly higher than the depleted MORB mantle value.

UPb0.6: Delaying the recycling of continental U until 600 Ma causes there to be less of a radiogenic Pb signature compared to UPb2.4 (Fig. 3.15c). The 'd' value in ^{207}Pb/^{204}Pb vs ^{206}Pb/^{204}Pb space is slightly increased compared to UPb2.4, as is τ_{Pb} which is 2.11 Gyr. Conversely, the 'd' value in ^{208}Pb/^{204}Pb vs ^{206}Pb/^{204}Pb space is greatly reduced, showing very limited deviation from a straight line. The gradient is more similar to the data in this case, falling in between MORBs and OIBs. As in UPb2.4 and CONTU, the radiogenic anomalies in the mantle are large and generally appear on basaltic material (Fig. 3.8c). UPb0.6 has the strongest U enrichment compared to ^{204}Pb at the surface of any of the cases (Fig. 3.17a). The very low μ in the melting layers slowly increases with depth, all the while remaining lower than UPb2.4 until just above the CMB. The value of κ measured in the melts is higher than in UPb2.4 and CONTU, closer to that of the BSE value.

4.5GYR In this run there is additional fractionation before 3.6 Ga compared to UPb2.4 due to melting. This is not a large enough effect to significantly change τ_{Pb}, however it does affect the scatter, with 'd' increasing by 4× (Fig. 3.15d). In ^{208}Pb/^{204}Pb vs ^{206}Pb/^{204}Pb space the gradient is further reduced from what was already a low gradient in UPb2.4 (Fig. 3.16d) however 'd' is relatively unchanged, while κ is reduced by only 0.1. As in UPb2.4 and UPb0.6 there are large wavelength Pb anomalies throughout the mantle. In the mid-mantle these tend to be linear and orientated radially (Fig. 3.14c). The radial profiles of μ, ^{206}Pb/^{204}Pb, and ^{204}Pb are all very similar to UPb2.4 (Fig. 3.17a,b).

HEAT: While the heating rate for this case does decay over time, the overall effect is an increased amount of processing. After 3.6 Byr around 75% of particles in the mantle have experienced at least one melting event for this case, compared to about 67% for cases with constant, homogenous heating. The spread of Pb ratios is similar to UPb2.4, but with larger standard deviations and 'd' values (Figs. 3.15,3.16e). τ_{Pb} is not affected compared to UPb2.4, however the gradient in ^{208}Pb/^{204}Pb vs ^{206}Pb/^{204}Pb space is steeper. The value of κ is increased compared to UPb2.4 to ≈ 3.0. Fig. 3.8e shows large areas of the surface and mantle having a strongly radiogenic composition forming long wavelength anomalies. While cases CONTU, UPb2.4, UPb0.6, and 4.5GYR all feature high μ and high ^{206}Pb/^{204}Pb in the transition zone (Fig. 3.17a,b), in HEAT this enrichment is even more pronounced.

SCALE: In the case of the scaled run the fraction of particles that have experienced at least one melting event is 97%, compared to 67% for unscaled cases. The distribution of Pb ratios in the mantle is more similar to cases with fractionation controlled by partition coefficients (Fig. 3.14f) with only short wavelength anomalies existing, generally at more radiogenic values. Consequently, the melt is also radiogenic in nature (Figs. 3.15,3.16f). In ^{207}Pb/^{204}Pb vs ^{206}Pb/^{204}Pb space, both the scatter and τ_{Pb} are quite similar to UPb2.4 (Fig. 3.15f). The scatter in ^{208}Pb/^{204}Pb vs ^{206}Pb/^{204}Pb space is

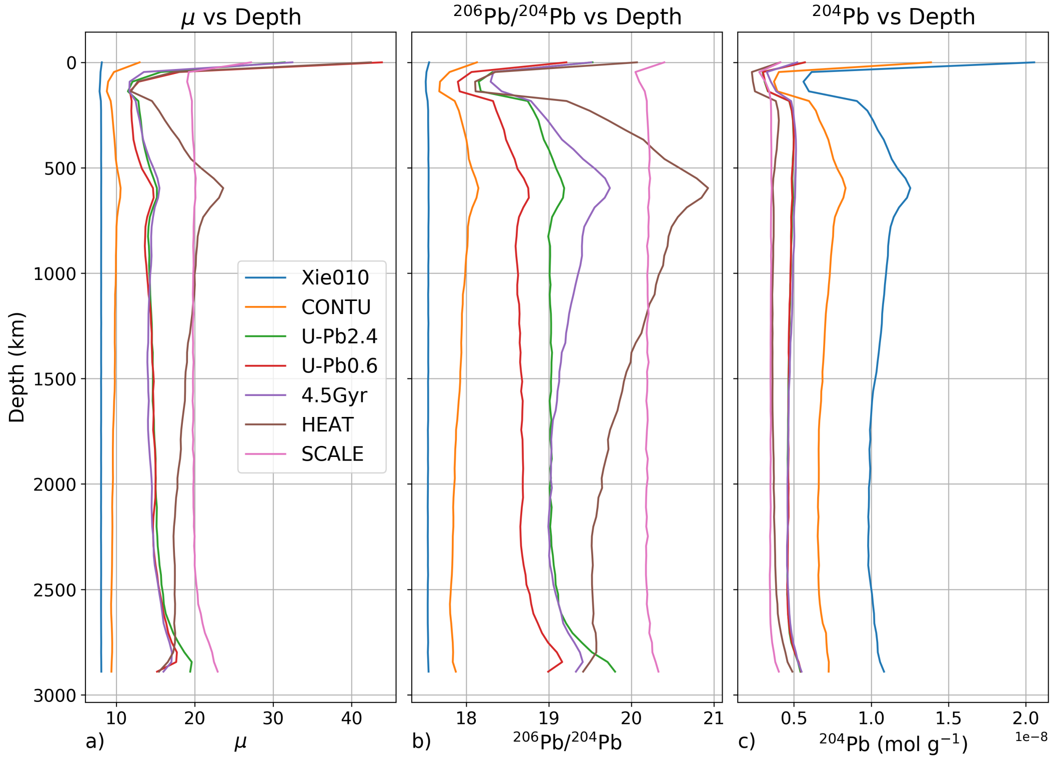

Fig. 3.17 Layer averaged depth plots for cases XIE010, CONTU, UPb2.4, UPb0.6, 4.5GYR, HEAT, SCALE, displaying (a) μ, (b) ^{206}Pb/^{204}Pb, (c) ^{204}Pb abundance.

also similar to UPb2.4, but the gradient for this case is more similar to measured values (Fig. 3.16f). Similarly to HEAT, κ is larger than that of oceanic basalts at ≈ 3.0. Radially there is very little variation in μ and ^{206}Pb/^{204}Pb throughout the mantle with the exceptions being the surface and near the CMB (Fig 3.17a,b). The surface has higher μ and ^{206}Pb/^{204}Pb than the rest of the mantle, and the magnitude of this difference is lower than in other cases with U recycling and Pb sequestering. Through the bottom 400 km of mantle both μ and ^{206}Pb/^{204}Pb gradually increase towards the CMB.

3.8.2 Discussion

The Pb isotope results of CONTU show that recycling continental U results in a more radiogenic mode composition, similar to MORBs and OIBs (Fig. 3.15e). The more radiogenic material is seen in visualisations (Fig. 3.14a) and is generally found in basaltic material because continental U is added to particles at the surface. An important observation from measurements of OIBs and MORBs is that mantle derived rocks plot to the right of the geochron in

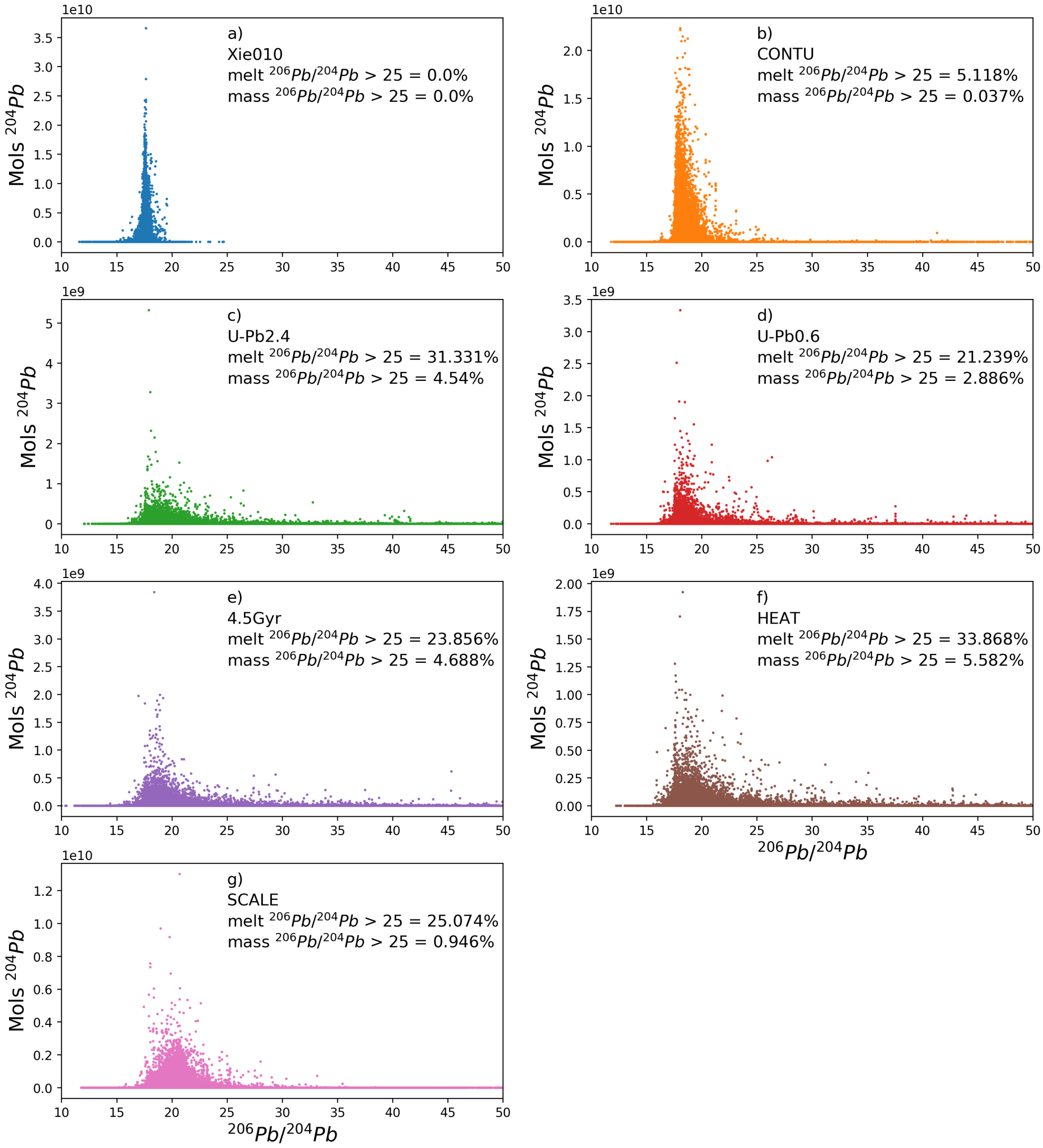

Fig. 3.18 For cases XIE010, CONTU, UPb2.4, UPb0.6, 4.5GYR, HEAT, SCALE. ^{206}Pb/^{204}Pb vs concentration ^{204}Pb for melt produced at present day. Labelled % of melting particles that have ^{206}Pb/^{204}Pb $>$ 25, and the % Pb mass that this represents of all the melt.

Table 3.6 Continent reservoir isotopic composition at present day

	$^{238}U/^{204}Pb$	$^{232}Th/^{238}U$	$^{206}Pb/^{204}Pb$	$^{207}Pb/^{204}Pb$	$^{208}Pb/^{204}Pb$
CONTU	4.009	7.781	16.69	15.35	37.374
UPb2.4	2.389	7.782	16.31	15.297	36.488
UPb0.6	2.406	7.784	16.665	15.336	36.528
4.5GYR	2.447	7.790	16.164	15.270	36.365
HEAT	2.052	7.783	16.258	15.293	36.34
SCALE	2.00	7.795	16.208	15.279	36.284

$^{206}Pb/^{204}Pb$ Vs $^{207}Pb/^{204}Pb$ space. This is referred to as the fist Pb paradox, as it is expected that mantle derived rocks would be depleted in radiogenic Pb due to U being more incompatible than Pb on melting (Hofmann 2003; Anderson 1982). In the first four cases presented (Fig. 3.15a-d), the majority of melt plots to the left of the geochron. This implies that the models are failing to capture some important processes that happen on Earth. In CONTU, the majority of melt plots to the right of the geochron due to input of uranium from the continental reservoir. Despite this, CONTU still does not produce significant amounts of the most radiogenic Pb compositions measured in OIBs ($^{206}Pb/^{204}Pb=21$, $^{207}Pb/^{204}Pb=15.75$, $^{208}Pb/^{204}Pb=40$) Moreover, Fig. 3.16a clearly shows excess ^{206}Pb ingrowth compared to ^{208}Pb. This is due to particles receiving uranium from the continents without thorium, and so an excess of ^{207}Pb and ^{206}Pb accumulates compared to ^{208}Pb. Clearly this could be remedied by addition of ^{232}Th from the continents. The problem with this is that thorium is known to be extremely non fluid-mobile and consequently would not be added by seafloor alteration to the mafic crust in the same way U^{6+} is (Hart and Staudigel 1982; Hart and Staudigel 1989). This does not prevent subduction of thorium enriched sediments, however it is known from studying the composition of arc lavas, both with and without a strong sediment input, that uranium experiences a net subduction effect whereas Th does not (Hawkesworth et al. 1997; Elliott et al. 1999). Although the $^{208}Pb/^{204}Pb$ vs $^{206}Pb/^{204}Pb$ in the melt is unrealistic for CONTU, a low τ_{Pb} of 1.76 Gyr whilst melt fractionation is permitted from 3.6 Ga, and the radiogenic nature of $^{206}Pb/^{204}Pb$ and $^{207}Pb/^{204}Pb$ are encouraging signs that recycling of U from a continental reservoir is a good approximation of surface processes on Earth.

Case UPb2.4 includes Pb removal during melting as well as U recycling from the continental crust. Pb removal from the mantle slowly decreases

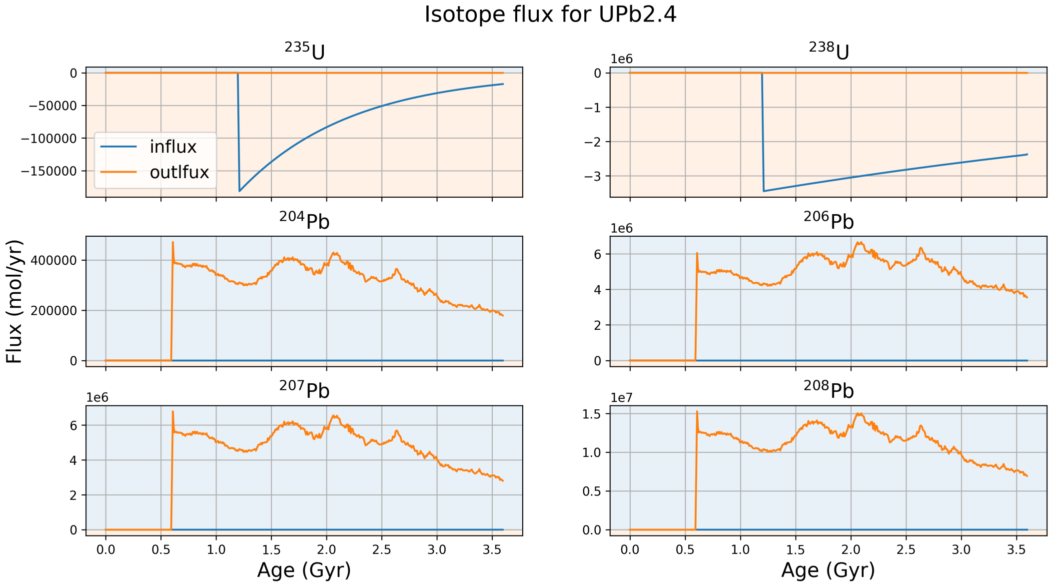

Fig. 3.19 Flux of isotopes over time for case UPb2.4, note variable y-axis scale for each isotope. Blue lines are influx into the mantle from continental reservoir and orange lines are outflux from mantle to continental reservoir.

with time as the amount of Pb in the mantle and the amount of melting decreases (Fig. 3.19). The melt in this case is more homogeneously distributed across the observed Pb ratios (Fig. 3.15,3.16b) compared to cases without Pb removal (these isotope plots do not have such a pronounced central high concentration of Pb). Some of the melt produced has the most radiogenic Pb compositions that are observed in OIBs (Fig. 3.15b) and as with CONTU, almost all of the melt plots to the right of the geochron. There must be a complementary un-radiogenic reservoir somewhere, evidently this is not located in the mantle (Fig. 3.14b). It is instead found in the continental reservoir. All three radiogenic Pb isotope ratios are low in the continental reservoir for all cases that include recycling of U (Table 3.6). Previous proposals that the continental crust could host un-radiogenic Pb have suggested that it exists in the lower crust (Zartman and Haines 1988; Kramers and Tolstikhin 1997), something that our model cannot directly determine as we only have bulk continental crust values. The continental crust Pb ratios for the cases in (Table 3.6) fall in between the estimates of Zartman and Haines (1988) and Kramers and Tolstikhin (1997). Assuming that the upper continental crust is more radiogenic than the lower continental crust, then our results fit best with the estimates of Kramers and Tolstikhin (1997). The $^{238}U/^{204}Pb$ of all cases in Table 3.6 is much lower than estimated continental values whilst

^{232}Th/^{238}U is much too large. This discrepancy could be solved if less ^{238}U were subducted or if there were some treatment of Th were lost from the continental reservoir coupled with less Pb removal into the crust.

Timing of fractionation

Case UPb2.4 is an end member scenario where recycling of continental U occurs from 2.4 Ga, coinciding with estimates for the earliest time at which significant quantities of O_2 were present in Earth's atmosphere (Lyons et al. 2014). Another end member case is to begin recycling continental U from 0.6 Ga (case UPb0.6), to coincide with full oceanic oxidation (Andersen et al. 2015). In this case 50% of the U available at 0.6 Ga was flagged for recycling, therefore less U is recycled into the mantle but over a shorter period of time. The rate of U recycling is greater in UPb0.6 compared to UPb2.4 and the recycled U is shared over fewer particles. Consequently Pb ingrowth is rapid, so despite having less time in which to accumulate a radiogenic Pb signature, large wavelength anomalies develop (Fig. 3.14g). The layer averaged ^{206}Pb/^{204}Pb for UPb0.6 is lower than UPb2.4 throughout the mantle. Like UPb2.4 the layer averaged ^{206}Pb/^{204}Pb for the surface is reasonable at 19.21, despite the high percentage of particles with very large ratios (Fig. 3.18).

The scatter in ^{207}Pb/^{204}Pb vs ^{206}Pb/^{204}Pb space measured by 'd' value is fairly similar between UPb2.4 and UPb0.6 (Fig. 3.15b,c), but almost 30× different between them in ^{208}Pb/^{204}Pb vs ^{206}Pb/^{204}Pb space (Fig. 3.16b,c). The gradient in ^{207}Pb/^{204}Pb vs ^{206}Pb/^{204}Pb space is also significantly larger in UPb0.6 compared to UPb2.4. In our model the onset of U recycling is sudden; however in reality this is not likely to have been the case. In the time from atmospheric oxygenation during the GOE at 2.4 - 2.1 Ga (Lyons et al. 2014; Holland 1985), to full oceanic oxygenation at 0.6 Ga (Andersen et al. 2015), the amount of U being recycled back into the mantle is likely to have steadily increased. Our simplified end member cases UPb2.4 and UPb0.6 do not capture this gradational change and so there is either too much or zero U entering the mantle early on (Figs. 3.19,3.20). A better approximation would be increase the amount of U recycling increasing from 2.4 Ga to just after 0.6 Ga. This would bring the gradient and scatter in ^{208}Pb/^{204}Pb vs ^{206}Pb/^{204}Pb space closer to the data values.

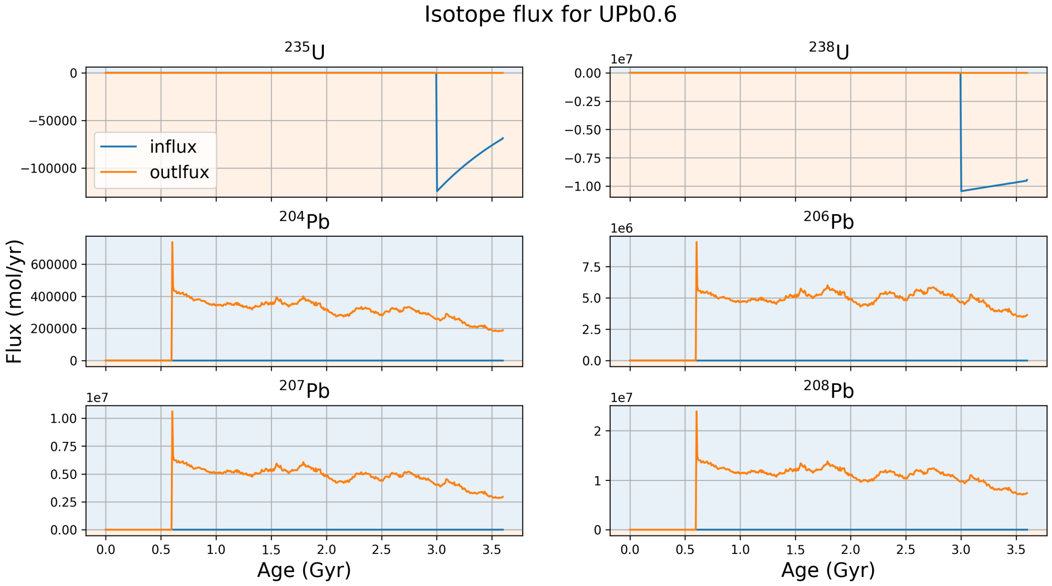

Fig. 3.20 Flux of isotopes over time for case UPb0.6. Blue lines are influx into the mantle from continental reservoir and orange lines are outflux from mantle to continental reservoir.

Mixing

A solution to reducing the unreasonably high Pb ratios could be to include a process which account for fine scale mixing. Xie and Tackley (2004b) included a fine scale mixing process in their models where a strain threshold is set, at which bulk chemistry and trace elements on particles are homogenised with local particles. Such a process is not implemented in TERRA but we invoke an alternative mixing process which simulates the mixing that occurs in the melt zone. This has similarities to the statistical upper mantle assemblage (SUMA) model Meibom and Anderson (2003) and the statistical box models of Rudge et al. (2005) and Rudge (2006). In SUMA, heterogeneity exists throughout the mantle but is homogenised upon sampling, decreasing the range of isotope ratios observed in MORBs compared to what actually exists in the mantle. This allows for mantle that contains some higher Pb isotope ratios which, when averaged with material with low Pb isotope ratios, produces the isotope array that we observe. Evidence for such heterogeneity has been shown to exist down to the crystal scale (Lambart et al. 2019). We can approximate pre-eruptive melt zone mixing by averaging melts produced close to one another. In Table 3.7 various outputs are compared for the standard case with no mixing, and cases where 10 and 50 particles are averaged together

Table 3.7 Table of τ_{Pb}, scatter and gradient in $^{208}Pb/^{204}Pb$ vs $^{206}Pb/^{204}Pb$ space for unmixed case and also after mixing is applied for n=10 and n=50 where n is number of particles that are averaged together.

		CONTU	**UPb2.4**	**UPb0.6**	**4.5GYR**	**HEAT**	**SCALE**
Unmix	τ_{Pb}	1.758	1.876	2.112	1.895	1.88	1.894
	$\mathbf{d_{207}}$	0.0041	0.0112	0.14	0.0464	0.0121	0.0118
	$\mathbf{grad_{208}}$	0.019	0.659	1.119	0.531	0.764	0.928
	$\mathbf{d_{208}}$	0.3325	0.4405	0.0153	0.4238	0.4813	0.4819
n=10	τ_{Pb}	1.772	1.931	2.168	1.99	1.932	1.851
	$\mathbf{d_{207}}$	0.0027	0.0059	0.0063	0.0315	0.006	0.0056
	$\mathbf{grad_{208}}$	0.036	0.71	1.116	0.585	0.838	0.924
	$\mathbf{d_{208}}$	0.2192	0.3007	0.0016	0.2733	0.3110	0.2083
n=50	τ_{Pb}	1.807	2.005	2.25	2.105	1.982	1.868
	$\mathbf{d_{207}}$	0.0016	0.0047	0.0039	0.0263	0.0033	0.003
	$\mathbf{grad_{208}}$	0.063	0.771	1.111	0.671	0.935	0.907
	$\mathbf{d_{208}}$	0.0875	0.2392	0.001	0.209	0.1815	0.0619

before sampling. We also present plots of the Pb ratios after the mixing has been applied for a n=50 (Fig. 3.21).

In general, the mixing process eliminates the most extreme Pb ratios and reduces the scatter. In the case of SCALE, where the mantle is more chemically homogeneous than other cases (Fig. 3.14), the mixing process has little effect on τ_{Pb}. Where mantle is more chemically heterogeneous, the mixing process causes τ_{Pb} to slightly increase with increasing n. Averaging groups of 50 melt packages causes the fraction of particles with extremely high $^{206}Pb/^{204}Pb$ in case UPb2.4 to fall from 31.33% to 7.58% while the fraction of Pb in the melt that this represents is reduced from 4.54% to 1.15% (Fig. 3.22). Rudge (2006) showed that τ_{Pb} has a weak dependence on n (the number of melt parcels mixed) and that is indeed what we see in our models too, with τ_{Pb} for case UPb2.4 changing from 1.76 Gyr to 1.81 Gyr for n = 50. The effect of mixing on scatter, τ_{Pb}, and gradient decreases with increasing n. There does not seem to be a simple scaling rule that can be applied for the mixing though, with different cases being affected by n in different ways. For example in HEAT, d_{207} is approximately halved between no mixing and n = 10, and approximately halves again between n = 10 and n = 50. Meanwhile d_{207} in UPb0.6 is reduced by around 95% between no mixing and n = 10, and then by around 40% between n = 10 and n = 50. τ_{Pb} for case UPb2.4 is larger than that of CONTU. This may be because of the ancient heterogeneity generated by Pb removal from 3.0 Ga. The standard deviations

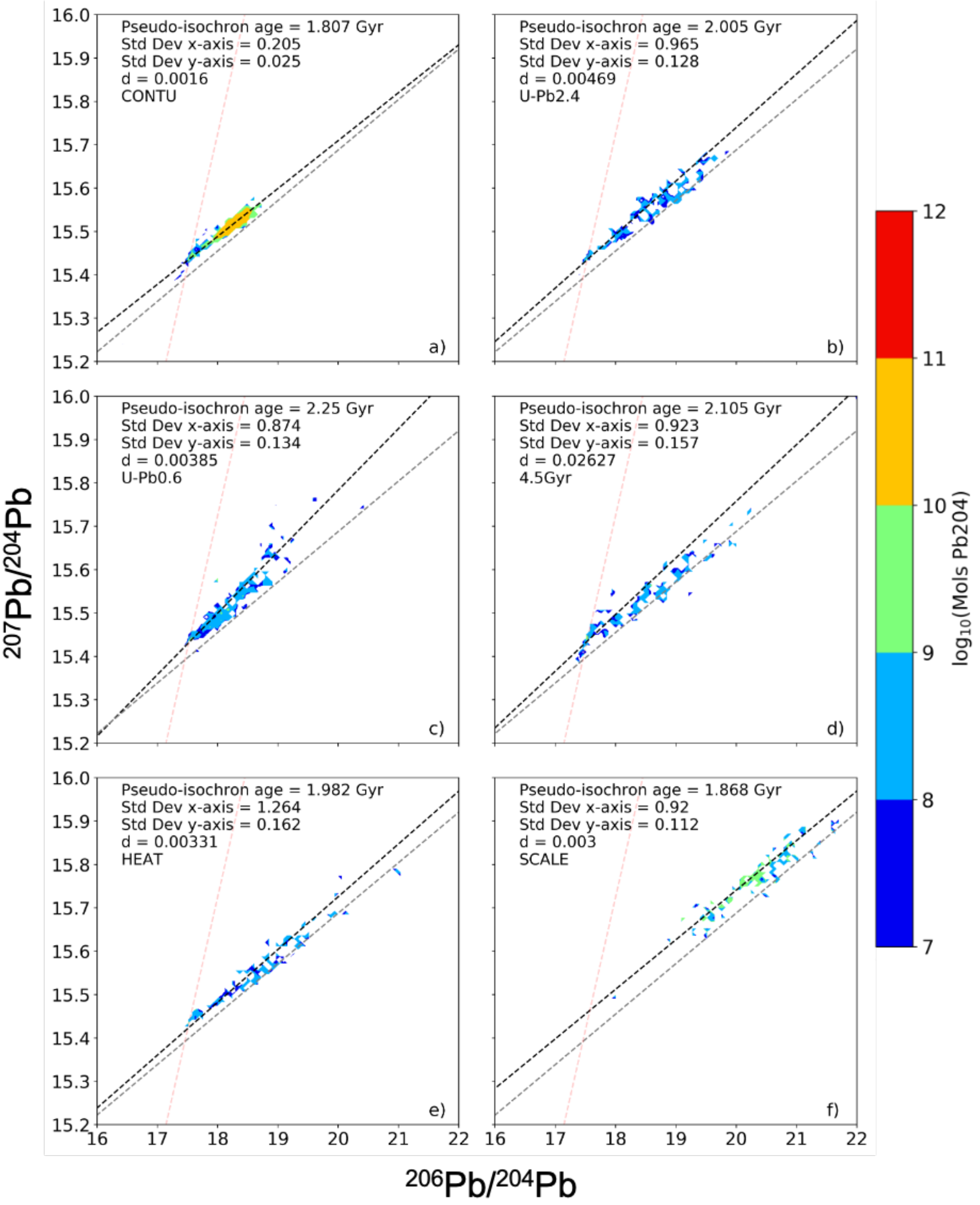

Fig. 3.21 ^{207}Pb/^{204}Pb vs ^{206}Pb/^{204}Pb for cases CONTU, UPb2.4, UPb0.6, 4.5GYR, HEAT, and SCALE after mixing process has been applied with n=50.

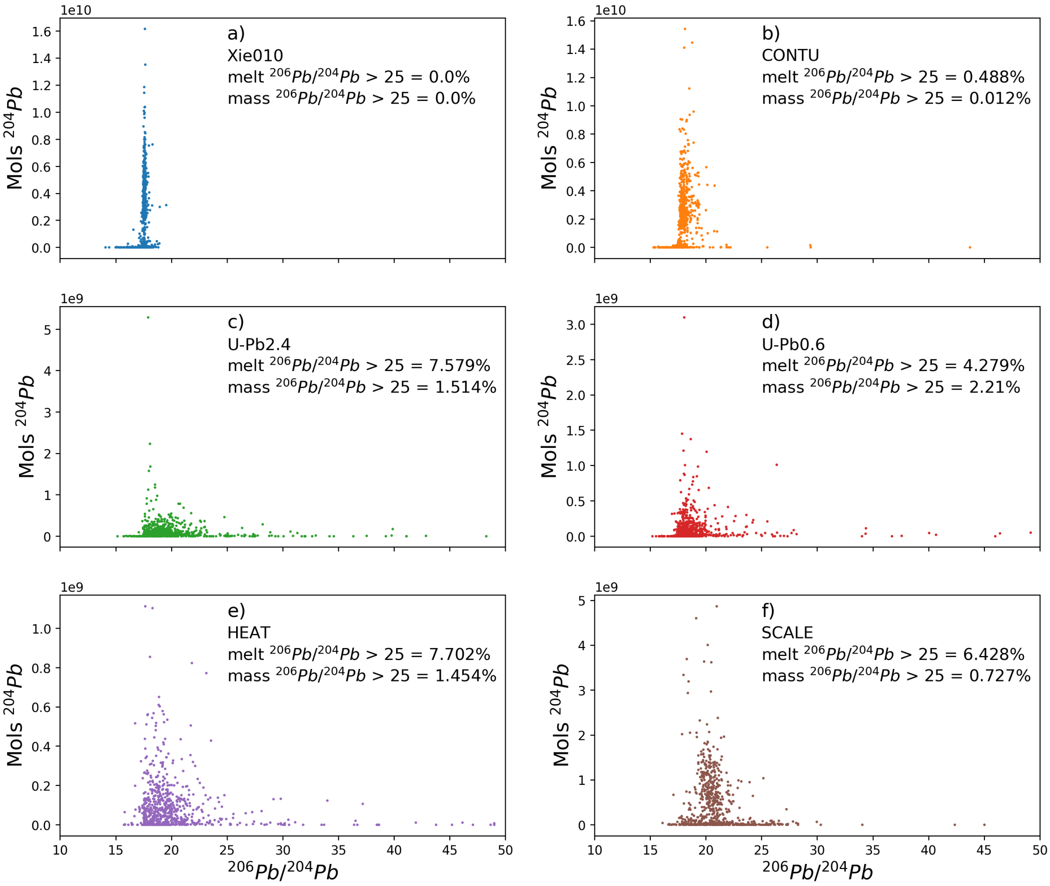

Fig. 3.22 For cases XIE010, CONTU, UPb2.4, UPb0.6, 4.5GYR, HEAT, SCALE. ^{206}Pb/^{204}Pb vs concentration ^{204}Pb for melt produced at present day with n = 50 mixing applied. Labelled % of mixed melting particles that have ^{206}Pb/^{204}Pb $>$ 25, and the % Pb mass that this represents of all the melt.

in Pb isotope ratios are much greater in than CONTU and greater even than the observed values. Even so the 'd' value in ^{207}Pb/^{204}Pb vs ^{206}Pb/^{204}Pb space (Fig. 3.15b) is still only about half of the of the observed values. After applying the mixing process this drops to less than quarter. Conversely the 'd' value in ^{208}Pb/^{204}Pb vs ^{206}Pb/^{204}Pb space for UPb2.4 (Fig. 3.16f, 0.440) is much higher than MORBs and OIBs (0.119 and 0.172 respectively). If the mixing process is applied then 'd' is reduced to 0.240, still much greater than measured values. This indicates how important mixing is in controlling the range of isotope ratios that are measured in oceanic basalts.

Degree of processing

4.5GYR, HEAT, and SCALE all experience greater degrees of processing than other cases. For case 4.5GYR the extra processing is due to the model being initialised at 4.5 Ga rather than 3.6 Ga, allowing for an extra 0.9 Gyr of fractionation due to melting to occur. The large increase in scatter between Fig. 3.15b and Fig. 3.15d and the slight decrease in scatter between Fig. 3.16b and Fig. 3.16d are due to the half lives of the parent isotopes involved. Both ^{238}U and ^{232}Th have half lives much longer than 0.9 Gyr, hence little change in the scatter in Fig. 3.16d, while ^{235}U's half live is shorter than 0.9 Gyr. This implies that the assumption that we have been using, that the mantle was well mixed to the point of being chemically homogenous before 3.6 Ga, may be unsatisfactory. Allowing fractionation for a longer period of time allows for more Earth-like scatter to develop, whilst also having a negligible effect on τ_{Pb} compared to UPb2.4 (Fig. 3.15d). This also indicates that the effects of U recycling and Pb removal carry much more weight in determining the pseudo-isochron than melting fractionation. An Earth-like τ_{Pb} was also achieved for models that were run for 4.5 Gyr in Xie and Tackley (2004b) and Brandenburg et al. (2008), although in the latter this was not quantified as τ_{Pb}. Xie and Tackley (2004b) required there to be no fractionation between Pb and U before 2.5 Ga. This is unlikely to be a good representation of Earth as experimentally determined partition crystal/melt partition coefficients for Pb and U are different (Hauri et al. 1994; Workman and Hart 2005). Brandenburg et al. (2008) required a change in the treatment of Pb to reconcile the ^{207}Pb/^{204}Pb vs ^{206}Pb/^{204}Pb slope. In their model at 2.25 Ga the 'extraction coefficient' of Pb is decreased to reduce the amount of Pb relative to U being extracted from the mantle. This is somewhat reminiscent of our models where we invoke a change in the behaviour of U at 2.4 Ga to allow it to be recycled from the continental reservoir. Both processes have the effect of increasing the μ of the mantle, however in our model this is also compounded with the removal of Pb from the mantle from 3.0 Ga. We must be careful though not to draw too many conclusions from case 4.5GYR as the conditions of early Earth are uncertain. Certainly the mantle will have had much lower viscosities than it does at present due to higher mantle temperatures (Zhong et al. 2000), but there is also potential for a magma ocean (Ohtani 1985), the simulation of which is beyond current modelling capabilities.

In HEAT, there is strong internal heating early on due to much radioactive decay occurring then. The heating rate decreases with time, from 62.4 TW to 15.9 TW. Due to the stronger heating there is significantly more melting early on in the calculation. This causes a relatively large amount of primordial

^{204}Pb to be removed over time relative to radiogenic Pb as the radiogenic Pb experiences ingrowth later on when the melting rate has reduced, while ^{204}Pb does not. Consequently, Pb ratios throughout the mantle in HEAT are more radiogenic than in cases with constant heating (Fig. 3.17b). This dos not show up in the melts as the melting zone has similar Pb ratios to other cases. The increased processing in both HEAT and SCALE incurs little effect on τ_{Pb}, but has a definite effect on the gradient in ^{208}Pb/^{204}Pb vs ^{206}Pb/^{204}Pb space. Box modelling by Xie and Tackley (2004b) indicates that while increased processing rates do lower τ_{Pb}, it is required to be a very strong increase into the past to be the sole explanation for the low τ_{Pb} of MORBs and OIBs. Of course, this box model does not account for U recycling from the continent or Pb sequestering into the continent, and so may not be applicable in this case. Rapid early processing allows for high Th/Pb anomalies to develop before the GOE, hence higher ^{208}Pb/^{204}Pb. The 'd' values in both HEAT and SCALE are remarkably similar to UPb2.4. While increased processing means greater fractionation, it also makes for more efficient mixing. It seems then that these two competing factors somewhat cancel out leaving the 'd' unchanged.

Due to temporal scaling the mantle effectively overturns more frequently in case SCALE. Material at the surface therefore receives less recycled U before it is enters a downwelling region and is cycled into the mantle. Consequently material enriched by uranium recylcing does not develop such high μ at the surface as in unscaled cases. The average μ in SCALE is higher through the rest of the mantle than other cases (Fig. 3.17a). This is only due to Pb removal being a function of the number of melting events, rather than a prescribed rate, so this could be adjusted to match unscaled cases with carefully chosen parameters. Despite the high μ, large wavelength Pb anomalies do not develop as the increased processing rate mixes recycled oceanic crust from the surface back into the mantle efficiently. This explains the almost constant layer averaged μ and ^{206}Pb/^{204}Pb. The Pb ratios of melts in SCALE (Figs. 3.15,3.16i) are much more radiogenic than measured in oceanic basalts (Fig. 3.1). The cause of this appears to be two-fold. The mantle is strongly depleted in ^{204}Pb compared to other cases so as radiogenic Pb is produced from recycled U larger ratios develop. Secondly the efficient mixing in the scaled case prevents the melting layer from developing an un-radiogenic Pb composition as happens in un-scaled cases (Fig. 3.11b). Material sampled from the melting layer therefore has a similar composition to the rest of the mantle.

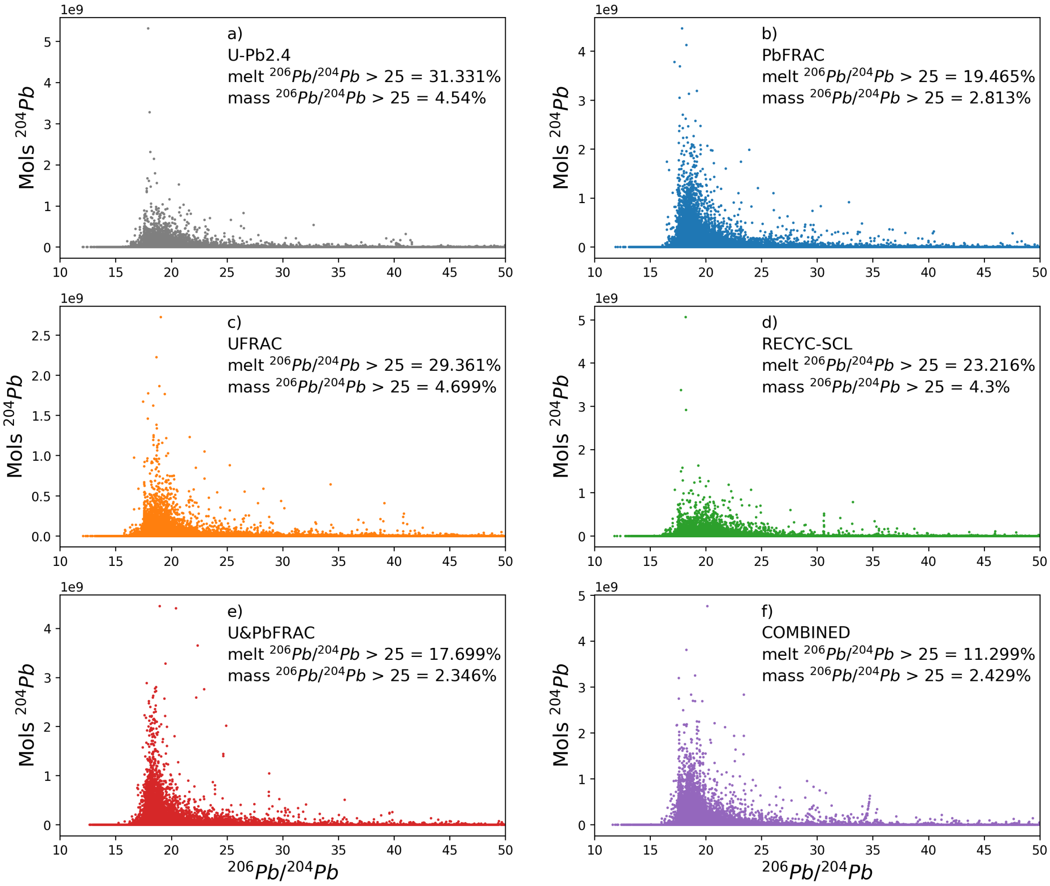

Fig. 3.23 ^{206}Pb/^{204}Pb vs ^{204}Pb abundance for (a) UPb2.4 for reference, (b) PbFRAC, (c) UFRAC, (d) RECYC-SCL, (e) U&PbFRAC, (f) COMBINED.

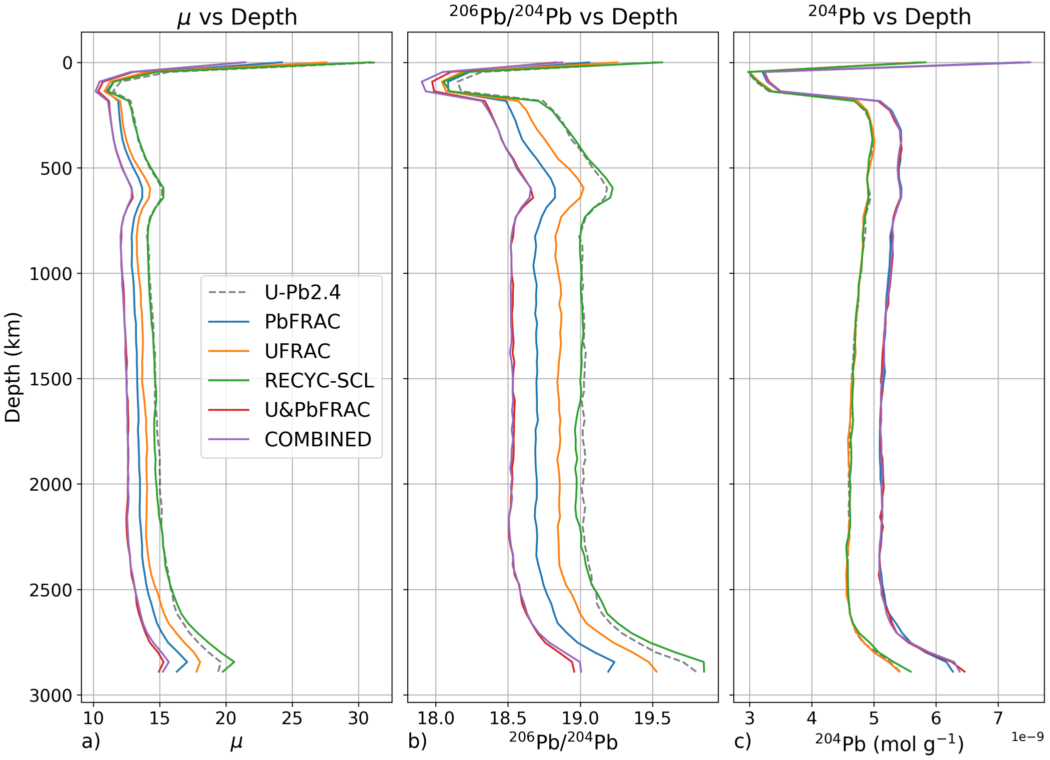

Fig. 3.24 Radial layer averages of (a) μ (b) ^{206}Pb/^{204}Pb (c) ^{204}Pb for cases PbFRAC, UFRAC, RECYC-SCL, U&PbFRAC, COMBINED and UPb2.4 for reference.

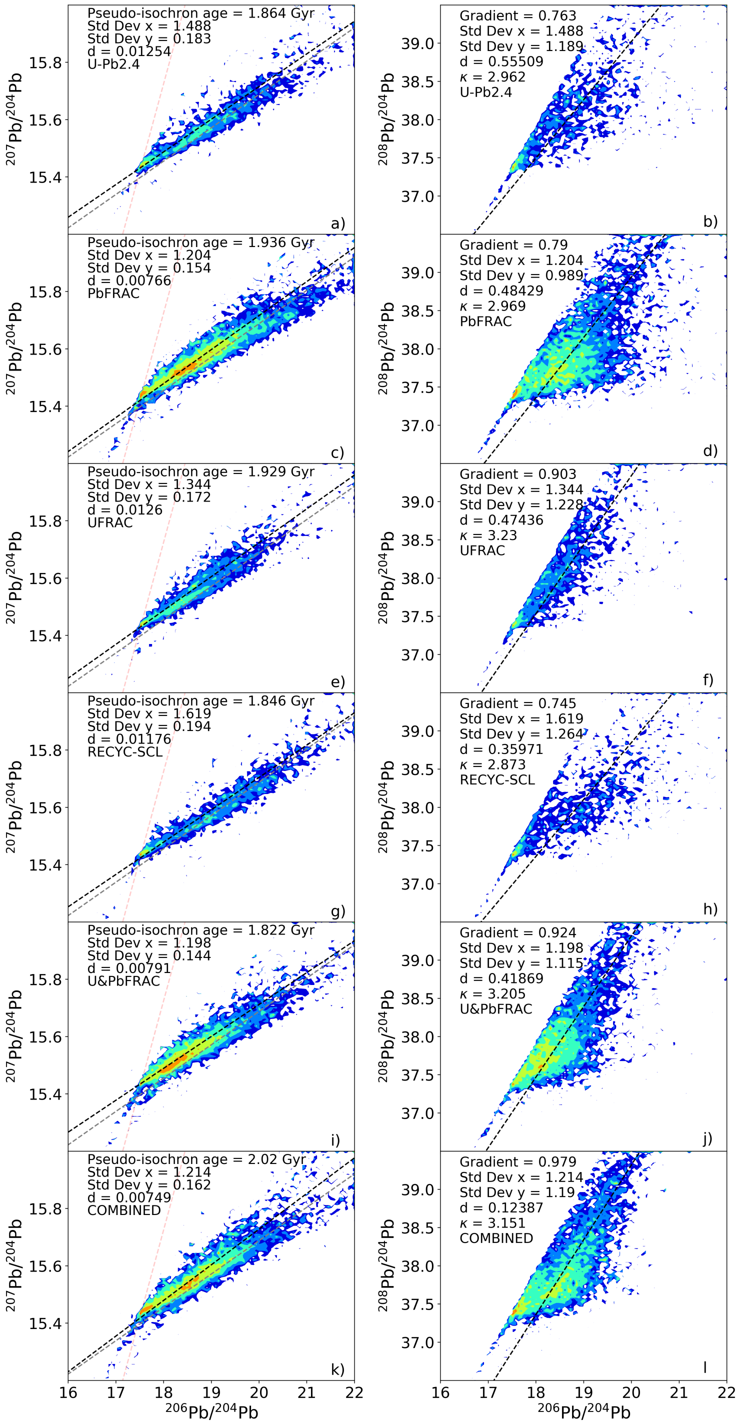

Fig. 3.25 (a,c,e,g) $^{207}\mathrm{Pb}/^{204}\mathrm{Pb}$ vs $^{206}\mathrm{Pb}/^{204}\mathrm{Pb}$ and (b,d,f,h) $^{208}\mathrm{Pb}/^{204}\mathrm{Pb}$ vs $^{206}\mathrm{Pb}/^{204}\mathrm{Pb}$ for (a,b) UPb2.4 (c,d) PbFRAC (e,f) UFRAC (g,h) RECYC-SCL, (i,j) U&PbFRAC, (k,l) COMBINED.

High Pb ratios in the melt

Cases in which there is material exchanged between the continental reservoir and mantle all suffer with having a large amount of melt that has Pb ratios much higher than anything that is measured in oceanic basalts (Figs. 3.14, 3.15, 3.16). This is clearly an issue so we will investigate what can be done to reduce this. We have already shown that a mixing process, representing the mixing of melts in a magma chamber prior to eruption, reduces the fraction of melts with extremely high Pb ratios.

In the surface layer, the average μ is very high for cases UPb2.4, UPb0.6, 4.5GYR and HEAT (Fig. 3.17a). Uranium recycling from the continental reservoir, melt fractionation and Pb removal all act here to increase U/Pb. The transition zone is also home to high μ values because of subducted basalt becoming trapped here due to the olivine phase change. The high μ of particles at the surface causes rapid enrichment in radiogenic Pb relative to ^{204}Pb (Fig. 3.14b), generating large scale anomalies. Highly radiogenic compositions are clearly seen in the blue shades and are generally found in basaltic material. It is worth noting that just below the surface, in the melt zone, the average μ is 10-12 for cases UPb2.4, UPb0.6, 4.5GYR, and HEAT. The average μ for MORBs as reported in White (1993) falls nicely into this range being 11.20, however the range of μ measured in samples varies dramatically from 24.99 to 3.03. While the extremely high μ of some particles is clearly inconceivable for terrestrial samples, there is still scope for a spectrum of μ to exist side by side.

Many melt parcels have extremely high ^{206}Pb/^{204}Pb (^{206}Pb/^{204}Pb > 25, the upper end of OIB composition). In fact, they account for 33.33% of the melt producing particles at the end of the calculation for UPb2.4. The same particles also have very low ^{204}Pb concentrations (Fig. 3.18c). Consequently the Pb in melt with extremely high ^{206}Pb/^{204}Pb accounts for only 4.54% of all Pb in the melt. Fig. 3.17b shows this, as the layer averaged ^{206}Pb/^{204}Pb at the surface is not unreasonably high, at 19.5. Similarly in cases UPb0.6, 4.5GYR, HEAT and SCALE a high proportion of melting particles have extremely high ^{206}Pb/^{204}Pb. UPb0.6 has 21.24% of melting particles with ^{206}Pb/^{204}Pb > 25, representing 2.89% of the mass of Pb in the melt (Fig. 3.18d). This is significantly lower than UPb2.4. Case CONTU has substantially fewer particles with such extreme Pb compositions while HEAT has by far the most,

Table 3.8 Parameter settings for cases testing production of extremely high Pb ratios. Pb cont frac is the fraction of Pb that is removed from the melt to continental reservoir after 3.0 Ga. U recycle is the fraction of continental U that is set aside for recycling to the mantle from 2.4 Ga. Recycle style is whether the recycled U is shared across all surface particles evenly (Equal) or scaled to their ^{204}Pb content (Scaled).

Case	Pb cont frac	U recycle	Recycle style
UPb2.4	0.25	0.5	Equal
PbFRAC	0.1	0.5	Equal
UFRAC	0.25	0.33	Equal
U&PbFRAC	0.1	0.33	Equal
RECYC-SCL	0.25	0.5	Scaled
COMBINED	0.1	0.33	Scaled

suggesting that the amount of Pb that is being removed has strong influence in generating particles with extremely high Pb ratios.

From the observations above it seems extremely high Pb ratios are caused by particles that have extremely high μ. This in turn may occur for two reasons. Some particles have extremely low Pb concentrations due to experiencing many melt events then acquire recycled continental U, so only a small amount of radiogenic Pb ingrowth is required to make high Pb ratios. Alternatively particles may receive large amounts of recycled U if they spend a lot of time in the surface layer and so can accumulate large amounts of radiogenic Pb. In practice, a combination of both processes probably affects many of the particles that produce melt with high Pb ratios.

Potential solutions to this would be to reduce the amount of Pb that is removed during melting, reduce the amount of U that is returned to mantle, and to weight the amount of uranium added to particles by their ^{204}Pb abundance. Cases are run to test each of these scenarios and then another test is run with all scenarios applied at once (Table 3.8).

In reducing the amount of Pb that is removed from the melt to the continental reservoir (PbFRAC), the fraction of melt that contains $^{206}\text{Pb}/^{204}\text{Pb} > 25$ is reduced from 28.6% to 19.5%, representing 2.8% of the mass of Pb in the melt (Fig. 3.23a). Less Pb leaves the mantle system so the continental crust contains 91% of the ^{204}Pb that case UPb2.4 does. Consequently both μ and Pb ratios are lower throughout the mantle (Fig. 3.24b). Present day melts have a slight increase in both τ_{Pb} and the gradient of $^{208}\text{Pb}/^{204}\text{Pb}$ vs $^{206}\text{Pb}/^{204}\text{Pb}$ and also a slightly higher κ (Fig. 3.25a,b) compared to UPb2.4.

Absolute terrestrial Pb fluxes are difficult to define and therefore comparing model Pb fluxes to Earth is not possible. A better constraint to use is the relative distribution of Pb between the continents and the mantle. Using the present day amount of Pb calculated from the initial values for our models (Table 3.3) and the estimated amount of Pb in Earth's continents (Rudnick and Gao 2013) approximately 43% of the total Pb in the silicate Earth resides in the continents. This can be used to guide how much Pb we end up with in our continental reservoir. Lead that is removed from the melt in our model corresponds to any melt that is removed from Earth's convecting mantle. This could be through arc magmatism or incorporation into the lithospheric wedge. There is also a possibility that some Pb has been sequestered to the core in sulphides (Kramers and Tolstikhin 1997; Maltese and Mezger 2020), but this is not included in our models. We therefore find it reasonable to assume that $< 50\%$ of the total Pb in the Earth system should end up in the continental reservoir. For case UPb2.4, 54.49% of the total Pb is in the continental reservoir by present day. This is reduced to 49.59% when 10% Pb is removed from the melt.

In cases where 50% of the continental U at 2.4 Ga is set aside for recycling, this is equivalent to recycling about 1.7×10^{14} mol of ^{235}U and 6.9×10^{15} mol of ^{238}U, as mentioned in 3.4.3. In UFRAC, U&PbFRAC and COMBINED this is reduced to 1.1×10^{14} mol of ^{235}U and 4.6×10^{15} mol of ^{238}U (Fig. 3.26). For reference the mantle contains a total of 1.77×10^{16} mol of ^{235}U and 3.31×10^{17} mol of ^{238}U at 2.4 Ga, so this reduction equates to $\sim 0.7\%$ of Earth's uranium budget. Reducing the amount of U that is eroded into the mantle is not particularly effective at decreasing the fraction of particles with extremely high Pb ratios (Fig. 3.23b). The strongest effect it has is increasing the μ and decreasing the κ of the continental reservoir (Table 3.9). Consequently, κ in the melt is increased, but remains lower than the value of 3.8 that is calculated from the Pb ratios (Galer and O'Nions 1985). Less U entering the mantle also decreases μ and Pb ratios throughout the mantle (Fig. 3.24a,b).

Case U&PbFRAC combines a reduction in the fraction of Pb sequestered to the continental reservoir with a reduction of the fraction of continental U that is recycled into the mantle. The fraction of Pb that ends up in the continental reservoir is most strongly influenced by the smaller fraction of Pb being moved from the melt to the continental reservoir, while the increase in μ and decrease in κ are most strongly affected by the reduction in U recycling (3.9). The values of μ and κ have moved closer to bulk crustal values

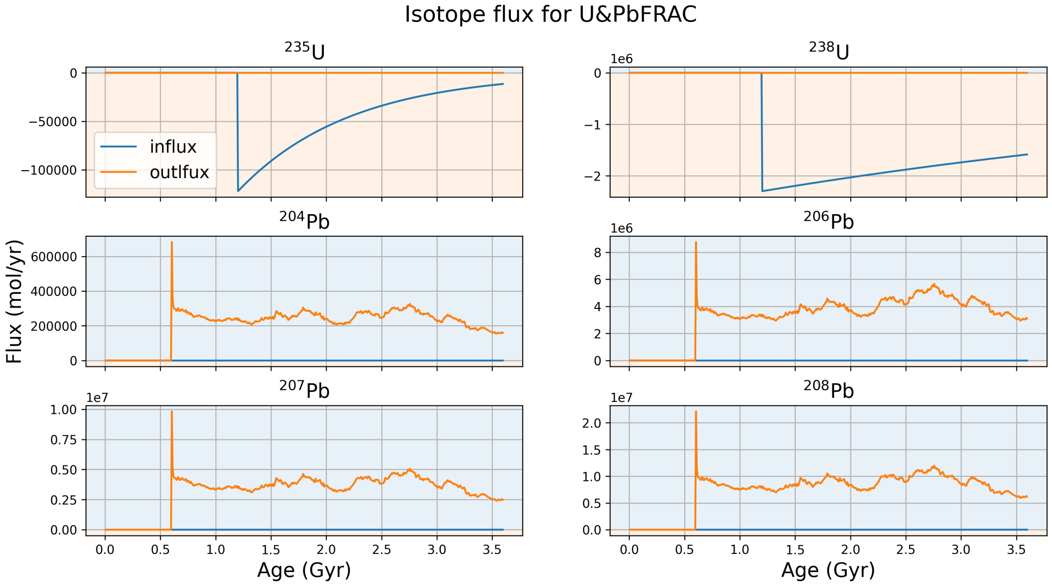

Fig. 3.26 Flux of isotopes over time for case U&PbFRAC. Blue lines are influx into the mantle from continental reservoir and orange lines are outflux from mantle to continental reservoir.

suggested by Kramers and Tolstikhin (1997) however μ is slightly on the low side and κ slightly on the high side. Reduced Pb removal and U recycling also results in the lowest μ and ^{206}Pb/^{204}Pb at each depth (Fig. 3.24a,b). The continental reservoir contains just less than 50% of all Pb, inline with first order estimates (Rudnick and Gao 2013). Each Pb ratio in the continental reservoir is increased relative to cases UPb2.4, PbFRAC, and UFRAC. This is due to the combination of increased ingrowth of radiogenic Pb in the continental reservoir (because less U is recycled) and less ^{204}Pb added to the continental reservoir. However, the continetnal crust Pb composition is still unradiogenic (Table 3.9), similar to what is required for the models of Kramers and Tolstikhin (1997). Conceivably this un-radiogenic Pb could be located in the lithospheric mantle wedge or in the lower continental crust, having been emplaced there after being removed from subducted slabs (Halla 2005; King et al. 2007). It is noted that our models do not include any processes for the erosion or sequestration of Th and this may have an effect on our models' fit to some constraints.

Scaling the amount of recycled U added to particles at the surface yielded only a slight reduction in the fraction of melt with extremely high Pb ratios (Fig. 3.23d); however, the mass of Pb that this melt represents is still similar to UPb2.4. By far the most effective way to reduce the fraction of melt with

Table 3.9 Continent reservoir isotopic composition at present day for cases testing influences on extremely radiogenic Pb compositions. Also included is the Pb in the continental reservoir expressed as a fraction (% Pb cont) of the total Pb in the silicate Earth.

	μ	κ	**^{206}Pb/^{204}Pb**	**^{207}Pb/^{204}Pb**	**^{208}Pb/^{204}Pb**	**%Pb Cont**
UPb2.4	2.389	7.782	16.31	15.297	36.488	54.49
PbFRAC	2.635	7.784	16.41	15.309	36.657	49.59
UFRAC	3.213	5.834	16.487	15.314	36.52	54.21
U&PbFRAC	3.515	5.84	16.57	15.325	36.655	49.667
RECYC-SCL	2.409	7.785	16.353	15.3	36.524	54.07
COMBINED	3.514	5.841	16.575	15.326	36.655	49.67

high Pb ratios is combining a reduction in Pb removal from the melt, with a reduction in the amount of U recycling and scaling recycled U to the receiving particle's ^{204}Pb (Fig. 3.23f). In case UPb2.4 the continental crust had a very low μ (2.39) and very high κ (7.78) compared to what is estimated from the chemical models of Kramers and Tolstikhin (1997), which suggest μ of 4.16 and 10.2 for the lower and upper crust respectively and κ of 3.78 and 4.64 for the lower and crust respectively. Case PbFRAC has a slightly higher continental crust μ at 2.64 and UFRAC has a higher μ, 3.21, and lower κ, 5.83. Cases COMBINED and U&PbFRAC have the highest continental crust μ of all the cases, at 3.51, and κ is decreased relative to UPb2.4 to 5.84. These values for μ and κ are still slightly low and high respectively compared to Kramers and Tolstikhin (1997), but generally a good match for terrestrial estimates. Unlike UPb2.4, the gradient in ^{208}Pb/^{204}Pb vs ^{206}Pb/^{204}Pb is close to 1.0. The pseudo-isochron age τ_{Pb} is notably larger than U&PbFRAC and on the upper end of what would be acceptable for an average of oceanic basalts at 2.0 Gyr. This is a difference of nearly 200 Myr compared to U&PbFRAC. Given that there is no conceivable mechanism by which the amount of recycled continental U that a section of oceanic crust receives is related to its Pb composition, it is best to not include this mechanism in further models.

Initial trace element distribution

In this chapter, all the cases have been initialised with the assumption that the mantle was well mixed before 3.6 Ga, that is they are chemically homogeneous at the beginning of the calculation (Christensen and Hofmann 1994). A more chemically heterogeneous initial condition could be argued for in the event of incomplete homogenisation of the mantle, for example if

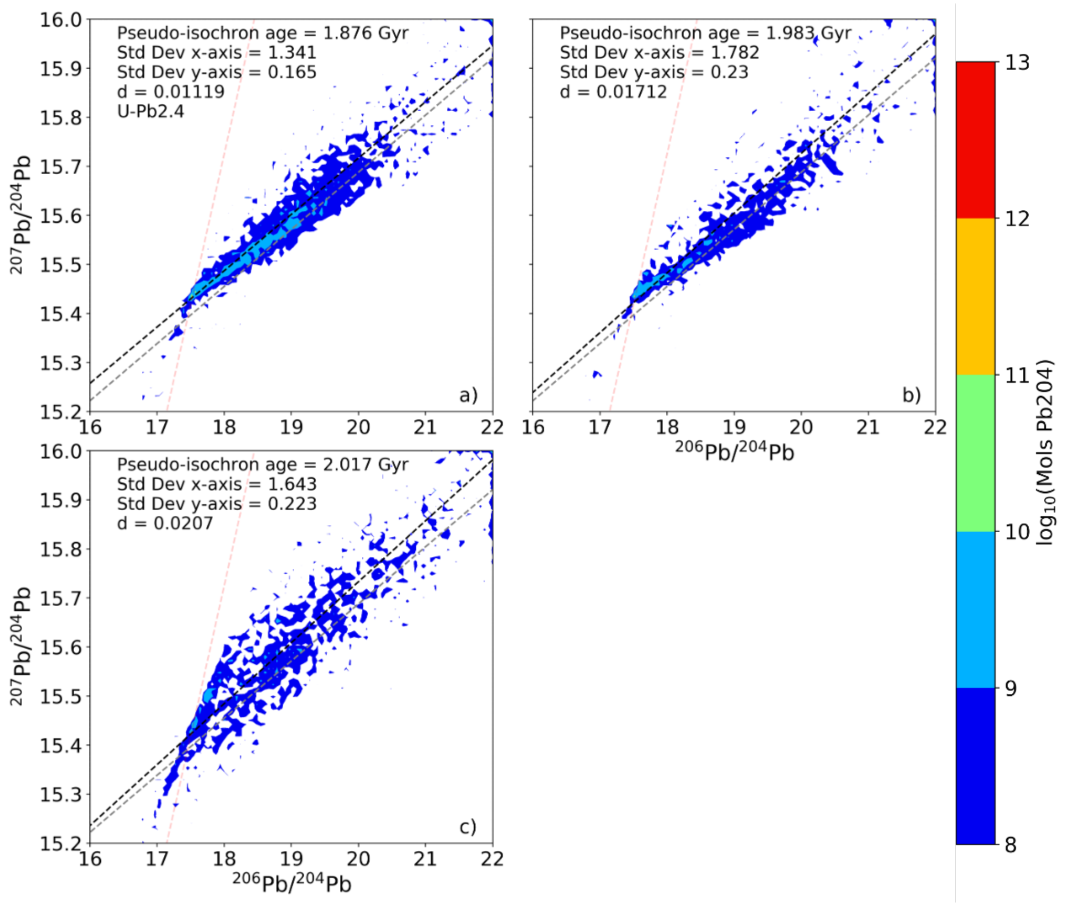

Fig. 3.27 ^{207}Pb/^{204}Pb vs ^{206}Pb/^{204}Pb for (a) Case UPb2.4 for reference. At initialisation all particles are given same amount of each trace element. (b) Particles assigned random amount of isotopes between 0.75 and 1.25 amount that particles receive in UPb2.4. All isotopes are correlated (c) Similar isotopes are correlated.

early Earth conditions were cooler and so the mantle convected less vigorously (Valley et al. 2002). To assess this possibility we run cases where the initial trace element composition of the particles is varied. The initial trace element composition that would be attributed to the particle is scaled by a random number between 0.75 and 1.25 to give a variation of up to ± 25%. The random numbers are chosen by a mechanism that causes them to be have a normal distribution with a mean of 1. In the first case (Fig. 3.27b), all isotopes are correlated with each other, that is the random scaling number is applied to all isotopes. In the second case (Fig. 3.27c), a different random scaling number is applied to groups of similar isotopes on each particle. For example ^{238}U, ^{235}U, and ^{232}Th all have the same scaling number applied which is different to that applied to ^{208}Pb, ^{207}Pb, ^{206}Pb, ^{204}Pb. This is similar to strong early fractionation of the mantle being moderately well mixed by 3.6 Ga. In both instances τ_{Pb} and the scatter are increased. In the second case, where groups of similar isotopes are correlated, 'd' is nearly double from 0.011 to 0.021.

Time of subduction initiation

In section 3.4.2 we made the assumption that plate tectonics initiated around 3.0 Ga. Consequently, the best fit values that we have found for U recycling rates and Pb removal rates apply only under this assumption. We remind the reader that this is of importance in our models as this time controls when Pb begins to be removed from the melts to the continental reservoir. This process models the removal of Pb from subducted oceanic lithosphere and subsequent emplacement in the lower continental crust or lithospheric mantle wedge (Kramers and Tolstikhin 1997; Kellogg et al. 2007). Although 3.0 Ga is a generally well accepted value for the onset of plate tectonics (Tang et al. 2016; Laurent et al. 2014; Shirey and Richardson 2011), there is a whole spectrum of estimates for when modern style plate tectonics may have started. On one end there are those who would say that there is evidence for plate tectonics beginning in Hadean, around 4.2 Byr ago (Maruyama et al. 2018). On the other end there are those who would say the evidence suggests that plate tectonics as we know it would not have started until the Neoproterozoic, around 1 Byr ago, making it a very recent phenomenon (Stern 2005). Given the uncertainty in when modern plate tectonics may have started, it would be useful to get a feeling to what degree varying this assumption affects the Pb composition of melts and the continental crust.

Our favoured case up to this point is U&PbFRAC. In this case Pb is removed from the mantle from 3.0 Ga at a rate that corresponds to around 2.5×10^5 mol yr^{-1} of ^{204}Pb while 1.1×10^{14} mol of ^{235}U and 4.5×10^{15} mol of ^{238}U are recycled into the mantle from 2.4 Ga. Taking this case as the control, we run various cases adjusting the time at which Pb begins to be moved from the melt to the continental reservoir (t_{tec}). Test cases span 600 Myr either side of 3.0 Ga in steps of 200 Myr. The results are summarised by in Fig. 3.28.

The results show that changes by all metrics are not linear, but the rate of change is greater for older t_{tec}. Older plate tectonic start times result in older τ_{Pb} of the melt, up to 2.6 Ga when t_{tec} = 3.6 Ga (Fig. 3.28a). The rate of decrease of τ_{Pb} is very slow after 2.8 Ga, indicating it has possibly reached a minimum. τ_{Pb} cannot logically be reduced below 2.4 Ga because this is that time at which continental U is recycled into the mantle, implying plate tectonics has already started. Although less Pb is present further into the past, the change in % Pb in the continental reservoir increases more rapidly with increasing t_{tec}. This is because of the more rapid processing rates earlier on in the calculation which remove Pb from the mantle more efficiently and also as there is more time over which Pb is removed from the mantle. The Pb and U ratios all decrease with increasing t_{tec}. This is explained by a greater total amount of ^{204}Pb being removed from the convecting mantle with increasing t_{tec}. While more ^{206}Pb, ^{207}Pb, and ^{208}Pb is also removed, these isotopes experience radiogenic ingrowth while ^{204}Pb does not.

Distribution of melting ages

Following the method of Rudge (2006), the pseudo-isochron age can also be calculated from the distribution of melting ages. The method is outlined below for reference. The pseudo-isochron age (τ_{PDF}) is solved for via

$$\frac{\left(e^{\lambda_{235}\tau_{\mathrm{ddi}}}-1\right)^2}{\left(e^{\lambda_{238}\tau_{\mathrm{ddi}}}-1\right)^2}=\frac{E(e^{\lambda_{235}\hat{T}_{\mathrm{m}}}-1)^2}{E(e^{\lambda_{238}\hat{T}_{\mathrm{m}}}-1)^2} \tag{3.5}$$

where

$$Ef\left(\hat{T}_{\mathrm{m}}\right)=\int_0^{\tau_{\mathrm{s}}} f(\tau)q_{\mathrm{m}}(\tau)d\tau. \tag{3.6}$$

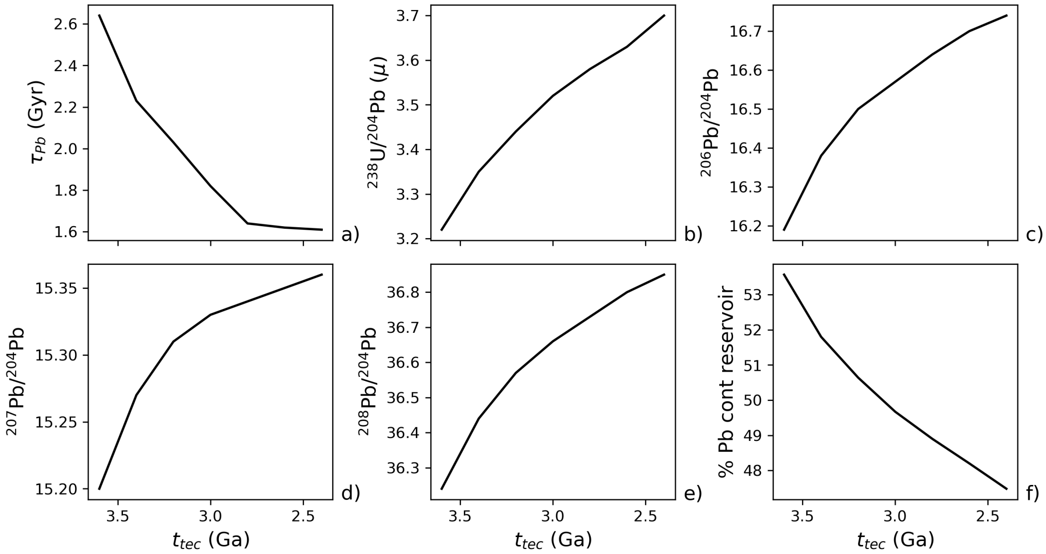

Fig. 3.28 Various model results for different times of plate tectonic initiation, t_{tec} (Ga). a) τ_{Pb}, b) mean μ, c) mean $^{206}\mathrm{Pb}/^{204}\mathrm{Pb}$, d) mean $^{207}\mathrm{Pb}/^{204}\mathrm{Pb}$, e) mean $^{208}\mathrm{Pb}/^{204}\mathrm{Pb}$, f) % total Pb in continental reservoir.

$f(\tau)$ is an arbitrary function, in this case (eg, $E(e^{\lambda_{238}\hat{T}_\mathrm{m}} - 1)^2)$, and $q_\mathrm{m}(\tau)$ is the probability density function of particle melting ages. $\hat{T}_\mathrm{m}$ is a random variable which gives the distribution of melting ages for particles which have undergone melting and τ_s is the length of time that the model is run for, in this case 3.6 Byr.

Using a simulation similar to case HI-DPb, van Heck et al. (2016) showed that there was a good correlation between τ_PDF and τ_Pb, calculated from Pb isotopes in the melt, throughout the calculation. The greatest misfit was found to be in the first $\sim$ 500 Myr of the calculation, before the mantle has become well mixed. The distribution of melting ages at different times throughout case HI-DPb are used to calculate τ_PDF (Fig. 3.29b). Similar to van Heck et al. (2016), there is a good match between τ_PDF and τ_Pb, with the misfit after 3.6 Gyr being $\sim$ 2%. Due to similar dynamics, τ_PDF is identical for cases HI-DPb and U&PbFRAC, but clearly τ_Pb for case U&PbFRAC does not match well with τ_PDF (Fig. 3.29b). This is due to the added complexities of U recycling and Pb removal, which are not included in Rudge (2006). It is also noted that the method of Rudge (2006) assumes a well mixed mantle, however the Pb composition of the mantle in case U&PbFRAC is highly heterogeneous due to U recycling and Pb removal, similar to cases shown in figure 3.14.

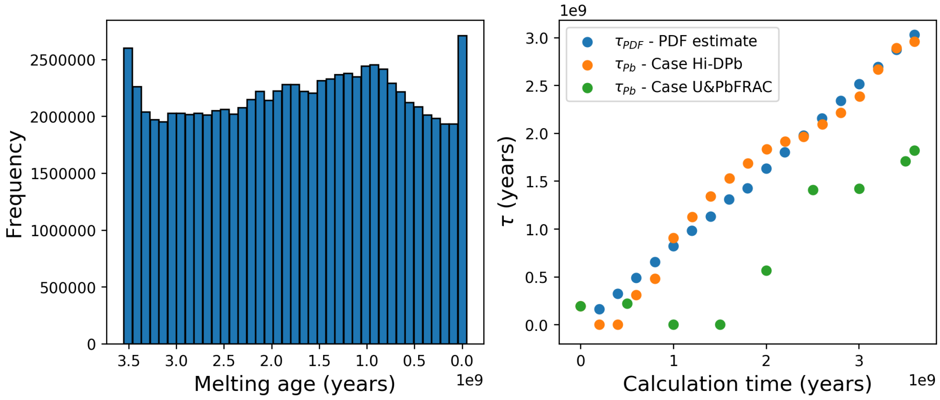

Fig. 3.29 a) Distribution of melting ages (time since last melting) at 3.6 Gyr for particles which have undergone melting in case HI-DPb. b) Comparison of τ_{PDF}, calculated from the distribution of melting ages (blue circles) and τ_{Pb}, calculated from the distribution of Pb isotopes in the melt for cases HI-DPb (orange circles) and U&PbFRAC (green circles). Note that τ_{PDF} is identical for cases HI-DPb and U&PbFRAC due to similar dynamics.

3.9 Conclusions

From the results of our models investigating the effect of partition coefficients on the Pb composition of melts, it is clear that the timing of fractionation has a strong effect on τ_{Pb}. This also has an effect on the scatter of the Pb isotope ratio of melts, with earlier fractionation generating more scatter. This class of model (with fractionation via differences partition coefficients) falls short of being able to produce the degree of scatter that is measured in oceanic basalts. These models also fail at reproducing the observation that almost all Pb measured in oceanic basalts plots to the right of the geochron.

We implement a continental reservoir to store trace elements that make up the continental crust and allow communication between this and the mantle. This reservoir is crucial in fitting the observation that Pb in oceanic basalts plot to the right of the geochron. In order to achieve Earth-like τ_{Pb} and scatter we require a strong fractionation generated by the recycling of continental U into the mantle after the GOE. This has been suggested in the past as a mechanism by which to solve the mantle Pb paradox; however, we find that Pb removal from the mantle is also required in order to explain the $^{208}\mathrm{Pb}/^{204}\mathrm{Pb}$ vs $^{206}\mathrm{Pb}/^{204}\mathrm{Pb}$ of melts. Where both Pb removal and U recycling are involved, the timing of melting induced fractionation does not affect τ_{Pb}, but it does affect the scatter, with earlier melting producing more scatter. Our results indicate that rather than continentally derived U suddenly becoming an input into the mantle, it is more likely to have steadily increased as the atmosphere and ocean steadily slowly became more oxidising. We find that recycling 1.1×10^{14} mol of ^{235}U and 4.6×10^{15} mol of ^{238}U, combined with Pb removal that corresponds to a rate of $\approx 2.5 \times 10^5$ mol ^{204}Pb yr^{-1} since 3.0 Ga gives a reasonable match to all of the known constraints, including τ_{Pb}, scatter, gradient in ^{208}Pb/^{204}Pb vs ^{206}Pb/^{204}Pb, and the fraction of Pb that resides in the continental crust. In this case the bulk continental crust is required to have an unradiogenic Pb composition which could be accommodated in the lower crust with Pb removed from subducted oceanic crust.

In our models, simulating magma chamber mixing is important for decreasing the range of isotope ratios that are measured at the surface. Mixing helps to eliminate the most extreme Pb ratios that exist on subgroup of particles in the mantle. There is a weak dependency of τ_{Pb} on the degree of mixing, though generally there is with a slight increase in τ_{Pb} with increased mixing. The initial distribution of trace elements on particles also affects τ_{Pb} and the scatter. With a non-homogeneous isotope distribution across particles at the beginning of the calculation τ_{Pb} and scatter are both increased relative to the homogeneous case.

CHAPTER 4

INFLUENCES ON THE NOBLE GAS COMPOSITION OF THE MANTLE AND ATMOSPHERE

Abstract

Noble gases impose strong constraints on geodynamic models from their outgassing rates and their composition in the atmosphere and mantle derived rocks. The differences in composition between mid-ocean ridge basalts (MORBs) and ocean island basalts (OIBs) has given rise to conceptual models for the interior structure of Earth's mantle. Geodynamic models have been used to test the validity of these conceptual models, though they are seldom tested against more than a couple of constraints. Most numerical investigations have focussed on understanding the ^{3}He/^{4}He composition of the mantle. In this chapter I simultaneously address two noble gas systems, helium and argon and how these are affected by two different parameters. The first is bulk composition dependence of density. The density of tracer particles with a basaltic composition is varied from being 0% to 10% denser than particles with a harzburgitic composition to cause greater degrees of segregation of basaltic material to the lower mantle. The second parameter investigated is the degassing efficiency of melts, and hence how efficiently the mantle is degassed. I go on to consider the effect of mantle processing rates.

Results indicate a heterogeneous initial trace element distribution can produce modern melts with the full range of ^{3}He/^{4}He measured in oceanic basalts. These models show that it is possible for material with high helium ratios to exist throughout the mantle and to be sampled by being entrained into plumes. This removes the need for the survival of an intrinsically

dense layer of primordial material at the base of the mantle. Due to the low convective vigour and lack of ridge volcanism, these models may not be well suited for generating MORB-like compositions, however the median helium ratio of erupted material becomes MORB-like for a degassing efficiency of 70%. This indicates that retention of noble gases during melting and their subsequent recycling is important in generating the ^{3}He/^{4}He distribution of MORBs. Additionally, when the processing rate of the mantle is increased to arguably more Earth-like values, the mean ^{3}He/^{4}He of melts becomes similar to MORBs. Simultaneously primordial helium is sampled by melts. This could be evidence for the SUMA model, indicating that MORBs and OIBs do not have a distinct source, just different degrees of pre-eruption mixing.

Increased density of basalt in the lower mantle causes the mean composition of melts to become more radiogenic as the average residence time of basalt increases. For a lower mantle excess basalt density of 4-5% relative to harzburgite, much of the segregated basalt eventually becomes entrained into mantle upwellings causing large pulses of melting. For a lower mantle excess basalt density of 6% relative to harzburgite, much of the basalt that segregates to the base of the mantle persists until present day but remains mobile enough to be swept in to piles which act as volatile reservoirs. Earth-like atmospheric ^{40}Ar concentrations can be achieved through a combination of mantle and continental crust degassing. Regardless of degassing efficiency, density of basalt, or convective vigour, the present day atmospheric argon ratio is similar and is found to be most strongly influenced by the amount of primordial ^{36}Ar in the system.

4.1 Introduction

Noble gases are ideal tracers in geodynamic models. Their inert nature and systematic mass dependency of their physical behaviours makes them relatively simple to model. Despite this, the noble gases have very distinct compositions. The light noble gas Ne as measured in diamond inclusions (Honda et al. 1987; Ozima and Zashu 1991) and plume material (Trieloff et al. 2000) has a composition similar to that of the solar wind. This implies that solar gases were incorporated into Earth during accretion. The isotopic composition of the heavier noble gases Ar, Kr, and Xe as measured in plume derived material is more similar to the Earth's atmospheric noble gas composition (Trieloff et al. 2000; Holland and Ballentine 2006). This difference between the mantle composition of heavy and light noble may be explained by the subduction of material which is enriched in an atmospheric component (Holland and Ballentine 2006) or due to Earth's noble gases being acquired due to gravitational capture, thereby fractionating heavier elements more strongly (Ozima and Zahnle 1993).

The noble gas composition of the mantle is studied by measuring their composition in mantle derived gases and rocks, a task which is notoriously difficult. Helium, the lightest of the noble gases, experiences atmospheric escape due to its low mass (MacDonald 1963) and so exists only in low concentrations in the atmosphere. The relative rates of atmospheric escape for different isotopes is not well constrained, making the atmospheric composition of helium a poor constraint on the terrestrial evolution of noble gases. Heavier noble gases do not suffer the same fate so remain trapped in the atmosphere once degassed from the mantle. This makes it tricky to unpick the noble gas signature of mantle derived rocks from atmospheric contamination (Patterson et al. 1990; Farley et al. 1995; Graham 2002). Nonetheless, the noble gas composition of mantle derived rocks places good constraints on geochemical and mantle convection models.

4.1.1 Constraints

Helium constraints

The two isotopes of helium, ^{3}He and ^{4}He have different origins. Most terrestrial ^{3}He is primordial, so was incorporated into Earth during accretion.

Small amounts are also delivered to Earth in interplanetary dust particles although the exact amount is not quite clear (Anderson 1993; Allégre et al. 1993). ^{4}He is radiogenic and within Earth it is largely produced along the decay chains of ^{238}U, ^{235}U, and ^{232}Th. The flux of ^{3}He from the mantle is commonly used as a constraint on models of mantle convection and degassing. Craig et al. (1975) estimated the flux of ^{3}He to be approximately 1070 ± 270 mol yr^{-1} based on the excess ^{3}He in different ocean basins. The approximate value of 1000 mol yr^{-1} ^{3}He flux from the mantle to the oceans has since become widely accepted and is used as the basis of calculations for the mantle fluxes of other noble gases (Ballentine 2007) and carbon dioxide (Marty and Jambon 1987). Further evidence for this value was presented in Farley et al. (1995) in which oceanic circulation models and seafloor spreading rates were used calculate the distribution of ^{3}He in the oceans. A mantle flux of around 1000 mol yr^{-1} was found and the distribution of ^{3}He qualitatively matched Earth's. More recently there has been some doubt cast over the accepted value of ^{3}He flux. Bianchi et al. (2010) coupled modern ocean circulation models, which produce good matches to the global distribution of several oceanic tracers, with helium isotope data. They find that a ^{3}He flux of 527 ± 102 mol yr^{-1} from the mantle to the oceans is required to satisfy well known ocean ventilation tracer observations. Similarly, Schlitzer (2016) found that a lower flux of 450 ± 50 mol yr^{-1} ^{3}He is required to satisfy a coarse resolution ocean circulation model with good constraints imposed by ^{14}C and chlorofluorocarbon data. All of these estimates come with the caveat that they are averages over the last ≈ 1000 years, the mean turnover time for oceans. This means that although we have an idea for the modern mantle ^{3}He flux, how this translates into the past is unknown. A calculation of the mantle ^{3}He has recently been made independent of the ocean He concentrations. Tucker et al. (2018) used a disequilibrium degassing model to calculate pre-degassing concentrations of various gases. They estimate ^{3}He fluxes of 800 ± 170 mol yr^{-1}, close to the upper estimates made in the past of around 1000 mol yr^{-1}.

The isotope ratio ^{3}He/^{4}He is commonly quoted in terms of R/R$_{a}$, the measured ratio of ^{3}He/^{4}He divided by the atmospheric ratio ($R_a = 1.39 \times 10^{-6}$). A long standing observation is that the helium composition of MORB samples is similar across different ocean basins (Fig. 4.1). MORB samples range between 6 and 16 R/R$_{a}$ (Farley and Neroda 1998), with the majority plotting in the range 7-9 R/R$_{a}$. The mean value as calculated by Anderson (2000) is 9.14 ± 3.59 R/R$_{a}$, for the 503 samples available in their study. The

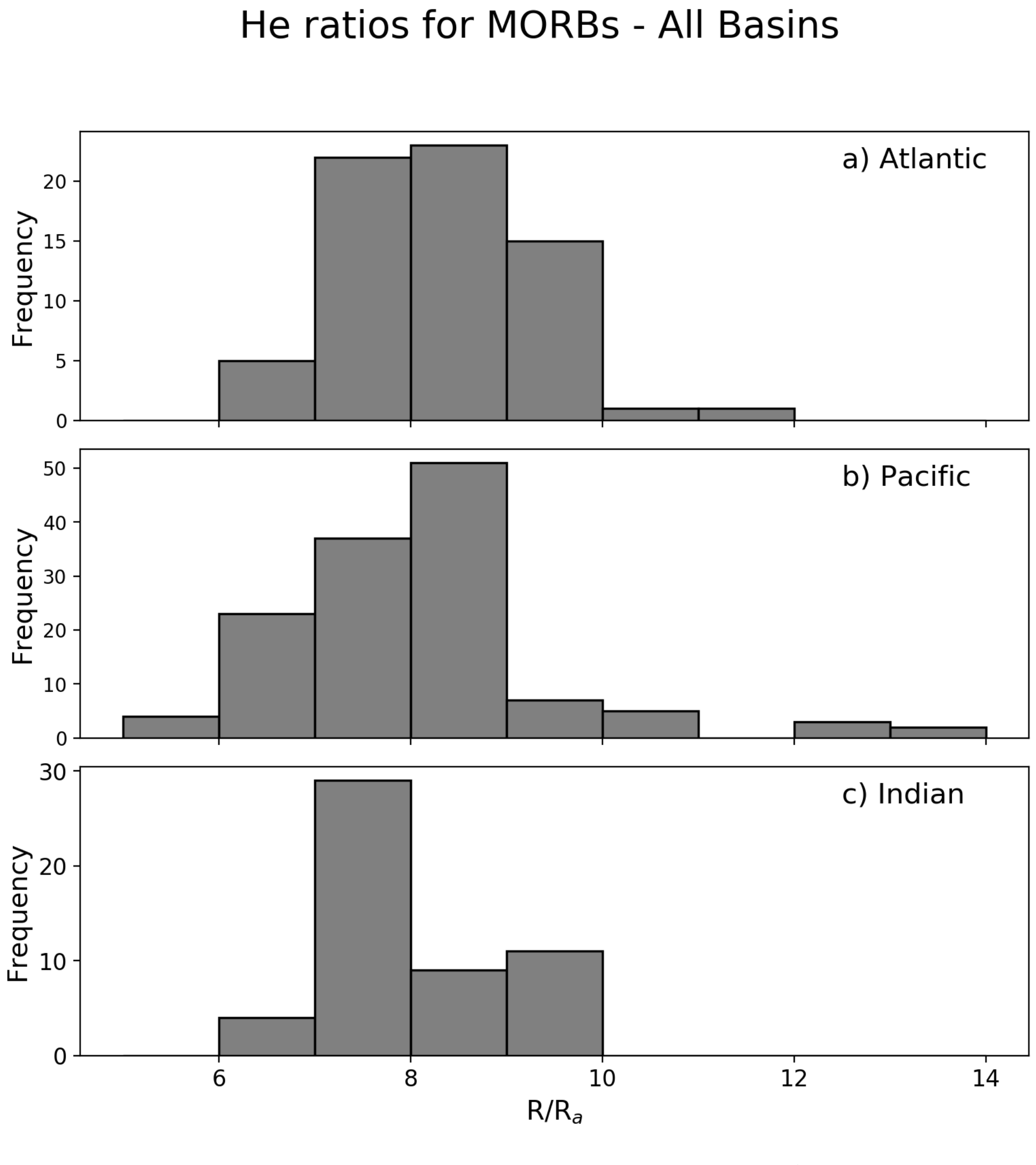

Fig. 4.1 Histograms for the occurrence of different ^{3}He/^{4}He compositions in MORBs in (a) Atlantic, (b) Pacific, (c) Indian oceans. The data were downloaded from the PetDB Database (www.earthchem.org/petdb) on 4th July 2020 using the following search parameters: Tectonic Setting = Spreading Center; ^{3}He/^{4}He EXISTS

median value for the same samples is 8.51 R/R_a. As MORBs are thought to sample the upper mantle, the similar He isotopic composition is interpreted as meaning the upper mantle is well mixed with a fairly uniform composition. Contamination causes small scale anomalies which are sometimes detected at mid-ocean ridges. Ratios greater than median value of 8.51 R/R_a are often associated with the interaction between ridge volcanism and nearby hotspots (Graham et al. 1992), while lower values are associated with ancient ridges (Anderson 2000). OIBs have a much more variable He composition, varying from 3 up to 50 R/R_a (Stuart et al. 2003), and generally display higher He ratios than MORBs (Kurz et al. 1982). High R/R_a is most often attributed to be the signature of primordial material which has remained undifferentiated since accretion. There is also a case for high R/R_a to be derived from the core (Porcelli and Halliday 2001) though some experimental evidence suggests that silicate-metal partitioning of noble gases is extremely low at high pressures (Matsuda et al. 1993) which would severely limit the amount of noble gas that could be sequestered to the core. Although OIBs show a greater range in He isotope ratios than MORBs, there is still a strong peak at about 8 R/R_a (Fig. 4.2), indicating that upper mantle material is an important constituent of OIBs.

The most accepted explanation for the differences between the MORB and OIB He composition is that OIBs must sample some source that the MORBs do not. Historically, geochemists had favoured the model of a layered mantle, in which the upper and lower mantle have distinct compositions, and communication between the two reservoirs is limited (Allégre et al. 1986b; Allégre et al. 1996). These models have fallen out of favour due to the evidence that has amassed for deep rooted plumes bringing material from the lower mantle to the surface (Rhodes and Davies 2001; French and Romanowicz 2015) and subducted crust penetrating the lower mantle (Grand et al. 1997), indicating that the mantle convects as a whole. Additionally, mantle convection models fail to produce layered mantle convection when using reasonable physical parameters with high viscosities in the lower mantle (Van Keken and Ballentine 1998; Ferrachat and Ricard 2001).

Argon constraints

There are two main stable isotopes of Ar that are of interest to geochemists. Most of the terrestrial ^{36}Ar, like ^{3}He, is primordial and constitutes $\sim 0.3\%$ of

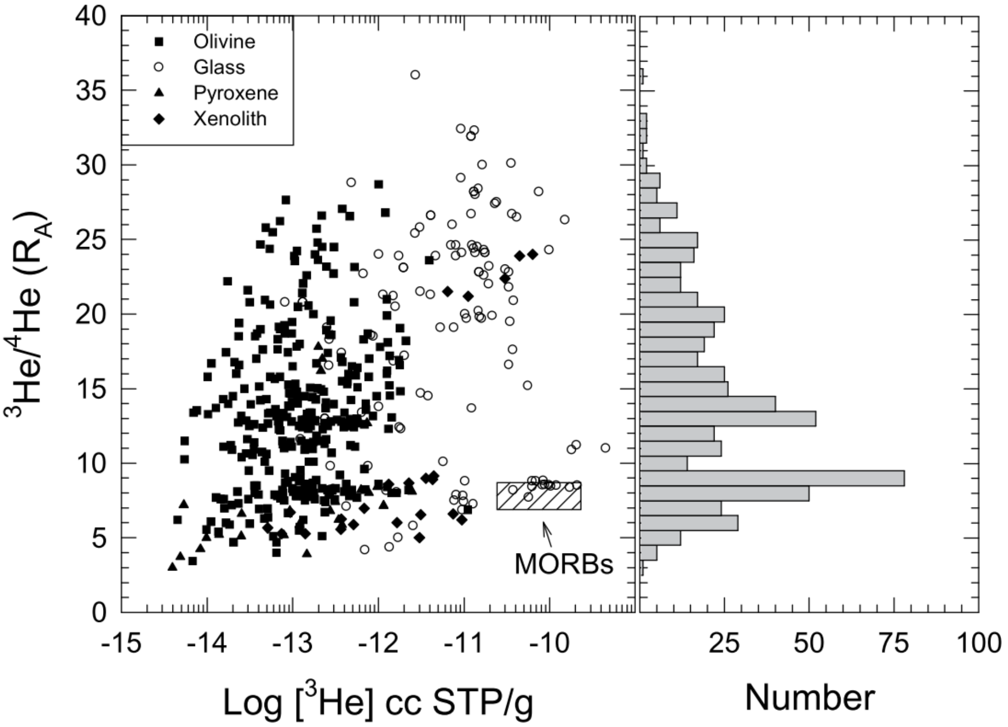

Fig. 4.2 Distribution of He isotope ratios in OIBs and the relationship with He concentration. Figure reproduced from Farley and Neroda (1998).

Earth's argon budget. It is also formed from the decay of ^{36}Cl in the continental curst however its production rate is so low that it may be neglected (Ballentine and Burnard 2002). ^{40}Ar, is much more abundant than ^{36}Ar, and radiogenic from the decay of ^{40}K. Being a heavy noble gas it is assumed that the argon composition of the atmosphere is the sum of the initial atmospheric composition shortly after accretion, plus the sum of all argon that has been degassed since. Nier (1950) measured the atmospheric ^{40}Ar/^{36}Ar = 295.5 ± 0.5 and this was long used as the atmospheric standard. A re-determination of this value now puts the atmospheric argon composition at ^{40}Ar/^{36}Ar = 298.56 ± 0.31 (Lee et al. 2006).

As well as the atmospheric argon ratio, the amount of ^{40}Ar in the atmosphere also imposes an important constraint on modelling the argon evolution of the Earth system. There is approximately 6.6×10^{16} kg of ^{40}Ar in Earth's atmosphere (Allégre et al. 1996). Given an estimate for the BSE concentration of K being between 250 and 286 ppm (Allégre et al. 1996) it is estimated that approximately half of all the ^{40}Ar produced resides in the atmosphere (Allégre et al. 1986b). The atmospheric ^{40}Ar is the sum of all that has been outgassed from the mantle and the continents since accretion. The remaining 50% (6.3×10^{16} - 8.0×10^{16} kg) must then reside elsewhere in the Earth system. Most of this is thought to exist in the mantle and the remainder in the continental crust, with the possibility of a very small fraction residing in the core (Oversby and Ringwood 1972).

The K content of the MORB source could be used to calculate how much ^{40}Ar is expected to be produced in the source region. From the present day concentration of K in MORBs, it is estimated that the source region would have a K concentration around 50 ppm (Allégre et al. 1996). If this were a reflection of the whole mantle K concentration then the mantle would only produce around 1/3 of the expected ^{40}Ar. An alternative would be to use the ^{40}Ar flux from mid-ocean ridges to constrain the ^{40}Ar concentration of the source region. The ^{40}Ar flux is estimated from the mantle He flux (Craig et al. 1975) and ^{4}He/^{40}Ar of MORBs, which varies from 2 to 15 (Sarda et al. 1985). Assuming again that this is representative of the whole mantle concentration then only 2-3% of all the ^{40}Ar that is expected to reside in the mantle is accounted for. This apparent deficit of ^{40}Ar is the 'missing argon' problem, referring to the fact that there appears to be an unaccounted reservoir with high concentrations of ^{40}Ar. In the past layered mantle convection with an enriched lower mantle was postulated as the reason for the apparent lack of ^{40}Ar in the mantle (Allégre et al. 1996; Allégre et al. 1986a), but as discussed earlier in 4.1.1 this has fallen out of favour.

The argon composition of MORBs is extremely variable. ^{40}Ar/^{36}Ar varies from atmosphere-like values, up to 40,000 (Burnard et al. 1997). The majority of measurements are at the lower end of this range though (Fig. 4.3). This seems to be in conflict with the He composition of MORBs, which has a much more restricted range (Fig. 4.1). The variation is generally prescribed to various degrees of mixing between the mantle component with high ^{40}Ar/^{36}Ar and an atmospheric component (Patterson et al. 1990; Marty and Ozima 1986). Helium does not suffer the same contamination due its low concentration in Earth's atmosphere. Given that the ^{40}Ar/^{36}Ar of the atmosphere is significantly lower than what is measured in the mantle, this implies that the maximum ^{40}Ar/^{36}Ar of MORBs represents an estimate for the minimum ^{40}Ar/^{36}Ar of the source. OIBs have lower ^{40}Ar/^{36}Ar than MORBs, with a maximum of around 10,000 but generally $< 3,000$ (Trieloff et al. 2000; Kaneoka et al. 1986). These un-radiogenic compositions have

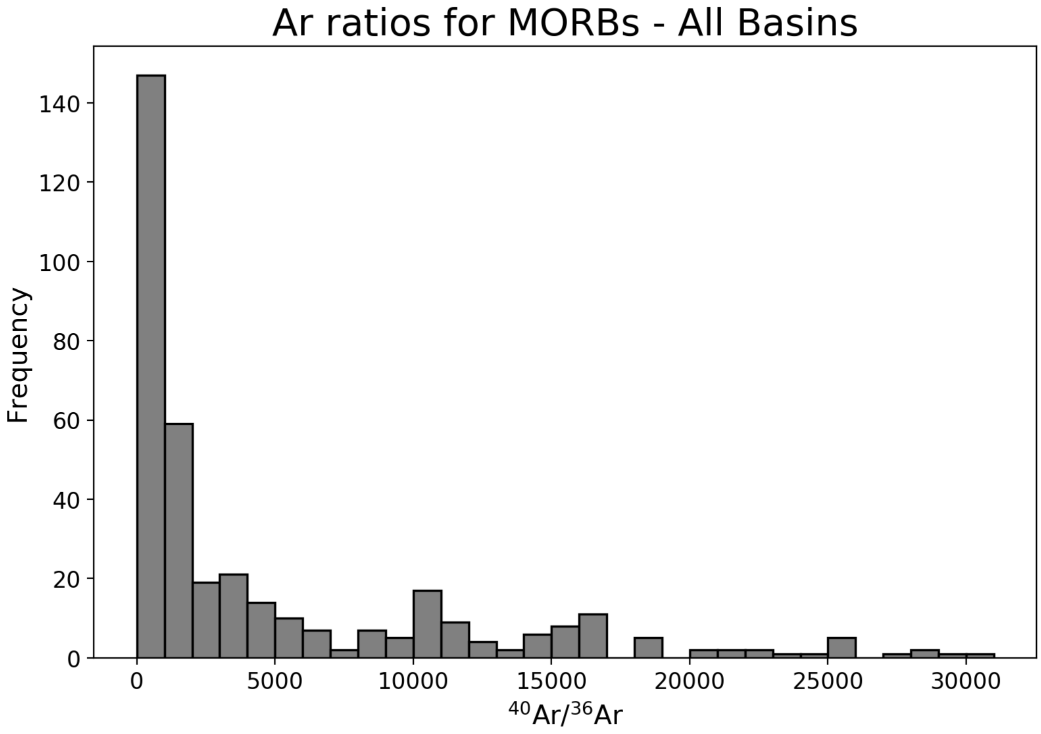

Fig. 4.3 Histogram of ^{40}Ar/^{36}Ar values of MORB samples. n=375. The data were downloaded from the PetDB Database (www.earthchem.org/petdb) on 8th July 2020 using the following search parameters: Tectonic Setting = Spreading Center; ^{40}Ar/^{36}Ar EXISTS.

been interpreted to be the product of early subduction of an atmospheric component into the deep mantle (Trieloff et al. 2003).

4.2 Modelling

A number of previous studies have tried to reconcile the differences between MORB and OIB noble gas compositions by investigating mechanisms proposed by geochemists. Models explicitly aimed at investigating whether a layered mantle can provide separate reservoirs for the different MORB and OIB helium compositions were explored by Van Keken and Ballentine (1998) and Van Keken and Ballentine (1999). They include various physical mechanisms proposed to encourage layered mantle convection such as temperature and pressure dependent rheology, high lower mantle viscosity, and a 670 km deep phase transition. They find that although mixing efficiency may be decreased using reasonable parameters, separating the convection of the upper and lower mantle is not achievable. Upper and lower mantle are therefore almost indistinguishable in their He composition, with only small scale heterogeneity existing. It is notable that these models could degas sufficient ^{40}Ar to fit the observation that 50% of the global ^{40}Ar produced is in the atmosphere. Ferrachat and Ricard (2001) also investigate mechanisms to develop the large scale mantle heterogeneity required to satisfy MORB and OIB He constraints. With regard to layered mantle convection they confirm the results of Van Keken and Ballentine (1998) and Van Keken and Ballentine (1999) in failing to develop a layered mantle with a high viscosity lower mantle.

Ferrachat and Ricard (2001) investigate trapping of oceanic crust in the D" region as a means of producing high ^{3}He/^{4}He in the lower mantle. In their model tracers are passive so segregation is approximated by removing tracers which come from the oceanic crust and enter the bottom most 200km into a separate reservoir representing D". The removed particles are basaltic and enriched in U, leaving the lowermost mantle composed of melt residue which is depleted in U. Low radiogenic ingrowth causes this material to retain high ^{3}He/^{4}He. This simplified mechanism does not allow for segregated material to be re-incorporated into the mantle, a process that is expected due to some OIBs showing HIMU signatures, associated with recycled oceanic crust (Stracke et al. 2005).

Samuel and Farnetani (2003) investigate the model of Kellogg et al. (1999) that requires a 300 to 1000 km thick dense layer above the CMB that is enriched in heat producing elements and remains stable enough to prevent its material from being incorporated into the shallow mantle. This un-degassed layer provides a source for the high ^{3}He/^{4}He observed in OIBs. The material overlying this layer stirs much more vigorously and therefore produces a much narrower range of ^{3}He/^{4}He. Using certain reasonable parameters they are able to achieve stability of the layer for 2.3 Gyr. Their models require that the dense layer formed rapidly before 2.0 Ga, however it is unclear what process could be responsible for this. It's also thought that the undulating surface of such a layer should be visible in seismic tomography (Tackley 2002), yet there is currently no evidence for this. Numerical models have also shown a deep, dense, primordial layer can produce a spatially and temporally variable R/R$_a$ in hotspot volcanism (Williams et al. 2015). This occurs due to the time dependent nature of entrainment from dense primordial layer.

Segregation of subducted oceanic crust was revisited by Xie and Tackley (2004a) who used tracer particles with intrinsic density that affects the flow. Their models explored the effect of different lower mantle densities for subducted basalt. OIB-like ^{3}He/^{4}He develops in the lower mantle when subducted basalt is buoyant in the lower mantle. Although an interesting finding, it is well accepted from the evidence provided by mineral physics that recycled oceanic crust is denser than ambient mantle compositions in the lower mantle (Hirose et al. 2005). In order to achieve MORB-like ^{3}He/^{4}He in the shallow source region, it was found that He must be either made extremely incompatible or significant amounts of recycled crust must be incorporated into the upper mantle to reduce ^{3}He/^{4}He sufficiently. It is noted that heterogeneity exists at all length scales irrespective of the parameters used. This could be an effect of too little processing.

As well as geodynamic models, conceptual models have been proposed that aim at fitting noble gas constraints whilst considering both the geochemical and geophysical observations. Davies (2009) and Davies (2010) proposed that material, termed hybrid pyroxenite, may be responsible for carrying most of the mantle's noble gases. This material is formed by reaction of melt from old subducted crust which does not fully degas and the surrounding peridotitic mantle (Fig. 4.4). A different model by Gonnermann and Mukhopadhyay (2009) proposes that recycling degassed oceanic crust into

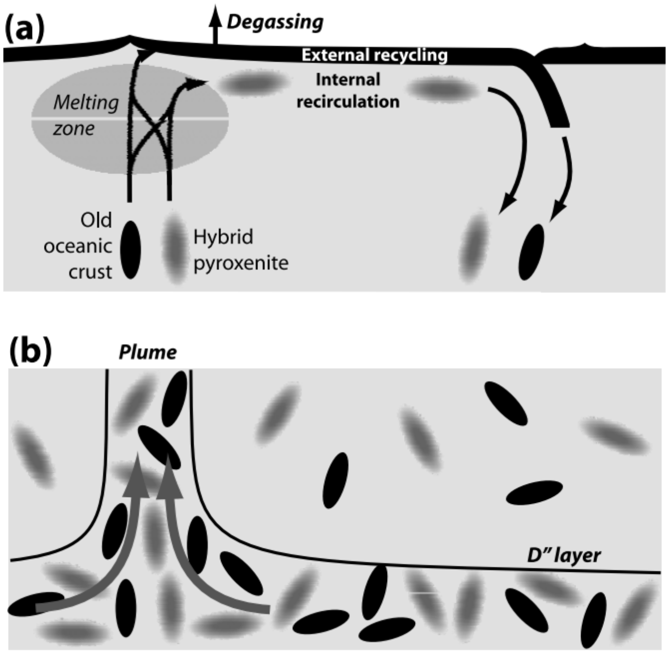

Fig. 4.4 Sketches from Davies (2010) showing conceptual model for the creation and recycling of hybrid pyroxenite. a) Some material melts but does not degas significantly and reacts with peridotite in melting zone to become hybrid pyroxenite. This is recycled with subducted oceanic crust and may be resampled when it enters a melt zone. b) Both recycled oceanic crust and hybrid pyroxenite accumulate in the D" layer and may both be sampled by plumes.

the depleted mantle will dilute the noble gas concentration and therefore the degassing rates of noble gasses monotonically decreases with time. High concentrations are preserved in the lower mantle relative to the upper mantle as the upper mantle is processed more frequently than lower mantle material, which is significantly more viscous. These two models are particularly attractive as they allow a high degree of heterogeneity in the mantle, without strong layering.

In this chapter I will build on previous modelling with cases that systematically vary the density of basalt in the lower mantle (ρ_b) and the degassing efficiency of melts to identify their relationship with various noble gas constraints. Whereas previous modelling has been conducted in various 2D geometries, I will investigate the problem using 3D mantle convection models. Additionally, the presented models include reservoirs representing the atmosphere and continental crust. This allows the models to address more noble gas constraints and include processes such as recycling of material from the continental crust. I also present models that consider the processing rate of the mantle and the initial distribution of trace elements in the mantle.

4.3 Methods

4.3.1 Dynamic model

As in the previous chapter, I run mantle convection models using the 3D geodynamic code TERRA. For an explanation of the governing equations the reader is referred to 2.3 and for an explanation of the implementation of particles as a means to track chemical information the reader is referred to 2.4. The models presented here use a simple two-layer viscosity profile with a ×30 viscosity increase at 660 km (Van Keken and Ballentine 1998). The relative low viscosity of the upper mantle helps to achieve more realistic surface velocities.

Cases are presented with three different internal heating modes. One mode is constant rate of internal heat production that is evenly distributed throughout the mantle (Table 4.1). In the other two heating modes, the heating per time step is controlled by the decay of radioactive isotopes and so the heating rate decreases with time. One of these modes has the heating uniformly distributed throughout the mantle whilst in the other the amount of heating in an individual cell is dependent on the amount radioactive decay

Table 4.1 Model parameters. Note that thermal diffusivity (κ) is derived from the relationship $\kappa = k/(\rho C_p)$ and the upper mantle viscosity is equal to the reference viscosity.

Parameter	**Symbol**	**Value**
Surface temperature	T_s	300 K
CMB temperature	T_{CMB}	3000 K
Internal heating rate	H	5×10^{-12} W kg^{-1}
Reference viscosity	η	3×10^{22} Pa s
Density	ρ_0	4500 kg m^{-3}
Thermal conductivity	k	4 W m^{-1} K^{-1}
Thermal expansivity	α_0	2.5×10^{-5} K^{-1}
Specific heat capacity	C_p	1100 J kg^{-1} K^{-1}

that has occurred there. This last heating mode therefore has both temporal and spatial variability.

The olivine system phase transitions are included in the model, parameters for which can be found in Table 4.2. The 'basalt barrier' in the mantle transition zone is caused by the delayed transition to dense, lower-mantle mineral phases in cold subducted oceanic crust from 660 km to 750 km (Irifune and Ringwood 1993). This causes basalt to become buoyant compared to the ambient mantle compositions between these depths (Hirose et al. 1999). This is modelled by making basalt 5% more buoyant in the transition zone compared to harzburgite (Davies 2008). Above the transition zone basalt is 4% denser than harzburgite and in the lower mantle I use various values of excess ρ_b. By varying the excess density of basalt in the lower mantle I am also varying the buoyancy ratio (B). The buoyancy ratio has been shown to be the most important parameter in maintaining stable dense layer in the lower mantle (Li et al. 2014; Deschamps and Tackley 2009). It is given by:

$$B = \frac{\Delta\rho_C}{\alpha_s \rho_s \Delta T_{SA}} \tag{4.1}$$

where $\Delta\rho_C$ is the density difference between dense material and ambient mantle, α_s is the coefficient of thermal expansion, ρ_s is the reference density, and ΔT_{SA} is the superadiabatic temperature difference across the mantle.

Table 4.2 Olivine phase change parameters

Depth (km)	$\Delta\rho$ kg m^{-3}	Clapeyron slope (MPa K^{-1})
410	230	1.5
660	380	-1.0

Table 4.3 Initial mantle concentrations, atmospheric abundances, and partition coefficients for isotopes that are tracked in models presented in this chapter.

Isotope	Mantle 3.6 Ga (Mol/g)	Atmos 3.6 Ga (Mol)	D
^{3}He	2.47×10^{-14}	-	0.007
^{4}He	2.00×10^{-10}	-	0.007
^{36}Ar	1.22×10^{-13}	3.11×10^{15}	0.007
^{40}Ar	1.25×10^{-10}	5.43×10^{15}	0.007
^{40}K	6.14×10^{-9}	-	0.010
^{232}Th	3.91×10^{-10}	-	0.007
^{235}U	2.11×10^{-11}	-	0.007
^{238}U	1.47×10^{-10}	-	0.007

4.3.2 Initialisation

An initial thermal state is generated by running the model forward from a random temperature field for 5 Gyr. Due to the uncertain conditions of the early Earth I follow previous studies in commencing the calculations at 3.6 Ga (van Heck et al. 2016; Brandenburg et al. 2008; Brandenburg and Van Keken 2007; Xie and Tackley 2004a; Christensen and Hofmann 1994). Doing so avoids having to model times of potentially very low mantle viscosities.

Bulk composition is initialised so that 3/8 of particles have a composition of C=0 (harzburgitic), 1/2 have a composition of C=0.25, and 1/8 have a composition of C=1 (basaltic). These compositions are evenly distributed throughout the mantle. This setup implicitly assumes that melting has occurred prior to 3.6 Ga and that the basalt and depleted residue have been efficiently mixed into the mantle.

The model tracks the radioactive isotopes ^{238}U, ^{235}U, ^{232}Th, ^{40}K and the products of their decay. For the work in this chapter the decay products ^{40}Ar and ^{4}He are of most interest to us. Also tracked are the primordial isotopes ^{36}Ar and ^{3}He. Initial values for each trace element isotope can be found in Table 4.3. The present day value for ^{238}U is calculated from an estimate of its current concentration in bulk silicate Earth (BSE). From this, the concentration of ^{235}U and ^{232}Th are estimated from their respective

Table 4.4 Decay constants, daughter ratios and energy per decay for radioactive isotopes tracked in models presented in this chapter.

Isotope	Decay constat	Daughter 1	Daughter 2	Decay Energy (MeV)
^{40}K	5.54×10^{-10}	$0.1048 \times {}^{40}$Ar	-	1.34
^{232}Th	4.95×10^{-11}	^{208}Pb	$6 \times {}^{4}$He	42.66
^{235}U	9.85×10^{-10}	^{207}Pb	$7 \times {}^{4}$He	46.40
^{238}U	1.55×10^{-10}	^{206}Pb	$8 \times {}^{4}$He	51.70

present day molar and mass ratios to ^{238}U. The present day amount of ^{40}K is worked out from the present day K/U of the silicate Earth (Arevalo et al. 2009) and the fraction of K that exists as ^{40}K. The amount of each isotope at 3.6 Ga is then calculated via the decay equation

$$N_t = N_{pd} e^{+\lambda_N t} \tag{4.2}$$

where N_t is the amount of isotope N at time t, N_{pd} is the present day amount of isotope N and λ_N is the decay constant for isotope N. Relevant decay constants can be found in Table 4.4. Initial noble gas abundances (including initial atmospheric abundance of Ar isotopes) have been calculated using the He evolution model of Porcelli and Elliott (2008) assuming an end member crustal extraction model (Armstrong 1968). The model is tuned to fit the modern day ^{3}He flux and MORB ^{3}He/^{4}He. ^{36}Ar is calculated from an accretionary ^{3}He/^{36}Ar = 0.2 (Porcelli and Ballentine 2002). There is assumed to be no ^{40}Ar upon accretion so it is entirely derived from the radioactive decay of ^{40}K. Initial abundances for all of these are found in Table 4.3. The initial atmospheric abundance of He isotopes is not important due to He suffering from an unknown rate of atmospheric escape.

Initial concentrations are converted to abundances using the mass of particles. I assume that rapid continental crust extraction has taken place before the start of the calculation (Armstrong 1968). To account for this each particle is depleted by 1/3 in ^{238}U, ^{235}U, ^{232}Th, ^{40}K, with the depletion going to the continental reservoir. Following the results of the previous chapter, 1/3 of all the U that is available in the continental reservoir at 2.4 Ga is set aside to be recycled into the mantle. This corresponds to recycling 1.1×10^{14} mol of ^{235}U and 4.6×10^{15} mol of ^{238}U over the past 2.4 Gyr.

4.3.3 Fractionation

Melting is a key process for generating heterogeneity in the mantle. The melting process in TERRA is self consistent and varies with depth, pressure and bulk composition. The mechanics of this are explained in 2.4.3. The choice of partition coefficients for each element is important as their relative magnitude will determine how different elements fractionate during melting. All partition coefficients can be found in Table 4.3. The given partition coefficient for uranium isotopes is 0.007 (Hofmann 1988). The partition coefficient for noble gases is notoriously hard to determine. An upper bound for the partition coefficient of helium between olivine and basalt melt is given as 0.07 by Hiyagon and Ozima (1986). A much lower value of 0.00017 is reported in Heber et al. (2007). Noble gases are all extremely incompatible and it is thought that the differences between their partition coefficients is insignificant (Heber et al. 2007). For simplicity I have set $D_{He} = D_{Ar} = D_U$. This is the same as the partition coefficients used in previous studies (Xie and Tackley 2004a) so gives some level of comparability. Although the relative partitioning between between U and He is important for the evolution of He composition of the mantle, this is explored in Xie and Tackley (2004a) and so I will not be varying D_{He} in these calculations. The partition coefficient for potassium is $D_K = 0.01$, similar to values calculated in Chamorro et al. (2002). The difference in partition coefficient between K and Ar leaves the residue relatively enriched in K compared to Ar after melting. This will cause the residue to go on to develop higher $^{40}\text{Ar}/^{36}\text{Ar}$.

Degassing is thought to be an efficient process. Estimates range from nearly 100% to 10s%. The suite of simulations investigating the effect of the density of recycled basalt have a 90% degassing efficiency. This accounts for incomplete degassing during melting and loss of noble gasses during slab dehydration (Smye et al. 2017). Other simulations will investigate the effect of various degrees of degassing efficiency. The degassed fraction is instantaneously added to the atmospheric reservoir. While there is no fractionation between U and He during melting, so the residue retains the same U/He, the degassing process means that the melt has an elevated U/He and K/Ar. This causes the basaltic crust to develop low $^{3}\text{He}/^{4}\text{He}$ and high $^{40}\text{Ar}/^{36}\text{Ar}$. U/He is also increased due to the recycling of U from the continental reservoir. This process is fully explained in 3.4.3.

Table 4.5 Table of case names, excess ρ_b in the lower mantle compared to harzburgite (C=0) and the corresponding buoyancy ratio, B. Each case was run in three different heating modes, described in 4.3.1

Case	Excess ρ_b	Max B
XSDENS0	0%	0.0
XSDENS2	2%	0.22
XSDENS4	4%	0.44
XSDENS5	5%	0.55
XSDENS6	6%	0.66
XSDENS8	8%	0.88
XSDENS10	10%	1.11

4.4 Parameters investigated

4.4.1 Excess lower mantle basalt density

The density of subducted oceanic crust is well known for conditions in the upper mantle (Aoki and Takahashi 2004), however for lower mantle conditions this is less well constrained. Mineral physics suggests that the net effect of mineral phase changes that occur in basalt in the lower mantle is increase the density by 3-4% (Hirose et al. 2005) with respect to the preliminary reference Earth model (PREM) (Dziewonski and Anderson 1981). Two dimensional mantle convection models have shown that this can cause subducted basalt to segregate to the base of the mantle (Xie and Tackley 2004b; Ballmer et al. 2016) given reasonable parameters for the excess ρ_b and lower mantle viscosity. However, recent combined geodynamic and geochemical modelling has called for excess lower mantle basalt densities of up to 10% (Jones et al. 2019). I investigate a range of lower mantle basalt densities and different mantle heating regimes with a focus on how this affects the noble gas composition of the mantle and atmosphere. The excess ρ_b and corresponding buoyancy ratios for cases explored are detailed in Table 4.5. Note that while excess density is quoted as excess density of basaltic material (C=1) relative to harzburgitic material (C=0), the buoyancy number is calculated using the excess density relative to ambient mantle density. The relative densities of basalt compared to harzburgite at different mantle depths for cases XSDENS2 and XSDENS10 are shown for reference in figure 4.5.

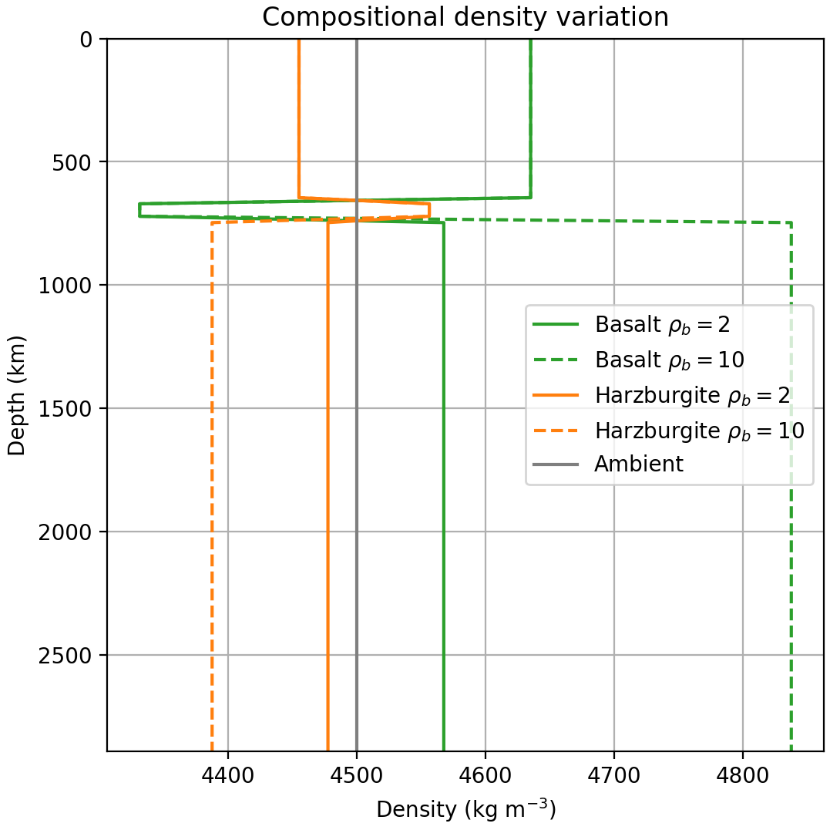

Fig. 4.5 Relative density of basalt (green) compared to harzburgite (orange) for cases with an excess lower mantle density of 2% (solid line) and 10% (dashed line).

Table 4.6 Case names and corresponding degassing efficiencies.

Case	Degassing efficiency
DGAS30	30%
DGAS50	50%
DGAS70	70%
DGAS90	90%
DGAS100	100%

4.4.2 Degassing efficiency

Mid-ocean ridge basalts are known to be degased, but the exact degassing efficiency of noble gasses may be anywhere between 99.9% and a few %. Noble gases that remain in oceanic crust are eventually recycled into the mantle when the material is subducted. There may also be some degree of recycling of noble gases into the mantle via subduction of altered oceanic basalts (Sarda 2004). Gases in sediments and oceanic crust may become trapped upon alteration of minerals so they can be recycled into the mantle. In the standard case, the net effect of these two processes is assumed to be a 90% degassing efficiency, in line with previous studies (Xie and Tackley 2004a). In the hybrid pyroxenite model, un-degassed melts react with ambient mantle to become localised reservoirs of volatiles that are circulated through the mantle (Davies 2009; Davies 2010). While varying the degassing efficiency of melts does not directly model hybrid pyroxenite formation, it gives a sense for whether the model is required to retain more or less gases in order to fit the observations. Table 4.6 gives the names of cases run and the degassing efficiency for each case, including a case where 100% of noble gases are degassed from the melt. Cases with < 90% degassing efficiency are thought of as having some degree of the hybrid pyroxenite formation. Hybrid pyroxenite is predicted to be formed off of the mid-ocean ridge axis or fairly deep under it, and then cycled into the mantle with its complement of incompatible elements almost fully intact, having evaded degassing (Fig. 4.4). On its return to the surface, some pyroxenite will be sampled, imparting a primordial signature on OIBs. The presented parameterisation captures the essence of this. Reducing the amount of degassing leaves the basalt with a relative enrichment of noble gases. Hybrid pyroxenite is expected to be recycled into the mantle with subducted oceanic crust and is also expected to be denser than ambient mantle compositions, so modelling as a less degassed oceanic crust is a good first order approximation. The dynamics of the model are unchanging for each case, as the noble gas concentration of particles has no bearing on the physical properties of the mantle. In each case lower mantle excess ρ_b is set to 3% relative to harzburgite.

4.5 Dynamic results

4.5.1 Temperature evolution

In this section I will discuss the effects of both excess ρ_b and different heating modes on the temperature evolution of the mantle. Each case begins from the same initial condition. In all three heating modes ρ_b has only a small effect on the average mantle temperature, with the increased ρ_b generally resulting in lower mantle temperatures (Figs. 4.6a-c). In the constant heating mode the cooling rate of the mantle decreases with time (Fig. 4.6a) whereas when the mantle is heated by radioactive decay the mantle warms up for the first 500 Myr before beginning to cool at an almost constant rate (Figs. 4.6b,c). In each heating mode the present day (3.6 Byr) cooling rate of the mantle over time is greater than what Earth's mantle cooling rate is expected to be (Davies 1993). This is likely a product of the viscosity structure of these models - the lack of a relatively strong lithosphere at the surface allows the mantle to cool more efficiently. The present day surface heat flux for the models presented is slightly lower than estimates for Earth's surface heat flux, ~ 47 TW (Davies and Davies 2010). Generally the surface heat flux is lower and CMB heat flux is higher for cases with a constant heating rate than those with radioactive heating. Both of these observations are probably caused by the lower mantle temperatures. In all heating modes the average mantle temperature, surface and CMB heat fluxes are very similar for cases of 0% and 2% excess density. At 4% excess ρ_b there is a noticeable drop in the CMB heat flux however the surface heat flux remains similar to cases with lower ρ_b. For $\rho_b = 5\% - 10\%$ both the surface and CMB heat flux decrease with increasing ρ_b.

Radial averages of temperature for different excess basalt densities and heating modes are plotted in Fig. 4.7. With increasing excess ρ_b the basal thermal boundary layer increases in thickness, regardless of the heating mode. While the lower mantle increases in temperature with increasing excess basalt densities, shallower depths (200 - 1500 km) are cooler. The temperature profiles for XSDENS0 and XSDENS2 are almost identical in each heating mode, with XSDENS4 having a slightly thicker thermal boundary

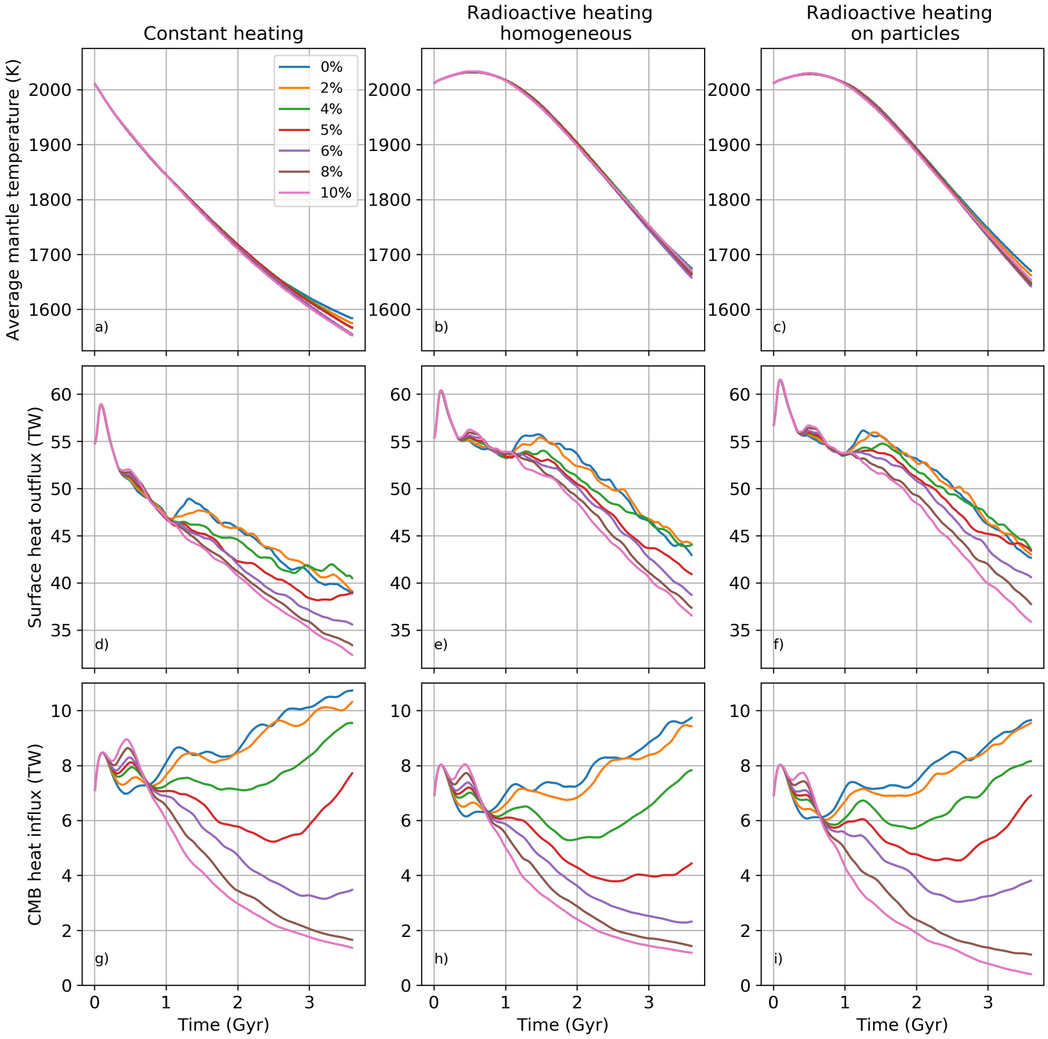

Fig. 4.6 Evolution of (a-c) average mantle temperature, (d-f) surface heat outflux, (g-i) CMB heat influx for cases of variable excess lower mantle ρ_b for 3 heating modes. Left column heated at constant rate, distributed homogeneously. Middle column has time varying heating rate distributed homogeneously. Right column heated by decay of radioactive isotopes on particles. Note that whole mantle heating rates are the same for middle and right columns.

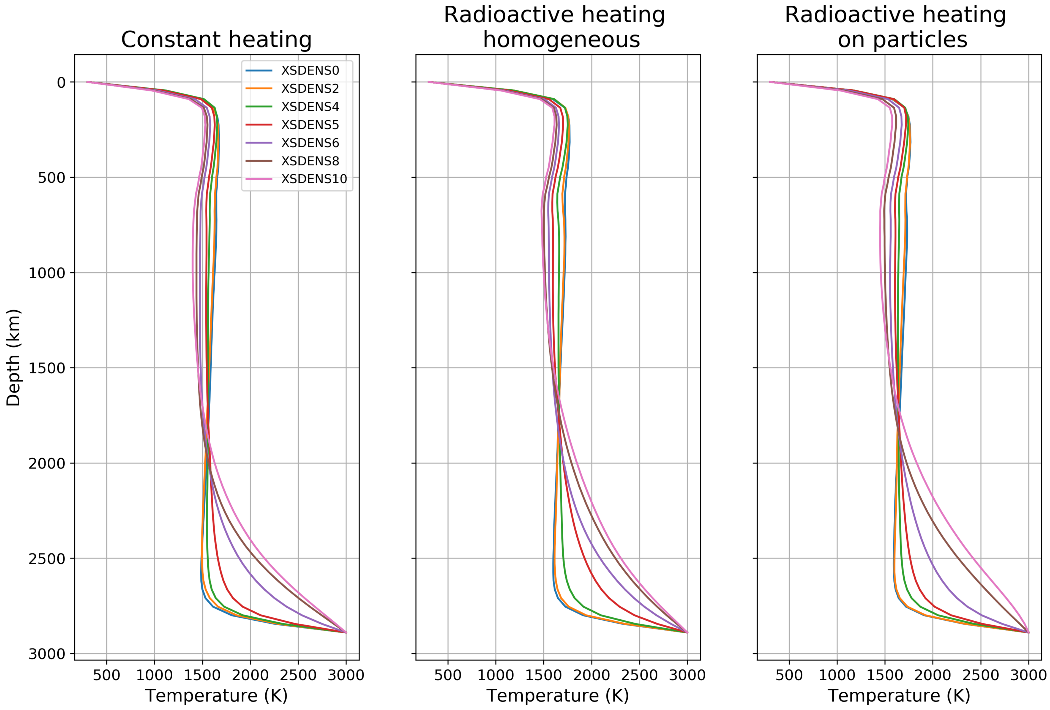

Fig. 4.7 Radial average of temperature for different excess lower mantle basalt densities. a) Constant heating rate, b) time varying heating rate distributed homogeneously, c) heated by decay of radioactive isotopes on particles. Note that whole mantle heating rates are the same for b and c.

layer. The thermal boundary layer continues to thicken with increasing excess ρ_b but at different rates for different heating modes. XSDENS5 and XSDENS6 are hotter in the lower mantle cases heated homogeneously by radioactive heating compared to cases with radioactive heating on particles, while XSDENS10 in hotter when heating is heterogeneous.

In Fig. 4.8 the mantle temperature anomaly is visualised for various excess basalt densities at 1 Gyr, 2Gyr and 3.6 Gyr. The visualisations have been made using output from models heated by radioactive decay on the particles. Generally speaking there are hot, upwelling, plume like structures that are rooted at the CMB and a network of linear, cold downwelling regions at the surface. The temperature structure is similar for each case at 1 Gyr but hot structures are subdued in the models with higher excess ρ_b. By 2 Gyr each case has begun to develop its own system of individual plumes and downwellings. At 3.6 Gyr XSDENS6 has particularly large plumes with wides bases.

The power spectrum for the temperature field for each excess ρ_b in cases heated by radioactive heating on particles is plotted in Figure 4.9. Note that the 4π normalisation convention is used, as is common in geodesy. The lower mantle is dominated by features of spherical harmonic degree 5-15, corresponding to wavelengths of approximately 4000-1500 km (at the CMB). In each case features of approximately degree 12 have the highest power at the surface, corresponding to wavelengths of approximately 3000 km. The power spectrum decreases with increasing L slowest at the upper and lower boundaries.

4.5.2 Bulk chemistry

Radial average of the bulk composition (Fig. 4.10) show similarities with the radial averages of temperature (Fig. 4.7). An increase from 0% to 2% excess ρ_b does not change the average radial composition, however incrementally increasing ρ_b further causes more basalt to segregate into the lower mantle. A slight peak in average bulk composition in the mantle transition zone indicates that basalt is being trapped here due to the effect of the 'basalt barrier' (Davies 2008). Less basalt is trapped in mantle transition zone with increasing ρ_b. The peak in bulk composition at the surface is due to the melting process forming a basaltic oceanic crust. At depths greater than around 2300 km, for excess ρ_b of 5-6%, the average bulk composition is

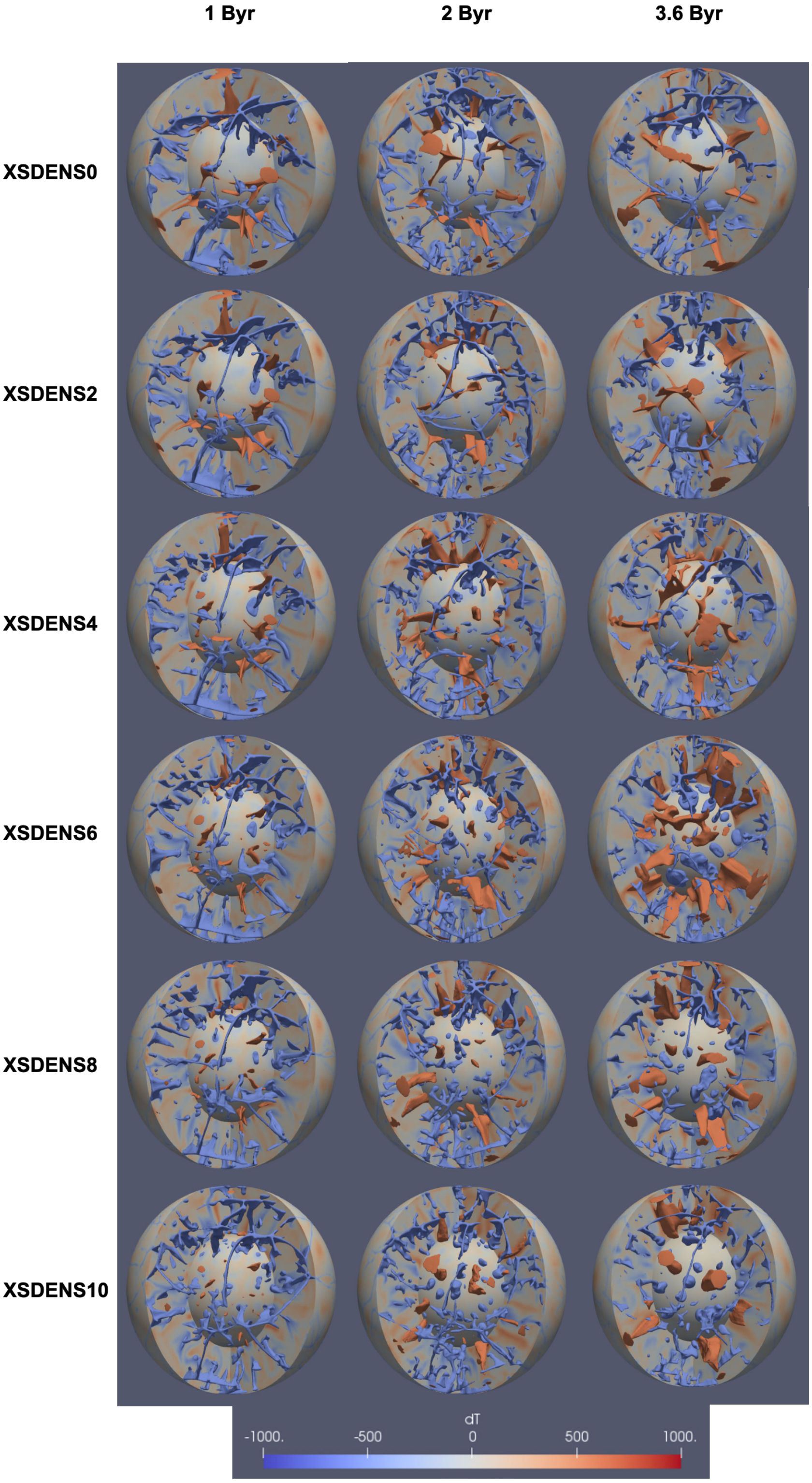

Fig. 4.8 View of the internal mantle temperature anomaly for 0%, 2%, 4%, 6%, 8%, 10% excess density of basalt in the lower mantle at 1 Gyr, 2 Gyr and 3.6 Gyr. Blue and red iso-surface drawn at -500 K and +500 K respectively.

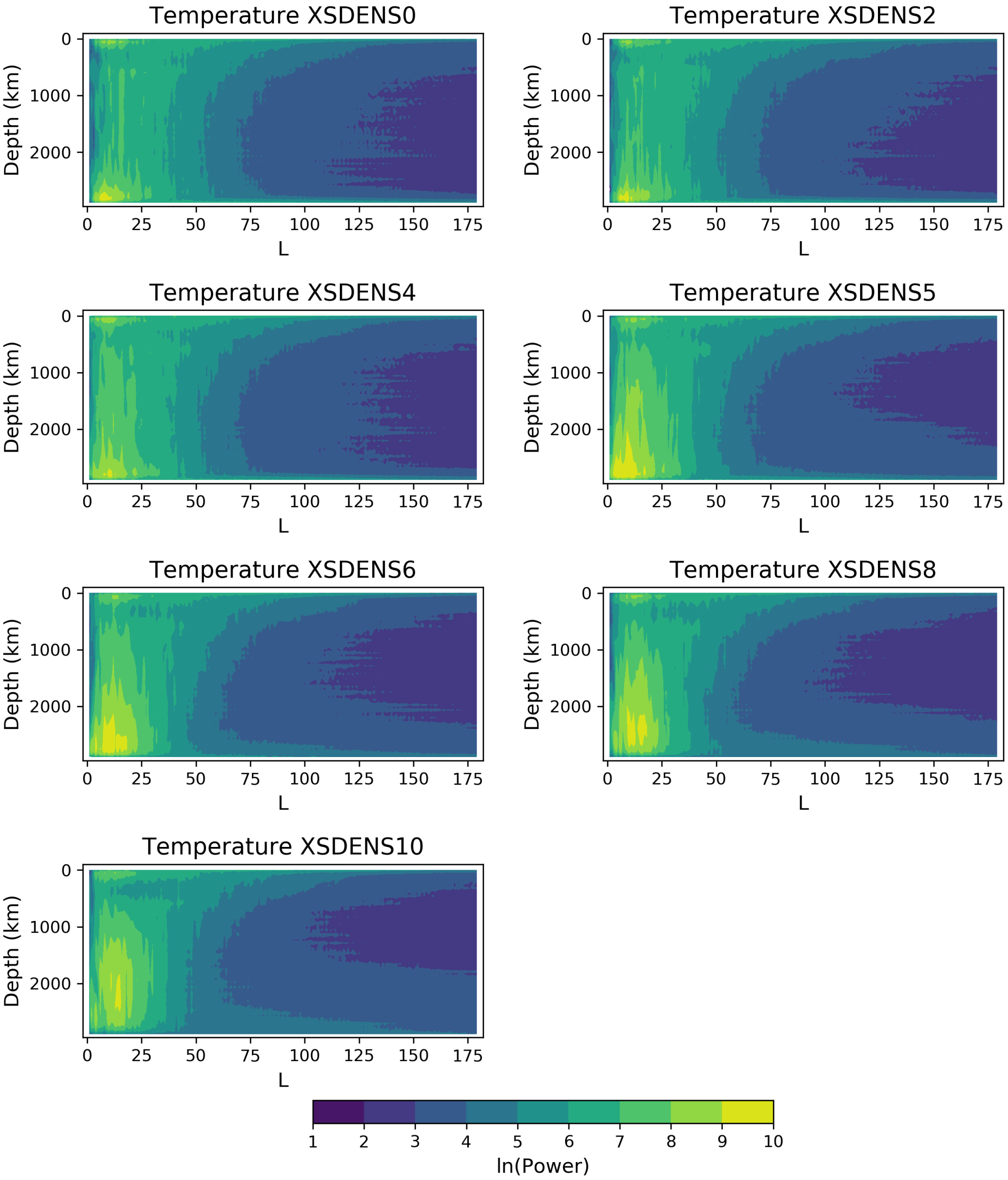

Fig. 4.9 4π normalised spherical harmonic of the temperature field from degree 1 to 180 for cases a) XSDNES0, b) XSDENS2, c) XSDENS4, d) XSDNES5, e) XSDENS6, f) XSDENS8, g) XSDENS10.

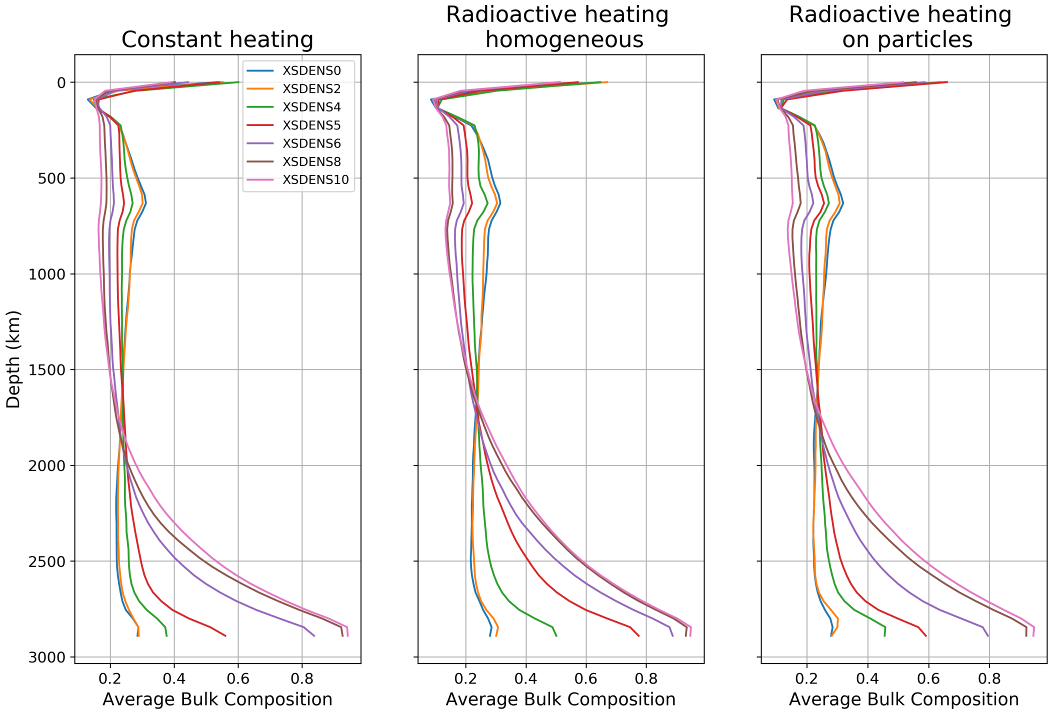

Fig. 4.10 Radial average of bulk composition for different excess lower mantle basalt densities. a) Constant heating rate, b) time varying heating rate distributed homogeneously, c) heated by decay of radioactive isotopes on particles. Note that whole mantle heating rates are the same for b and c.

around 0.1 higher when the model is heated homogeneously by radioactive decay (Fig. 4.10b), compared to when heating varies laterally (Fig. 4.10c).

Figure 4.11 shows the evolution of bulk composition in the mantle for different excess ρ_b. The visualisations are generated using output from cases heated via radioactive decay on the particles. After 1 Gyr most of the mantle remains unmelted. Basalt and depleted residue are subducted together and while the depleted material is buoyant in the lower mantle, some still make it to the CMB. Already after 1 Gyr the cases with extremely high excess ρ_b have more basalts accumulating at the CMB than those with lower ρ_b. After 2 Gyr the accumulations of basalt at the CMB in XSDENS0 and XSDENS2 are roughy the same size as they were at 1 Gyr, indicating that whilst more basalt is being transported to the CMB, an equivalent amount is being remixed into the mantle. The basaltic accumulations have grown somewhat between 1 Gyr and 2 Gyr for case XSDENS4, but for cases XSDENS6/8/10 they have grown significantly. After 3.6 Gyr there is far less basalt at the base of the mantle in cases XSSDENS0/2/4 than there was at 2 Gyr. For these cases the mantle has a marbled structure with heterogeneity at many wavelengths and the surface has a lower fraction of basalt than it did earlier on. XSDENS6 has a comparable amount of basalt accumulated at the CMB at 3.6 Gyr as it did at 2 Gyr. The accumulations are less diffuse later on having been swept together by the pushing and pulling of downwellings and plumes, but not entrained and remixed into the mantle to the same extent as lower ρ_b cases. In XSDENS6 much of the mantle is composed of depleted material, punctuated by thick and thin strands of basalt being entrained by thermal upwellings. The basaltic accumulations in both XSDENS8 and XSDENS10 are less mobile than other cases and almost entirely cover the CMB. This is not to say that continuous layer of subducted material has formed though. The basalt is not well consolidated and has complex topography. Above this there is a transition to ambient mantle compositions and then to depleted compositions (Fig. 4.11).

The spherical harmonic power spectrum of the compositional field shows the largest wavelength structures generally appearing in the base of the mantle and in the transition zone (Fig. 4.12). For XSDENS0/2 the power decreases with increasing harmonic degree at a constant rate through much of the mantle, with the exception being the upper mantle. With increasing excess ρ_b the reduction in power with L decreases with depth, showing that larger structures are forming in the lowermost mantle. There are strong

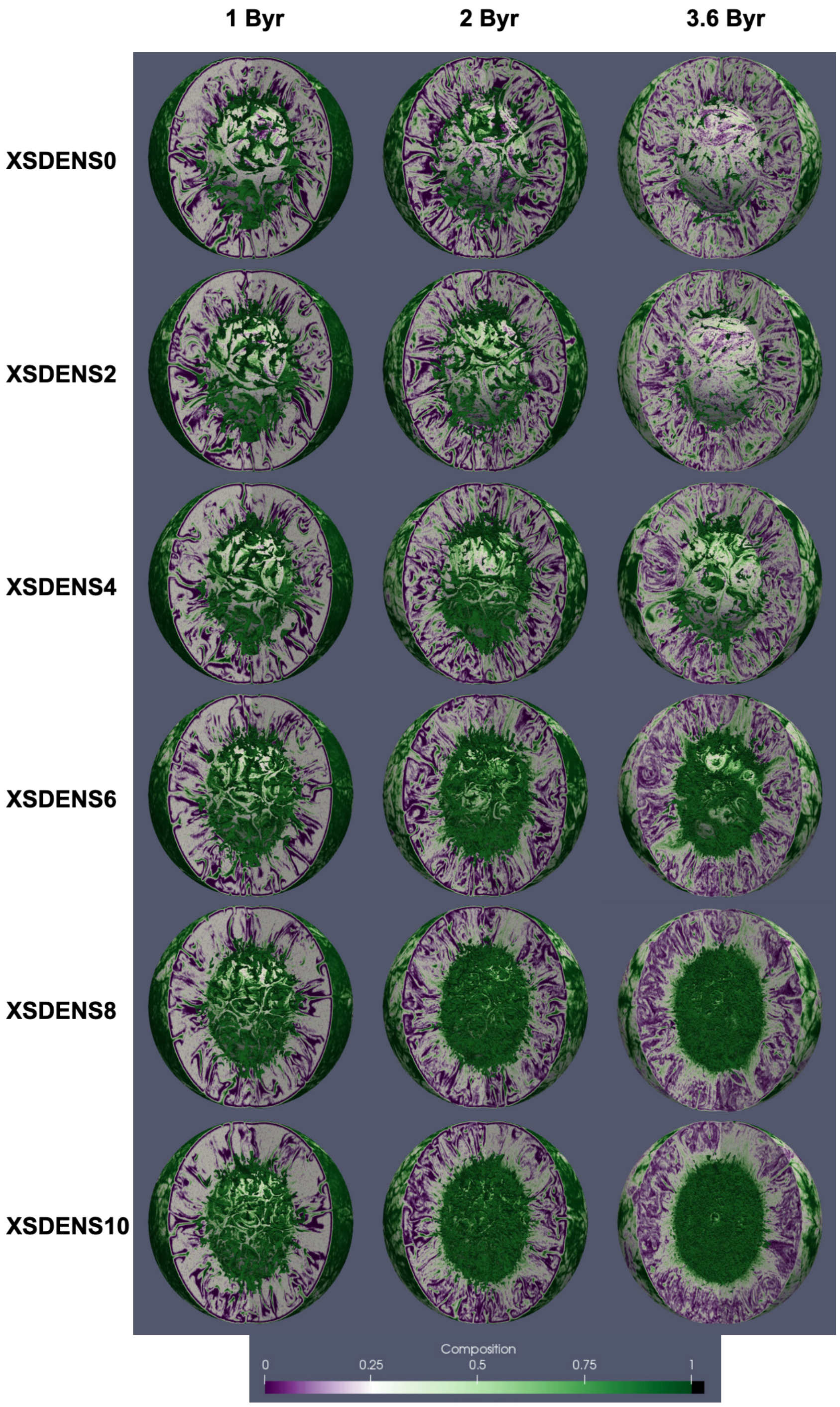

Fig. 4.11 Internal view of the bulk composition of the mantle for 0%, 2%, 4%, 6%, 8%, 10% excess density. Green colours are enriched in basaltic component and purple colours are depleted with grey representing ambient mantle composition of C=0.25. An iso-surface for C=1 material is drawn of the bottom 1000 km of the mantle to help visualise the accumulation of basalt. The visualisations have been generated using the open source 3D visualisation software, Paraview.

peaks at $L = 2 - 10$ just above the CMB in the XSDENS5/6, corresponding to features with wavelengths of approximately 9000-2500 km. Features of similar wavelength also exist in XSDNES4/8/10 but to a lesser degree. Although basalt accumulated at the CMB in XSDENS8/10, it forms a layer around the whole sphere so dominates the power spectrum at degree 0 (not plotted). In all cases the mantle transition zone hosts larger wavelength structures than the mantle immediately above and below it.

4.6 Geochemistry results

In this section I will first present results for cases that investigate the effect of varying excess ρ_b in the lower mantle followed by cases investigating the effect of varying the degassing efficiency of melt. In each case the heating mode is by radioactive decay on the particles.

4.6.1 Excess density of lower mantle basalt

Noble gas fluxes remain similar for the first $\sim$ 0.5 Gyr in all cases (Fig. 4.13). XSDENS0/2 have very similar fluxes for their entire history. XSDENS4/5 have lower fluxes than XSDENS0/2 for a large part of the calculation but then overtake so that they have higher present day fluxes of all noble gas isotopes. XSDENS6/8/10 have progressively lower fluxes with increasing ρ_b. The flux of ^{3}He is of particular interest as this is a fairly solid constraint on Earth's mantle degassing. Compared to the recent estimate of present day ^{3}He flux from Tucker et al. (2018) of 800 mol yr^{-1}, each of the cases presented has a ^{3}He flux 2.5 - 5 times too large.

Plots of the radial averages for R/R$_a$ (Fig. 4.14e) show that the helium ratio at the surface and in the melting zone (top 135 km) are similar in all cases. The melting zone has the highest R/Ra in the whole mantle. For XSDENS0/2 the lowest average R/Ra is in the mantle transition zone while in XSDENS4-10 R/Ra is lowest at the CMB. At depths greater than 1700 km, ^{40}Ar/^{36}Ar is greater for higher excess ρ_b and increases towards the CMB while R/R$_a$ decreases. In all cases the lowest argon ratios are found in the mantle transition zone. The spherical harmonic power spectrum for the R/R$_a$ field is similar to the bulk composition field. For XSDENS0/2 the dominant signal is from the transition zone and just above the CMB in structure of degree $L < 40$. For XSDENS5/6 the lowermost mantle

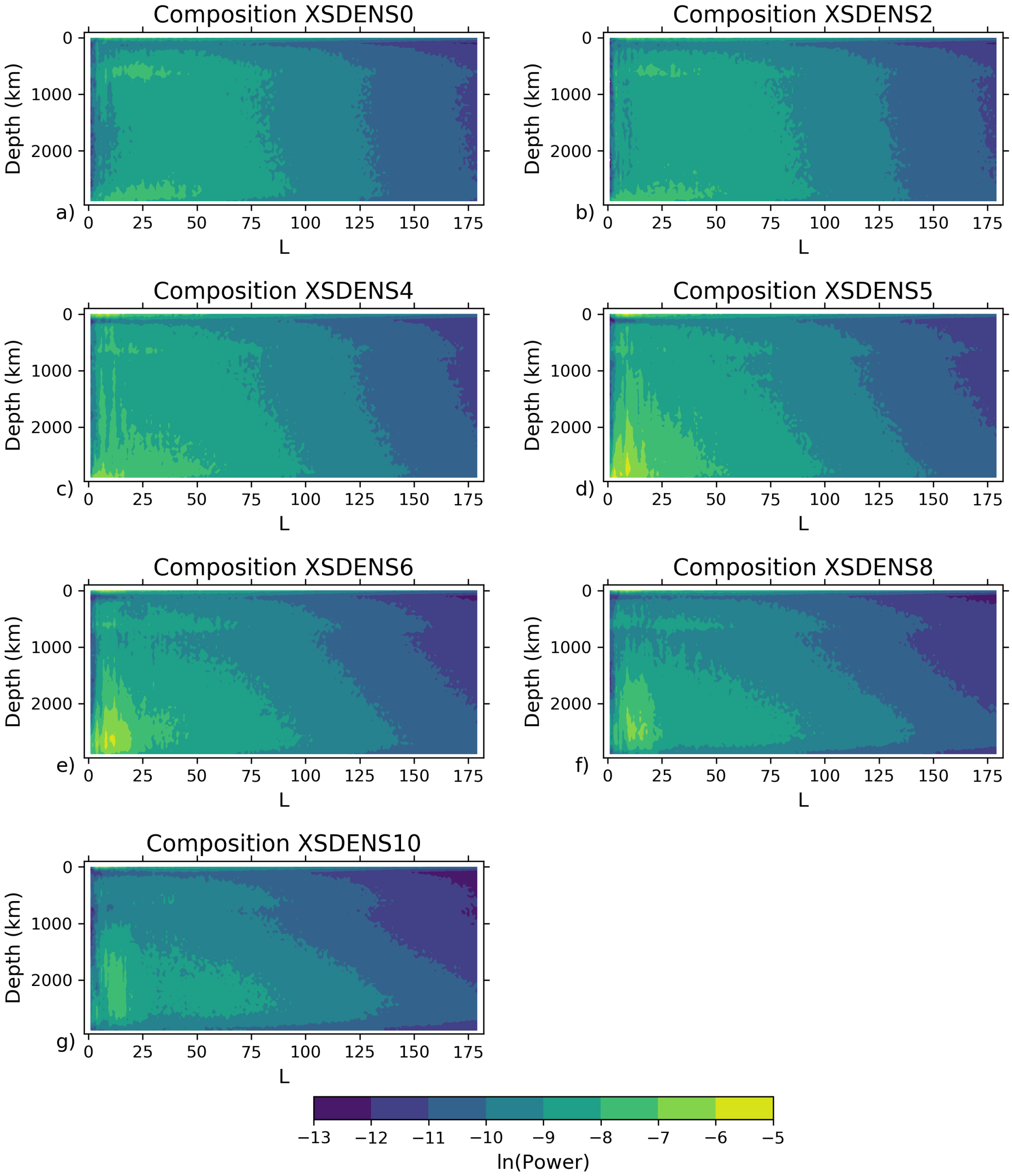

Fig. 4.12 4π normalised spherical harmonic of the composition field from degree 1 to 180 for cases a) XSDNES0, b) XSDENS2, c) XSDENS4, d) XSDNES5, e) XSDENS6, f) XSDENS8, g) XSDENS10.

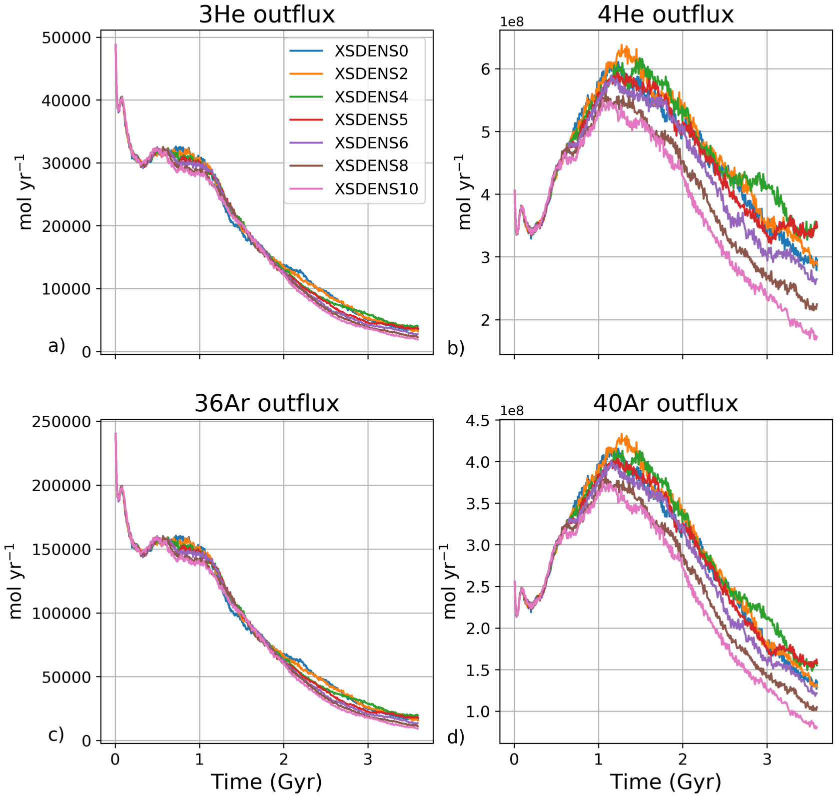

Fig. 4.13 Noble gas flux from the mantle to atmosphere for various values of excess ρ_b. a) ^{3}He, b) ^{4}He, c) ^{36}Ar, d) ^{40}Ar

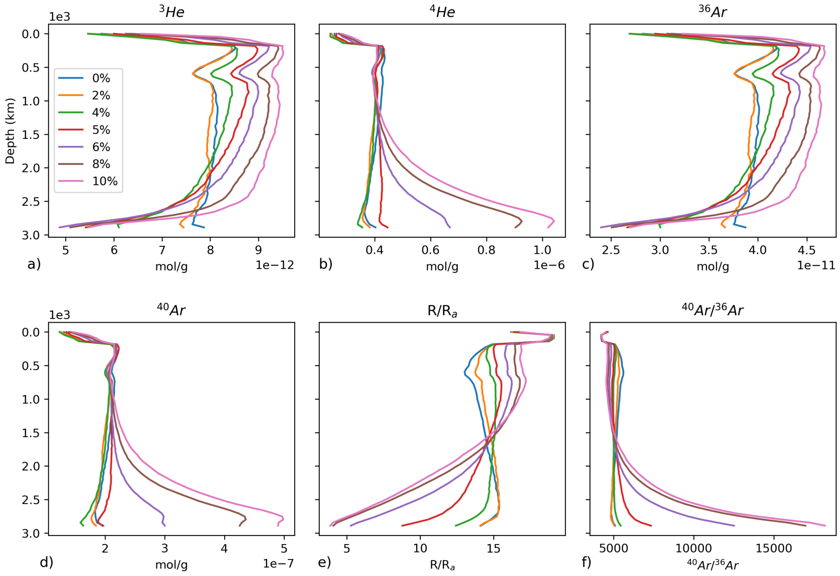

Fig. 4.14 Radial averages for noble gases in the mantle a) concentration of ^{3}He b) concentration of ^{4}He, c) concentration of ^{36}Ar, d) concentration of ^{40}Ar, e) ^{3}He/^{4}He with respect to the current atmospheric ratio R_a, f) ^{40}Ar/^{36}Ar.

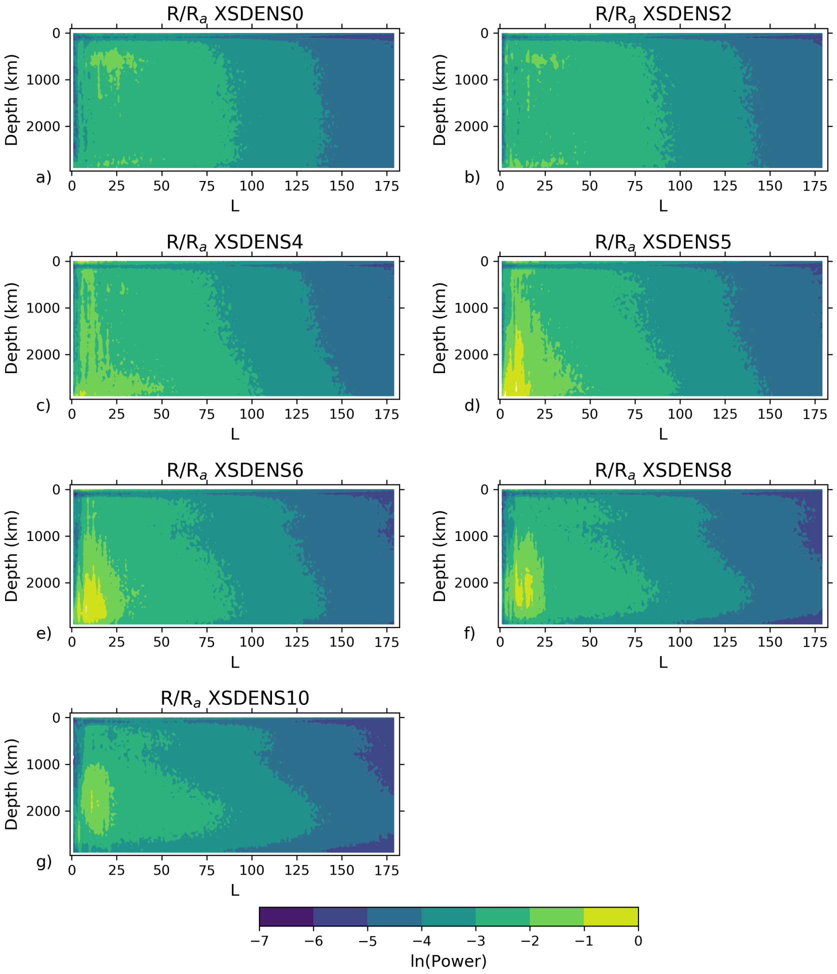

Fig. 4.15 4π normalised spherical harmonic of the R/R$_a$ field from degree 1 to 180 for cases a) XSDNES0, b) XSDENS2, c) XSDENS4, d) XSDNES5, e) XSDENS6, f) XSDENS8, g) XSDENS10.

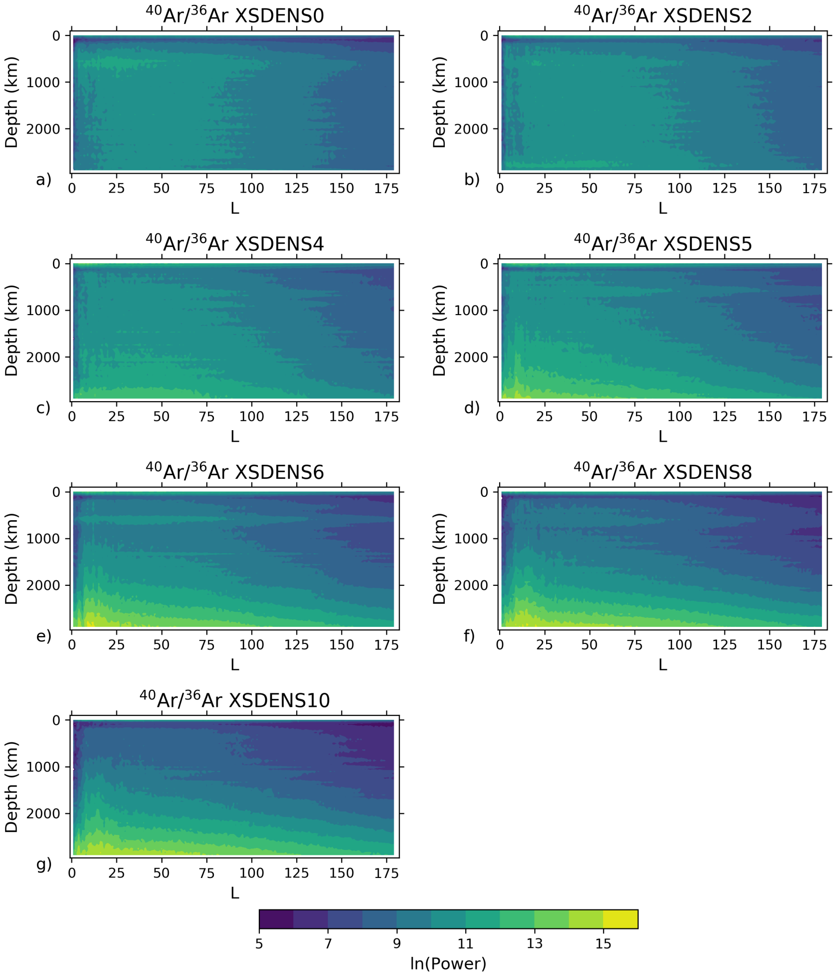

Fig. 4.16 4π normalised spherical harmonic of the ^{40}Ar/^{36}Ar field from degree 1 to 180 for cases a) XSDNES0, b) XSDENS2, c) XSDENS4, d) XSDNES5, e) XSDENS6, f) XSDENS8, g) XSDENS10.

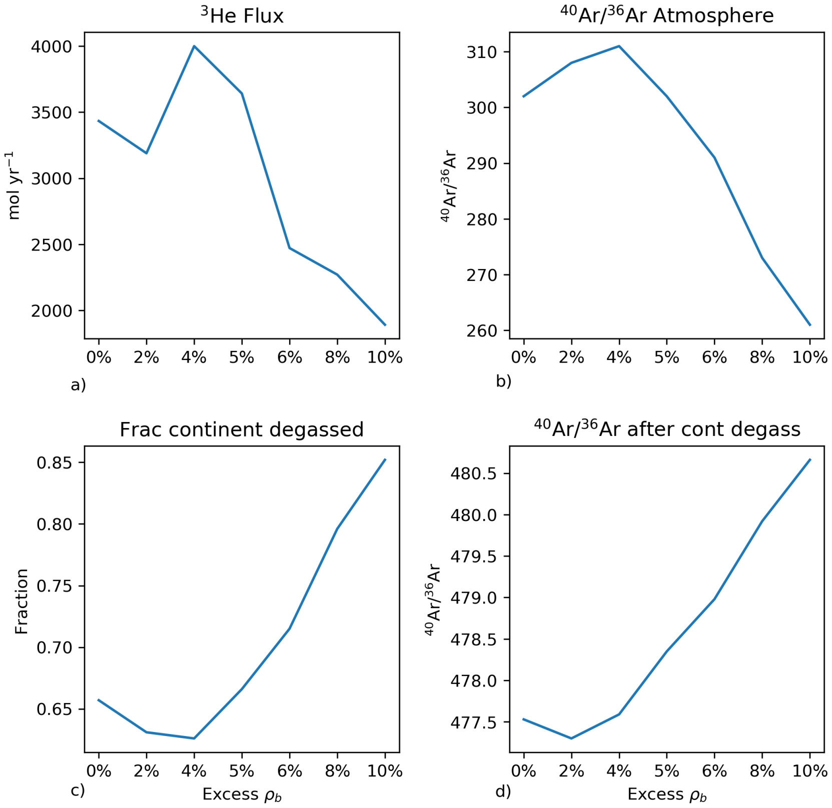

Fig. 4.17 Trends for different isotopes observations with varying excess ρ_b. a) Present day ^{3}He flux out of the mantle, b) atmospheric ^{40}Ar/^{36}Ar, c) the fraction of the continent that would have to degas in order for the atmosphere to contain 50% of the global ^{40}Ar budget, d) the corresponding atmospheric argon ratios after the amount of continent degassing in c).

is dominated by structures of degree $L < 20$ (Fig. 4.15). This seems to disappear in XSDENS8/10 because the lower mantle signature is dominated by $L = 0$ signal due to the subducted basalt accumulating at and enveloping the CMB. The spectrum for the ^{40}Ar/^{36}Ar field is somewhat different to the R/R$_a$ field. In XSDENS0/2 the power is fairly evenly distributed across all depths and decreases with increasing L at a similar rate through most of the mantle (Fig. 4.16a,b). From XSDENS4-10 there is increasingly more power in structures at and just above the CMB (Fig. 4.16c-g). At depth, the power decreases slowly with increasing L , indicating a large range of structure sizes. This implies a decoupling from the compositional field which is mostly made up of larger wavelength structures in the lowermost mantle for case (Fig. 4.12c-g).

Figure 4.17 shows trends of various geochemical observations with varying excess ρ_b. The current atmospheric ^{40}Ar/^{36}Ar is 298 (Lee et al. 2006).

Model atmospheric argon ratios increase from 302-311 from XSDENS0-4, then fall from 302-261 for XSDENS5-10 (Fig. 4.17b). Mantle degassing in the models cannot account for all of the ^{40}Ar in Earth's atmosphere which is known to be $\sim 9.9 \times 10^{41}$ atoms (Allégre et al. 1996), however degassing of the continental reservoir can make up the difference. Figure 4.17c shows to what degree the continent would have to degas in order to satisfy the terrestrial astompsheric ^{40}Ar concentration observation. The minimum amount of continent degassing is case XSDENS4 at 63% and the maximum is cases XSDENS10 at 85%. Figure 4.17f shows the effect that continent degassing has on the atmospheric ^{40}Ar/^{36}Ar. When continent degassing is taken into account the atmospheric argon ratio increases for each cases to a narrow range of values from 478-481.

The distribution of isotope ratios that are measured in oceanic basalt is another key constraint on the mantle. MORBs have a narrow range of R/Ra, generally from 7-9 and a wide range of ^{40}Ar/^{36}Ar, generally between the atmospheric ratio and 40,000. OIBs on the other hand have a wide range of R/Ra, from 4-50, and a narrow range of ^{40}Ar/^{36}Ar. The mantle convection models presented here do not have Earth-like plate tectonics and as such the volcanism is neither distinctly MORB-like or OIB-like. Melting occurs in top 135 km and therefore samples the upper mantle, as MORBs are thought to. However melting takes place at the top of hot plume-like upwellings which bring material from the lower mantle up to the surface and therefore sample deep material, as OIBs are thought to. It would be expected then that the melt in the presented models has a component of both. Xie and Tackley (2004a) showed how changing the method of sampling the model changes the isotope distribution. I present noble gas ratios for samples of the gas flux out of the mantle and at the CMB. In each case I perform 'mixing' in which the trace elements of 10 particles (or the degassed fraction of 10 particles in the gas flux case) that are located geographically close to each other are combined. This accounts for finer scale mixing processes such as melt mixing and diffusion which are not included in the model. Combining particles smoothes out the isotope histograms because particles that have been highly degassed, which therefore have low gas abundances, have a smaller weighting on the new isotope ratio (Fig. 4.18). The smoothing is particularly strong where isotopes are presented for the CMB layer or melting layer because the same number of particles are sampled ($\sim 40,000$)

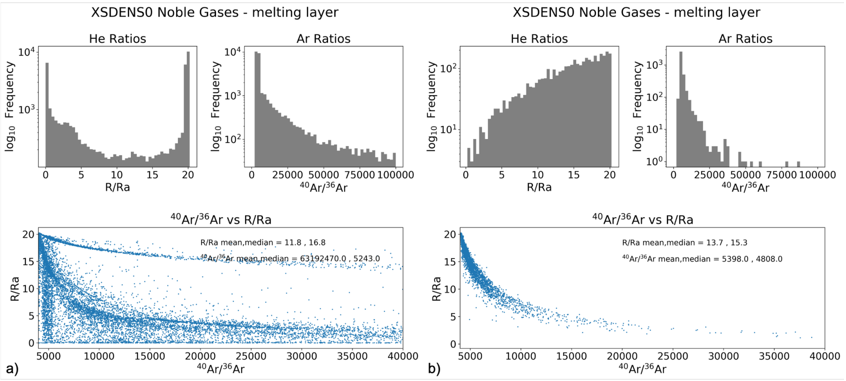

Fig. 4.18 Noble gas composition in the melting layer for case XSDENS0 a) unmixed b) after mixing applied (n=10).

but they are spread over a much larger area (the whole CMB) rather than just concentrated in areas experiencing melting (at plumes heads).

For each value of excess ρ_b investigated the present day distribution of noble gas ratios in the degassing material is fairly similar (Fig. 4.19). The helium distribution is dominated by two distinct peaks at low and high R/R$_a$. In each case at least half of the degassing material has R/R$_a$ < 5.2. The peak at R/R$_a$ close to zero (Fig. 4.19) represents material that has been strongly degassed but experienced radiogenic ingrowth of ^{4}He. There are two conceivable scenarios that this would happen in the models. One is that well degassed particles at the surface are enriched by melt (which contains U and Th) from particles melting beneath them. The second scenario is that the particle is enriched in U that is recycled from the continental reservoir. As there is no mechanism by which the particle may gain ^{3}He relative to ^{4}He, particles that receive melt or recycled U will develop very low R/R$_a$. The peak at 20 R/R$_a$ represents the implicit maximum helium ratio that can exist due to the prescribed initial mantle concentrations of ^{3}He and ^{4}He and initial homogeneous distribution of isotopes. Again as there is no way to gain ^{3}He, or to fractionate ^{3}He and ^{4}He, there is no way to increase this ratio.

The argon distribution has a peak at ^{40}Ar/^{36}Ar = 2,000, with the frequency of compositions decreasing approximately exponentially towards higher ratios (Fig. 4.19). The relationship between R/R$_a$ and ^{40}Ar/^{36}Ar is a negative exponential correlation. The relationship is negative because the convention used for the helium and argon ratios puts the radiogenic isotope as the denominator and numerator respectively. The exponential nature of this relationship is due to radioactive decay being an exponential process and the ingrowth of ^{4}He and ^{40}Ar occurring at different rates. There is generally more scatter at lower excess ρ_b. The mean helium and argon ratios both become more radiogenic with increasing excess ρ_b (Fig. 4.19h), with the mean R/R$_a$ decreasing from 14.8 to 9.6 between XSDENS0 and XSDENS10, and the mean ^{40}Ar/^{36}Ar increasing from $\sim$ 5000 to $\sim$ 7500. The median value for each of these ratios is most radiogenic for case XSDENS4.

It is of interest to look at the noble gas composition at the CMB as it is thought that OIBs sample material from here. R/R$_a$ shifts from being negatively skewed in XSDENS0/2/4, to being normally distributed in XSDENS5, and then positively skewed in XSDENS6/8/10 (Fig. 4.20). At excess ρ_b of 0-4% there is a narrow range of argon ratios measured at the CMB, generally ^{40}Ar/^{36}Ar $< 30,000$ and with a strong peak at 2,000. With further increasing ρ_b there is an increasing amount of material with ^{40}Ar/^{36}Ar $> 40,000$. Similar to the composition of the surface noble gas flux there is a negative exponential correlation between helium and argon ratios.

4.6.2 Degassing efficiency

For the first 2 Gyr degassing rates are lower for cases with lower degassing efficiencies. At just over 2 Gyr there comes a point when this is reversed for the primordial isotopes ^{3}He and ^{36}Ar (Figs. 4.21a,c). At 3.6 Gyr the degassing rate of primordial isotopes in DGAS100 looks to be increasing to become larger than DGAS90, and the degassing rate of primordial isotopes DGAS70 is approaching that of DGAS50/30. Between 0 and 1.4 Gyr there is the largest difference in degassing rates between all cases. Generally greater degassing efficiencies lead to a greater ^{4}He flux at all times, however the ^{40}Ar flux is similar for all degassing efficiencies after around 3 Gyr.

Higher degassing efficiencies result in a mantle that is more depleted in noble gases (Fig. 4.22a-d). In DGAS70/90/100 the surface has the lowest concentration of noble gases. In cases DGAS30/50 the lowest concentrations of noble gases are in the melting layers just below the surface. The radial average R/R$_a$ and ^{40}Ar/^{36}Ar is calculated from the average helium isotope abundances on particles in each layer, so the radial average ratio is dominated by the un-degassed particles. It would be more appropriate to refer to the radial averages of isotope ratios as weighted radial averages. The transition zone and CMB have radiogenic argon and helium ratios, generally getting more radiogenic with increasing degassing efficiency (Fig. 4.22e,f).

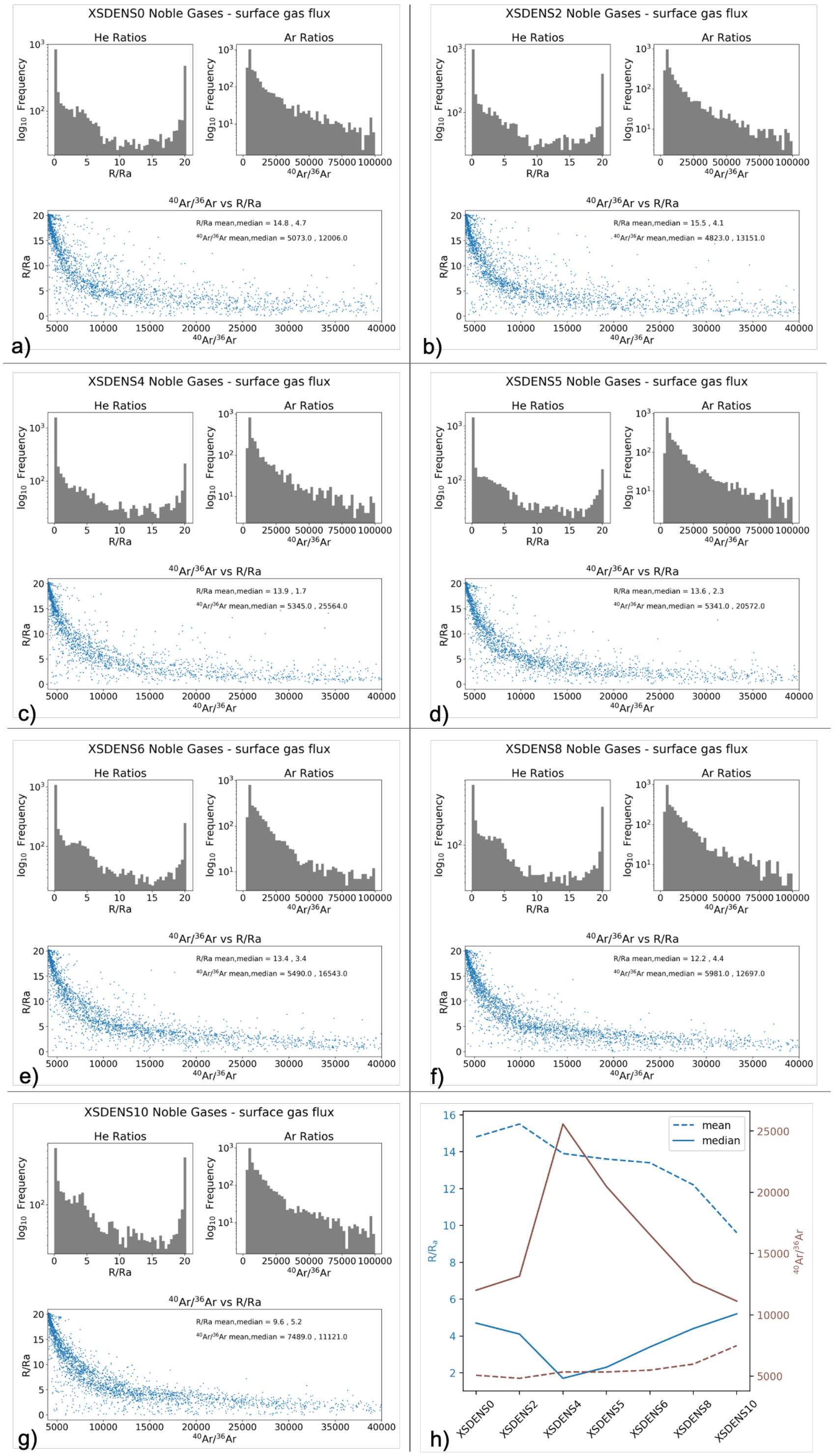

Fig. 4.19 Noble gas composition of degassed material at present day (mixed, n=10) for a) XSDENS0, b) XSDENS2, c) XSDENS4, d) XSDENS5, e) XSDENS6, f) XSDESN8, g) XSDESN10. h) Plot to show variation of average helium and argon ratios for different values of excess ρ_b with dashed lines showing mean values and solid lines showing median values.

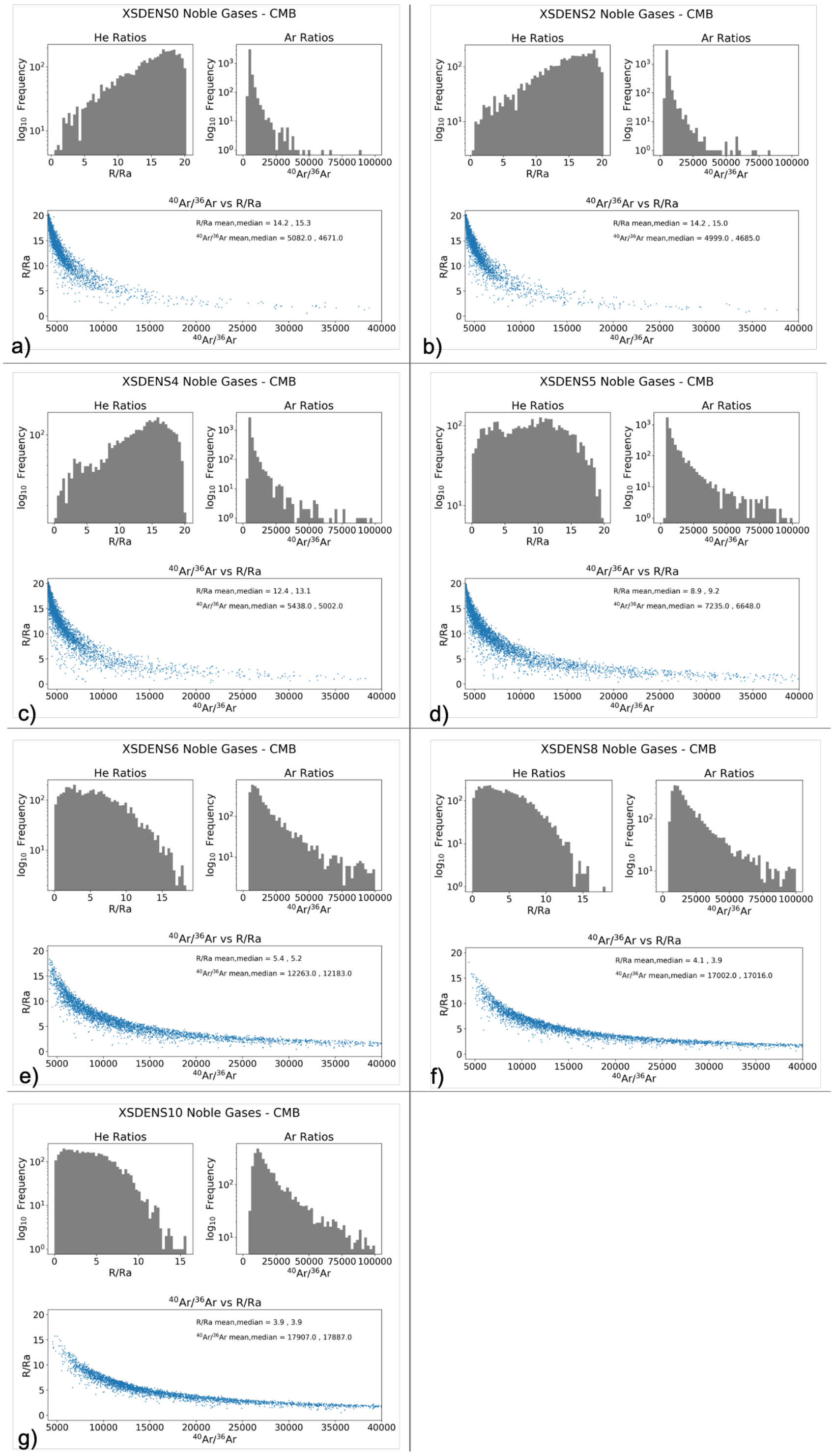

Fig. 4.20 Noble gas composition of material at the CMB at present day (mixed, n=10) for cases a) XSDENS0 b) XSDENS2 c) XSDENS4 d) XSDENS5 e) XSDENS6 f) XSDENS8 g) XSDENS10.

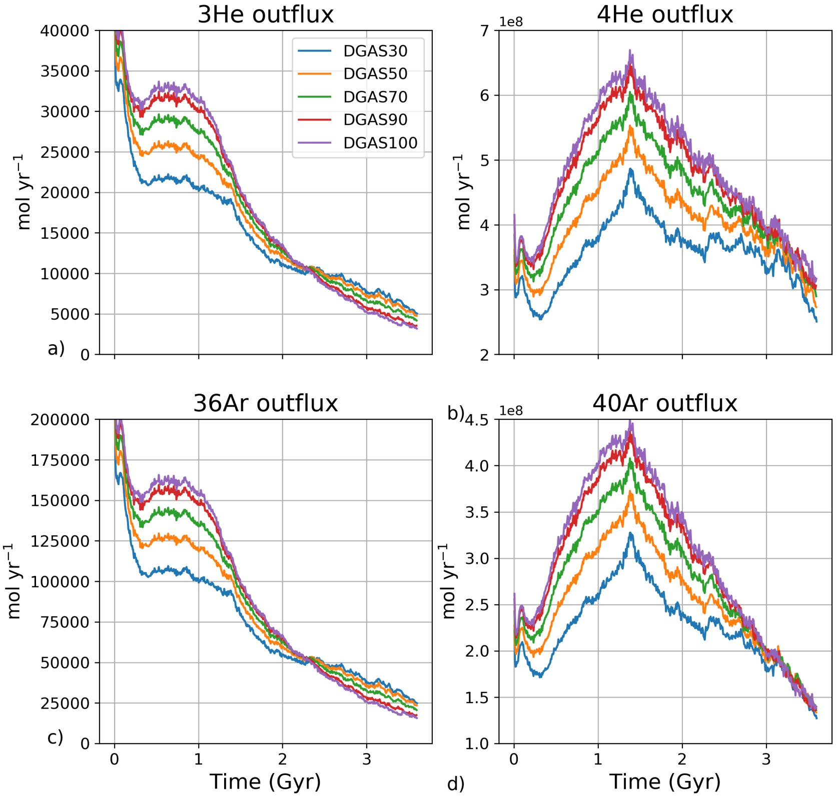

Fig. 4.21 Noble gas flux from the mantle to atmosphere for various degassing efficiencies. a) ^{3}He, b) ^{4}He, c) ^{36}Ar, d) ^{40}Ar

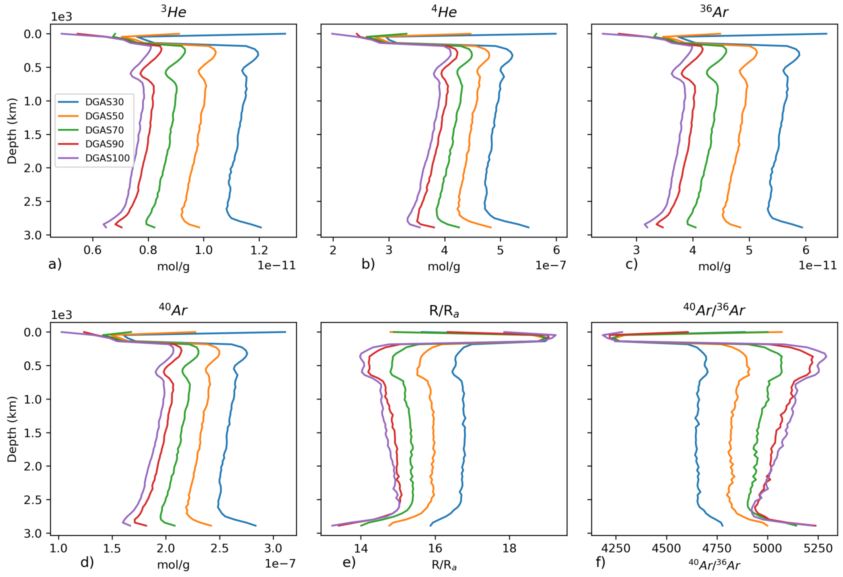

Fig. 4.22 Radial averages for noble gases in the mantle a) concentration of ^{3}He b) concentration of ^{4}He, c) concentration of ^{36}Ar, d) concentration of ^{40}Ar, e) ^{3}He/^{4}He with respect to the current atmospheric ratio R_a, f) ^{40}Ar/^{36}Ar.

Regardless of degassing efficiency, radial averages of R/R_a and $^{40}Ar/^{36}Ar$ are least radiogenic in the melting zone and most radiogenic at the CMB and in the mantle transition zone. High R/R_a in the melting zone seems at odds with the what would be expected for the Earth, where MORBs have a narrow range of R/R_a from 7-10. For DGAS70/90/100 helium and argon ratios both become less radiogenic with depth from a high in the transition zone down to just above the CMB, after which there is a sudden jump to more radiogenic values. DGAS30/50 have fairly constant ratios throughout the mantle apart from right above the CMB where there is an increase to more radiogenic values.

The atmospheric argon ratio tends towards a more radiogenic composition with increasing degassing efficiency (Fig.4.23 b), from $^{40}Ar/^{36}Ar = 243$ in DGAS30 to 319 in DGAS100. Cases with lower degassing efficiency require greater input of ^{40}Ar from the continent in order to meet the constraint of $\sim 9.9 \times 10^{41}$ atoms of ^{40}Ar in the atmosphere (Fig. 4.23c), with DGAS100 requiring 59% of the continent to be degassed and DGAS30 requiring 89%. The atmospheric argon ratio after continent degassing consistently exceeds the terrestrial value with a range from 487 for DGAS30 to 476 for DGAS100.

For all degassing efficiencies there are strong peaks in R/R_a at the highest and lowest ratios (Fig. 4.24). Ignoring material with these compositions the remaining ones are negatively skewed in DGAS30 and DGAS50, before becoming more normally distributed in DGAS70 and positively skewed in DGAS90, hence the median R/R_a of outgassing material decreases with increasing degassing efficiency. DGAS100 breaks this trend with a median helium ratio of $R/R_a = 5.5$. The $^{40}Ar/^{36}Ar$ of outgassed material is positively skewed in all cases. For cases DGAS30-DGAS90 the mean argon ratio is $\sim 5,000 - 5,500$. Median $^{40}Ar/^{36}Ar$ increases with increasing degassing efficiency from $\sim 4,800$ in case DGAS30 to $\sim 16,000$ in DGAS90. DGAS100 does not follow this trend, with a median argon ratio that is lower than DGAS90. Similar to cases where excess ρ_b is varied, there is an inverse exponential relationship between R/R_a and $^{40}Ar/^{36}Ar$, with strong scatter in all cases.

At the CMB there is a negative skew in R/R_a for all degassing efficiencies (Fig. 4.25). From DGAS30-100 the mean R/R_a decreases from 15.0 - 13.4. $^{40}Ar/^{36}Ar$ is positively skewed for all degassing efficiencies and has a narrow range. Mean $^{40}Ar/^{36}Ar$ increases between DGAS30 and DGAS90 from 4993 to 5234. DGAS100 has a slightly lower mean $^{40}Ar/^{36}Ar$ than DGAS90, at 5173.

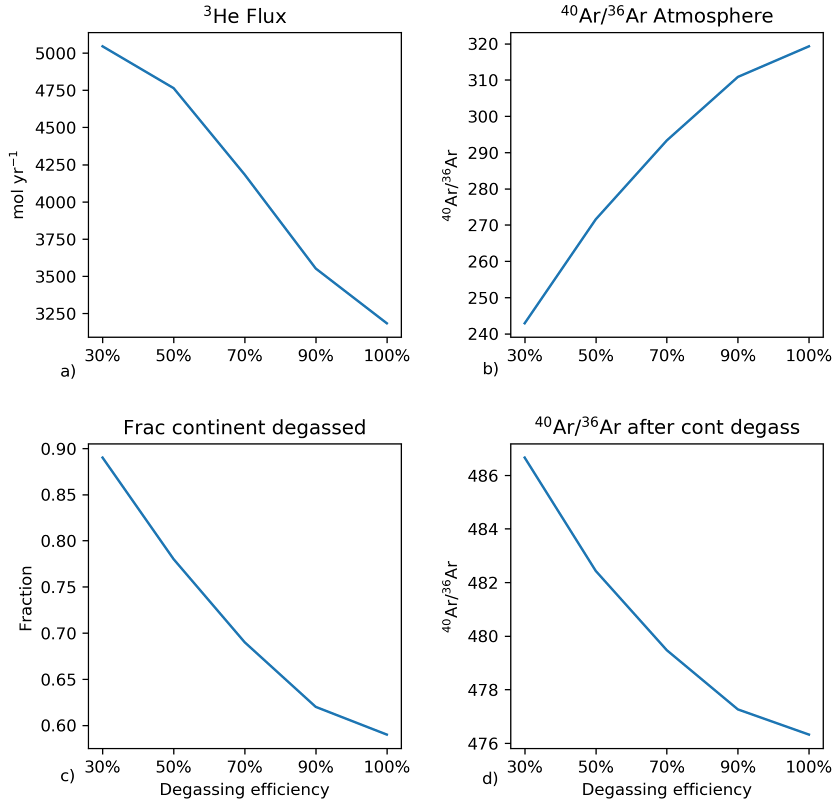

Fig. 4.23 Trends for different isotopes observations with varying degassing efficiencies. a) Present day ^{3}He flux out of the mantle, b) atmospheric ^{40}Ar/^{36}Ar, c) the fraction of the continent that would have to degas in order for the atmosphere to contain 50% of the global ^{40}Ar budget, d) the corresponding atmospheric argon ratios after the amount of continent degassing in c).

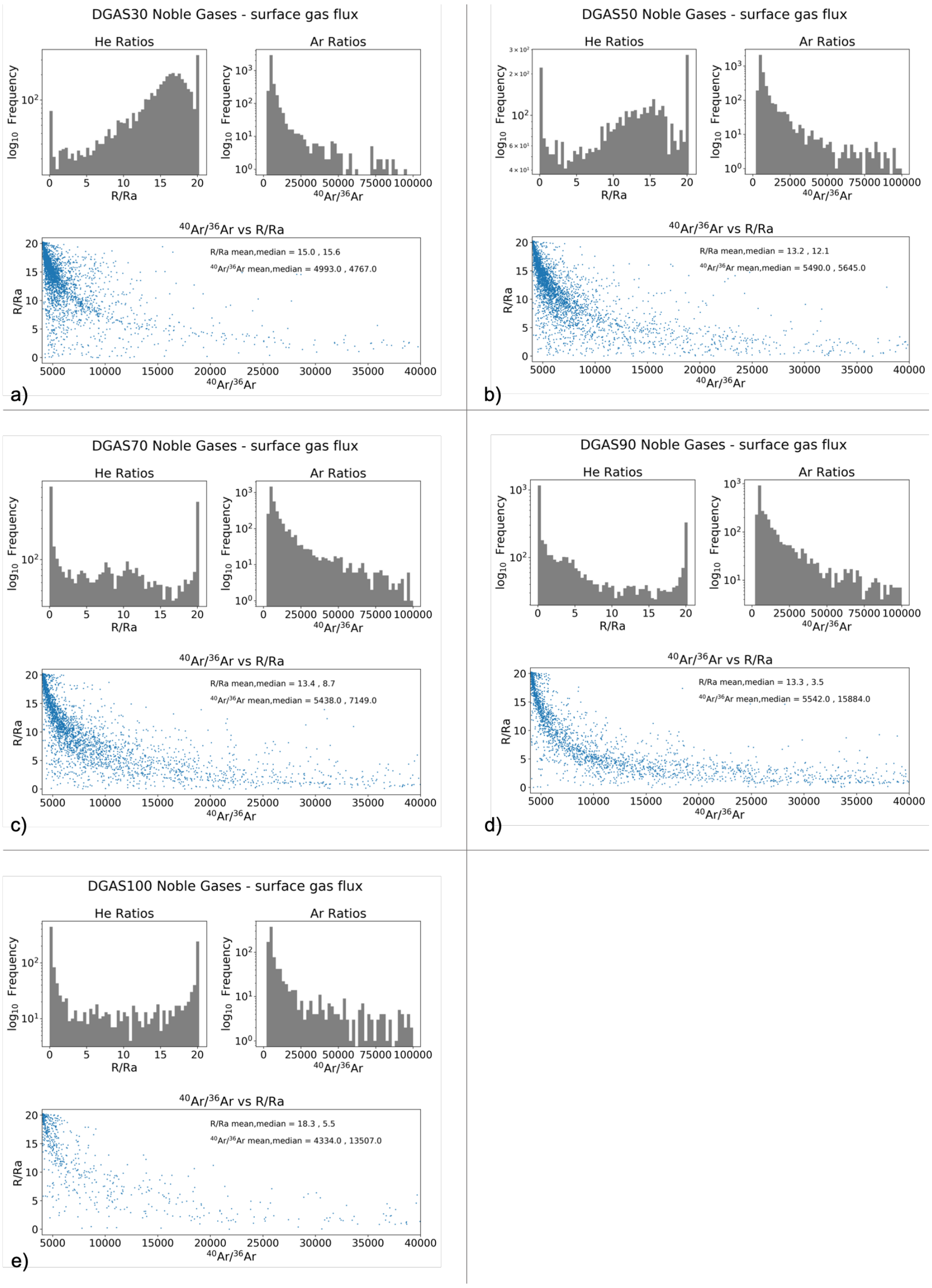

Fig. 4.24 Noble gas composition of degassed material (mixed, n=10) for cases a) DGAS30, b) DGAS50, c) DGAS70, d) DGAS90, e) DGAS100. Histograms are shown for the R/R_a and $^{40}Ar/^{36}Ar$ composition and scatter of R/R_a vs $^{40}Ar/^{36}Ar$.

There is significantly less scatter in R/R$_a$ vs ^{40}Ar/^{36}Ar space for material sampled at the CMB (Fig. 4.25) compared to the degassed material (Fig. 4.24).

4.7 Discussion of results

4.7.1 Excess lower mantle basalt density

Heating modes

The effect of the style of heating on the temperature evolution of the models was investigated by running each excess ρ_b in three different heating modes. The constant, homogeneous heating mode saw the largest decrease in mantle temperatures (Fig. 4.6a) as integrated over time this mode input less thermal energy than the modes heated by radioactive decay. Consequently the surface heat flux also dropped off fastest in the constant, homogeneous style of heating (Fig. 4.6d).

For all styles of heating, higher excess ρ_b generally results in lower energy fluxes at both the top and bottom boundaries. This is likely due to higher density material with a high buoyancy ratio requiring hotter temperatures in order to overcome its negative chemical buoyancy. Denser material would therefore have longer residence times at the CMB. Having hotter material at this boundary reduces the heat flux across the CMB due to a smaller temperature difference across the CMB and retaining hot material in the lower mantle prevents it from cooling down at the surface. Longer residence times are confirmed by radial profiles of the mean time since last melting (Fig. 4.26). For cases XSDENS5/6 there is considerably more heat flux at both boundaries at 3.6 Gyr when radioactive heating is on the particles (Figs. 4.6f,i) rather than distributed homogeneously across the grid (Figs. 4.6e,h). This is due to the accumulated basaltic material heating up more rapidly in cases where heating is on the particles because the basaltic material is enriched in radioactive isotopes. The basaltic material overcomes chemical buoyancy more rapidly in these cases so is transported away from the CMB earlier on. This is particularly visible in XSDNES6 where massive upwellings have developed by 3.6 Ga (Fig. 4.8). Cooler material taking the place of hotter material increases the CMB heat flux while the upwelled hot material increases the surface heat flux. There is little difference in CMB heat flux between cases XSDENS8 and XSDENS10 in all three heating modes due to

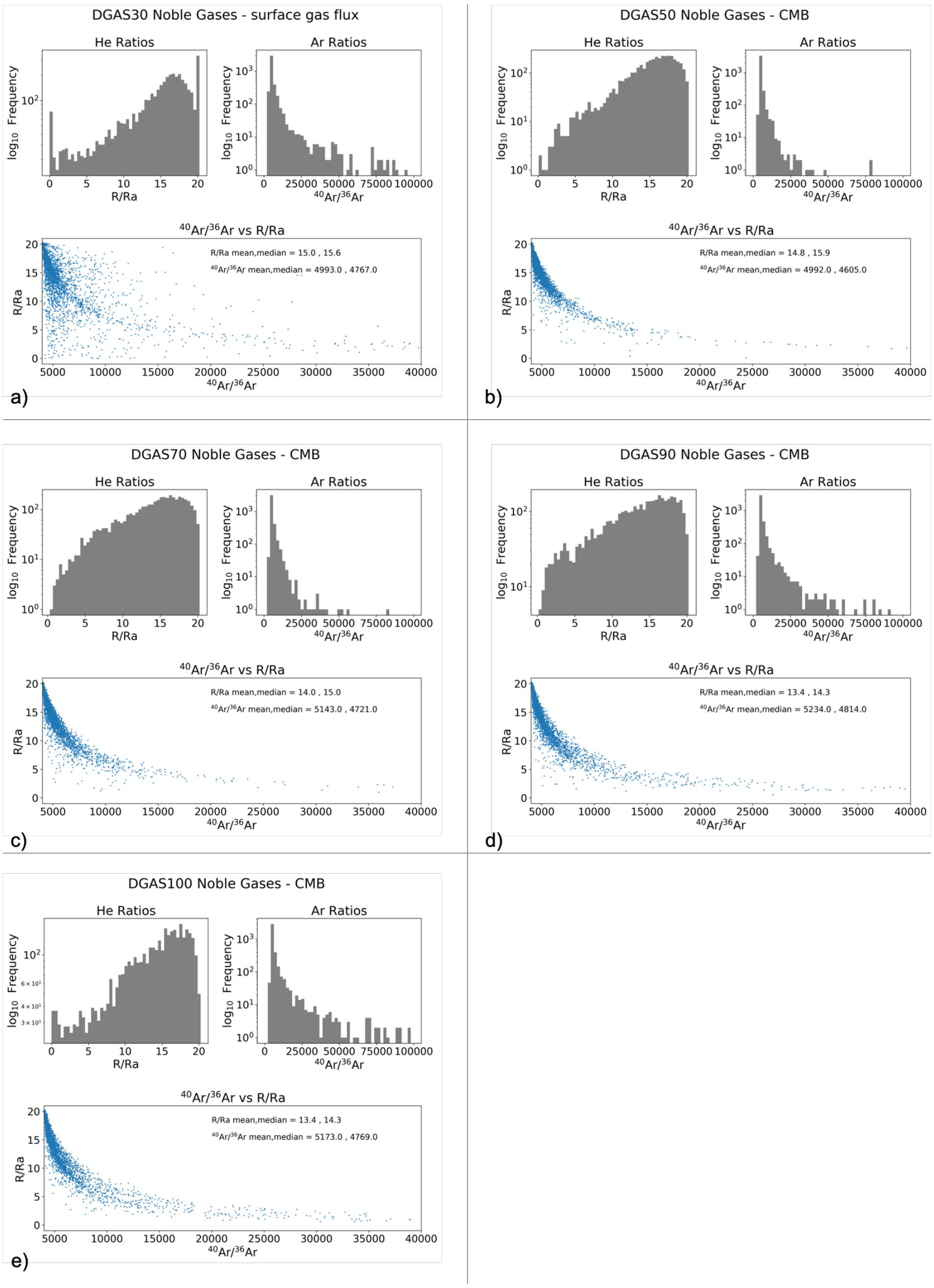

Fig. 4.25 Noble gas composition of material at the CMB (mixed, n=10) for cases a) DGAS30, b) DGAS50, c) DGAS70, d) DGAS90, e) DGAS100. Histograms are shown for the R/R_a and $^{40}Ar/^{36}Ar$ composition and scatter of R/R_a vs $^{40}Ar/^{36}Ar$.

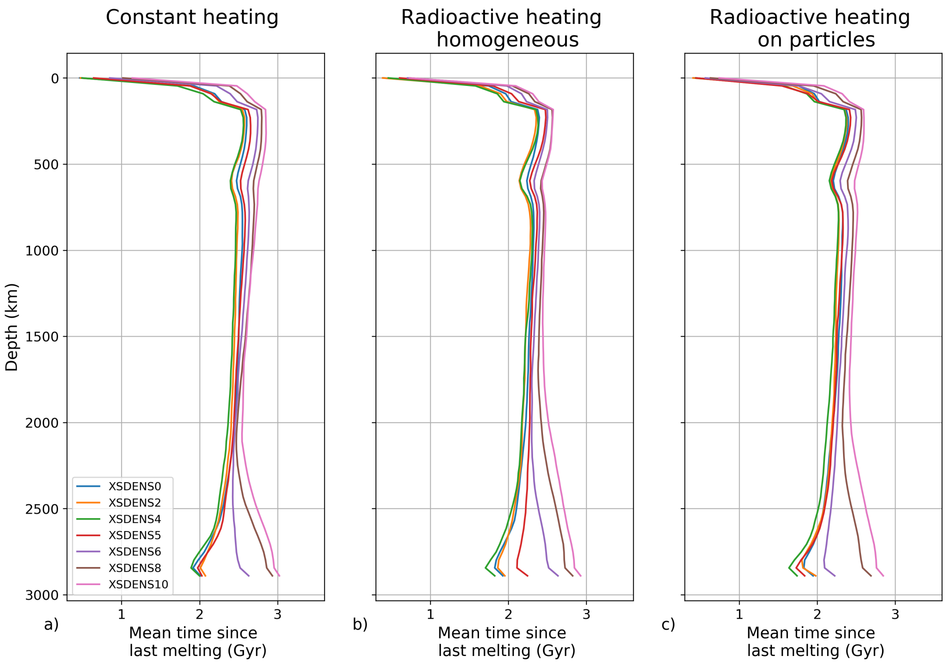

Fig. 4.26 Average time of last melting in each radial layer for cases with a) constant homogeneous heating, b) homogeneously distributed radioactive heating, c) radioactive heating on particles.

the persistence of the basaltic accumulations at the CMB. The mean melting age near the CMB for cases XSDENS8 and XSDENS10 is oldest for the case with constant heating (Fig. 4.26a), showing that the total heating over time affects how much of the dense material can be entrained away from the CMB. For the same cases the mean melting age near the CMB is lowest for models heating by radioactive decay on the particles because the basaltic piles are enriched in heat producing elements (Fig. 4.26c).

Accumulation of basalt

The end member cases XSDENS0 and XSDENS10 show two distinct behaviours with respect to segregation of subducted basalt. As would be expected the higher ρ_b causes basalt to collect in the lower mantle where is can reside for long periods of time, while in the neutrally buoyant case basalt that makes it to the CMB has a short residency before being remixed into the mantle. Case XSDENS2 shows little difference to XSDENS0 in both the dynamics (Fig. 4.8, 4.12a,b) and the chemistry (Figs. 4.11a,b; 4.14; 4.17). A gradual increase in the amount of accumulated material can be seen in cases XSDENS4-8. The amount of basalt that has accumulated in the deep mantle increases sigmoidally between the cases presented (Fig.4.10) indicating that beyond 10% excess ρ_b there wouldn't be much of an increase in the amount of subducted basalt accumulating in the lower mantle. 10% excess ρ_b is higher than what most current mineral physics suggests (Hirose et al. 2005), however combined geodynamic and geochemical modelling of the Lu-Hf and Sm-Nd isotope systems has favoured a 10% excess ρ_b in order to build enriched piles at the CMB (Jones et al. 2019). It is also important to note that a more realistic viscosity structure, with a viscous lithosphere and lower viscosities near the CMB would make for more favourable conditions to retains recycled oceanic crust at the base of the mantle (Li et al. 2014), lowering the required excess density of basalt required to achieve similar remelting rates. Visualisations show that at 1 Gyr and 2 Gyr, there is more basalt in the lower mantle than at 3.6 Gyr for cases XSDNES0-6 (Fig. 4.11). This is due to the entrainment of old subducted material, which has overcome its negative chemical buoyancy, into mantle upwellings. As crustal production rates are lower later on, there is not as much basalt being subducted to take its place so the accumulations decrease in size. For intermediate excess ρ_b of 5-6% the subducted basalt is swept into pile shapes by the pushing and pulling of downwellings and upwellings respectively. From seismic tomography it is known that two superstructures known as LLSVPs (large low-shear-velocity provinces) exist in the lowermost mantle (Cottaar and Lekić 2016). There is much debate as to how these structures form and whether they are thermal, chemical, or thermo-chemical anomalies (eg. Davies et al. (2015a) and Thomson et al. (2019)). Assuming they are thermochemical, it is plausible that LLSVPs are composed of ancient subducted oceanic crust, which has heated up due to long residence times in the lower mantle. If this is the case then these models predict that excess ρ_b of 8-10% is too great to allow such structures to form. The dense material at the CMB in cases XSDENS8 and XSDENS10 moves extremely slowly so does not form piles but a heterogeneous layer. Cases with low excess $\rho_b < 5\%$ struggle to retain subducted basalt in the lower and decreasing oceanic crustal production rates cannot replenish it fast enough to allow pile-like structures to form (Mulyukova et al. 2015). A narrow range of intermediate excess ρ_b of 5-6% trap basalt near the CMB (Fig. 4.11) while allowing it to remain mobile so it can be swept into pile like structures of spherical harmonic degree 2-7 (Fig. 4.12d-e). Similar structures have been shown to form at lower excess ρ_b for models initialised with a dense layer above the CMB (Tackley 2011; Li et al. 2014). Given that the piles in the models presented here are not completely homogeneous in composition (Fig. 4.11), their effective excess density is lower that of purely basaltic material. Temperature and compositional dependence of viscosity may increase the stability of subducted basalt (Heyn et al. 2018) and therefore require lower excess ρ_b for LLSVP-like piles to develop.

Noble Gases

It is difficult to meaningfully try to reconcile both the MORB and OIB helium isotope compositions together in these models as they lack plate tectonics and therefore lack ridge volcanism. The melting occurs in the top 135 km of the mantle at the heads of plumes. Plumes are broad and melt material over a wide area, so there are aspects of both MORB and OIB volcanism in these structures. Considering just the OIB constraints, the range of R/R_a produced in these models is much lower than what has been observed (Fig. 4.2). Samples from Loihi volcano in Hawaii display R/R_a up to 35 (Rison and Craig 1983) and picritic basalts from Baffin island have R/R_a up to 50 (Stuart et al. 2003). Increased excess ρ_b allows recycled crust, which is degassed but also enriched in radioactive isotopes, to accumulate in the lower mantle. This generates significant chemical stratification with the deep mantle developing low R/R_a and high $^{40}Ar/^{36}Ar$ compared to the upper mantle for excess $\rho_b > 5\%$ (Fig. 4.14e). This shows that storage of ^{40}Ar in the lower mantle is possible without the need for layered mantle convection, however is at odds with the model that OIBs sample a deep primordial reservoir with high R/R_a (Graham 2002). It also does not match well with predictions that the plume source has a low $^{40}Ar/^{36}Ar$ relative to the depleted mantle (Matsuda and Marty 1995). Thermal plumes in these simulations originate at the CMB, an area which is enriched in particles with a radiogenic signature at high excess ρ_b (Fig. 4.20). Because of this it might be expected that at higher excess ρ_b particles with low R/R_a and high $^{40}Ar/^{36}Ar$ signature are entrained, causing the melts to have more radiogenic helium and argon signatures with greater excess ρ_b. Indeed, the mean $^{40}Ar/^{36}Ar$ increases from $\sim 5000 - 7500$ between XSDENS0 and XSDENS10, and the mean R/R_a reduces from 14.8 - 9.6. The median argon and helium isotope ratios are similar between the end member cases XSDENS0 and XSDENS10 (Fig. 4.19a,g). Case XSDENS4 has the most radiogenic median noble gas composition. The reason for this can be seen in animated visualisations (Appendix C). The increased ρ_b gives subducted basaltic material a longer residence time at the CMB. In case XSDENS4 basaltic material eventually becomes hot enough to overcome its chemical buoyancy and be entrained into the mantle in large volumes. This is also the case in XSDENS5 but less basaltic material is being sampled in the final time step of the calculation. For cases with higher ρ_b much of the basalt that has segregated to the CMB remains there at the end of the simulation. If the plumes in these models mainly sampled deep mantle material it would be expected that degassed material in cases XSDENS8 and XSDENS10 would have a much more radiogenic noble gas composition that XSDENS0. The fact that this is not observed in the models suggests the plumes sample from all mantle depths and that material entrained from the deep mantle may only make up a small fraction of the melt.

The distribution of helium isotopes in erupted material in these models (Fig. 4.21) is not a good match to MORBs, which is associated with a narrow range of values generally with $\mathrm{R/R}_a = 7 - 10$. The homogeneity of MORBs is widely considered to evidence a well mixed upper mantle (Lupton 1983; Kellogg et al. 2002). The high degree of mixing is made possible by low upper mantle viscosities (Mitrovica and Forte 1997) and the constant processing along Earth's network of mid-ocean ridges. Such a homogeneous upper mantle does not form in these models, potentially due to the lack of ridge volcanism. The mean helium ratio of outgassed material decreases with increasing excess ρ_b, from $\mathrm{R/R}_a = 14.8$ in XSDENS0 to 9.6 in XSDENS10 (Fig. 4.19). This is due to dense oceanic crustal material having a longer residence times in the lower mantle and so accumulating more ^{4}He from radioactive decay. The increased helium concentration gives these radiogenic compositions large weighting when calculating the average $\mathrm{R/R}_a$. Although the $\mathrm{R/R}_a$ of melts tends towards the MORB value with increasing ρ_b, this cannot explain the narrow range of helium ratios measured in MORBs, as the lowest $\mathrm{R/R}_a$ material must must be entrained from the lowermost mantle (Fig. 4.14e).

The range of $\mathrm{R/R}_a$ that is produced by these models does not cover all those which are observed in OIBs (Fig. 4.19). As there is no way to directly fractionate ^{3}He from ^{4}He, the only way that different helium ratios develop is through changing the parent-daughter isotope ratio. Particles which receive melt or recycled continental U will develop a lower $\mathrm{R/R}_a$ due to ^{4}He ingrowth. Higher helium ratios do not develop in the depleted residue because helium and uranium are set to have the same partition

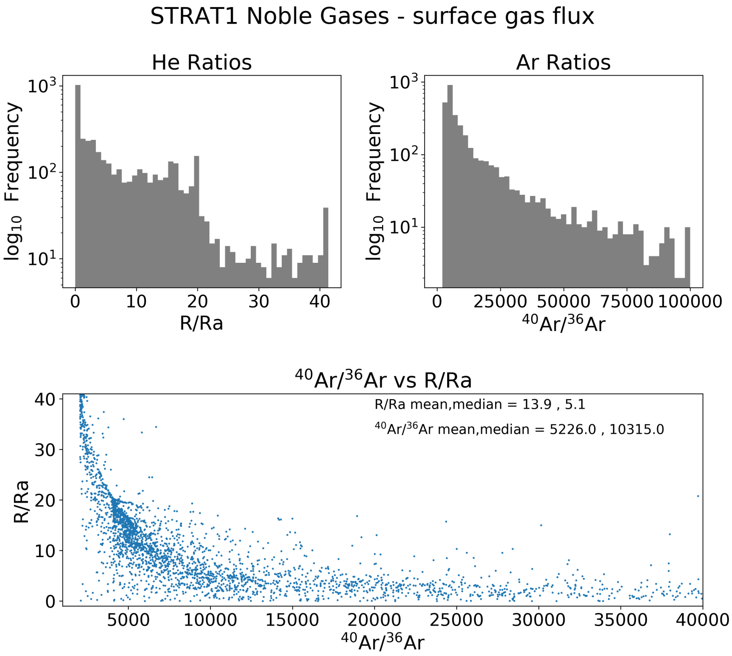

Fig. 4.27 Noble gas composition of degassed material for case with initial stratification of trace elements (mixed, n=10).

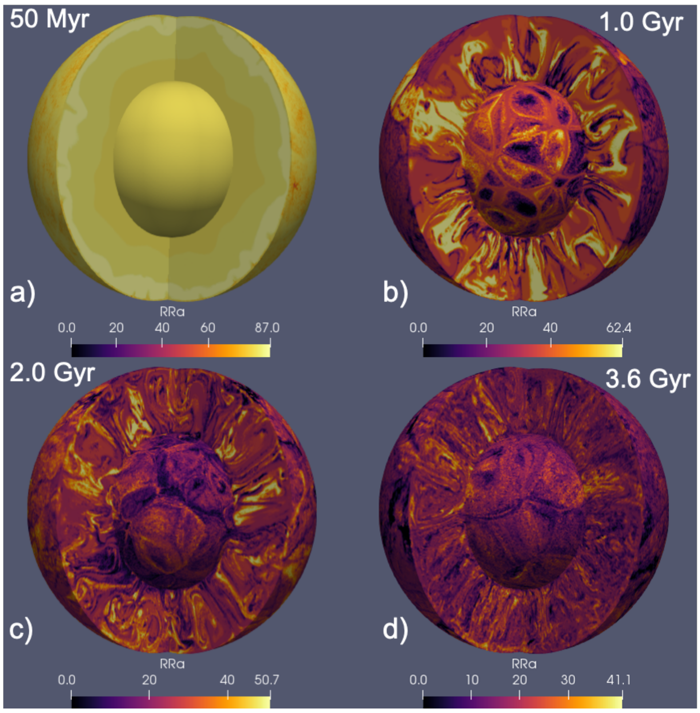

Fig. 4.28 Snapshots of the R/R_a distribution in the mantle for case with an initially stratified mantle trace element composition at a) 50 Myr, b) 1 Gyr, c) 2 Gyr, d) 3.6 Gyr.

coefficient. To generate a more OIB-like range of R/R$_a$ the implicit maximum R/R$_a$ must be increased. This could be achieved by initialising the mantle with more ^{3}He, however this would also increase the present day ^{3}He flux, which is already too high for all cases. Xie and Tackley (2004a) set helium to be more compatible than U and Th to allow residues to develop larger R/R$_a$. This is not ideal though as helium is expected to be equally, if not less compatible than uranium on melting (Heber et al. 2007). Alternatively the mantle could be initialised with a heterogeneous trace element composition. Motivation for such an initial condition comes from the likelihood that Earth accreted heterogeneously (Rubie et al. 2011). During accretion giant impacts heterogeneously degassed the mantle to form distinct reservoirs, as implied by xenon isotopes (Pepin and Porcelli 2006; Mukhopadhyay 2012). Figure 4.27 shows the noble gas composition of degassed material for a case which is initialised with a mantle that is compositionally stratified in trace elements. Particles in the initially homogeneous mantle are depleted in their incompatible trace element budget by a factor of 2/3 from the surface down until 1/3 of the global amount of each isotope has been removed. This depletion is added equally across particles in the bottom 1000 km of the mantle, resulting in them becoming around 5× enriched in incompatible trace elements compared to those which were depleted. Note that in this case basalt is 3% denser than harzburgite in the lower mantle. A snapshot after 50 Ma shows R/R$_a$ developing at different rates in 3 layers through the mantle (Fig 4.28a) due to differential rates of ^{4}He ingrowth relative to ^{3}He abundance. The helium composition of the degassed material at present day shows a wider range of R/R$_a$ than cases that start with a homogeneous trace element composition (Fig. 4.27). There is no distinct reservoir for high R/R$_a$ material but it is distributed throughout the mantle (Fig 4.28d).

The high R/R$_a$ of OIBs is often interpreted as meaning the mantle plumes sample a deep primordial reservoir. This run suggests that a deep reservoir is not required, but that primordial material may be entrained into mantle plumes from almost anywhere in the mantle. It must be noted though that due to the lack of ridge volcanism in these models, the upper mantle may not be depleted to the same degree as Earth's. Nonetheless, it is not required that primitive high R/R$_a$ material exists as a large mass, rather that may be distributed at many length scales. This is reminiscent of the marble cake mantle model (Allégre and Turcotte 1986) and consistent with

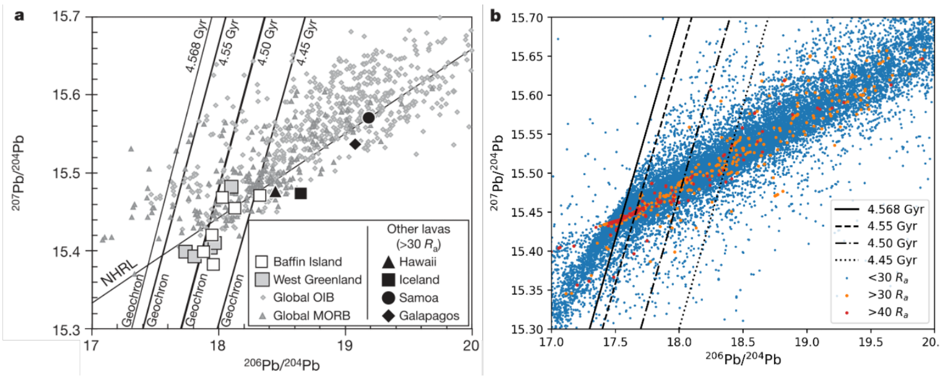

Fig. 4.29 a) Figure showing distribution of Pb ratios in ^{207}Pb/^{204}Pb vs ^{206}Pb/^{204}Pb space for global set of MORBs and OIBs. Samples with R/R$_a$ > 30 are highlighted and those with the highest helium ratios (Baffin Island and West Greenland) cluster in between the 4.55 Gyr and 4.45 Gyr geochrons. Reproduced from Jackson et al. (2010). b) Pb ratios of melt from case with an initially stratified trace element distribution. Melt with R/R$_a$ < 30 plotted as blue dots, those with R/R$_a$ > 30 plotted as orange dots and those with the highest helium ratios of R/R$_a$ > 40 plotted with red dots.

the recent observations that heterogeneity exists at the smallest of length scales (Lambart et al. 2019).

Evidence for high R/R$_a$ material being primitive in nature comes from the lavas Baffin island and West Greenland, which record the highest terrestrial helium ratios. These lavas have Pb and Nd ratios which indicate an ancient source age (Jackson et al. 2010). The evidence from Pb isotopes is that the highest R/R$_a$ material consistently plots between the 4.55 and 4.45 Gyr geochron (Fig. 4.29a). For the simulation presented above, Pb isotope data was plotted in ^{207}Pb/^{204}Pb vs ^{206}Pb/^{204}Pb space (Fig. 4.29b). 75% of the melt with a helium composition of R/R$_a$ > 30 plots to the left of the 4.45 Gyr geochron. When considering only melt with a helium composition of R/R$_a$ > 40, 95% of the melt plots to the left of the 4.45 Gyr geochron. This is well understood for these models as material with the highest helium ratios is required to have remained un-differentiated for the whole calculation.

The assumption that OIBs displaying the highest helium ratios are primitive is challenged by Anderson (1998b). They show that, material with high R/R$_a$ is not enriched in ^{3}He, but deficient in ^{4}He. A model presented by Anderson (1998a) explains the observations by the recharging of refactory shallow mantle, which is depleted in U and Th, with high ^{3}He/U compositions due to melting near ocean ridges. In the case presented above the highest helium ratios develop on particles which were initially depleted in trace elements. Similarly to Anderson (1998a), the material with highest R/R_a in the case presented above develops due to slow radiogenic ^{4}He ingrowth, as this material was initially depleted in trace elements. However, particles with the highest helium ratios are also those which have avoided melting, and so retain their initial ^{3}He composition. Most particles with low R/R_a have degassed and therefore the average ^{3}He abundance is higher for particle with $R/R_a > 30$ than those with $R/R_a < 30$.

Initialising the mantle with a heterogeneous distribution of trace elements to produce a wider range of helium ratios removes the need for alternative helium sources of primordial helium. The two main alternative sources of primordial helium are a dense primordial layer (Jackson et al. 2010) and the core (Porcelli and Halliday 2001). A dense primordial layer could have formed by 'upside down differentiation' of a magma ocean (Solomatov and Stevenson 1993; Lee et al. 2010). It is likely that such a layer would have to be both intrinsically dense and highly viscous in order to survive to the present day (Li et al. 2014). If LLSVPs are formed from such primordial material (Zhang et al. 2016), then these could act as sources of high ^{3}He/^{4}He material. If the core is a source of primordial helium then it would have acquired primordial helium at some point in the past. Early high pressure experiments cast doubt on whether the core could act as a reservoir for primordial helium, after discovering extremely low degrees of noble gas partitioning between silicates and metals (Matsuda et al. 1993). This would prevent significant amount of helium from being sequestered to the core, thus voiding it as a primordial helium source. More recent experimental work has determined much larger partition coefficients for noble gases between metals and silicates (Bouhifd et al. 2020). This raises the possibility of the core having significant volumes of helium with a primordial ^{3}He/^{4}He composition. Whether the core is a viable source of primordial helium is beyond the scope of this work, but it is worth noting this possibility.

There is a negative correlation between excess ρ_b and present day ^{3}He flux, which for all cases is greater than current best estimates of 800-1000 mol yr^{-1} (Fig. 4.17a). For XSDENS10 this is still around 2.5 times higher than the 800 mol yr^{-1} calculated by Tucker et al. (2018). The present day degassing rate of ^{3}He is dependent on the present day melting rate, and how degassed the material being melted at the present day is. Lower temperatures at the surface of models with greater excess ρ_b (Fig. 4.7) incur smaller heat fluxes and therefore slightly lower melting rates. Greater excess ρ_b also increases the efficiency of segregation of subducted oceanic crust into the lower mantle, leaving an upper mantle constituted of a higher percentage depleted residue (Fig. 4.11). The combination of these effects is less degassing over time and so a mantle that is more enriched in gases (Fig. 4.14). Despite having the least degassed mantle, XSDENS10 still has the lowest present day flux of ^{3}He.

Lower mantle excess ρ_b of 0-5% self consistently produced atmospheric ^{40}Ar/^{36}Ar close to the terrestrial value of 298. XSDENS10 had the lowest present day ^{40}Ar/^{36}Ar at $\sim$ 260. These values do not account for continent degassing though. To meet the constraint of atmospheric ^{40}Ar the continents must be degassed between 63% for XSDENS4 and 85% for XSDENS10. There is no general consensus on how degassed the continents are, however if we assume a constant degassing over time then this corresponds to continental crust degassing rates of 1.59×10^8 and 2.09×10^8 mol yr^{-1}. This is slightly higher than estimates made by Bender et al. (2008) but within the range given for various rates of continental crust formation. The flux of ^{40}Ar from Earth's mantle, based on the mantle ^{3}He flux, ^{3}He/^{4}He, and ^{4}He/^{40}Ar is 0.27×10^8 mol yr^{-1} (Bender et al. 2008), around 6 times less than the fluxes in each of the models presented here (Fig. 4.13d). This is similar to the excessive ^{3}He fluxes, and implies that the melting process is degassing too efficiently. This may be due to the lack of ridge volcanism in these models, which would preferentially sample the deleted upper mantle. The plumes that control melting in mantle convection model may entrain material from throughout the mantle, much of which is more enriched than material in the melting zone. The 'missing argon problem', as outlined in Allégre et al. (1996), comes about because the concentration of ^{40}Ar in MORBs is too low to account for all the ^{40}Ar that should exist in the mantle, assuming ^{40}Ar is uniformly distributed. It has been argued that the calculated ^{40}Ar budget of Earth is too high due to estimates of the potassium content of the BSE being too large (Lassiter 2004). The models presented here suggest that high ^{40}Ar concentrations can exists throughout the mantle. If the excess ρ_b is such that subducted oceanic crust can reside at the base of the mantle for long periods of time then this becomes a particularly important reservoir, however it is not necessary as elevated ^{40}Ar may exist throughout the mantle.

4.7.2 Degassing efficiency

Shortly after 2 Gyr there is a switch in the relative degassing fluxes for cases DGAS30-100. Before this time DGAS100 had the greatest degassing flux, decreasing monotonically with decreasing degassing efficiency (Fig. 4.21). The opposite is true after this time, but only for the primordial noble gases ^{3}He and ^{36}Ar. As each case DGAS30-DGAS100 has the same dynamics, the switch likely happens because around this time the amount of material getting resampled overtakes the amount of material getting sampled for the first time. Unsurprisingly lower degassing efficiencies cause the mantle to be less degassed (Fig. 4.22a-d). This fits with the model of Gonnermann and Mukhopadhyay (2009) in which recycling of highly degassed oceanic crust dilutes the nobles gasses in the mantle, lowering fluxes. As these model have a 'marbled' texture, there exists pockets of highly un-degassed material. If enough of this un-degassed material were to melt at once then models with higher degassing efficiencies would give rise to greater ^{3}He flux. This makes this relationship difficult to relate to Earth as the dynamics of a model will never truly match those of Earth's. The dominant volcanism on Earth is at ridges, which are thought to sample just the upper mantle and thus deplete it. As melting in these models exclusively occurs at hot mantle upwellings it is likely that the upper mantle is not depleted in the same way Earth's is. The flux of radiogenic isotopes out of the mantle is positively correlated to degassing efficiency throughout most of the calculation (Fig. 4.21b,d) due to radiogenic ingrowth replenishing highly degassed particles. The estimated degassing rate of ^{40}Ar from Earth's mantle is 0.27×10^{8} mol yr^{-1} (Bender et al. 2008), around 6 times lower than that of these cases. Similarly to what is discussed in 4.7.1, this may be because of the lack of ridge volcanism in these models, which would preferentially sample a highly depleted upper mantle.

The case with the highest mean helium ratios in the degassed material is DGAS100, with $R/R_a = 18.3$. This is because any particle which has undergone a melting event will have been completely stripped of primordial ^{3}He, so will always have $R/R_a = 0$. Particles which have not yet melted are the only ones with any ^{3}He, and these particles will have a helium composition of $R/R_a = 20$ unless they have received recycled uranium. When all the degassing material is averaged, the un-degassed particles have the most helium and therefore have the largest weighting. In cases DGAS30-90 the central maxima in the distribution of R/R$_a$ for degassing material moves gradually to lower R/R$_a$ with increasing degassing efficiency (Fig. 4.24). Consequently the median also moves to lower values, decreasing from 15.6 at 30% degassing efficiency, to 3.5 at 90% degassing efficiency. This shows that intermediate R/R$_a$ compositions are controlled by the degree of noble gas recycling with more degassing, and therefore less recycling, generating low R/R$_a$. These intermediate compositions are important as almost all MORB and the mode composition of OIB is R/R$_a$ $\sim$ 8. The mean R/R$_a$ of degassing material has little variation between DGAS30 and DAGS90 as, like the radial averages, this is dominated by particles which have been enriched in U so have high helium abundances. Based on the cases presented here, a median R/R$_a$ similar to MORB values would be achieved with a degassing efficiency of around 70%, however this alone would still fall short of being able to replicate the range of R/R$_a$ measured in OIBs. It must also be noted that while the median R/R$_a$ is close to that of MORBs for a degassing efficiency of 70%, the mean value is much higher at R/R$_a$ $= 13.4$. This means that if large scale averaging were to take place prior to eruption, similar to the SUMA model (Meibom and Anderson 2003), then the melts would have helium ratios greater than that of MORBs. The distribution of helium ratios in DGAS100 is highly bimodal (Fig. 4.24e) and does not come close to representing either MORB or OIB compositions. The requirement for incomplete degassing implies that some degree of noble gas recycling is necessary in order to achieve a noble gas distribution of both MORBs and OIBs. Exactly how these noble gases are recycled is unclear as the method used here does not distinguish between incomplete degassing, recycling of noble gases trapped in altered oceanic crust, or formation of hybrid pyroxenites. It is possible that all three processes occur to some degree.

There is a large range of atmospheric ^{40}Ar/^{36}Ar, ranging from $\sim$ 242 for 30% degassing efficiency, to $\sim$ 319 for 100% degassing efficiency. After considering continental crust degassing, the atmospheric ^{40}Ar/^{36}Ar has a much narrower range, from $\sim$ 487 for 30% degassing efficiency, to $\sim$ 476 for 100% degassing efficiency. These are similar to values for atmospheric ^{40}Ar/^{36}Ar in cases varying excess ρ_b and around 60% higher than the terrestrial atmospheric ratio. This similarity is because in all cases most of the global budget of ^{36}Ar resides in the atmosphere, with 70% of particles in the system having undergone at least one melting event. The processing rate of the mantle is lower than studies in 2D geometry, where up to 90% of the mantle may be processed (Xie and Tackley 2004a). There are arguments for the mantle to be almost completely processed (Davies 2002; Huang and Davies 2007), however the models presented here require that primordial material exists in order for the highest R/R_a signatures to be sampled. The effect of increased processing is discussed in 4.7.4. For the initial concentrations used in these calculations the minimum atmospheric $^{40}Ar/^{36}Ar$ is 456 if the atmosphere contains 9.9×10^{41} atoms of ^{40}Ar and the total global budget of ^{36}Ar has been degassed to the atmosphere. Taking an average value of atmospheric $^{40}Ar/^{36}Ar$ for cases DGAS30-100 to be 488, initialising the calculations with 1.65× more ^{36}Ar, bringing the total ^{36}Ar in the system to $\sim 6.0 \times 10^{15}$ mols, would generate present day atmospheric $^{40}Ar/^{36}Ar$ close to 298. This would also require 1.65× more ^{3}He to be initialised in the system to maintain $^{3}He/^{36}Ar = 0.2$ in accordance to the noble gas distribution model used (Porcelli and Ballentine 2002). As ^{36}Ar and ^{3}He are both primordial and passive, the results of previous runs can be scaled by a factor of 1.65 where ^{36}Ar and ^{3}He are concerned. As such, the maximum R/R_a increases modestly up to 33 but also the present day ^{3}He flux increases. As mentioned above, the higher than expected modern ^{3}He flux of these models could be due to the lack of plate tectonics in these mantle convection models. If this is the case then indeed it may be possible to increase amount of ^{36}Ar the system in order to produce the correct atmospheric $^{40}Ar/^{36}Ar$ whilst having a low ^{3}He flux. Alternatively the condition that $^{3}He/^{36}Ar = 0.2$ may be incorrect. In order to fit the atmospheric $^{40}Ar/^{36}Ar$ constraint without changing the amount of ^{3}He in the system these models require $^{3}He/^{36}Ar = 0.12$.

The $^{40}Ar/^{36}Ar$ distribution of degassing material is similar in each case (Fig. 4.24) to the distribution seen in MORBs (Fig. 4.3), albeit with some more radiogenic compositions. This distribution comes simply from fractionation of K from Ar during melting and degassing, and does not require differential atmospheric contamination. Atmospheric contamination may of course still occur and in fact is necessary in order to reduce the highest $^{40}Ar/^{36}Ar$ values. The radial average $^{40}Ar/^{36}Ar$ of these models (Fig. 4.22) does not match well with predictions of the source reservoir $^{40}Ar/^{36}Ar$ composition for MORBs and OIBs, estimated to be 32,000 and 8,000 respectively (Trieloff et al. 2003). The largest ratios are found in the transition zone and at the base of the mantle.

4.7.3 Combining effects

To summarise findings from above, excess ρ_b has a strong effect on generating chemical stratification. Despite large differences in the radial chemical composition of the mantle for different values of ρ_b, the noble gas distribution of material sampled at the surface is surprisingly similar. This may be because plumes entrain and sample material from throughout the mantle. With increasing excess ρ_b, and therefore increased residence time of enriched basaltic material at the CMB, the mean helium and argon ratios measured in melts become more radiogenic. The median value for noble gas ratios in melts is most radiogenic for excess $\rho_b = 4\%$. This is explained by basaltic material being retained at the CMB for a long period of time, giving it a highly radiogenic signature, but eventually heating up sufficiently to overcome its chemical buoyancy and be resampled by melting. For the same reason the present day flux of ^{3}He is highest for excess $\rho_b = 4\%$. An excess ρ_b of $\sim$6% results in basaltic accumulations that are stable enough to form into large pile-like structures at the base of the mantle. These piles offer a place to sequester ^{40}Ar. A mechanism to generate the range of R/R$_a$ observed in OIBs (R/R$_a$ $= \sim 2 - 50$) is to initialise the mantle with a stratified trace element distribution.

The degassing efficiency of melt strongly affects the present day flux of noble gases, however this effect varies with time depending on how much primordial material is being sampled compared to depleted and enriched material. It is found that for these models, at $\rho_b = 3\%$ a degassing efficiency of $\sim$70% gives the erupted material a R/R$_a$ distribution that has a peak close to the MORB range. In order to meet the constraint for atmospheric ^{40}Ar/^{36}Ar, these models require 1.65× more ^{36}Ar than they were initialised with.

Taking the findings from above I will now present cases where the degassing efficiency is varied for cases which are initialised with a stratified trace element composition and have $\rho_b = 6\%$ so that piles may form from subducted oceanic crust. The mantle also begins with 1.65× more ^{36}Ar than previous cases, making a total of $\sim 6.0 \times 10^{15}$ mols ^{36}Ar in the system. Degassing efficiencies of 70, 80, 90, 100% are presented. As with the previous cases where degassing efficiency has been varied, higher degassing efficiencies have a lower present day ^{3}He degassing rate (Table 4.7). It is notable that the present day degassing rate of ^{3}He in DGASDENS90 is 2184 mol

Table 4.7 Table showing results for cases varying degassing efficiency where each case is initialised with a stratified trace element composition, excess ρ_b is 6% and the initial ^{3}He/^{36}Ar is set to 0.017. Number at end of case name indicates the degassing efficiency of run (eg. DGASDENS70 = 70% degassing efficiency).

Case	**^{3}He Flux (mol/yr)**	**Frac continent degassed**	**Atmosphere ^{40}Ar/^{40}Ar**
DGASDENS70	2663	63%	289.3
DGASDENS80	2433	60%	288.8
DGASDENS90	2184	57%	288.3
DGASDENS100	2052	54%	287.8

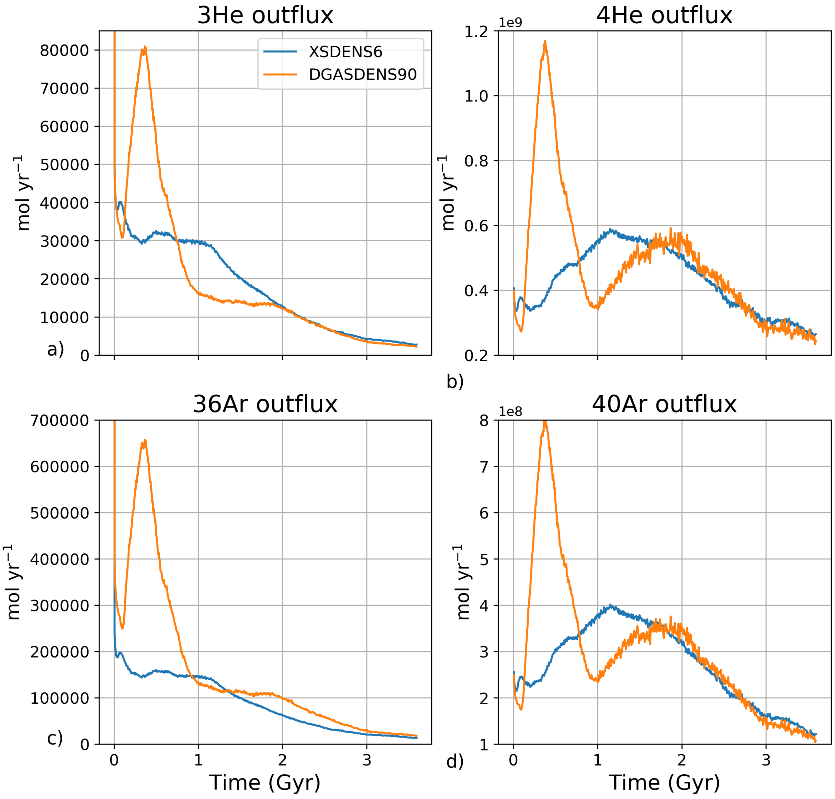

Fig. 4.30 Comparison of surface flux of noble gases a) ^{3}He, b) ^{4}He, c) ^{36}Ar, ^{40}Ar out of the mantle for cases XSDENS6 and DGASDENS90.

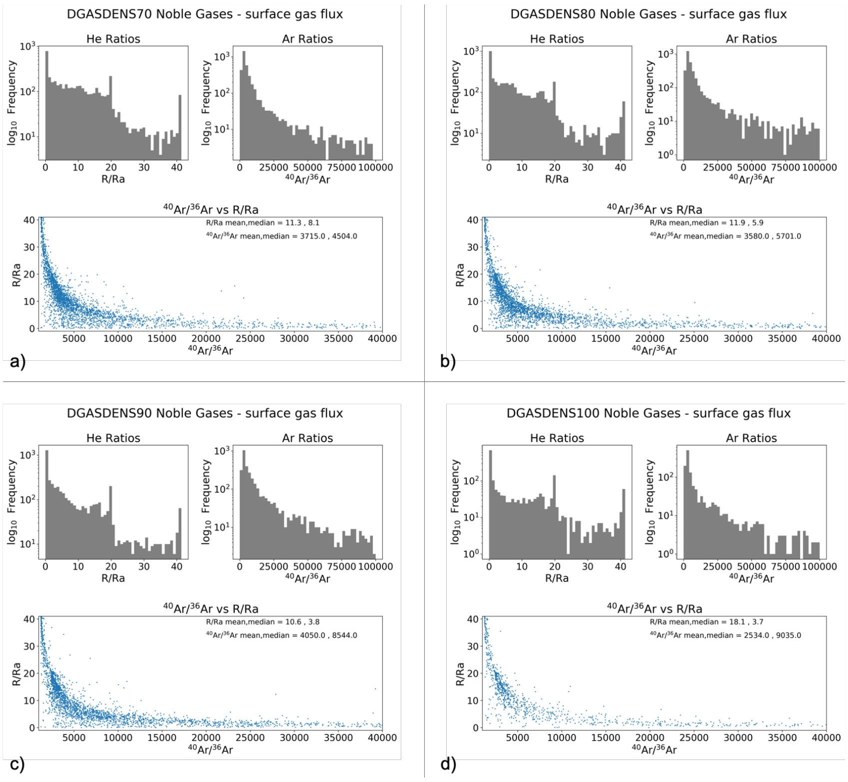

Fig. 4.31 Noble gas composition of degassing material (mixed, n=10) for cases a) DGASDENS70, b) DGASDENS80, c) DGASDENS90, d) DGASDENS100.

yr^{-1}, around 12% less than XSDENS6 which has the same parameters with just a different initial trace element distribution. The high concentration of trace elements towards the base of the mantle causes early degassing rates to be low in case DGASDENS90 compared to XSDENS6 (Fig. 4.30). The high concentration of radiogenic isotopes creates large heating rates in the lower mantle, so this enriched material rapidly rises to the surface. Around 150 Myr after the start of the calculation there begins to be a rapid increase in the flux of all noble gases at the surface as more enriched material begins to be sampled (Fig. 4.30). Around 400 Myr in to the calculation the noble gas flux begins to rapidly decrease as the mantle continues to overturn and sample more depleted material.

In order for the atmosphere to contain 9.9×10^{41} atoms of ^{40}Ar (Allégre et al. 1996), these cases require the continental reservoir to be degassed between $\sim$ 63% in DGASDENS70, and $\sim$ 54% in DGASDENS100 (Table 4.7). Assuming a constant degassing rate this corresponds to between 1.65×10^{8} mol yr^{-1} in DGASDENS70 and 1.43×10^{8} mol yr^{-1} in DGASDENS100. The atmospheric ^{40}Ar/^{36}Ar after continental crust degassing is similar for all degassing rates, varying between 289.3 and 287.8 for cases DGASDENS70 and DGASDENS100 respectively. The similarity between the atmospheric argon ratios for each case indicates that degassing efficiency is not the limiting factor on Earth's atmospheric argon composition. This is due to remelting causing further depletion of the particle's primordial noble gases.

As with the stratified case presented in section 4.7.1, the degassing material has a range of helium ratios ranging from < 1 to ~ 41 R/R$_a$. In general the distribution is positively skewed with peaks at ~ 21 and ~ 41 R/R$_a$. Similar to cases that start with a homogeneous trace element distribution, the median R/R$_a$ decreases with increasing degassing efficiency and the mode ^{40}Ar/^{36}Ar composition is ~ 3000, decreasing exponentially towards higher ratios (Fig. 4.31). Similar to case DGAS100, case DGASDENS100 has the highest mean helium ratio of degassed material with R/R$_a = 18.1$. The mean helium ratio for cases with less efficient degassing is lower than when degassing is complete but consistently has R/R$_a > 10$. This indicates that even with high degrees of melt mixing, the resultant composition would not match the MORB composition of R/R$_a \sim 7-10$.

4.7.4 Processing

For each case presented, $\sim 70\%$ of particles have been processed after 3.6 Gyr of model time. Some numerical studies have advocated much higher degrees of mantle processing of up to 97% (Davies 2002). The potential lack of processing in the presented models is due to the convective vigour being too low. The Rayleigh number for cases presented range from $1.3-2.7\times10^7$, up to 2 orders of magnitude lower than what is expected for convection within Earth, which may have an effective Rayleigh number on the order of 10^8-10^9 (Bunge et al. 1997). The low Rayleigh number leads to fewer mantle overturns than would be expected over the same period of time for Earth's mantle. This is especially true in the deep past, when higher mantle temperatures would have also meant lower mantle viscosities and therefore more vigorous convection. We have seen that in models which are initialised with a stratified trace element distribution, some material with primordial high helium ratios remains unprocessed in the mantle up to the present day. These anomalies may exist at many length scales (Fig. 4.28d) and are sampled by melting up to present day (Fig. 4.27). Increased degrees of mantle processing may eliminate these anomalies and prevent the full range

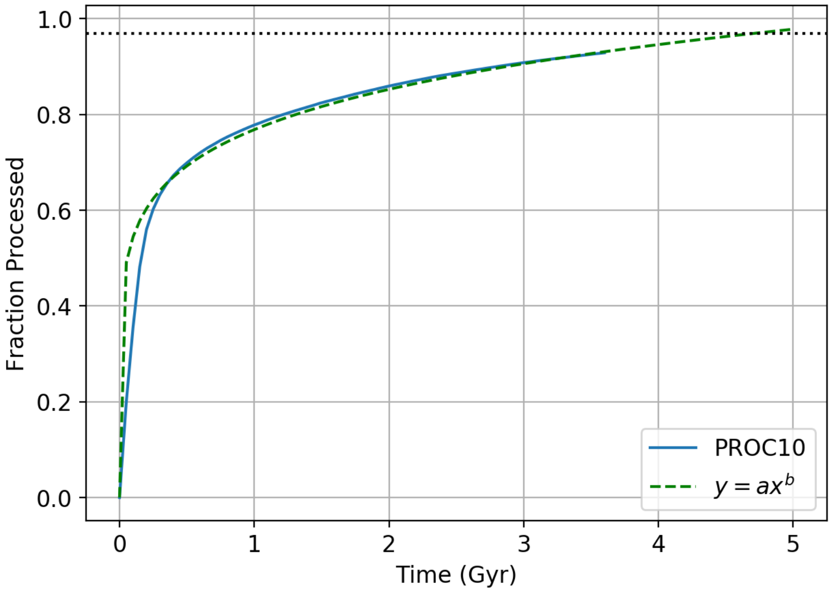

Fig. 4.32 Fraction of particles that have been processed over time for case PROC10 (solid blue line) and curve $y = ax^b$ fitted to the data (dashed green line) where $a = 0.544$ and $b = 0.150$. Note that the time has been re-scaled back to Earth-time (see text or Huang and Davies (2007)). Dotted horizontal line at 97% particles processed.

of helium ratios from being sampled, which could discredit the possibility of a heterogeneous initial mantle from explaining the range of helium ratios measured in OIBs. In order to achieve more mantle overturns and increase the amount of mantle material that is processed I use temporal scaling factors, similar to Huang and Davies (2007). Scaling factors of 2, 5 and 10 are used to increase the length of time that the calculation is run for (3.6 Gyr of model time becomes 7.2 Gyr of model time for a scale factor of 2). The half life of radioactive isotopes is also scaled by the same factor. In each case the mantle is initialised with a stratified trace element concentration, degassing efficiency is set to 90% and excess ρ_b is 6%.

For a scaling factor of 10 the number of particles that have been processed at least once is 93%, which approaches upper estimates obtained from modelling of 97% of the mantle having been processed over 4.5 Gyr (Huang and Davies 2007). An extrapolation of a curve fitted to the fraction of particles that have melted over time (Fig. 4.32) predicts that for a scaling factor of 10, 97% of particles would have been melted if the calculation as run for 4.7 Gyr. This indicates that a slightly higher scaling factor would bring the processing rate of these models in-line with those of Huang and Davies (2007).

Table 4.8 Results for cases with increased processing (PROC—) and case DGASDENS90 for reference. The number in the case name for cases with increased processing is the scaling factor used. Cases with a lower case 'a' at the end of the case name do not have the degassing efficiency scaled and those with a 'b' do. Results shown are present day ^{3}He flux, fraction of continental crust that is degassed to achieve 9.9×10^{41} atoms of ^{40}Ar in the atmosphere, the atmospheric argon ratio after continent degassing, and the fraction of particles that have melted at least once.

Case	**^{3}He Flux (mol/yr)**	**Frac continent degassed**	**Atmosphere ^{40}Ar/^{40}Ar**	**Frac Processed**
DGASDENS90	2185	57%	288	70%
PROC2a	1180	76%	291	74%
PROC2b	1858	97%	294	74%
PROC5a	729	58%	287	85%
PROC5b	1097	55%	292	85%
PROC10a	469	39%	283	93%
PROC10b	804	68%	289	93%

By increasing the degree of processing the remelting rate of material also increases. Continued remelting of particles could leave particles almost entirely depleted of primordial gases. It is possible that this would cause extremely radiogenic compositions to develop. If this is the case then the models would require that the degassing rate is reduced in order to preserve noble gases in the mantle. To investigate the effect of this the scaled cases are run both with a standard degassing rate of 90%, and also with the degassing rate reduced by the scaling factor so that approximately the same amount of degassing occurs as in unscaled cases. Case names and results are listed in Table 4.8. Each case is run with constant heating rate of 5.0×10^{-12} W kg^{-1}.

Scaling the length of time for which the models are run effectively increases the rate of mantle overturns. This more efficient mixing reduces the length scale of trace element anomalies in the mantle (Fig. 4.33a,c,d,f,g,i). High helium ratios in PROC10 are reduced to very short wavelength features, leaving the mantle almost homogenous both laterally and radially. The short wavelength argon anomalies appear to get more radiogenic with increasing degree of processing (Fig. 4.33f,g,i). This is likely due to increased degassing of primordial ^{36}Ar relative to ^{40}Ar, leaving the mantle with an overall more radiogenic argon composition (Fig. 4.34f). The size of bulk composition anomalies is also reduced and accumulations at the CMB have shorter residence times. This prevents lower mantle basalt accumulations

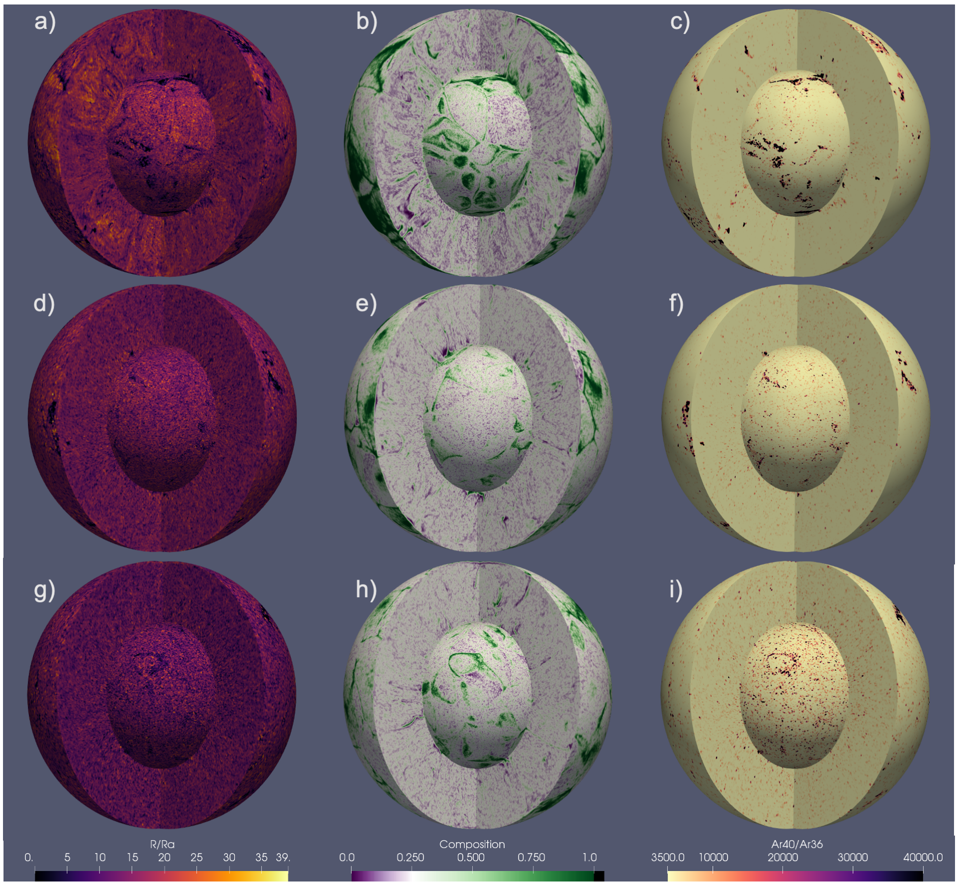

Fig. 4.33 Snapshots of the present day internal mantle structure for cases a-c) PROC2a, d-f) PROC5a, g-i) PROC10a. Coloured by R/R_a (a,d,g), bulk composition (b,e,h) and $^{40}Ar/^{36}Ar$ (c,f,i).

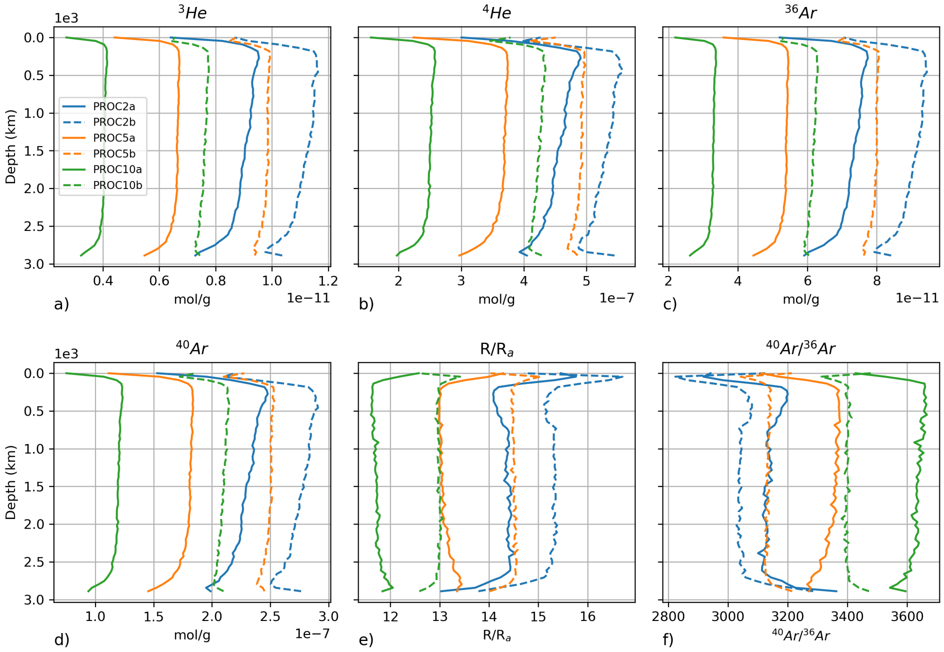

Fig. 4.34 Radial averages of a) ^{3}He, b) ^{4}He, c) ^{36}Ar, d) ^{40}Ar, e) R/R$_a$, f) ^{40}Ar/^{36}Ar for cases with scaling factors of 2 (blue), 5 (orange), 10 (green). Solid line represents cases with unscaled degassing rates, dashed line represents cases where the degassing rates has been scaled.

from persisting until the present day (Fig. 4.33b,e,h). It is possible that increased lower mantle viscosities would help to better retain subducted oceanic crust at the CMB (eg Li et al. (2014)). Although fewer unmelted particles exist in the mantle for higher processing rates, this material is more evenly distributed through the mantle and so particles with a primordial high helium ratio are still sampled by melting (Fig. 4.35). This shows that regardless of how well the mantle is mixed, erupted material is likely to have a primordial component.

With increasing processing the present day ^{3}He flux decreases (Table 4.8). Cases where degassing is not scaled by the scaling factor consistently have lower present day fluxes than cases which do scale the degassing rate, despite having a larger degassing fraction. This is explained by the repeated remelting of particles. The mantle in cases with an un-scaled degassing fraction rapidly becomes depleted in noble gases compared to cases where the degassing efficiency is reduced by the scaling factor (Fig. 4.34). Concentrations of noble gases in the mantle eventually get so low that even efficient degassing does not extract as much gas as inefficient degassing of a mantle with higher noble gas concentrations.

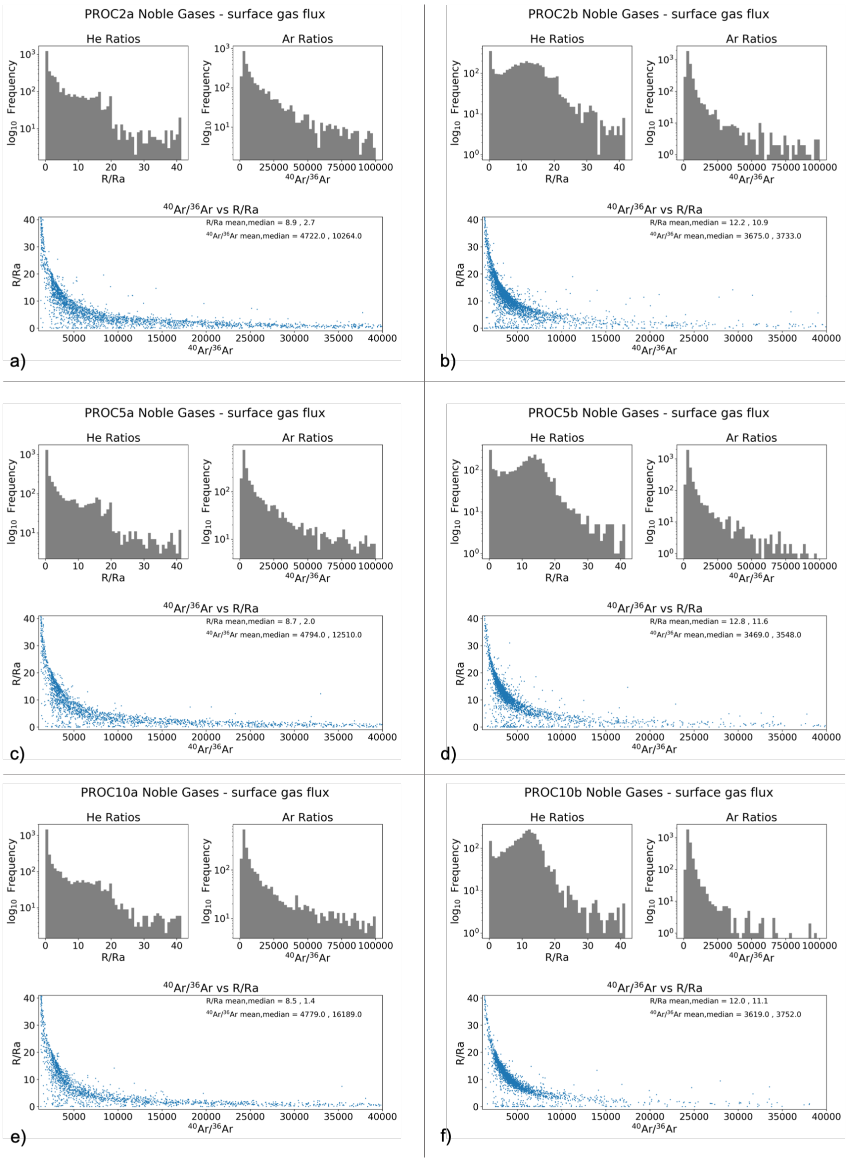

Fig. 4.35 Noble gas composition of degassed material (mixed, n=10) for a) PROC2a, b) PROC2b, c) PROC5a, d) PROC5b, e) PROC10a, f) PROC10b.

At a scaling factor of 2, the present day ^{3}He flux is within error of the estimate given by Craig et al. (1975) of 1070 $\pm$ 270 mol yr^{-1} for case PROC2a (Table 4.8). At a scaling factor of 5 the present day ^{3}He flux in case PROC5a is more similar to the slightly lower estimate of 800 $\pm$ 170 mol yr^{-1} (Tucker et al. 2018), however PROC5b is comparable to the higher estimate. For a scaling factor of 10 case PROC10b is similar to the estimate of Tucker et al. (2018). The lower ^{3}He flux in PROC10a is within error of the estimate of 527 $\pm$ 102 mol yr^{-1} from Bianchi et al. (2010) and similar to an estimate of 450 $\pm$ 50 mol yr^{-1} obtained by ocean circulation modelling (Schlitzer 2016). The models presented here shows that the various processing rates can account for different estimates of the ^{3}He flux from Earth's mantle. Of course only one can be correct for Earth. If the true present day degassing rate and the true degassing efficiency were known, then this would give an indication of the processing rate of Earth's mantle.

Between cases PROC2a, PROC5a, and PROC10a the noble gas compositions of the degassing material are quite similar (Fig. 4.35a,c,e). Each case has a wide range of ^{40}Ar/^{36}Ar, the mode compositions and range of which is higher than what is measured in MORBs (Fig. 4.35a,c,e). This is still compatible with observations because it is thought that argon measurements may be affected by atmospheric contamination which would lower the measured argon ratio due to the low argon ratio of the atmosphere (^{40}Ar/^{36}Ar = 298). The mean helium ratios for these cases decreases from $R/R_a = 8.9$ in PRCO2a to $R/R_a = 8.5$ in PROC10a (Fig. 4.35a,c,e). If significant mixing of melts occurred prior to eruption then these scaled cases would produce a MORB-like helium isotope composition (MORB $R/R_a = \sim 8.0$). This is not the case for the un-scaled models, for example cases XSDENS0 and XSDEN10 have mean helium of ratios of $\sim$ 15 and 10 respectively (Fig. 4.19). At the same time some un-fractionated material is sampled in each case so that the range of measured helium ratios is comparable to that of OIBs. In this respect the scaled cases are similar to the SUMA model (Meibom and Anderson 2003). The SUMA model is quite rigid though in that there is no distinction between the source material of MORBs and OIBs, and they just represent different degrees of homogenisation. In these simulations the distribution of helium ratios in melting material (Fig. 4.35) differs from that of OIBs (Fig. 4.2). The OIB distribution is positively skewed with minima at $R/R_a \sim 2.5$ and $R/R_a \sim 50$ whereas melts in cases without a scaled degassing rate have a maxima at very low helium ratios (Fig. 4.35a,c,e). Melts in cases where the degassing rate is scaled have a helium distribution which is arguably more similar to that of OIBs (Fig. 4.35b,d,f) but still has too much material with highly radiogenic R/R$_a$ (< 5). An explanation for this could be the lack of fine scale mixing, for example in melting zones and areas of high strain rate. As has been mentioned before, in these simulations particles do not exchange material apart from during melting events and rare splitting and merging events. Xie and Tackley (2004b) employ a method by which isotopes are locally redistributed from particles which have experienced a strain over a threshold value. It is possible that if such a method were incorporated into these models that this would preferentially affect the particles with highly radiogenic helium compositions. These particles are likely to have been at the surface in high strain rate environments like divergent zones away from plume heads and at downwellings. This is just speculation though and further investigation with such an implementation is required to find out if this would have an effect.

4.8 Conclusions

The way in which internal heating is implemented in mantle convection models is important, not just to achieve a realistic amount of thermal energy input, but also to ensure that the heating is distributed correctly. The mantle is not homogeneous so areas more enriched in heat producing elements will heat up faster. Accumulations of subducted basaltic material destabilise more rapidly when they experience strong internal heating due to being enriched in heat producing elements compared to when the mantle is heated homogeneously. The residence time of subducted basalt at the CMB increases with increasing excess ρ_b. For low excess ρ_b of 0-4% most of the subducted basalt will overcome its chemical buoyancy by the end of the simulation and become remixed into the mantle. High excess ρ_b of 8-10% causes large basaltic accumulations to develop which cover most of the base of the mantle. The accumulations are slow moving and difficult to break up so do not form structures that resemble those seen in seismic tomography. For intermediate excess ρ_b of 5-6% basalt accumulates at the base of the mantle and is mobile enough to be swept into pile-like structures of spherical harmonic degree 2-7. For these densities the rate at which piles are replenished compared to the rate at which they are eroded qualitatively seems to balance out. Such piles may form at lower excess ρ_b if viscosity has a strong temperature and compositional dependency. Assessing the seismic structure of the piles is beyond the scope of this study, but would be beneficial to determine their similarity to structures like LLSVPs as this would provide further evidence as to whether such observed mantle structures could be generated by subducted oceanic crust.

Longer residence time for basalt at the CMB affects the present day flux of noble gases from the mantle and the noble gas composition of melts. The mean R/R$_a$ and ^{40}Ar/^{36}Ar of melts becomes more radiogenic for higher excess ρ_b, but the median values and the present day flux of ^{3}He are most radiogenic at $\rho_b = 4\%$. This is because the mean noble gas ratio is strongly influenced by particles with high noble gas concentrations, that is unmelted particles and those which have received recycled continental uranium. The median R/R$_a$ and ^{40}Ar/^{36}Ar of the melt is a measure of the relative proportions of melting particles with highly radiogenic or un-radiogenic compositions. Highly radiogenic median compositions occur at excess $\rho_b = 4\%$ because in this case, subducted basalt has a long residence time but does eventually heat up enough that the majority overcomes its chemical buoyancy. Large volumes of subducted basalt can be entrained into mantle upwellings simultaneously, upon reaching the surface these pockets of hot basaltic material cause pulses of high degrees of melting, hence the highly radiogenic noble gas ratios and a high flux of primordial ^{3}He.

Models run with perfect 100% degassing efficiencies produce melts with highly bi-modal helium ratio, displaying peaks at very high and very low R/R$_a$. This demonstrates that at least some noble gas recycling is required in order to generate the helium compositions observed in MORBs and OIBs. Increased degassing efficiency is shown to lead to lower present day degassing rates. This relationship is thought to be strongly dependent on dynamics though so may differ for different excess ρ_b. Melting in mantle convection models is dominated by plumes rather than the ridge volcanism that dominates Earth's volcanism. Consequently the melting process samples material from throughout the mantle that has been entrained into plumes, rather than sampling just the depleted upper mantle. This shortcoming is likely to be a factor in the models presented showing excessive present day fluxes of noble gases and may contribute to the difficulty in reproducing the MORB distribution of R/R$_a$.

Increased degrees of processing can also decrease the present day flux of ^{3}He from the mantle. There are various estimates for what Earth's present day ^{3}He flux is, all of which can be explained by different mantle processing rates. Significantly, the mean helium ratio of melts produced in cases which are scaled to increase the model's processing rate is similar to the helium ratio of measured in MORBs. This indicates that high degrees of mixing, as is thought to occur in the MORB source region, would cause the melt to have helium ratios similar to that of MORBs. At the same time, primordial helium signatures are measured in the melt for all processing rates. This could be interpreted as evidence for the SUMA model, in which MORBs and OIBs are differentiated only by the degree of mixing prior to eruption.

In the standard setup of the models presented here, the most radiogenic helium ratio measured is $R/R_a \sim 20$, much lower than the highest helium ratios that have been measured in terrestrial mantle rocks (Stuart et al. 2003). I have shown that it is possible to produce high helium ratios by initialising the mantle with a heterogeneous (in this case radially stratified) incompatible trace element composition, where the bottom third of the mantle is enriched in incompatible trace elements by a factor of ~ 5 compared to those in the top third (a factor of $4/3$ compared to the mantle average). Initially depleted material evolves high helium ratios of up to $R/R_a \sim 41$ if left un-differentiated and is sampled at present day even, in cases with high processing rates. High R/R_a material exists throughout the mantle and may be entrained into plumes from all depths. This eliminates the requirement for either a deep high ^{3}He primordial reservoir or primordial helium compositions are source from the core.

On the problem of 'missing argon', noble gas concentrations are significantly lower in the upper mantle regions which are influenced by the melting process. Below this, for low to moderate excess ρ_b (≤ 5), the mantle is homogeneous in trace element composition, save the transition zone which filters out some of the subducting oceanic crust. For high excess ρ_b ($> 4\%$) the lower mantle becomes more radiogenic with depth and can act as storage for radiogenic argon. However this is not necessary as radiogenic argon may be stored throughout the mantle due to its 'marbled' composition. The constraint of 9.9×10^{41} atoms of ^{40}Ar in the present day atmosphere is achieved by $\sim 75\%$ of the continental crust being degassed for excess ρ_b 6% and a degassing efficiency of 90%. To achieve an Earth-like atmospheric $^{40}\mathrm{Ar}/^{36}\mathrm{Ar}$

the bulk Earth ^{3}He/^{36}Ar must be reduced from 0.2 to $\sim$0.12, keeping the same initial concentration of ^{3}He.

CHAPTER 5

LOWER MANTLE DENSITY OF BASALT AND PB COMPOSITION OF MELTS

Abstract

In previous chapters it has been shown that the Pb pseudo-isochron measured in mantle-derived rocks and the associated scatter can be reconciled by the action of geochemical processes, namely the preferential recycling of uranium from the continental crust and the preferential removal of Pb from subducted oceanic crust. It was also shown that the greater degrees of segregation of basaltic material to the CMB, caused by increased ρ_b, causes melt to have a more radiogenic noble composition. In this chapter I examine the effect that ρ_b has on both τ_{Pb} and the scatter of Pb isotope ratios. Results show that τ_{Pb} is influenced by the remelting rate of basaltic material, with longer re-melting times causing older pseudo-isochron ages. The measured scatter initially increases with higher ρ_b, then decreases with further increases to ρ_b. This is thought to be correlated to the fraction of recycled basaltic material which constitutes the melt, though there is also a dependency on the re-melting time of recycled basalt.

5.1 Introduction

In chapter 3 the timing of different geochemical processes and the rates which they occur were varied to assess their effect on the lead isotope distribution in melts. When an exaggerated difference in the partition coefficients of U and Pb is used to account for other fractionation processes, the pseudo-isochron age (τ_{Pb}) of melts is much higher than what is measured in MORBs. It is possible to reduce τ_{Pb} of the melt using the method of Xie and Tackley (2004b), where fractionation is limited to after the GOE (2.4 Ga) to account for an increase in uranium solubility due to the rise in atmospheric oxygen. This does not prove to be entirely satisfactory because the scatter in Pb isotope ratios is much lower than what is measured in MORBs. It was shown that a new method of modelling the recycling of continentally derived uranium by transferring U isotope from the continental reservoir to particles in at the surface of the model causes the melt to develop τ_{Pb} and scatter that closely resembles that of MORBs. In order to achieve an Earth-like distribution in $^{208}\mathrm{Pb}/^{204}\mathrm{Pb}$ vs $^{206}\mathrm{Pb}/^{204}\mathrm{Pb}$ space and a high degree of scatter it is also required that Pb is removed from the melt to the continental reservoir. This is likened to the preferential stripping of Pb from the subducted slab by subduction related fluids and subsequent removal from the mantle in arc volcanism (Kelley et al. 2005).

In chapter 4 the effect of excess lower mantle basalt density (ρ_b) on the noble gas composition of the mantle and melting material was investigated. Investigating various values for ρ_b is of interest because the behaviour of basalt in the lower mantle is poorly constrained. Mineral physics suggests that basalt may be 3-4% denser in the lower mantle relative to PREM (Hirose et al. 2005), however some combined geochemical and geodynamic studies have suggested excess densities of up to 10% (Jones et al. 2019). Identifying the range of excess ρ_b in which subducted basalt is retained in the lower mantle for long periods of time is of particular interest to the study of LLSVPs, as it is postulated that they may be composed of recycled oceanic crust (Davies et al. 2015b). For the model parameters used excess ρ_b of 6% (relative to harzburgite) was enough to significantly segregate basalt to the lower mantle whilst allowing it to maintain mobility to be swept into pile-like structures by the pushing and pulling of downwellings and upwellings. For lower values of ρ_b much of the basaltic material which segregates to the

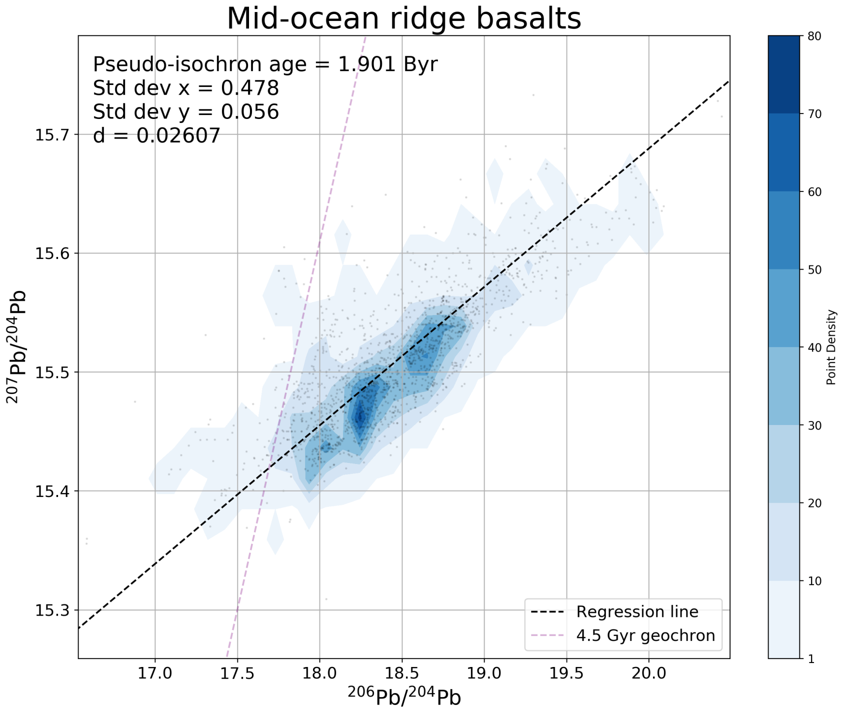

Fig. 5.1 ^{207}Pb/^{204}Pb vs ^{206}Pb/^{204}Pb for a global set of MORBs. Data points are shown in black and contoured in blue for comparison against model data. Black dashed line indicates is the regression line through the data (Pb pseudo-isochron) calculated via and orthogonal distance regression. The dashed purple line is the 4.5 Ga geochron on which the bulk Earth lead isotope ratio should fall. The ’d’ value is the average orthogonal distance from each data point to the regression line, which gives a measure of scatter. Data obtained from PetDB (Lehnert et al., 2000, www.earthchem.org/petdb) on 18th February, 2020, using search criteria, ’Spreading Ridges & Ocean Islands’, ’igneous:volcanic:mafic:basalt’.

CMB will heat up enough to overcome its negative chemical buoyancy and is remixed into the mantle. For higher excess ρ_b segregated material forms a non-continuous layer across the whole CMB. Now that I have established how varying ρ_b affects the formation of lower mantle basaltic accumulations, I will analyse the effect this has on the Pb isotope composition of melt in these models.

5.2 Initialisation

In this chapter I will be using chemical output from the runs XSDENS0-10, which were introduced in chapter 4. For information on model setup and parameters the reader is referred to 4.3. Initial mantle trace element values, decay constants and partition coefficients are listed in Table 5.1. On initialisation trace elements are shared out over all particles in the system, with the amount received by each particles weighted by its mass so that each particle has the same concentration. Each particle is then depleted by 1/3 in each isotope of potassium, uranium, thorium and lead. The depletion is moved to the continental reservoir so this method implicitly assumes rapid continental crust extraction prior to 3.6 Ga. Models are heated by the decay of radioactive isotopes on particles, making the heating regime both temporally and spatially variable. Note that this differs from the majority of the cases in chapter 3, which were heated at a constant rate, however the effect of radiogenic heating regime is also covered in that chapter. Chemical processes are implemented in the models after the best case discussed in chapter 3. Pb isotopes and ^{40}K begin to be removed from the melt into the continental reservoir from 3.0 Ga, which is an estimated time for the onset of plate tectonics (Tang et al. 2016; Laurent et al. 2014; Shirey and Richardson 2011). The removal rate of Pb is equivalent to $\sim 2.5 \times 10^6$ mol ^{204}Pb yr^{-1}. Uranium isotopes are recycled from the continental reservoir to the mantle after the GOE (2.4 Ga). In total 1.1×10^{14} mol of ^{235}U and 4.6×10^{15} mol of ^{238}U are recycled. The density of basaltic material in the lower mantle ($>$ 720km depth) is varied in each case presented, case names and associated excess ρ_b are listed in Table 5.2.

Table 5.1 Initial isotope concentrations, decay constants, and partition coefficients.

Isotope	Initial values	Decay Constant (s^{-1})	D
^{40}K	6.14×10^{-9} mol g^{-1}	5.54×10^{-10}	0.007
^{235}U	2.11×10^{-11} mol g^{-1}	9.85×10^{-10}	0.007
^{238}U	1.47×10^{-10} mol g^{-1}	1.55×10^{-10}	0.008
^{232}Th	3.91×10^{-10} mol g^{-1}	4.95×10^{-11}	0.01
^{204}Pb	1.05×10^{-11} mol g^{-1}	-	0.01
^{206}Pb/^{204}Pb	11.52	-	0.01
^{207}Pb/^{204}Pb	13.52	-	0.01
^{208}Pb/^{204}Pb	31.33	-	0.01

Table 5.2 Table of case names, excess ρ_b in the lower mantle compared to harzburgite (C=0) and the corresponding buoyancy ratio, B.

Case	Excess ρ_b	Max B
XSDENS0	0%	0.0
XSDENS2	2%	0.22
XSDENS4	4%	0.44
XSDENS5	5%	0.55
XSDENS6	6%	0.66
XSDENS8	8%	0.88
XSDENS10	10%	1.11

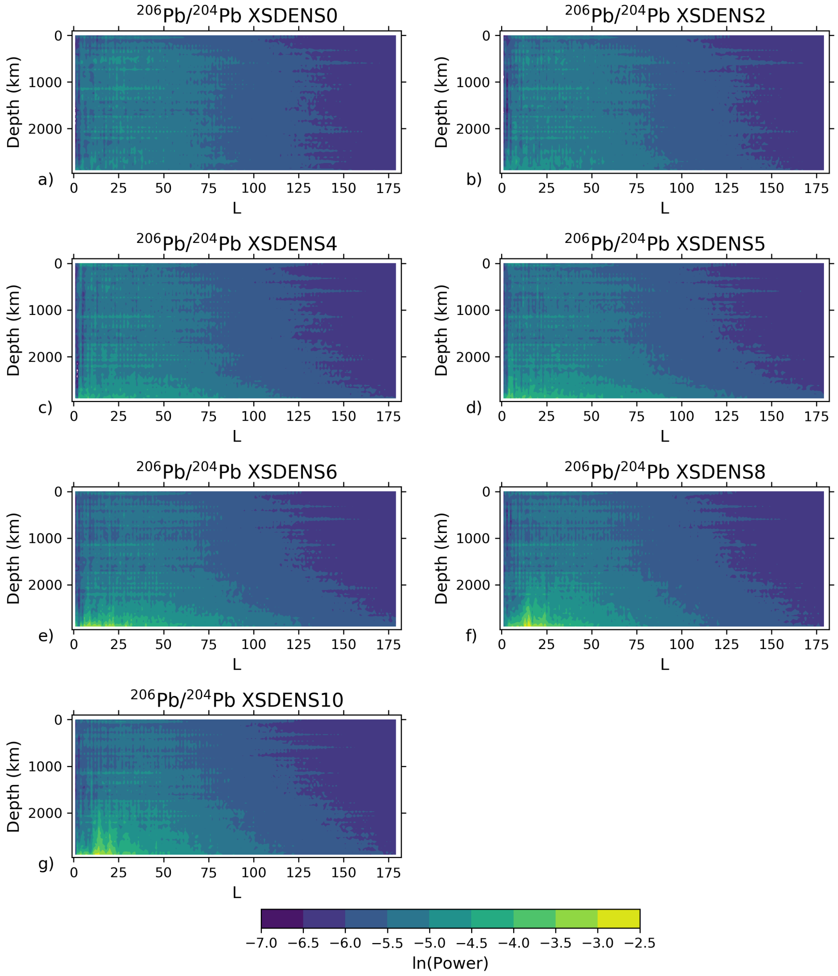

Fig. 5.2 4π normalised power spectrum for the ^{206}Pb/^{204}Pb field for cases a) XSDENS0, b) XSDENS2, c) XSDENS4, d) XSDENS5, e) XSDENS6, f) XSDENS8, g) XSDENS10.

5.3 Results

As the dynamic results for temperature and bulk composition have already been presented and discussed in Chapter 4 these will not be presented here. For cases XSDENS0/2 the is little variation in the power spectrum with depth indicating a well mixed mantle (Fig. 5.2a,b). Cases XSDENS4/5 begin to show a slight increase in power with depth, especially for structures of harmonic degree < 50 (Fig. 5.2c,d). In XSDENS6 high power structures of degree 5-25 dominate the bottom 200 km of the mantle (Fig. 5.2e). In cases XSDENS8/10 the highest power in structure of degree 10-15 (Fig. 5.2f,g).

At high excess ρ_b, Pb is stored in the lower mantle (Fig. 5.3c) in the dense basaltic material for long periods of time. Sequestering of Pb in the

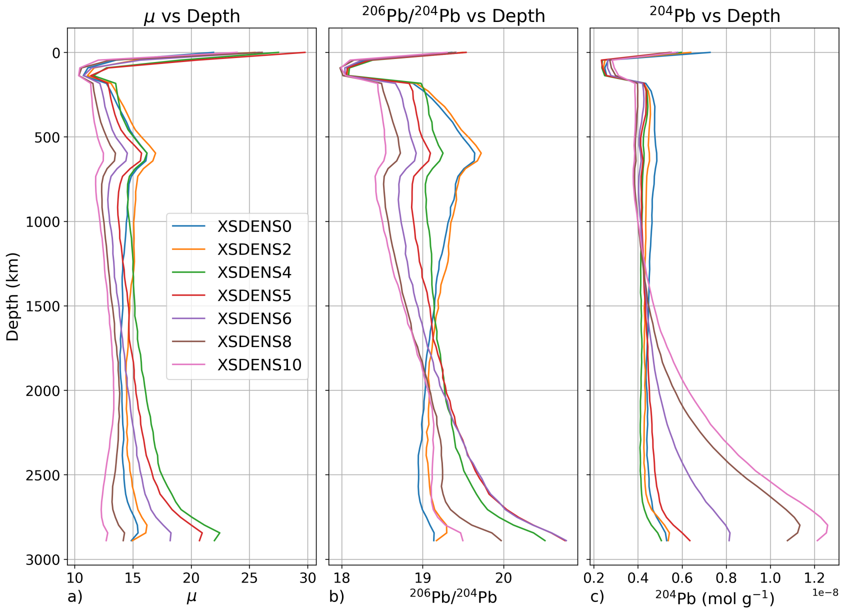

Fig. 5.3 Radial averages for each case of a) μ (^{238}U/^{204}Pb), b) ^{206}Pb/^{204}Pb, c) ^{204}Pb concentration.

lower mantle makes less available in the upper mantle to be removed to the continental crust during melting. Over time this amounts to XSDENS10 losing around 20-25% less Pb from the mantle than XSDENS0 (Fig. 5.4). Cases XSDENS2,4,5 each see more Pb removal from the mantle over time compared to XSDENS0 (Fig. 5.4). Lead ratios through the mantle are also strongly affected by ρ_b. Cases XSDENS0 and XSDENS2 have similar ratios at all depths. In the top $\sim$ 1500 km the average ^{206}Pb/^{204}Pb is lower for high excess ρ_b, while in the lowermost mantle XSDENS5 and XSDENS6 have the most radiogenic Pb ratios (Fig. 5.3b). The radial average of μ shows XSDENS10 and 8 to have the lowest values throughout the whole mantle (Fig. 5.3a). In the lower mantle XSDENS4 has the highest μ, followed by XSDENS5 and XSDENS6.

Figure 5.5 shows Pb isotopes ratios of the melt of each case. Although each distribution has a similar shape, there is variation in τ_{Pb} and the scatter. Cases XSDNES0-4 have similar τ_{Pb}, but this then generally increases between XSDENS4 and XSDENS10, from 2.0 Gyr to 2.3 Gyr. The scatter does not vary with ρ_b in the same way that τ_{Pb} does. Scatter increases between XSDENS0 and XSDENS5 from $\sim$0.01 to 0.019, then decreases with increasing excess ρ_b to $\sim$0.007 in XSDENS10.

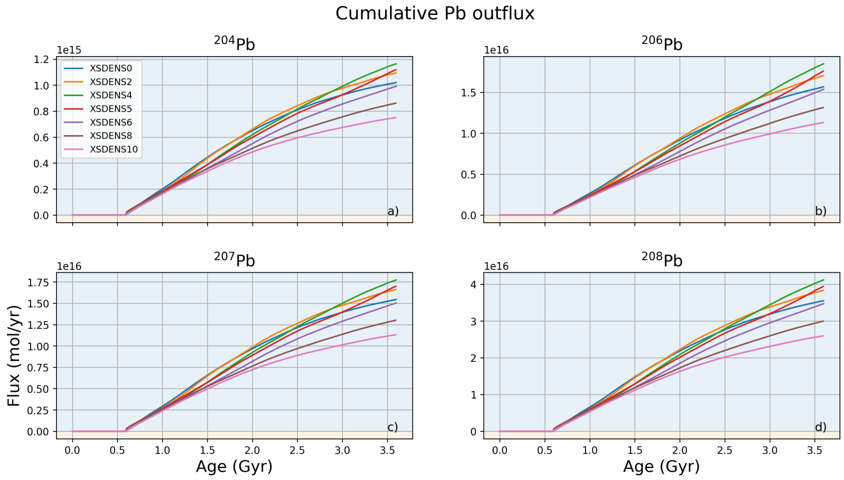

Fig. 5.4 Cumulative flux of Pb a) ^{204}Pb, b) ^{206}Pb, c) ^{207}Pb, d) ^{208}Pb, out of the mantle to the continental reservoir for each case.

Figure 5.6 shows histograms of the melting age (time of last melting) for all particles in the system. The peak at zero Gyr in each case is due 28-25% of particles which have not undergone a melting event. Distributions in XSDENS0-4 have a similar shape, with a peak at $\sim$ 2.6 Gyr. From XSDENS5-10 melting ages shift towards older values, becoming positively skewed. The fraction of particles which have melted also decreases between these cases, from $\sim$75% in XSDENS5 to $\sim$72% in XSDENS10.

5.4 Discussion of results

The fraction of particles which have melted over the course of the calculation is similar for cases XSDENS0-4 but then decreases from XSDENS5 to XSDEN10 (Fig. 5.6). The cause of this was discussed in chapter 4 but I will re-iterate the point here. Surface heat fluxes are similar over time for cases XSDENS0-4 (Fig. 5.7a). This shows that although the dynamics are varying slightly with increasing excess ρ_b, the amount of melting will be fairly similar in each case. Case XSDENS5 has a low surface heat flux compared to cases XSDENS0-4 until $\sim$2.8 Gyr (Fig. 5.7a). This point in time is when dense basaltic material, which had segregated into the lower mantle, has heated up sufficiently to overcome its chemical buoyancy and has been entrained in significant quantities into upwellings. As these large volumes of hot material approach the surface the heat flux increases and there is significant melting. For cases XSDENS6-10 higher excess ρ_b increases the residency

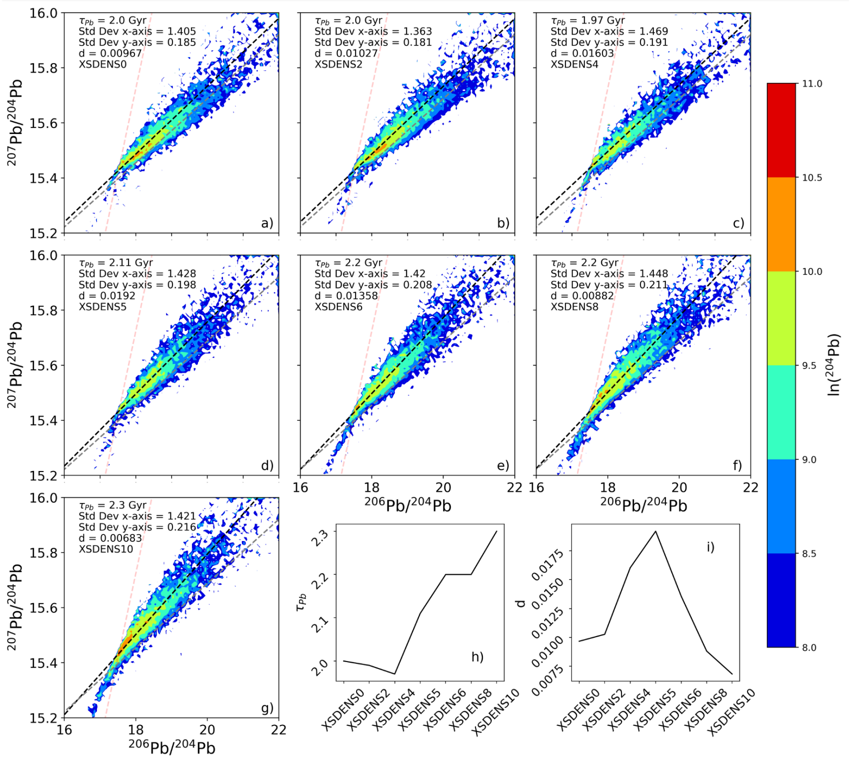

Fig. 5.5 a-g) Contoured distribution of Pb isotope ratios of the melt for cases XSDENS0-XSDENS10, coloured by ^{204}Pb abundance. Red dashed line indicates the 4.5 Gyr geochron, grey dashed line is the pseudo-isochron for data from a global set of MORBs (τ_{Pb} = 1.9 Gyr). Black dashed line is the pseudo-isochron for the model data calculated from an orthogonal distance regression. h) Plot of τ_{Pb} against case, i) 'd' against case.

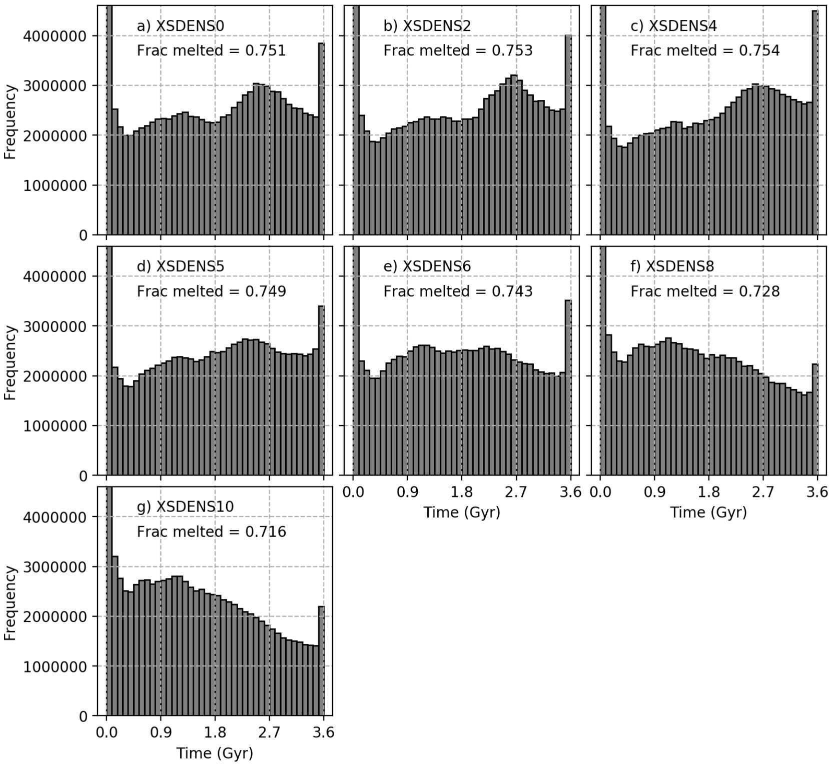

Fig. 5.6 Histograms of melting age of all particles in the system for cases a) XSDENS0, b) XSDENS2, c) XSDENS4, d) XSDENS5, e) XSDENS6, f) XSDENS8, g) XSDENS10. Melting age of 3.6 Gyr has melted most recently, melting age of 0 has not yet melted. Frequency clipped to focus on distribution of particles that have melted. Each histogram is also labelled with the fraction of particles which have undergone at least one melting event by the end of the calculation.

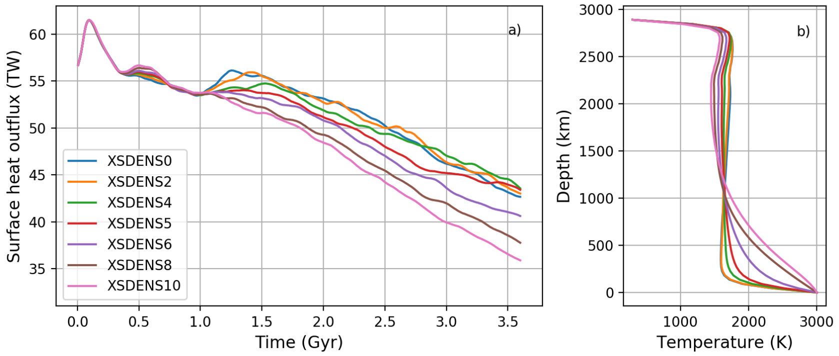

Fig. 5.7 a) Surface heat flux (TW) over model time for each case. b) Radial average temperature for each case.

time of basalt in deep accumulations, causing the lower mantle to heat up (Fig. 5.7b) and reducing the surface heat flux. It is this reduction of transfer of hot, enriched material from the lower mantle to the upper mantle which causes the decrease in the melting between XSDENS5 and XSDENS10.

Cases XSDENS0,2,4 have very similar τ_{Pb} but increasingly large scatter as excess ρ_b increases. The cumulative flux of Pb out of the mantle increases from XSDENS0-4. As more of both radiogenic and primordial Pb isotopes have been removed in XSDENS4 and XSDNES2 compared to XSDENS0, it is tempting to conclude that more particles have been processed in these cases. In fact, for cases XSDENS0-5 $\sim$ 75% of particles have been processed by the end of the calculation (Fig. 5.6a-d). The extra Pb removed from the mantle in cases XSDENS2/4 compared to XSDENS0 must come from remelting particles. The cumulative flux of Pb from the mantle is initially lower in XSDNES2 and XSDNES4 than XSDENS0, overtaking after around 1.75 Gyr and 2.4 Gyr respectively (Fig. 5.4). A possible mechanism for extra Pb removal is that basaltic particles with an excess density are more likely to reach the CMB than those which are neutrally buoyant, as in XSDENS0. At the CMB the particles are entrained into upwellings and rise up through the mantle until they can melt again. The higher scatter in cases XSDENS2/4 compared to XSDENS0 may be due to slightly lower ^{204}Pb concentrations (Fig. 5.3c) allowing radiogenic Pb ratios to develop more rapidly. More radiogenic Pb ratios could also be achieved with longer re-melting times, which might be expected for higher excess ρ_b. The similarity in the power spectrum and (Fig. 5.2a,b) and radially averaged isotope ratios (Fig. 5.3a,b) shows that an excess ρ_b of 2% compared to 0% has little effect on the dynamics. Also similarity in the distribution of melting ages for cases XSDENS0/2

(Fig. 5.6a,b) suggests that excess ρ_b of 2% has little effect on the remelting time of particles. In XSDENS4 the peak of particles with a melting age of 2.6 Gyr is more subdued, and there are also fewer particles with melting ages < 1.8 Gyr than in cases XSDENS0/2. The number of particles with a melting age ~ 3.6 Gyr is $\sim 10\%$ higher in XSDENS4 than in XSDENS2. This shows there has been more melting recently in XSDENS4 compared to XSDENS2. One potential reason for this that it is more difficult for basalt to overcome its chemical buoyancy at high excess ρ_b. The recent pulse of melting in XSDENS4 may be associated with a large amount of basalt being entrained into upwellings at once, having spent enough time in the lower mantle to heat up sufficiently. Visualisations show that basaltic accumulations remain in the lower mantle for longer periods of time in XSDENS4 compared to XSDENS0/2 (see Appendix C or Fig. 4.11 in Chapter 4).

XSDENS5 has the largest scatter of all cases and $\tau_{\mathrm{Pb}} \sim 0.1 Gyr$ older than XSDENS0-4. The cumulative flux of Pb from the mantle is higher in XSDENS5 than XSDENS0 but lower than XSDENS4 and there are higher concentrations of ^{204}Pb in the lower mantle. This implies that basaltic particles which are sampled in the melt on average have longer residency times in XSDENS5 than XSDENS4 and that this influences the scatter. There are notably fewer particles with a melting ages between 2.4 Gyr and 3.6 Gyr in XSDENS5 compared to cases XSDENS0-4 (Fig. 5.6d). This suggests less melting in last ~ 1 Gyr compared to XSDENS0-4. More particles exist with melting ages between $\sim$0.9 Gyr and 2.4 Gyr in XSDENS5 compared to XSDNES0-4, again suggesting lower remelting rates. The animated visualisations show that subducted material begins to leave the lower mantle in large volumes later on in the calculation, within the last ~ 600 Myr. Much of this material may not have yet re-entered melting zones, hence the low number of particles with very young melting ages.

In XSDENS6 much fewer particles have melting ages > 2.5 Gyr and there are more particles with melting ages of $0.5 - 2.5$ Gyr than cases XSDENS0-5 (Fig. 5.6e). This shows that re-melting is less frequent in case XSDENS6, and explains why less Pb is removed from the mantle to the continental crust in case XSDENS6 than case XSDENS0. The distribution of melting ages shifts further towards older values in cases XSDENS8 and XSDENS10 (Fig. 5.6f,g). As excess ρ_b increases from 6% - 10% the scatter decreases (Fig. 5.5i) while τ_{Pb} increases (Fig. 5.5h). This disconnect between τ_{Pb} and the scatter shows that

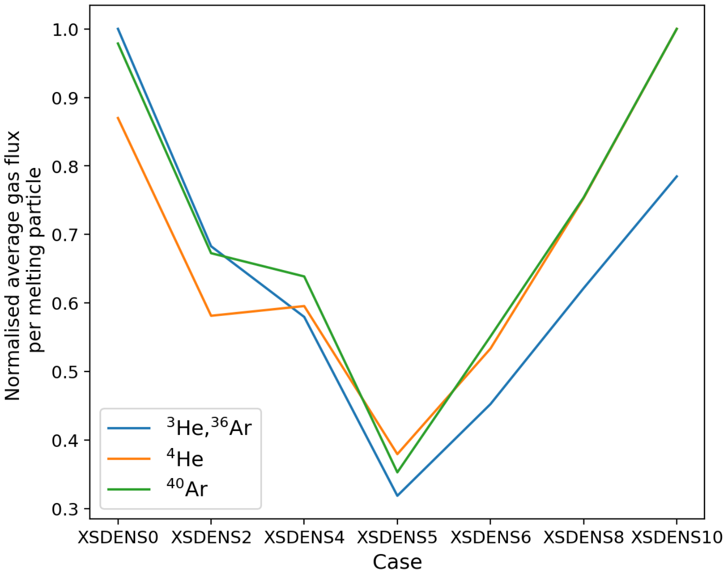

Fig. 5.8 Average amount of each noble gas degassed per melting particle at 3.6 Gyr for cases XSDENS0 - XSDENS10, normalised to the highest mean degassing flux. Note that due to normalisation ^{3}He and ^{36}Ar have identical curves.

each of these measurements is sensitive to the dynamic effects of changing excess ρ_b in different ways.

The variation of 'd' with excess ρ_b is non-linear. The peak scatter is measured in the melts of case XSDENS5, with 'd' decreasing towards both higher and lower excess ρ_b (Fig. 5.5i). This is similar to how the present day surface heat flux varies with excess ρ_b (Fig. 5.7a). The relationship between ρ_b and scatter is also reminiscent of how the number of particles with a melting age of 3.6 Gyr varies with ρ_b (Fig. 5.6). There is not a perfect correlation though, as case XSDENS4 has largest amount of recent melting (Fig. 5.6c), but a lower scatter than XSDENS5. From this it seems likely that the scatter measured in melts is strongly influenced by the fraction of the melt which comprises recycled basaltic material, but is also influenced to some degree by the average re-melting time of material. Unfortunately output from the models does not directly measure the fraction of material that is comprises recycled basaltic material. It is possible instead to use a proxy for example the mean amount of gas being degassed per melting particle. It would be expected that for an increasing fraction of basaltic particles being sampled by the melt, the mean amount of gas flux per melting particle would decrease due to the particles having already been degassed at least once. Figure 5.8

shows the mean gas flux per melting particle is lowest for case XSDENS5 and increases towards cases with higher and lower ρ_b, a strong anti-correlation against 'd'. The peak in 'd' at excess $\rho_b = 5\%$ is due to large volumes of recycled basaltic material being re-sampled simultaneously as they have recently heated up sufficiently to overcome their chemical buoyancy. Cases with a lower excess ρ_b have less scatter because basaltic accumulations have been efficiently remixed into the mantle (see Appendix C) and on average has shorter re-melting times so develops a less radiogenic Pb signature between melt events. On the other hand, cases with excess $\rho_b > 5$ retain much of their basaltic accumulations at the CMB at 3.6 Gyr, so less is available near the surface to be re-sampled. If these models were run for longer it would be expected that the scatter measured in melts of XSDENS6 would become greater than those of XSDENS5 as segregated basalt is removed from the lower mantle.

The pseudo-isochron age, τ_{Pb}, increases approximately linearly with increasing excess ρ_b. This could be interpreted as meaning that the mean residency time of the basaltic material which is being resampled is what most strongly influences τ_{Pb}. Indeed cases XSDENS0-4 all have similar τ_{Pb} and their particle melting age distributions are also similar (Fig. 5.6a-c). Additionally, in snapshots of the thermal structure at 3.6 Gyr (Chapter 4 Fig. 4.8) the locations of plumes and downwellings are well correlated for these cases, showing that the dynamics are similar. From XSDENS5-10, increasing fewer particles with melting ages > 2.4 Gyr (Fig. 5.6d-g) indicates lower average remelting rates and therefore longer residency times, hence increasingly old τ_{Pb}. This agrees with results from Christensen and Hofmann (1994), where a case with significant segregation of recycled basaltic material to the CMB results in an older pseudo-isochron age than the case where such segregation does not occur.

As discussed in 4.7.1, if LLSVPs are to be made from the accumulation of subducted oceanic lithosphere, then these simulations require excess ρ_b of $\sim 6\%$. At this density, basaltic material segregates to the CMB and remains mobile enough to be swept into piles by the pushing and pulling of thermal downwellings and upwellings. The results of these numerical experiments show that if LLSVPs were to form in such a way (eg. Davies et al. (2015b)), this would likely result in higher τ_{Pb} of oceanic basalts than if subducted oceanic lithosphere were efficiently stirred back into the mantle and the formation of LLSVPs were controlled by some other mechanism,

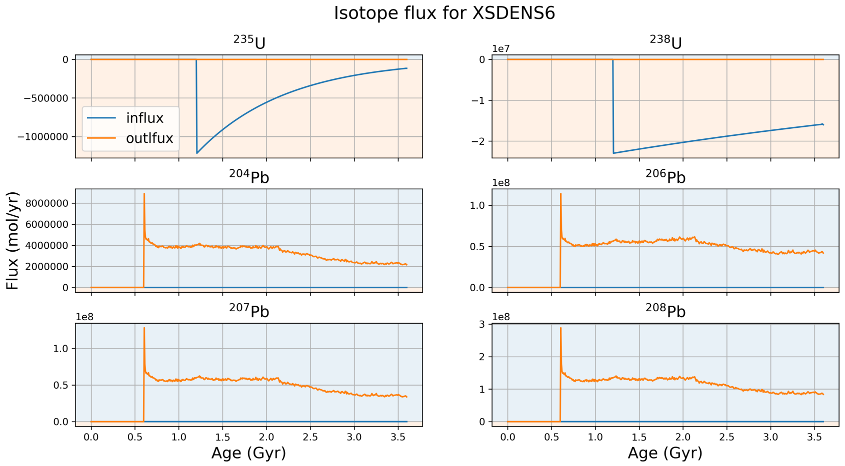

Fig. 5.9 Flux of uranium isotopes into the mantle and lead isotopes out of the mantle over time for case XSDENS6.

for example the cooling of basal magma ocean (Zhang et al. 2016; Ballmer et al. 2017). Assuming that LLSVPs are formed from the accumulation of subducted oceanic basalts, then case XSDENS6 would be the favoured case for modelling this. The Pb pseudo-isochron age calculated for this case is 2.2 Gyr, higher than the 1.9 Gyr that is calculated for MORBs. One reason for this discrepancy could be that the geochemical model that I have used is incorrect. In these models the amount of uranium recycling is controlled by reserving a fraction of the uranium budget of the continental reservoir that is available at the time of the GOE. As this reserved amount of uranium decays over time, so too does the recycled uranium flux (Fig. 5.9). It could be argued that it would be more realistic for the uranium flux to slowly increase from the GOE given that there would be a lag associated with the time it takes for the atmosphere to become more oxygen rich and the time it takes to oxidise and erode uranium from continental rocks. A gradual increase in the uranium flux would lead to less radiogenic Pb ratios developing and so may reduce τ_{Pb} that is measured in the present day melts.

Another reason for the high τ_{Pb} compared to MORBs could be due to the style of melting that occurs in these models. Most melting on Earth occurs at mic-ocean ridges which are not present in these models. Instead all of the melting is concentrated at the top of mantle plumes, which may sample the mantle in a similar way to hot spot volcanism. On Earth, OIBs have a more radiogenic Pb composition that MORBs (Fig. 5.10) which indicates that the two may be sampling different sources. It is thought that ridge volcanism

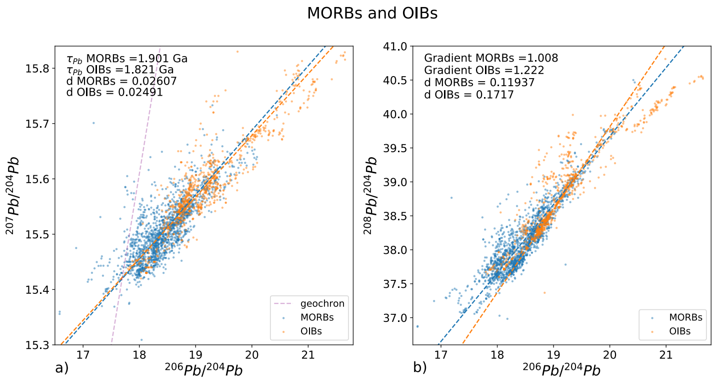

Fig. 5.10 Pb isotope distribution of MORBs (blue) and OIBs (orange) in a) ^{207}Pb/^{204}Pb vs ^{206}Pb/^{204}Pb space and b) ^{208}Pb/^{204}Pb vs ^{206}Pb/^{204}Pb space.

samples a highly depleted upper mantle (Lupton 1983; Kellogg et al. 2002), while OIBs are thought to sample material from the deepest regions of the mantle (Hanan and Graham 1996). To understand the effect of different styles of melting it would be required that the geochemical models used in these simulations are combined with mantle circulation models, using dynamic plate reconstructions as a surface boundary condition, or more advanced models with self consistent ridge volcanism. Such models could also be used to attempt to understand the slight variations in τ_{Pb} that are observed in different ocean basins.

5.5 Conclusions

By increasing excess ρ_b the degree of segregation of basalt to the CMB is also increased as is the residency time of basalt in the lower mantle. The results of the numerical experiments presented here show that, for the class of models investigated, the variation of τ_{Pb} and scatter with changing excess ρ_b do not directly correlate.

The degree of scatter initially increases with increasing degree of segregation up to $\rho_b = 5\%$, after which the scatter decreases with increasing segregation. This is thought to be correlated to the fraction of recycled basaltic material that makes up the melt, but also dependent on the average re-melting time of recycled basalt. As excess ρ_b increases from 0%, basalt more readily segregates to the lower most mantle. Here it can be entrained into mantle upwellings, brought to the surface and re-sampled, rather than being repeatedly mixed around in the mid-mantle. Increasing excess ρ_b

also requires material to heat up more in order to overcome its negative chemical buoyancy. For the models presented here with excess $\rho_b \geq 5\%$, substantial basaltic accumulations persist at the CMB right up to the present day, therefore preventing this material from being sampled by melting at the surface.

The melts in models with excess $\rho_b = 0 - 4\%$ have a similar τ_{Pb} and also have a similar distribution of melting ages well as fraction of mantle processed. This suggests that averaged over time, the melting history of these cases is comparable. With further increases in excess ρ_b, the τ_{Pb} of melts increases while melting ages shift to older values, showing a positive relationship between τ_{Pb} and re-melting rates.

CHAPTER 6

SUMMARY OF RESEARCH, LIMITATIONS AND FUTURE WORK

The aim of this thesis has been to use geochemical constraints, namely lead, helium and argon isotopes, to gain understanding of the processes that influence their distribution. Doing so may also provide clarity to some fundamental questions on Earth's evolution and history.

6.1 Research Summary

6.1.1 Influences on the lead composition of mantle-derived rocks

Chapter 3 focussed on the determining what processes affect the distribution of Pb in mantle derived rocks. This work built on previous studies which were limited by their approximation of multiple geochemical processes into exaggerated differences in partition coefficients between Pb and radioactive U and Th. Additionally the work presented in this chapter is the first to investigate processes affecting Pb isotopes in 3D spherical geometry. Importantly, the work presented in Chapter 3 does not just focus on constraining the influences on the Pb pseudo-isochron, but also on the scatter observed in the data.

The results of Xie and Tackley (2004b) which show that limiting fractionation of U and Pb until after 2.4 Ga (after the GOE) can produce a pseudo-isochron age (τ_{Pb}) similar to that of MORBs, were replicated for simulations in 3D geometry. This implementation proves unsatisfactory as it does not produce enough scatter in the Pb ratios to account for that measured in oceanic basalts. In fact all cases in which fractionation is controlled solely by differences in partition coefficients cannot produce Earth-like scatter. A new method was introduced for modelling the effect of the onset of U recycling to the mantle associated with the rise in atmospheric oxygen after the GOE. This involves moving uranium isotopes from the continental reservoir to the particles at the surface of the model. The new method produces a MORB-like τ_{Pb} and leads to a higher degree of scatter than previous methods, however does not produce an Earth like Pb isotope distribution in $^{208}\mathrm{Pb}/^{204}\mathrm{Pb}$ vs $^{206}\mathrm{Pb}/^{204}\mathrm{Pb}$ space. It is found that incorporating Pb removal from the mantle, motivated by preferential stripping of Pb isotopes from subducted slabs (Kelley et al. 2005), produces a more Earth-like Pb isotope distribution in $^{208}\mathrm{Pb}/^{204}\mathrm{Pb}$ vs $^{206}\mathrm{Pb}/^{204}\mathrm{Pb}$ space and also increases the degree of scatter in Pb ratios. In the best case, Pb is removed from the mantle at a rate of 2.5×10^6 mol $^{204}\mathrm{Pb}$ yr^{-1} and $1.1{\times}10^{14}$ mol of $^{235}\mathrm{U}$ and $4.6{\times}10^{15}$ mol of $^{238}\mathrm{U}$ are recycled from the continental reservoir to the mantle from 2.4 Ga. Results suggest that the rate of continental U recycling to the mantle is likely to have gradually increased rather than suddenly commenced, however further tests would be required to investigate this. The new implementation of U recycling and Pb removal leads to some particles having extremely radiogenic Pb compositions. Mixing an important process to model as this helps to eliminate extremely radiogenic compositions which are not observed in mantle derived rocks.

6.1.2 Influences on the noble gas composition of the mantle and atmosphere

Noble gases impose strong constraints on the composition of mantle derived rocks and mantle degassing. The main aim of chapter 4 was to determine to what degree these constraints are influenced by the degassing efficiency of the mantle and the long term storage of subducted basalt at the CMB, controlled by the excess density of basalt in the lower mantle relative to harzburgite (ρ_b). A parameter space was investigated in which both the degassing efficiency and ρ_b were varied. The effect of the heating mode on mantle dynamics was also touched on. When the distribution of internal heating is dependent on the distribution of radioactive isotopes in the mantle it was shown that basaltic accumulations destabilise more rapidly due to them being enriched in heat producing elements. This potentially has implications for the formation and stability of LLSVPs, which may be formed from the accumulation of subducted basalt (Davies et al. 2015a).

Higher ρ_b increases the residency time of basalt in the lower mantle, which affects both the present day flux of noble gases and the noble gas composition of melts. The weighted mean noble gas ratios of ^{3}He/^{4}He and ^{40}Ar/^{36}Ar in the melt become more radiogenic with increasing ρ_b due to longer residency times allowing for more radiogenic ingrowth. Present day ^{3}He flux is highest for the case where $\rho_b = 4\%$. This is due to the basaltic material having a long residency time in the lower mantle where it heats up, eventually to the point where it can overcome its chemical buoyancy and be entrained into upwellings in large volumes, causing pulses of high degrees of melting at the surface. Estimates of Earth's present day mantle ^{3}He flux are much lower than that of the cases run with variable ρ_b, however can be reduced with higher degassing rates. This is because most of the present day melt comprises material which has already been degassed multiple times. The melt at present day therefore has much lower noble gas concentrations in cases with high degassing efficiencies compared to cases with low degassing efficiencies. Degassing efficiency strongly affects the distribution of noble gas ratios in the melts, with the median value becoming significantly more radiogenic for increasing degassing efficiencies. The mean noble gas composition, however, is less sensitive to changing degassing efficiencies. Complete degassing of melts leads to a strong bimodal distribution of helium ratios, with most particles having either very high or very low R/R$_a$ and the weighted mean helium ratio being close to the primordial value. The implication of this is that incomplete degassing and recycling of helium is important in producing the helium ratios measured in mantle-derived rocks.

Simulations initialised with a homogeneous distribution of trace elements across all particles cannot produce helium ratios high enough to account for the full range that is observed in OIBs. Picritic basalts from Baffin island have been recored with helium ratios of up to R/R$_a$ = 50 (Stuart et al. 2003), whereas primordial material in these simulations had helium ratios of R/R$_a$ = 20. It was shown that if the simulations are initialised with a stratified trace element distribution, where particles in the bottom third of the mantle have a concentration of incompatible trace elements 5× that of particles in the top third of the mantle then primordial material at the end of the calculation will have helium ratios of up to R/R$_a$ = 41. Motivation for such an initial condition comes from the possibility of heterogenous accretion (Rubie et al. 2011) or heterogeneous depletion following giant impacts. This provides a possible explanation for the range of helium ratios measured in OIBs without requiring input of primordial helium from the core (Porcelli and Halliday 2001) or a deep reservoir of high ^{3}He primordial material.

The effect of higher mantle processing rates was explored by using a temporal scaling factor to increase the number of mantle overturns. The present day ^{3}He flux decreases with increased mantle processing rates, for similar reasons as to why it decreases with increasing degassing efficiency. Estimates for the present day ^{3}He flux range between 450 ± 50 mol yr^{-1} (Schlitzer 2016) and 1070 ± 270 mol yr^{-1} (Craig et al. 1975), all of which can be accounted for by various degrees of mantle processing. With increasing mantle processing rates the weighted mean helium ratio of melts approaches that of MORBs (~ 8 R/R$_a$). Additionally, when initialised with a stratified heterogeneous trace element distribution, as described above, simulations with higher processing rates still sample primordial material with the highest helium ratios at present day. The primordial material is not restricted to the the deepest mantle, as has been speculated (Anderson 1998b), but distributed throughout. This could be taken as evidence for a SUMA-like model (Meibom and Anderson 2003), in which OIBs and MORBs are distinguished only by the degree of mixing prior to eruption.

6.1.3 Influences on the noble gas composition of the mantle and atmosphere

Chapter 5 revisited the problem of the Pb pseudo-isochron, this time investigating the dynamic effect of varying ρ_b and the influence this has on τ_{Pb} and scatter. The models were set up identically to those in chapter 4 which looked at the effect of ρ_b on noble gases. Results show that there is not a direct correlation between ρ_b, τ_{Pb}, or the measured scatter. The scatter of Pb isotope ratios in $^{207}\mathrm{Pb}/^{204}\mathrm{Pb}$ vs $^{206}\mathrm{Pb}/^{204}\mathrm{Pb}$ space increases from $\rho_b = 0 - 5\%$, then decreases with further increasing ρ_b. The scatter in $^{207}\mathrm{Pb}/^{204}\mathrm{Pb}$ vs $^{206}\mathrm{Pb}/^{204}\mathrm{Pb}$ space appears to correlate to the fraction of melt that comprises recycled basalt but to some extent scatter is also be affected by the re-melting time for enriched basaltic material.

Cases with $\rho_b = 0 - 4\%$ have a similar τ_{Pb} which then increases for $\rho_b = 5 - 10\%$. The distribution of particle melting ages is similar in cases with $\rho_b = 0 - 4\%$ and shifts to older ages with further increasing ρ_b. Because of this it was concluded that average remelting rates have a strong influence on τ_{Pb}, with longer re-melting times of basaltic material leading to older pseudo-isochron ages.

6.2 Limitations

One of the biggest limitations presented by modelling in 3D spherical geometry is the trade-off between computing resources, time and resolution. As explained in 2.3.3, for a given TERRA setup, a 2× increase in resolution may require up to 4× as much computing resources in order to run. Additionally the increase in resolution will cause the calculation to take 16× longer to run due to the Courant-Friedrichs-Lewy condition which prevents flow speeds from exceeding more than half a grid spacing in a single time step in order to maintain stability. Due to these restrictions and the number of simulations that were required for this body of work, a resolution of $mt = 128$ was chosen, equivalent to an average lateral resolution of ~ 60 km at the surface , 32.7 km at the CMB and an average radial resolution of 45.2 km as this was found to provide a good balance of resolution and simulation time. Some degree of finer resolution is offered by the particles, which exist within cells. In select cases, simulations were conducted at higher resolution for comparison of results. An example is shown for simulations with identical setups run at $mt = 128$ (Fig. 6.1a) and $mt = 256$ (Fig. 6.1b). Both runs started from identical initial thermal conditions by upscaling the initial condition for the $mt = 128$ calculation. The results are broadly similar, with the most significant difference being a variation in τ_{pb} of 8%. This gives me confidence that the results presented in this thesis and the conclusions drawn from them would not be significantly different if all simulations were conducted at a higher resolution.

Each of the simulations presented in this thesis has been a mantle convection model. This class of model has a free slip boundary condition at the surface, self-consistently evolving hot upwelling regions, similar to mantle plumes, and cool linear downwelling regions. All the melting occurs at the top of the plume-like structures, which differs from Earth where the majority of melting occurs along the network of mid-ocean ridges. Comparisons can still be made against mantle-derived rocks, as melting in these models

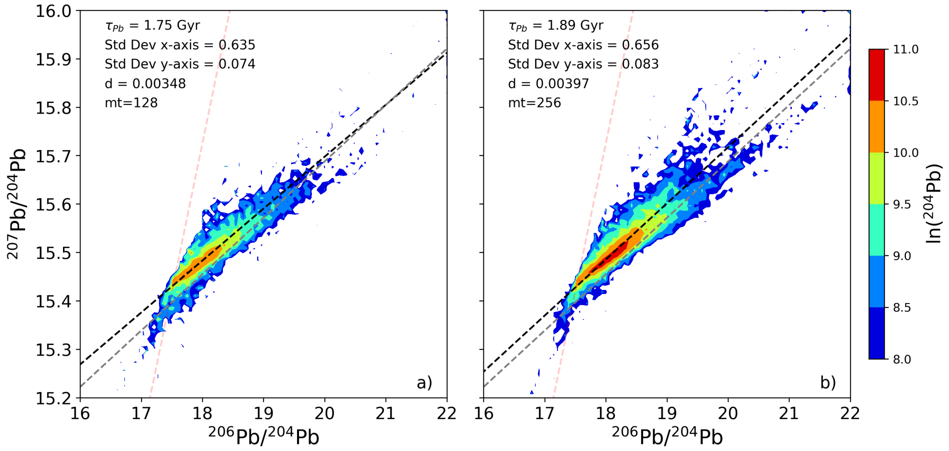

Fig. 6.1 Comparison of Pb isotope ratios for in ^{207}Pb/^{204}Pb vs ^{207}Pb/^{204}Pb space for simulations run at resolutions of a) $mt = 128$, b) $mt = 256$. Dashed black line is the pseudo-isochron calculated by a orthogonal distance regression, grey dashed line is the pseudo-isochron for MORBs and pink dashed line is the 4.5 Gyr geochron.

somewhat resembles that of both MORBs and OIBs. The plumes sample from all mantle depths, as OIBs are thought to, but also strongly deplete the melting layers, similar to how MORBs are thought to deplete the upper mantle. Nonetheless, this work has been limited to answering questions pertaining to global scale observations. Each of the isotopes investigated in this thesis do have distinctive differences depending on whether they are measured in OIBs or MORBs. In order to thoroughly investigate these differences a mantle convection model that has both plume and ridge volcanism is required. It is possible that this could be achieved by geodynamic models which self-consistently evolves a plate tectonics. This has been shown to be achievable in 3D spherical geometry by allowing lithospheric yielding under stress (van Heck and Tackley 2008). Such models are not currently able to produce some tectonic features, such as purely toroidal surface motion (equivalent to strike-slip faulting) or single sided subduction, although the latter has been generated in 2D simulations by applying a free-surface boundary condition on the outer layer (Crameri and Tackley 2015). Alternatively, plate motion histories can be used as a surface boundary condition for mantle circulation models. This forcing of surface velocities creates linear melting regions (ridges) and linear downwelling regions (subduction zones) as well as thermal plumes (Li and Zhong 2017). A caveat of using mantle circulation models is that plate motion histories are limited and patchy. The longest continuous kinematic plate reconstruction from the present day stretches back to 410 Ma (Matthews et al. 2016; Young et al. 2019). This can be extended with a kinematic plate reconstruction for the Neoproterozoic, covering 1000 Ma - 520 Ma (Merdith et al. 2017), however this still leaves a significant gap of un-constrained plate motion.

6.3 Potential for future work

The work in this thesis on investigating processes that affect the distribution of Pb isotopes in mantle-derived rocks has identified some key processes, namely the recycling of continental U after the GOE and the preferential removal of Pb from subducted oceanic crust. Rough values for the rate of Pb removal and U recycling have also been identified, however it was noted that the rate of U recycling is likely to have increased steadily rather than beginning suddenly. It would be prudent to investigate the effect of this as well as investigate more thoroughly the sensitivity of timings and fluxes.

Although the global averages for τ_{Pb} for MORBs is around 1.9 Gyr, there is significant variation in this between different ocean basins (Hofmann 2003). τ_{Pb} is highest in samples collected within the Pacific Ocean basin (East Pacific Rise and Galapagos Ridge) and lowest in samples collected along the Southeast Indian Ridge (Fig. 6.2). This spatial variability indicates long wavelength heterogeneity in the mantle.

Numerical models have shown that over periods of 100's of millions of years there is limited mixing between large volumes of the mantle separated by the boundaries between ocean basins (Barry et al. 2017). Subducted oceanic plates may act as the barrier to mixing, so there is potential for this process to have existed since subduction was initiated. This segregation of material may be what allows large scale isotopic anomalies to develop, for example the Dupal anomaly (Hart 1984). Future work could focus on reconciling these ocean-scale differences. The nature of this problem would require that mantle circulation models with kinematic plate reconstructions as a surface boundary condition are used in order that the model can be geo-referenced to Earth. As mentioned above, kinematic plate reconstructions currently extend back to 1 Ga, so are unable to cover Earth's entire history of plate tectonics which is thought to be significantly longer than this (eg. Laurent et al. (2014) and Tang et al. (2016). A potential 'hack' in order

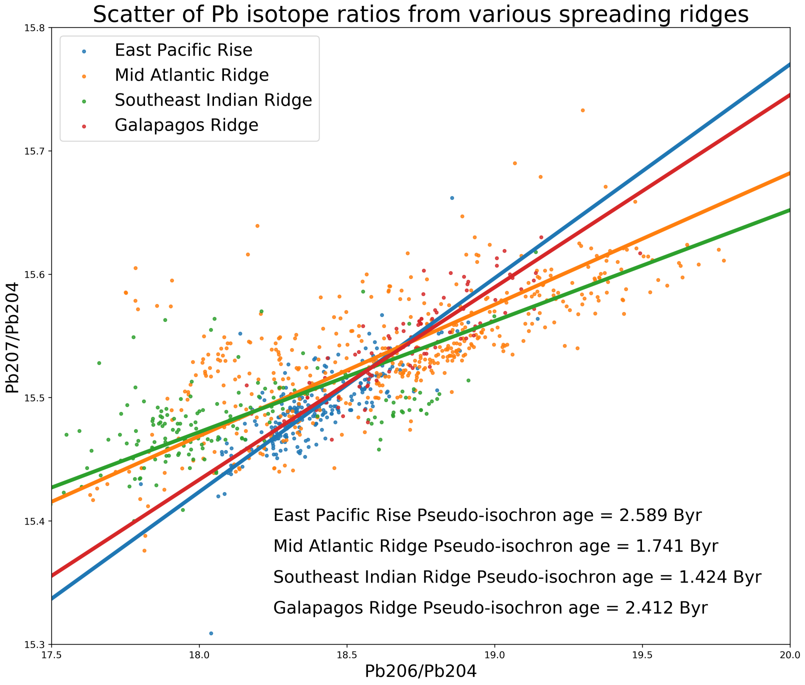

Fig. 6.2 Pb isotope composition of basalts sampled at different spreading ridges. Data obtained from PetDB (Lehnert et al., 2000, www.earthchem.org/petdb) on 18th February, 2020, using search criteria, 'Spreading Ridges & Ocean Islands', 'igneous:volcanic:mafic:basalt'.

achieve plate-like behaviour over a longer period of time using the current reconstructions could be to read in plate motion histories in reserve, however the effect that this would have on the mantle dynamics has not been assessed. Alternatively, false plate motion histories could be generated for times > 1 Ga. Such models would also aid in understanding specific differences between between OIBs and MORBs which have not been easily reconciled in the mantle convection models that were run for this thesis. Specifically these differences are the radiogenic nature of Pb isotopes measured in OIBs relative to those measured in MORBs, and the narrow range of helium isotope ratios which are measured in MORBs compared to the wide range which is measured in OIBs. Simulations run in this thesis suggested that the latter may be explained by various degrees of mixing prior to eruption, however mantle circulation modelling could offer different explanation.

REFERENCES

Albarede, F. (1998). Time-dependent models of U-Th-He and K-Ar evolution and the layering of mantle convection. *Chemical Geology* **145**, 413–429.

Allégre, C. J. (1969). Comportement des systemes U-Th-Pb dans le manteau superieur et modele d'evolution de ce dernier au cours des temps geologiques. *Earth and Planetary Science Letters* **5**, 261–269.

Allégre, C. J. (1982). Chemical geodynamics. *Tectonophysics* **81**, 109–132.

Allégre, C. J., Brévart, O., Dupré, B., and Minster, J.-F. (1980). Isotopic and chemical effects produced in a continuously differentiating convecting Earth mantle. *Philosophical Transactions of the Royal Society A* **297**, 447–477.

Allégre, C. J., Dupré, B., and Lewin, E. (1986a). Thorium / Uranium ratio of the Earth. *Chemical Geology* **56**, 219–227.

Allégre, C. J., Hofmann, A., and O'Nions, K. (1996). The Argon constraints on mantle structure. *Geophysical Research Letters* **23**, 3555–3557.

Allégre, C. J., Sarda, P., and Staudacher, T. (1993). Speculations about the cosmic origin of He and Ne in the interior of the Earth. *Earth and Planetary Science Letters* **117**, 229–233.

Allégre, C. J., Staudacher, T., and Sarda, P. (1986b). Rare gas systematics: formation of the atmosphere, evolution and structure of the Earth's mantle. *Earth and Planetary Science Letters* **81**, 127–150.

Allégre, C. J. and Turcotte, D. L. (1986). Implications of a two-component marble-cake mantle. *Nature* **323**, 123–127.

Allègre, C., Manhès, G., and Lewin, É. (2001). Chemical composition of the Earth and the volatility controlon planetary genetics. *Earth and Planetary Science Letters* **185**, 49–69.

Andersen, M. B., Elliott, T., Freymuth, H., Sims, K. W. W., Niu, Y., and Kelley, K. a. (2015). The terrestrial uranium isotope cycle. *Nature* **517**, 356–359.

Anderson, D. L. (1982). Isotopic evolution of the mantle: the role of magma mixing. *Earth and Planetary Science Letters* **57**, 1–12.

Anderson, D. L. (1993). Helium-3 from the mantle: Primordial signal or cosmic dust? *Science* **261**, 170–176.

Anderson, D. L. (1998a). A model to explain the various paradoxes associated with mantle noble gas geochemistry. *Proceedings of the National Academy of Sciences* **95**, 9087–9092.

Anderson, D. L. (1998b). The helium paradoxes. *Proceedings of the National Academy of Sciences of the United States of America* **95**, 4822–4827.

Anderson, D. L. (2000). The statistics of helium isotopes along the global spreading ridge system and the central limit theorem. *Geophysical Research Letters* **27**, 2401–2404.

Aoki, I. and Takahashi, E. (2004). Density of MORB eclogite in the upper mantle. *Physics of the Earth and Planetary Interiors* **143**, 129–143.

Arevalo, R. *., Mcdonough, W. F., and Luong, M. (2009). The K/U ratio of the silicate Earth: Insights into mantle composition, structure and thermal evolution. *Earth and Planetary Science Letters* **278**, 361–369.

Armstrong, R. L. (1968). A model for the evolution of strontium and lead isotopes in a dynamic Earth. *Reviews of Geophysics* **6**, 175–199.

Ballentine, C. J. (2007). Geochemistry: Earth holds its breath. *Nature* **449**, 294–296.

Ballentine, C. J. and Burnard, P. G. (2002). Production, release and transport of noble gases in the continental crust. *Reviews in Mineralogy and Geochemistry* **47**, 481–538.

Ballmer, M. D., Lourenço, D. L., Hirose, K., Caracas, R., and Nomura, R. (2017). Reconciling magma-ocean crystallization models with the present-day structure of the Earth's mantle. *Geochemistry, Geophysics, Geosystems* **18**, 2785–2806.

Ballmer, M., Houser, C., Hernlund, J., Wentzcovitch, R., and Hirose, K. (2016). Persistence of strong silica-enriched domains in the Earth's lower mantle. *Nature Geoscience* **10**.

Barry, T. L., Davies, J. H., Wolstencroft, M., Millar, I. L., Zhao, Z., Jian, P., Safonova, I., and Price, M. (2017). Whole-mantle convection with tectonic plates preserves long-term global patterns of upper mantle geochemistry. *Scientific Reports* **7**, 1870.

Baumgardner, J. R. (1983). Three-dimensional finite element model for mantle convection. PhD thesis.

Bender, M. L., Barnett, B., Dreyfus, G., Jouzel, J., and Porcelli, D. (2008). The contemporary degassing rate of 40Ar from the solid Earth. *Proceedings of the National Academy of Sciences of the United States of America* **105**, 8232–8237.

Bianchi, D., Sarmiento, J. L., Gnanadesikan, A., Key, R. M., Schlosser, P., and Newton, R. (2010). Low helium flux from the mantle inferred from simulations of oceanic helium isotope data. *Earth and Planetary Science Letters* **297**, 379–386.

Blichert-Toft, J., Zanda, B., Ebel, D. S., and Albarede, F. (2010). The Solar System primordial lead. *Earth and Planetary Science Letters* **300**, 152–163.

Bouhifd, M. A., Jephcoat, A. P., Porcelli, D., Kelley, S. P., and Marty, B. (2020). Potential of Earth's core as a reservoir for noble gases : Case for helium and neon. *Geochemical Perspectives Letters* **15**, 15–18.

Brandenburg, J. P., Hauri, E. H., Van Keken, P. E., and Ballentine, C. J. (2008). A multiple-system study of the geochemical evolution of the mantle with force-balanced plates and thermochemical effects. *Earth and Planetary Science Letters* **276**, 1–13.

Brandenburg, J. P. and Van Keken, P. E. (2007). Deep storage of oceanic crust in a vigorously convecting mantle. *Journal of Geophysical Research: Solid Earth* **112**, 1–15.

Bunge, H. P., Richards, M. A., Lithgow-Bertelloni, C., Baumgardner, J. R., Grand, S. P., and Romanowicz, B. A. (1998). Time scales and heterogeneous structure in geodynamic earth models. *Science* **280**, 91–95.

Bunge, H.-P. and Baumgardner, J. R. (1995). Mantle convection modeling on parallel virtual machines. *Computers in Physics* **9**, 207.

Bunge, H.-P., Richards, M. A., and Baumgardner, J. R. (1997). A sensitivity study of three-dimensional spherical mantle convection at 10 ⁸ Rayleigh number: Effects of depth-dependent viscosity, heating mode, and an endothermic phase change. *Journal of Geophysical Research: Solid Earth* **102**, 11991–12007.

Burnard, P., Graham, D., Turner, G., Burnard, P., Turner, G., and Graham, D. (1997). *Vesicle-Specific Noble Gas Analyses of "Popping Rock": Implications for Primordial Noble Gases in Earth Downloaded from*. Tech. rep., 568–571.

Castillo, P. R. (2016). A proposed new approach and unified solution to old Pb paradoxes. *Lithos* **252-253**, 32–40.

Chamorro, E. M., Brooker, R. A., Wartho, J. A., Wood, B. J., Kelley, S. P., and Blundy, J. D. (2002). Ar and K partitioning between clinopyroxene and silicate melt to 8 GPa. *Geochimica et Cosmochimica Acta* **66**, 507–519.

Chauvel, C., Hofmann, A. W., and Vidal, P. (1992). himu-em: The French Polynesian connection. *Earth and Planetary Science Letters* **110**, 99–119.

Christensen, U. R. and Hofmann, A. W. (1994). Segregation of subducted oceanic crust in the convecting mantle. *Journal of Geophysical Research: Solid Earth* **99**, 19867–19884.

Cordier, P. (2002). Dislocations and slip systems of mantle minerals. *Reviews in Mineralogy and Geochemistry* **51**, 137–180.

Cottaar, S. and Lekić, V. (2016). Morphology of Seismically Slow Lower Mantle Structures. *Geophys. J. Int.* **207**, 1122–1136.

Craig, H., Clarke, W. B., and Beg, M. A. (1975). Excess 3He in deep water on the East Pacific Rise. *Earth and Planetary Science Letters* **26**, 125–132.

Crameri, F. and Tackley, P. J. (2015). Parameters controlling dynamically self-consistent plate tectonics and single-sided subduction in global models of mantle convection. *Journal of Geophysical Research: Solid Earth* **120**, 3680–3706.

Davies, D. R., Davies, J. H., Bollada, P. C., Hassan, O., Morgan, K., and Nithiarasu, P. (2013). A hierarchical mesh refinement technique for global 3-D spherical mantle convection modelling. *Geoscientific Model Development* **6**, 1095–1107.

Davies, D. R., Goes, S., and Lau, H. C. (2015a). Thermally dominated deep mantle LLSVPs: A review. In: *The Earth's Heterogeneous Mantle: A Geophysical, Geodynamical, and Geochemical Perspective*. Springer International Publishing, 441–477.

Davies, D. R., Goes, S., and Lau, H. C. (2015b). Thermally dominated deep mantle LLSVPs: A review. In: *The Earth's Heterogeneous Mantle: A Geophysical, Geodynamical, and Geochemical Perspective*. Springer International Publishing, 441–477.

Davies, G. F. (1993). *Cooling the core and mantle by plume and plate flows*. Tech. rep., 132–146.

Davies, G. F. (2002). Stirring geochemistry in mantle convection models with stiff plates and slabs. *Geochimica et Cosmochimica Acta* **66**, 3125–3142.

Davies, G. F. (2008). Episodic layering of the early mantle by the ' basalt barrier ' mechanism. *Earth and Planetary Science Letters* **275**, 382–392.

Davies, G. F. (2009). Reconciling the geophysical and geochemical mantles: Plume flows, heterogeneities, and disequilibrium. *Geochemistry, Geophysics, Geosystems* **10**, n/a–n/a.

Davies, G. F. (2010). Noble gases in the dynamic mantle. *Geochemistry, Geophysics, Geosystems* **11**.

Davies, J. H. (2005). Steady plumes produced by downwellings in Earth-like vigor spherical whole mantle convection models. *Geochemistry Geophysics Geosystems* **6**, 1–14.

Davies, J. H. and Davies, D. R. (2010). Earth ' s surface heat flux. *Solid Earth* **1**, 5–24.

Deschamps, F. and Tackley, P. J. (2009). Searching for models of thermo-chemical convection that explain probabilistic tomography. II-Influence of physical and compositional parameters. *Physics of the Earth and Planetary Interiors* **176**, 1–18.

Dziewonski, A. M. and Anderson, D. L. (1981). Preliminary reference Earth model. *Physics of the Earth and Planetary Interiors* **25**, 297–356.

Elliott, T., Zindler, A., and Bourdon, B. (1999). Exploring the kappa conundrum: The role of recycling in the lead isotope evolution of the mantle. *Earth and Planetary Science Letters* **169**, 129–145.

Farley, K. A., Maier-Reimer, E., Schlosser, P., and Broecker, W. S. (1995). Constraints on mantle 3 He fluxes and deep-sea circulation from an oceanic general circulation model. *Journal of Geophysical Research: Solid Earth* **100**, 3829–3839.

Farley, K. A. and Neroda, E. (1998). Noble Gases in the Earth. *Annual Review of Earth and Planetary Sciences* **26**, 217–252.

Ferrachat, S. and Ricard, Y. (2001). Mixing properties in the Earth's mantle: Effects of the viscosity stratification and of oceanic crust segregation. *Geochemistry, Geophysics, Geosystems* **2**.

French, S. W. and Romanowicz, B. (2015). Broad plumes rooted at the base of the Earth's mantle beneath major hotspots. *Nature* **525**, 95–99.

Galer, S. J. G. and O'Nions, R. K. (1985). Residence time of thorium, uranium and lead in the mantle with implications for mantle convection. *Nature* **316**, 778–782.

Gast, P. W. (1960). Limitations on the composition of the upper mantle. *Journal of Geophysical Research* **65**, 1287–1297.

Gast, P. W., Tilton, G. R., and Hedge, C. (1964). Isotopic composition of lead and strontium from Ascension and Gough Islands. *Science* **145**, 1181–1185.

Goldmann, A., Brennecka, G., Noordmann, J., Weyer, S., and Wadhwa, M. (2015). The uranium isotopic composition of the Earth and the Solar System. *Geochimica et Cosmochimica Acta* **148**, 145–158.

Gonnermann, H. M. and Mukhopadhyay, S. (2009). Preserving noble gases in a convecting mantle. *Nature* **459**, 560–563.

Gordon, R. B. (1965). Diffusion creep in the Earth's mantle. *Journal of Geophysical Research* **70**, 2413–2418.

Graham, D. W. (2002). Noble gas isotope geochemistry of mid-ocean ridge and ocean island basalts: Characterization of mantle source reservoirs. *Reviews in Mineralogy and Geochemistry* **47**, 247–317.

Graham, D. W., Jenkins, W. J., Schilling, J. G., Thompson, G., Kurz, M. D., and Humphris, S. E. (1992). Helium isotope geochemistry of mid-ocean ridge basalts from the South Atlantic. *Earth and Planetary Science Letters* **110**, 133–147.

Grand, S. P., Van Der Hilst, R. D., and Widiyantoro, S. (1997). Global seismic tomography: A snapshot of convection in the earth. *GSA Today* **7**, 1–7.

Halla, J. (2005). Late Archean high-Mg granitoids (sanukitoids) in the southern Karelian domain, eastern Finland: Pb and Nd isotopic constraints on crust-mantle interactions. *Lithos* **79**, 161–178.

Hanan, B. B. and Graham, D. W. (1996). Lead and Helium Isotope Evidence from Oceanic Basalts for a Common Deep Source of Mantle Plumes. *Science* **272**, 991–995.

Hart, S. R. (1984). A large-scale isotopic anomaly in the southern hemisphere. *Nature* **309**, 753–756.

Hart, S. R. and Gaetani, G. A. (2006). Mantle Pb paradoxes: The sulfide solution. *Contributions to Mineralogy and Petrology* **152**, 295–308.

Hart, S. R., Hauri, E. H., Oschmann, L. A., and Whitehead, J. A. (1992). Mantle plumes and entrapment: Isotopic evidence. *Science* **256**, 517–520.

Hart, S. R. and Staudigel, H. (1989). Isotopic Characterization and Identification of Recycled Components. In: *Crust/Mantle Recycling at Convergence Zones*. Springer Netherlands, 15–28.

Hart, S. R. and Staudigel, H. (1982). *The control of alkalies and uranium in seawater by ocean crust alteration*. Tech. rep., 202–212.

Hartmann, W. K. and Davis, D. R. (1975). Satellite-Sized Planetesimals and Lunar Origin. *ICARUS* **24**, 504–515.

Hauri, E. H., Wagner, T. P., and Grove, T. L. (1994). Experimental and natural partitioning of Th, U, Pb and other trace elements between garnet, clinopyroxene and basaltic melts. *Chemical Geology* **117**, 149–166.

Hawkesworth, C. J., Turner, S. P., Mcdermott, F., Peate, D. W., and Calsteren, P. V. (1997). U-Th Isotopes in Arc Magmas : Implications for Element Transfer from the Subducted Crust. *Science* **276**, 551–556.

Hawkesworth, C., Cawood, P., and Dhuime, B. (2013). Continental growth and the crustal record. *Tectonophysics* **609**, 651–660.

Heber, V. S., Brooker, R. A., Kelley, S. P., and Wood, B. J. (2007). Crystal-melt partitioning of noble gases (helium, neon, argon, krypton, and xenon) for olivine and clinopyroxene. *Geochimica et Cosmochimica Acta* **71**, 1041–1061.

van Heck, H. J. and Tackley, P. J. (2008). Planforms of self-consistently generated plates in 3D spherical geometry. *Geophysical Research Letters* **35**.

van Heck, H. J., Davies, J. H., Elliott, T., and Porcelli, D. (2016). Global-scale modelling of melting and isotopic evolution of Earth's mantle: Melting modules for TERRA. *Geoscientific Model Development* **9**, 1399–1411.

Hernlund, J. W. and Tackley, P. J. (2008). Modeling mantle convection in the spherical annulus. *Physics of the Earth and Planetary Interiors* **171**, 48–54.

Heyn, B. H., Conrad, C. P., and Trønnes, R. G. (2018). Stabilizing Effect of Compositional Viscosity Contrasts on Thermochemical Piles. *Geophysical Research Letters* **45**, 7523–7532.

Hiess, J., Condon, D. J., McLean, N., and Noble, S. R. (2012). 238U/235U systematics in terrestrial uranium-bearing minerals. *Science* **335**, 1610–1614.

Hirose, K., Fei, Y., Ma, Y., and Mao, H. K. (1999). The fate of subducted basaltic crust in the Earth's lower mantle. *Nature* **397**, 53–56.

Hirose, K., Takafuji, N., Sata, N., and Ohishi, Y. (2005). Phase transition and density of subducted MORB crust in the lower mantle. *Earth and Planetary Science Letters* **237**, 239–251.

Hiyagon, H. and Ozima, M. (1986). Partition of noble gases between olivine and basalt melt. *Geochimica et Cosmochimica Acta* **50**, 2045–2057.

Hofmann, A. W. (1997). Mantle geochemistry: the message from oceanic volcanism. *Nature* **385**, 219–229.

Hofmann, A. W. (2003). Sampling Mantle Heterogeneity through Oceanic Basalts Isotopes and Trace Elements. In: *Treatise on geochemistry*. 2.03. Holland HD, Turekian KK (eds), 61–101.

Hofmann, A. W. (1988). Chemical differentiation of the Earth : the relationship between mantle , continental crust , and oceanic crust. *Earth and Planetary Science Letters* **90**, 297–314.

Hofmann, A. W. and White, W. M. (1982). Mantle plumes from ancient oceanic crust. *Earth and Planetary Science Letters* **57**, 421–436.

Holland, G. and Ballentine, C. J. (2006). Seawater subduction controls the heavy noble gas composition of the mantle. *Nature* **441**, 186–91.

Holland, H. D. (1985). The Chemical Evolution of the Atmosphere and Oceans. *Nature* **122**, 404–405.

Honda, M., Reynolds, J. H., Roedder, E., and Epstein, S. (1987). Noble gases in diamonds: Occurrences of solarlike helium and neon. *Journal of Geophysical Research* **92**, 12507.

Huang, J. and Davies, G. F. (2007). Stirring in three-dimensional mantle convection models and mplications for geochemistry: Passive tracers. *Geochemistry, Geophysics, Geosystems* **8**, 1–17.

Irifune, T. and Ringwood, A. E. (1993). Phase transformations in subducted oceanic crust and buoyancy relationships at depths of 600-800 km in the mantle. *Earth and Planetary Science Letters* **117**, 101–110.

Jackson, M. G., Konter, J. G., and Becker, T. W. (2017). Primordial helium entrained by the hottest mantle plumes. *Nature* **542**, 340–343.

Jackson, M. G., Carlson, R. W., Kurz, M. D., Kempton, P. D., Francis, D., and Blusztajn, J. (2010). Evidence for the survival of the oldest terrestrial mantle reservoir. *Nature* **466**, 853–856.

Jarvis, G. T. and Mckenzie, D. P. (1980). Convection in a compressible fluid with infinite Prandtl number. *Journal of Fluid Mechanics* **96**, 515–583.

Jones, R. E., Van Keken, P. E., Hauri, E. H., Tucker, J. M., Vervoort, J., and Ballentine, C. J. (2019). Origins of the terrestrial Hf-Nd mantle array: Evidence from a combined geodynamical-geochemical approach. *Earth and Planetary Science Letters* **518**, 26–39.

Kaneoka, I., Kaneoka', I., Takaoka, N., and Upton', B. G. J. (1986). Noble gas systematics in basalts and a dunite nodule from Réunion and Grand Comore Islands, Indian Ocean. *Chemical Geology: Isotope Geoscience Section* **59**, 35.

Kelley, K. A., Plank, T., Farr, L., Ludden, J., and Staudigel, H. (2005). Subduction cycling of U, Th, and Pb. *Earth and Planetary Science Letters* **234**, 369–383.

Kellogg, J. B., Jacobsen, S. B., and Connell, R. J. O. (2007). Modeling lead isotopic heterogeneity in mid-ocean ridge basalts. *Earth and Planetary Science Letters* **262**, 328–342.

Kellogg, J. B., Jacobsen, S. B., and O'Connell, R. J. (2002). Modeling the distribution of isotopic ratios in geochemical reservoirs. *Earth and Planetary Science Letters* **204**, 183–202.

Kellogg, L. H., Hager, B. H., and Van Der Hilst, R. D. (1999). Compositional stratification in the deep mantle. *Science* **283**, 1881–1884.

King, R. L., Bebout, G. E., Grove, M., Moriguti, T., and Nakamura, E. (2007). Boron and lead isotope signatures of subduction-zone mélange formation: Hybridization and fractionation along the slab-mantle interface beneath volcanic arcs. *Chemical Geology* **239**, 305–322.

Korenaga, J. (2009). A method to estimate the composition of the bulk silicate Earth in the presence of a hidden geochemical reservoir. *Geochimica et Cosmochimica Acta* **73**, 6952–6964.

Kramers, J. D. and Tolstikhin, I. N. (1997). Two terrestrial lead isotope paradoxes, forward transport modelling, core formation and the history of the continental crust. *Chemical Geology* **139**, 75–110.

Kurz, M. D., Jenkins, W. J., and Hart, S. R. (1982). Helium isotopic systematics of oceanic islands and mantle heterogeneity. *Nature* **297**, 43–47.

Labrosse, S., Hernlund, J. W., and Coltice, N. (2007). A crystallizing dense magma ocean at the base of the Earth's mantle. *Nature* **450**, 866–869.

Labrosse, S. and Jaupart, C. (2007). Thermal evolution of the Earth : Secular changes and fluctuations of plate characteristics. *Earth and Planetary Science Letters* **260**, 465–481.

Lambart, S., Koornneef, J. M., Millet, M. A., Davies, G. R., Cook, M., and Lissenberg, C. J. (2019). Highly heterogeneous depleted mantle recorded in the lower oceanic crust. *Nature Geoscience* **12**, 482–486.

Lassiter, J. C. (2004). Role of recycled oceanic crust in the potassium and argon budget of the earth: Toward a resolution of the "missing argon" problem. *Geochemistry, Geophysics, Geosystems* **5**, 1–16.

Laurent, O., Martin, H., Moyen, J. F., and Doucelance, R. (2014). The diversity and evolution of late-Archean granitoids: Evidence for the onset of "modern-style" plate tectonics between 3.0 and 2.5 Ga. *Lithos* **205**, 208–235.

Lee, C. T. A., Luffi, P., Höink, T., Li, J., Dasgupta, R., and Hernlund, J. (2010). Upside-down differentiation and generation of a primordial lower mantle. *Nature* **463**, 930–933.

Lee, J. Y., Marti, K., Severinghaus, J. P., Kawamura, K., Yoo, H. S., Lee, J. B., and Kim, J. S. (2006). A redetermination of the isotopic abundances of atmospheric Ar. *Geochimica et Cosmochimica Acta* **70**, 4507–4512.

Lehnert, K., Su, Y., Langmuir, C. H., Sarbas, B., and Nohl, U. (2000). A global geochemical database structure for rocks. *Geochemistry, Geophysics, Geosystems* **1**.

Li, M. and Zhong, S. (2017). The source location of mantle plumes from 3D spherical models of mantle convection. *Earth and Planetary Science Letters* **478**, 47–57.

Li, Y., Deschamps, F., and Tackley, P. J. (2014). The stability and structure of primordial reservoirs in the lower mantle: insights from models of thermochemical convection in three-dimensional spherical geometry. *Geophys. J. Int.* **199**, 914–930.

Livermore, B. D., Connelly, J. N., Moynier, F., and Bizzarro, M. (2018). Evaluating the robustness of a consensus 238U/235U value for U-Pb geochronology. *Geochimica et Cosmochimica Acta* **237**, 171–183.

Lupton, J. E. (1983). Terrestrial Inert Gases: Isotope Tracer Studies and Clues to Primordial Components in the Mantle. *Annual Review of Earth and Planetary Sciences* **11**, 371–414.

Lyons, T. W., Reinhard, C. T., and Planavsky, N. J. (2014). The rise of oxygen in Earth's early ocean and atmosphere. *Nature* **506**, 307–315.

Lyubetskaya, T. and Korenaga, J. (2007). Chemical composition of Earth's primitive mantle and its variance: 1. Method and results. *Journal of Geophysical Research: Solid Earth* **112**.

MacDonald, G. J. (1963). The escape of helium from the Earth's atmosphere. *Reviews of Geophysics* **1**, 305–349.

Malkus, W. V. (1968). Precession of the earth as the cause of geomagnetism. *Science* **160**, 259–264.

Maltese, A. and Mezger, K. (2020). The Pb isotope evolution of Bulk Silicate Earth: Constraints from its accretion and early differentiation history. *Geochimica et Cosmochimica Acta* **271**, 179–193.

Marty, B. and Jambon, A. (1987). C3He in volatile fluxes from the solid Earth: implications for carbon geodynamics. *Earth and Planetary Science Letters* **83**, 16–26.

Marty, B. and Ozima, M. (1986). Noble gas distribution in oceanic basalt glasses. *Geochimica et Cosmochimica Acta* **50**, 1093–1097.

Maruyama, S., Santosh, M., and Azuma, S. (2018). Initiation of plate tectonics in the Hadean: Eclogitization triggered by the ABEL Bombardment. *Geoscience Frontiers* **9**, 1033–1048.

Matsuda, J., Sudo, M., Ozima, M., Ito, K., Ohtaka, O., and Ito, E. (1993). Noble gas partitioning between metal and silicate under high pressures. *Science* **259**, 788–790.

Matsuda, J.-i. and Marty, B. (1995). The 40Ar/ 36Ar ratio of the undepleted mantle; A reevaluation. *Geophysical Research Letters* **22**, 1937–1940.

Matthews, K. J., Maloney, K. T., Zahirovic, S., Williams, S. E., Seton, M., and Müller, R. D. (2016). Global plate boundary evolution and kinematics since the late Paleozoic. *Global and Planetary Change* **146**, 226–250.

McDonough, W. F. and Sun, S. s. (1995). The composition of the Earth. *Chemical Geology* **120**, 223–253.

Mckenzie, D. P., Roberts, J. M., and Weiss, N. O. (1974). Convection in the earth's mantle: Towards a numerical simulation. *Journal of Fluid Mechanics* **62**, 465–538.

Meibom, A. and Anderson, D. L. (2003). The statistical upper mantle assemblage. *Earth and Planetary Science Letters* **217**, 123–139.

Merdith, A. S., Collins, A. S., Williams, S. E., Pisarevsky, S., Foden, J. D., Archibald, D. B., Blades, M. L., Alessio, B. L., Armistead, S., Plavsa, D., Clark, C., and Müller, R. D. (2017). A full-plate global reconstruction of the Neoproterozoic. *Gondwana Research* **50**, 84–134.

Michard, A. and Albarede, F. (1985). Hydrothermal uranium uptake at ridge crests. *Nature* **313**, 47–48.

Miller, D. M., Goldstein, S. L., and Langmuir, C. H. (1994). Cerium/lead and lead isotope ratios in arc magmas and the enrichment of lead in the continents. *Nature* **368**, 514–520.

Mitrovica, J. X. and Forte, A. M. (1997). Radial profile of mantle viscosity: Results from the joint inversion of convection and postglacial rebound observables. *Journal of Geophysical Research: Solid Earth* **102**, 2751–2769.

Morris, J. D. and Hart, S. R. (1983). Isotopic and incompatible element constraints on the genesis of island arc volcanics from Cold Bay and Amak Island, Aleutians, and implications for mantle structure. *Geochimica et Cosmochimica Acta* **47**, 2015–2030.

Mukhopadhyay, S. (2012). Early differentiation and volatile accretion recorded in deep-mantle neon and xenon. *Nature* **486**, 101–104.

Müller, R. D., Sdrolias, M., Gaina, C., and Roest, W. R. (2008). Age, spreading rates, and spreading asymmetry of the world's ocean crust. *Geochemistry, Geophysics, Geosystems* **9**.

Mulyukova, E., Steinberger, B., Dabrowski, M., and Sobolev, S. V. (2015). Survival of LLSVPs for billions of years in a vigorously convecting mantle: Replenishment and destruction of chemical anomaly. *Journal of Geophysical Research: Solid Earth* **120**, 3824–3847.

Nakagawa, T. and Spiegelman, M. W. (2017). Global-scale water circulation in the Earth's mantle: Implications for the mantle water budget in the early Earth. *Earth and Planetary Science Letters* **464**, 189–199.

Nier, A. O. (1950). A redetermination of the relative abundances of the isotopes of carbon, nitrogen, oxygen, argon, and potassium. *Physical Review* **77**, 789–793.

Ohtani, E. (1985). The primodial terrestrial magma ocean and its implication for stratification of the mantle. *Physics of the Earth and Planetary Interiors* **38**, 70–80.

O'Neill, H. S. C. (1991). The origin of the moon and the early history of the earth-A chemical model. Part 2: The earth. *Geochimica et Cosmochimica Acta* **55**, 1159–1172.

Ono, S., Ito, E., and Katsura, T. (2001). Mineralogy of subducted basaltic crust (MORB) from 25 to 37 GPa , and chemical heterogeneity of the lower mantle. *Earth and Planetary Science Letters* **190**.

Oversby, V. M. and Ringwood, A. E. (1972). Potassium distribution between metal and silicate and its bearing on the occurrence of potassium in the earth's core. *Earth and Planetary Science Letters* **14**, 345–347.

Oversby, V. M. and Gast, P. W. (1970). Isotopic Composition of Lead from Oceanic Islands. *Journal of Geophysical Research* **75**.

Ozima, M. and Zashu, S. (1991). Noble gas state of the ancient mantle as deduced from noble gases in coated diamonds. *Earth and Planetary Science Letters* **105**, 13–27.

Ozima, M. and Zahnle, K. (1993). Mantle degassing and atmospheric evolution: Noble gas view. *Geochemical Journal* **27**, 185–200.

Patterson, C. (1956). Age of meteorites and the earth. *Geochimica et Cosmochimica Acta* **10**, 230–237.

Patterson, D. B., Honda, M., and McDougall, I. (1990). Atmospheric contamination: A possible source for heavy noble gases in basalts from Loihi seamount, Hawaii. *Geophysical Research Letters* **17**, 705–708.

Pearce, J. A. and Peate, D. W. (1995). Tectonic implications of the composition of volcanic arc magmas. *Annual Review of Earth and Planetary Sciences* **23**, 251–285.

Pepin, R. O. and Porcelli, D. (2006). Xenon isotope systematics, giant impacts, and mantle degassing on the early Earth. *Earth and Planetary Science Letters* **250**, 470–485.

Peucker-Ehrenbrink, B., Hofmann, A. W., and Hart, S. R. (1994). Hydrothermal lead transfer from mantle to continental crust: the role of metalliferous sediments. *Earth and Planetary Science Letters* **125**, 129–142.

Porcelli, D. and Ballentine, C. J. (2002). Models for Distribution of Terrestrial Noble Gases and Evolution of the Atmosphere. *Reviews in Mineralogy and Geochemistry* **47**, 411–480.

Porcelli, D. and Halliday, A. N. (2001). The core as a possible source of mantle helium. *Earth and Planetary Science Letters* **192**, 45–56.

Porcelli, D. and Elliott, T. (2008). The evolution of He Isotopes in the convecting mantle and the preservation of high 3He/4He ratios. *Earth and Planetary Science Letters* **269**, 175–185.

Price, M. G., Davies, J. H., and Panton, J. (2019). Controls on the deep water cycle within three-dimensional mantle convection models. *Geochemistry, Geophysics, Geosystems* **20**, 1–15.

Rhodes, M. and Davies, J. H. (2001). Tomographic imaging of multiple mantle plumes in the uppermost lower mantle. *Geophysical Journal International* **147**, 88–92.

Ringwood, A. E. (1962). A model for the upper mantle. *Journal of Geophysical Research* **67**, 857–867.

Ringwood, A. E. (1968). Phase transformations in the mantle. *Earth and Planetary Science Letters* **5**, 401–412.

Rison, W. and Craig, H. (1983). Helium isotopes and mantle volatiles in Loihi Seamount and Hawaiian Island basalts and xenoliths. *Earth and Planetary Science Letters* **66**, 407–426.

Rubie, D. C., Frost, D. J., Mann, U., Asahara, Y., Nimmo, F., Tsuno, K., Kegler, P., Holzheid, A., and Palme, H. (2011). Heterogeneous accretion, composition and core-mantle differentiation of the Earth. *Earth and Planetary Science Letters* **301**, 31–42.

Rudge, J. F. (2006). Mantle pseudo-isochrons revisited. *Earth and Planetary Science Letters* **249**, 494–513.

Rudge, J. F., McKenzie, D., and Haynes, P. H. (2005). A theoretical approach to understanding the isotopic heterogeneity of mid-ocean ridge basalt. *Geochimica et Cosmochimica Acta* **69**, 3873–3887.

Rudnick, R. L. and Gao, S. (2013). Composition of the Continental Crust. In: *Treatise on Geochemistry: Second Edition*. 2nd ed. Elsevier Ltd. Chap. 4.1, 1–51.

Samuel, H. and Farnetani, C. G. (2003). Thermochemical convection and helium concentrations in mantle plumes. *Earth and Planetary Science Letters* **207**, 39–56.

Sarda, P. (2004). Surface noble gas recycling to the terrestrial mantle. *Earth and Planetary Science Letters* **228**, 49–63.

Sarda, P., Staudacher, T., and Allégre, C. J. (1985). 40Ar36Ar in MORB glasses: constraints on atmosphere and mantle evolution. *Earth and Planetary Science Letters* **72**, 357–375.

Schlitzer, R. (2016). Quantifying He fluxes from the mantle using multi-tracer data assimilation. *Philosophical Transactions of the Royal Society A: Mathematical, Physical and Engineering Sciences* **374**, 20150288.

Scott, D. J. and Gauthier, G. (1996). Comparison of TIMS (U-Pb) and laser ablation microprobe ICP-MS (Pb) techniques for age determination of detrital zircons from paleoproterozoic metasedimentary rocks from north-eastern Laurentia, Canada, with tectonic implications. *Chemical Geology* **131**, 127–142.

Shirey, S. B. and Richardson, S. H. (2011). Start of the wilson cycle at 3 Ga shown by diamonds from subcontinental mantle. *Science* **333**, 434–436.

Sinha, A. K. and Tilton, G. R. (1973). Isotopic evolution of common lead. *Geochimica et Cosmochimica Acta* **37**, 1823–1849.

Smye, A. J., Jackson, C. R., Konrad-Schmolke, M., Hesse, M. A., Parman, S. W., Shuster, D. L., and Ballentine, C. J. (2017). Noble gases recycled into the mantle through cold subduction zones. *Earth and Planetary Science Letters* **471**, 65–73.

Solomatov, V. S. and Stevenson, D. J. (1993). Suspension in convective layers and style of differentiation of a terrestrial magma ocean. *Journal of Geophysical Research* **98**, 5375–5390.

Spiegel, E. A. and Veronis, G. (1960). On the Boussinesq Approximation For A Compressible Fluid. *Astrophysical Journal* **131**, 442–447.

Stegman, D. R., Richards, M. A., and Baumgardner, J. R. (2002). Effects of depth-dependent viscosity and plate motions on maintaining a relatively uniform mid-ocean ridge basalt reservoir in whole mantle flow. *Journal of Geophysical Research* **107**.

Stern, R. J. (2005). Evidence from ophiolites, blueschists, and ultrahigh-pressure metamorphic terranes that the modern episode of subduction tectonics began in Neoproterozoic time. *Geology* **33**, 557–560.

Stracke, A., Hofmann, A. W., and Hart, S. R. (2005). FOZO, HIMU, and the rest of the mantle zoo. *Geochemistry, Geophysics, Geosystems* **6**, 1–20.

Stuart, F. M., Lass-Evans, S., Fitton, J. G., and Ellam, R. M. (2003). High 3He/4He ratios in picritic basalts from Baffin Island and the role of a mixed reservoir in mantle plumes. *Nature* **424**, 57–59.

Sun, S. S. and McDonough, W. F. (1989). Chemical and isotopic systematics of oceanic basalts: Implications for mantle composition and processes. *Geological Society Special Publication* **42**, 313–345.

Tackley, P. J. (2002). Strong heterogeneity caused by deep mantle layering. *Geochemistry, Geophysics, Geosystems* **3**, 1–22.

Tackley, P. J. (2011). Living dead slabs in 3-D: The dynamics of compositionally-stratified slabs entering a " slab graveyard" above the core-mantle boundary. *Physics of the Earth and Planetary Interiors* **188**, 150–162.

Tang, M., Chen, K., and Rudnick, R. L. (2016). Archean upper crust transition from mafic to felsic marks the onset of plate tectonics. *Science* **351**, 372–375.

Tatsumoto, M. (1966). Genetic Relations of Oceanic Basalts as Indicated by Lead Isotopes. *Science* **153**, 1094–1101.

Tatsumoto, M., Knight, R. J., and Allégre, C. J. (1973). Time differences in the formation of meteorites as determined from the ratio of lead-207 to lead-206. *Science* **180**, 1279–1283.

Taylor, S. R. (1964). Trace element abundances and the chondritic Earth model. *Geochimica et Cosmochimica Acta* **28**, 1989–1998.

Thomson, A. R., Crichton, W. A., Brodholt, J. P., Wood, I. G., Siersch, N. C., Muir, J. M. R., Dobson, D. P., and Hunt, S. A. (2019). Seismic velocities of CaSiO3 perovskite can explain LLSVPs in Earth's lower mantle. *Nature* **572**, 643–647.

Trieloff, M., Falter, M., and Jessberger, E. K. (2003). The distribution of mantle and atmospheric argon in oceanic basalt glasses. *Geochimica et Cosmochimica Acta* **67**, 1237–1253.

Trieloff, M., Kunz, J., Clague, D. A., Harrison, D., and Allégre, C. J. (2000). The nature of pristine noble gases in mantle plumes. *Science* **288**, 1036–1038.

Tucker, J. M., Mukhopadhyay, S., and Gonnermann, H. M. (2018). Reconstructing mantle carbon and noble gas contents from degassed mid-ocean ridge basalts. *Earth and Planetary Science Letters* **496**, 108–119.

Turcotte, D. L., Paul, D., and White, W. M. (2001). Thorium-uranium systematics require layered mantle convection. *Journal of Geophysical Research: Solid Earth* **106**, 4265–4276.

Valley, J. W., Peck, W. H., King, E. M., and Wilde, S. A. (2002). A cool early Earth. *Geology* **30**, 351–354.

Van Keken, P. E. and Ballentine, C. J. (1998). Whole-mantle versus layered mantle convection and the role of a high-viscosity lower mantle in terrestrial volatile evolution. *Earth and Planetary Science Letters* **156**, 19–32.

Van Keken, P. E. and Ballentine, C. J. (1999). Dynamical models of mantle volatile evolution and the role of phase transitions and temperature-dependent rheology. *Journal of Geophysical Research: Solid Earth* **104**, 7137–7151.

Van Keken, P. E., Ballentine, C. J., and Porcelli, D. (2001). A dynamical investigation of the heat and helium imbalance. *Earth and Planetary Science Letters* **188**, 421–434.

de Vries, J., Nimmo, F., Melosh, H. J., Jacobson, S. A., Morbidelli, A., and Rubie, D. C. (2016). Impact-induced melting during accretion of the Earth. *Progress in Earth and Planetary Science* **3**, 1–11.

Wänke, H. W. (1981). *Constitution of terrestrial planets*. Tech. rep., 287–302.

Weertman, J. (1978). Creep laws for the mantle of the Earth. *Philosophical Transactions of the Royal Society of London. Series A, Mathematical and Physical Sciences* **288**, 9–26.

Weis, D., Kieffer, B., Maerschalk, C., Barling, J., De Jong, J., Williams, G. A., Hanano, D., Pretorius, W., Mattielli, N., Scoates, J. S., Goolaerts, A., Friedman, R. M., and Mahoney, J. B. (2006). High-precision isotopic characterization of USGS reference materials by TIMS and MC-ICP-MS. *Geochemistry, Geophysics, Geosystems* **7**.

White, W. M. (1985). Sources of oceanic basalts: radiogenic isotopic evidence. *Geology* **13**, 115–118.

White, W. M. (1993). 238U204Pb in MORB and open system evolution of the depleted mantle. *Earth and Planetary Science Letters* **115**, 211–226.

Williams, C. D., Li, M., McNamara, A. K., Garnero, E. J., and Van Soest, M. C. (2015). Episodic entrainment of deep primordial mantle material into ocean island basalts. *Nature Communications* **6**, 1–7.

Wipperfurth, S. A., Guo, M., Šrámek, O., and McDonough, W. F. (2018). Earth's chondritic Th/U: Negligible fractionation during accretion, core formation, and crust–mantle differentiation. *Earth and Planetary Science Letters* **498**, 196–202.

Workman, R. K. and Hart, S. R. (2005). Major and trace element composition of the depleted MORB mantle (DMM). *Earth and Planetary Science Letters* **231**, 53–72.

Xie, S. and Tackley, P. J. (2004a). Evolution of helium and argon isotopes in a convecting mantle. *Physics of the Earth and Planetary Interiors* **146**, 417–439.

Xie, S. and Tackley, P. J. (2004b). Evolution of U-Pb and Sm-Nd systems in numerical models of mantle convection and plate tectonics. *Journal of Geophysical Research B: Solid Earth* **109**, 1–22.

Yang, W.-S. (1997). Variable viscosity thermal convection at infinite prandtl number in a thick spherical shell. PhD thesis.

Young, A., Flament, N., Maloney, K., Williams, S., Matthews, K., Zahirovic, S., and Müller, R. D. (2018). Global kinematics of tectonic plates and subduction zones since the late Paleozoic Era. *Geoscience Frontiers*.

Young, A., Flament, N., Maloney, K., Williams, S., Matthews, K., Zahirovic, S., and Müller, R. D. (2019). Global kinematics of tectonic plates and subduction zones since the late Paleozoic Era. *Geoscience Frontiers* **10**, 989–1013.

Yu, S. and Garnero, E. J. (2018). Ultralow Velocity Zone Locations: A Global Assessment. *Geochemistry, Geophysics, Geosystems* **19**, 396–414.

Zartman, R. E. and Haines, S. M. (1988). The plumbotectonic model for Pb isotopic systematics among major terrestrial reservoirs-A case for bi-directional transport. *Geochimica et Cosmochimica Acta* **52**, 1327–1339.

Zhang, Z., Dorfman, S. M., Labidi, J., Zhang, S., Li, M., Manga, M., Stixrude, L., McDonough, W. F., and Williams, Q. (2016). Primordial metallic melt in the deep mantle. *Geophysical Research Letters* **43**, 3693–3699.

Zhong, S., Zuber, M. T., and Moresi, L. (2000). Role of temperature-dependent viscosity and surface plates in spherical shell models of mantle convection. *Journal of Geophysical Research* **105**, 11, 063–11, 082.

Zindler, A. and Hart, S. (1986). Chemical geodynamics. *Annual review of Earth and planetary sciences. Vol. 14*, 493–571.

APPENDIX A

GLOSSARY

Abbreviations

Abbreviations found throughout the thesis:

Abbreviation	Definition
CMB	Core-mantle boundary
DMM	Depleted MORB mantle
EM	Enriched mantle
FOZO	Focal zone
Ga	Billion years ago
GOE	Great oxygenation event
Gyr	Billion years
HIMU	High mu (μ)
ICPMS	Inductively coupled plasma mass spectrometry
LLSVP	Large low-shear-velocity province
Ma	Million years ago
MORB	Mid-ocean ridge basalt
Myr	Million years
OIB	Ocean island basalt
PREM	Preliminary reference Earth model
TIMS	Thermal ionisation mass spectrometry
ULVZ	Ultra low velocity zone

Parameters, variables and other notation

Symbols and units for parameters used in the numerical models presented in this thesis:

Symbol	Parameter	Unit
C_V	Specific heat at constant volume	J kg^{-1} K^{-1}
$\mathbf{g}$	Gravitational acceleration	m s^{-2}
H	Radiogenic heat production	W m^{-3}
h	Mantle thickness	km
k	Thermal conductivity	W m^{-1} K^{-1}
$\mathbf{n}$	Normal vector	-
P	Pressure	Pa
Ra	Rayleigh number	-
T	Temperature	K
t	Time	s
$\mathbf{t}$	Tangential vector	-
$\mathbf{u}$	Fluid velocity	m s^{-1}
α	Thermal expansion coefficient	K^{-1}
γ	Grüneisen parameter	-
η	Viscosity	Pa s
κ	Thermal diffusivity	m^2 s^{-1}
ρ	Density	kg m^{-3}
σ	Stress tensor	Pa
τ	Deviatoric stress field	Pa

Other notation

Other notation found throughout the thesis:

Symbol	Description
B	Buoyancy ratio
C	Bulk Composition
d	Average distance from regression line
κ	^{232}Th/^{238}U
λ	Decay constant (s^{-1})
μ	^{238}U/^{204}Pb
ρb	Excess lower mantle basalt density
τ_{Pb}	Pb pseudo-isochron age

APPENDIX B

DERIVATION OF PB PSEUDO-ISOCHRON

Isochron equations take the general form,

$$R = R_i + R_P(e^{\lambda t} - 1) \tag{B.1}$$

where R is the measured ratio of the daughter isotope to a stable primordial isotope (^{204}Pb in the case of the U-Th-Pb system), R_i and R_P respectively are the initial ratio of the daughter isotope and parent isotope to the same stable primordial isotope, λ is the decay constant for the parent isotope and t is time. As such, the corresponding isochron equations for ^{238}U-^{206}Pb and ^{235}U-^{207}Pb are,

$$\frac{^{206}\mathrm{Pb}}{^{204}\mathrm{Pb}} = \left(\frac{^{206}\mathrm{Pb}}{^{204}\mathrm{Pb}}\right)_i + \frac{^{238}\mathrm{U}}{^{204}\mathrm{Pb}}\left(e^{\lambda_{238}t} - 1\right) \tag{B.2}$$

and

$$\frac{^{207}\mathrm{Pb}}{^{204}\mathrm{Pb}} = \left(\frac{^{207}\mathrm{Pb}}{^{204}\mathrm{Pb}}\right)_i + \frac{^{235}\mathrm{U}}{^{204}\mathrm{Pb}}\left(e^{\lambda_{238}t} - 1\right) \tag{B.3}$$

The generally well accepted value of ^{238}U/^{235}U within Earth is 137.88 (Tatsumoto et al. 1973). If we let

$$\frac{^{238}\mathrm{U}}{^{204}\mathrm{Pb}} = \mu \tag{B.4}$$

then

$$\frac{^{235}\mathrm{U}}{^{204}\mathrm{Pb}} = \frac{\mu}{137.88}. \tag{B.5}$$

Substituting B.4 and B.5 into B.2 and B.3 we get,

$$\frac{^{206}\mathrm{Pb}}{^{204}\mathrm{Pb}} = \left(\frac{^{206}\mathrm{Pb}}{^{204}\mathrm{Pb}}\right)_i + \mu\left(e^{\lambda_{238}t} - 1\right) \tag{B.6}$$

and

$$\frac{^{207}\mathrm{Pb}}{^{204}\mathrm{Pb}} = \left(\frac{^{207}\mathrm{Pb}}{^{204}\mathrm{Pb}}\right)_i + \frac{\mu}{137.88}\left(e^{\lambda_{238}t} - 1\right). \tag{B.7}$$

If we subtract the initial daughter to ^{204}Pb ratio from both sides then we can re-write the isochron equations as,

$$\delta\frac{^{206}\mathrm{Pb}}{^{204}\mathrm{Pb}} = \mu\left(e^{\lambda_{238}t} - 1\right) \tag{B.8}$$

and

$$\delta\frac{^{207}\mathrm{Pb}}{^{204}\mathrm{Pb}} = \frac{\mu}{137.88}\left(e^{\lambda_{235}t} - 1\right). \tag{B.9}$$

Combining the two new isochron equations gives us a new equation which depends only on Pb isotope ratios

$$\frac{\delta^{207}\mathrm{Pb}/^{204}\mathrm{Pb}}{\delta^{206}\mathrm{Pb}/^{204}\mathrm{Pb}} = \frac{\left(e^{\lambda_{235}t} - 1\right)}{137.88\left(e^{\lambda_{238}t} - 1\right)}. \tag{B.10}$$

APPENDIX C

LINKS TO ANIMATIONS

Here you will find hyperlinks to animated videos produced from output of simulations featured in this thesis. Clicking on the links will take you to a OneDrive folder containing the relevant files. Videos are also hosted on ORCA under supplementary material.

Chapter 3 Videos

Video1

Chapter 4 & 5 Videos

XSDENS cases
DGAS cases
STRAT
DGASDENS cases